

1

CAMPINAS STATE UNIVERSITY

2

DOCTORAL THESIS

3

4 **Search of Z and Higgs boson decaying into  $\Upsilon + \gamma$   
5 in pp collisions at CMS/LHC**

6

7 *Author:*

Felipe Torres da Silva de Araujo

*Supervisor:*

Dr. José Augusto Chinellato

*Co-Supervisor:*

Dr. Alberto Franco de Sá Santoro

8

*A thesis submitted in fulfillment of the requirements  
9 for the degree of Doctor of Physics*

10

*in the*

11

Graduate Program of  
12 "Gleb Wataghin" Institute of Physics

13

October 18, 2020

14 “Sometimes science is a lot more art than science. A lot of people don’t get that.”

15

Rick Sanchez

16 “Então, que seja doce. Repito todas as manhãs, ao abrir as janelas para deixar entrar o sol ou o  
17 cinza dos dias, bem assim, que seja doce. Quando há sol, e esse sol bate na minha cara amassada do  
18 sono ou da insônia, contemplando as partículas de poeira soltas no ar, feito um pequeno universo;  
19 repito sete vezes para dar sorte: que seja doce que seja doce que seja doce e assim por diante. Mas,  
20 se alguém me perguntasse o que deverá ser doce, talvez não saiba responder. Tudo é tão vago como  
21 se fosse nada.”

22

Caio Fernando Abreu

23 CAMPINAS STATE UNIVERSITY

24 *Abstract*

25 "Gleb Wataghin" Institute of Physics

26 Doctor of Physics

27 **Search of Z and Higgs boson decaying into  $\Upsilon + \gamma$  in pp collisions at CMS/LHC**

28 by Felipe Torres da Silva de Araujo

29 This thesis presents the study on searches for rare decays of Standard Model bosons to quarkonia.  
30 The searches are performed on data collected during the 2016 data taking of the CMS detector, at  
31 center-of-mass energy  $\sqrt{s} = 13$  TeV. Standard Model Higgs and Z bosons decaying to a  $\Upsilon(1S, 2S, 3S)$   
32 and a photon, with subsequent decay of the  $\Upsilon(1S, 2S, 3S)$  to  $\mu^+ \mu^-$  are performed using integrated  
33 luminosity of  $35.86 \text{ fb}^{-1}$  from proton-proton collisions. No significant excess above the background-  
34 only assumption is observed. A limit at 95% confidence level, is set on the  $H \rightarrow \Upsilon(1S, 2S, 3S) + \gamma$   
35 decay branching fraction at  $(6.8, 7.1, 6.0) \times 10^{-4}$  and on  $Z \rightarrow \Upsilon(1S, 2S, 3S) + \gamma$  decay branching  
36 fraction at  $(2.6, 2.3, 1.3) \times 10^{-6}$ , using the  $CL_s$  method. Contributions given from 2016 to 2018 to  
37 the operation, maintenance and R&D for Phase-2 Upgrade of Resistive Plate Chambers (RPC) at  
38 CMS are also presented.

DRAFT

39

## *Acknowledgements*

40 I would like to thank:

- 41 • the Campinas State University for providing the institutional support for this study;
- 42 • the Rio de Janeiro State University for the cooperation with Campinas State University in  
43 their high-energy physics program. This was a key factor for this study;
- 44 • the National Council for Scientific and Technological Development (CNPq) for the financial  
45 support for this work;
- 46 • the European Laboratory for Particle Physics (CERN) for the construction and operation of  
47 the Large Hadron Collider (LHC);
- 48 • the Compact Muon Solenoid (CMS) collaboration for the construction, operation and provi-  
49 sion of the instrumental means for this study.

DRAFT

## 50 Todo list

51	■ Spontaneous Symmetry break and the Higgs Boson . . . . .	11
----	--	----

DRAFT

# 52 Contents

53	<b>Abstract</b>	iii
54	<b>Acknowledgements</b>	v
55	<b>1 Introduction</b>	1
56	<b>2 Standard Model and rare Z and Higgs decays to quarkonia</b>	5
57	2.1 Standard Model and Local Gauge Invariance . . . . .	5
58	2.1.1 Local Gauge Invariance . . . . .	6
59	2.1.2 The Standard Model . . . . .	8
60	Quantum Chromodinamics . . . . .	9
61	Electroweak Theory . . . . .	10
62	Standard Model Lagrangian and the Scalar Sector . . . . .	11
63	2.2 SM and Higgs results . . . . .	11
64	2.2.1 Standard Model vector bosons at CMS . . . . .	11
65	2.2.2 Higgs boson at CMS . . . . .	14
66	2.3 Rare Z and Higgs decays to quarkonia . . . . .	18
67	2.4 Recent results . . . . .	21
68	<b>3 Experimental Setup</b>	25
69	3.1 The Large Hadron Collider . . . . .	25
70	3.2 The Compact Muon Solenoid - CMS . . . . .	27
71	3.2.1 Coordinate system . . . . .	29
72	3.3 Tracker . . . . .	30
73	3.4 Electromagnetic Calorimeter . . . . .	31
74	3.5 Hadronic Calorimeter . . . . .	32
75	3.6 Muon System . . . . .	33
76	3.6.1 Drift Tubes . . . . .	33
77	3.6.2 CSC . . . . .	34
78	3.6.3 RPC . . . . .	35
79	3.7 Trigger and Data Acquisition . . . . .	35
80	3.8 Particle Flow Algorithim . . . . .	35
81	<b>4 Physics Analysis</b>	39
82	4.1 Datasets and simulated events . . . . .	40
83	4.1.1 Data samples . . . . .	40

84	4.1.2 Simulated datasets . . . . .	40
85	4.2 Contribution of the $\Upsilon(nS)$ polarisation . . . . .	43
86	4.3 Kinematical studies using MC generator . . . . .	43
87	4.4 Event selection . . . . .	47
88	4.5 Trigger and physics object selection (Group I) . . . . .	47
89	4.5.1 Trigger . . . . .	47
90	4.5.2 Muon Identification . . . . .	48
91	4.5.3 Photon Identification . . . . .	49
92	4.5.4 Kinematical distributions . . . . .	49
93	4.6 Kinematical selection (Group II) . . . . .	59
94	4.7 Event categorization and yields . . . . .	67
95	4.7.1 R9 reweighting . . . . .	67
96	4.7.2 Event counting and yields . . . . .	68
97	4.8 Background modeling . . . . .	69
98	4.9 Signal modeling . . . . .	77
99	4.10 Systematic uncertainties . . . . .	83
100	4.10.1 Uncertainties on the predicted yields . . . . .	83
101	4.10.2 Uncertainties that affect the signal fits . . . . .	84
102	4.11 Modeling Cross checks . . . . .	87
103	<b>5 Results and conclusion</b>	<b>93</b>
104	5.1 The $CL_s$ formalism for upper limits setting at CMS . . . . .	93
105	5.2 Branching fraction upper limits . . . . .	96
106	<b>6 CMS Resistive Plate Chambers - RPC</b>	<b>99</b>
107	6.1 Resistive Plate Chambers . . . . .	99
108	6.1.1 Principles and operation modes . . . . .	99
109	6.2 CMS Resistive Plate Chambers . . . . .	101
110	6.2.1 Performance . . . . .	104
111	6.3 Contribution to the CMS RPC project . . . . .	106
112	6.3.1 RPC Operation - Shifts and Data Certification . . . . .	107
113	6.4 RPC Online Software . . . . .	108
114	6.4.1 iRPC R&D . . . . .	109
115	6.4.2 LS2 and the RPC Standard Maintenance . . . . .	115
116	HV maintenance . . . . .	115
117	LV and control maintenance . . . . .	116
118	Detector commissioning . . . . .	117
119	<b>Bibliography</b>	<b>119</b>

# 120 List of Figures

<small>121</small>	1.1	Dimuon mass distribution collected with various dimuon triggers. The light gray continuous distribution represents events collected with inclusive dimuon triggers with high $p_T$ thresholds. The dataset corresponding to an integrated luminosity of 13.1 $fb^{-1}$ was collected during the 25 ns LHC running period at 13 TeV in 2016. Source: [7].	<small>124</small> 2
<small>125</small>	2.1	Elementary particles of the Standard Model, with their masses charges and spin. Those particles can be divided in two classes: boson (the interaction/force carriers) and the fermions, which are divided in three generations. Source: [12].	<small>126</small> 6
<small>128</small>	2.2	(a) Di-boson cross section ratio comparison to theory: Theory predictions updated to latest NNLO calculations where available compared to predictions in the CMS papers and preliminary physics analysis summaries. Source: [20]. (b) Summary of the cross sections of pure Electroweak (EWK) interactions among the gauge bosons presented as a ratio compared to theory. Source: [20].	<small>130</small> 12
<small>133</small>	2.3	Summary of the cross section measurements of Standard Model processes at CMS. Source: [20].	<small>134</small> 13
<small>135</small>	2.4	(a) Standard Model Higgs boson production cross sections at $\sqrt{s} = 13$ TeV as a function of Higgs boson mass. The tH production cross section accounts for $t$ -channel and $s$ -channel only (no $tWH$ production). The VBF process is indicated here as $q\bar{q}H$ . The theoretical uncertainties are indicated as shaded bands around the lines. Source: [22]. (b) Standard Model Higgs boson decay branching ratios for different decay channels. The theoretical uncertainties are indicated as shaded bands around the lines. Source: [22].	<small>136</small> 15
<small>142</small>	2.5	Example of leading order Standard Model Higgs boson production model diagrams. Source: [23].	<small>143</small> 15
<small>144</small>	2.6	(a) The diphoton invariant-mass distribution for the 7 and 8 TeV datasets (points), with each event weighted by the predicted $S/(S + B)$ ratio of its event class. The solid and dotted lines give the results of the signal-plus-background and background-only fit, respectively. The light and dark bands represent the $\pm 1$ and $\pm 2$ standard deviation uncertainties respectively on the background estimate. The inset shows the corresponding unweighted invariant-mass distribution around $m_{\gamma\gamma} = 125$ GeV. Source: [4]. (b) Distribution of the observed four-lepton invariant mass from the combined 7 and 8 TeV data for the $H \rightarrow ZZ \rightarrow 4\ell$ analysis (points). The prediction for the expected $Z+X$ and $ZZ(Z\gamma^*)$ background are shown by the dark and light histogram, respectively. The open histogram gives the expected distribution for a Higgs boson of mass 125 GeV. Source: [4].	<small>150</small> 16
<small>154</small>			

155	2.7	Signal strength modifiers for the production modes, (a) $\mu^i$ , and for the decay channels, (b) $\mu^f$ . The thick (thin) black lines report the $1\sigma$ ( $2\sigma$ ) confidence intervals. The thick blue and red lines report the statistical and systematic components of the $1\sigma$ confidence intervals. Source: [34]. . . . .	17
156			
157			
158			
159	2.8	A summary of the measured Higgs boson mass in the $H \rightarrow ZZ \rightarrow 4l$ and $H \rightarrow \gamma\gamma$ decay channels, and for the combination of the two is presented here. The statistical (wider, yellow-shaded bands), and total (black error bars) uncertainties are indicated. The (red) vertical line and corresponding (grey) shaded column indicate the central value and the total uncertainty of the Run 1 + 2016 combined measurement, respectively. Source: [30]. . . . .	18
160			
161			
162			
163			
164			
165	2.9	(a) T the $m_{\mu\mu}$ distribution for the weighted combination of all event categories used in the analysis. The upper panel is dominated by the gluon-gluon fusion categories with many data events but relatively small $S/(S + B)$ . The lower panel shows the residuals after background subtraction, with the best-fit SM $H \rightarrow \mu\mu$ signal con- tribution with $m_H = 125.38$ GeV indicated by the red line. The measured signal strength is $1.19^{+0.41}_{-0.39}(\text{stat})^{+0.17}_{-0.16}(\text{sys})$ . Source: [25]. (b) The best-fit estimates for the reduced coupling modifiers extracted for fermions and weak bosons from the resolved $\kappa$ -framework model compared to their corresponding prediction from the SM. The error bars represent 68% CL intervals for the measured parameters. The lower panel shows the ratios of the measured coupling modifiers values to their SM predictions. Source: [25]. . . . .	19
166			
167			
168			
169			
170			
171			
172			
173			
174			
175			
176	2.10	Example of leading order diagrams for the indirect and direct production mechanisms. In theses diagrams, the $h$ can also be understood as a $Z$ or a Higgs boson. . . . .	21
177			
178	2.11	Expected relative variation of the branching ratio for the $H \rightarrow \Upsilon(nS) + \gamma$ to $k_b$ , where $k_b = g(Hb\bar{b})/g(Hb\bar{b})_{SM}$ is the ratio for the observed and expected Yukawa coupling oh $Hb\bar{b}$ . Source: [38] . . . . .	22
179			
180			
181	3.1	The LHC is the last ring (dark grey line) in a complex chain of particle accelerators. The smaller machines are used in a chain to help boost the particles to their final energies and provide beams to a whole set of smaller experiments. Source: [62]. . . . .	26
182			
183			
184	3.2	Overview of the CMS experiment and its subdetectors. Source: [67]. . . . .	28
185	3.3	Schematic cross section through the CMS tracker. Each line represents a detec- tor module. Double lines indicate back-to-back modules which deliver stereo hits. Source: [2]. . . . .	30
186			
187			
188	3.4	Longitudinal section view of the ECAL and its components. Source: [2]. . . . .	31
189	3.5	Longitudinal section view of the HCAL and its components. The barrel calorimeter (HB) covers the central region, inside the solenoid, the outer calorimeter covers also the central region, but it is positioned on the outside the solenoid. The endcap calorimeter (HE) covers the forward region and it is complemented by the forward calorimeter (HF), which uses Cherenkov light detectors made of radiation-hard quartz fibers. Source: [2]. . . . .	33
190			
191			
192			
193			
194			
195	3.6	Longitudinal section view of the ECAL and its components. Source: [75]. . . . .	34

196	3.7	The figure illustrates how the information from each subdetector is used in order to identify the different high-level objects in the Particle-Flow algorithm. Source: [79]. . .	36
197			
198	4.1	A diagram for the reconstructed invariant mass of the $\mu\mu\gamma$ final state. The blue and gray regions represent the Full Combinatorial and $\Upsilon+\gamma$ Combinatorial contributions, respectively, while the yellow and red regions represent the Resonant background and the signal region. . . . .	40
199			
200	4.2	Distributions of $\cos\theta$ of $\Upsilon \rightarrow \mu\mu$ and $\gamma^* \rightarrow \mu\mu$ . The orange distribution is the $Z \rightarrow \Upsilon(1S, 2S, 3S) + \gamma$ sample before reweighting (Unpolarized); the blue and gray distributions are $Z \rightarrow \Upsilon(1S, 2S, 3S)$ sample after reweighting, for the Transverse and Longitudinal Polarization. . . . .	44
201			
202	4.3	Generator level distributions of main variables for $Z \rightarrow \Upsilon(1S, 2S, 3S) + \gamma$ : Transverse momenta of the leading/trailing $p_T$ muon and the photon, pseudorapidity ( $\eta$ ) and $\phi$ of the muons and the photon, distances $\Delta R$ between the two muons and between the muons and the photon. All the distributions shown in the figure are normalized to the unity of area. . . . .	45
203			
204	4.4	Generator level distributions of main variables for $H \rightarrow \Upsilon(1S, 2S, 3S) + \gamma$ : Transverse momenta of the leading/trailing $p_T$ muon and the photon, pseudorapidity ( $\eta$ ) and $\phi$ of the muons and the photon, distances $\Delta R$ between the two muons and between the muons and the photon. All the distributions shown in the figure are normalized to the unity of area. . . . .	46
205			
206	4.5	The $p_T$ muon distributions from data and signal events for Z decaying in $\Upsilon(1S, 2S, 3S) + \gamma$ after Group I of selection cuts, where on left are presenting the trailing muons and on right are the leading muons. The plots are normalized to the unit of area. . . .	50
207			
208	4.6	The $\eta$ muon distributions from data and signal events of Z decaying in $\Upsilon(1S, 2S, 3S) + \gamma$ after Group I of selection cuts, where on left are presenting the trailing muons and on right are the leading muons. The plots are normalized to the unit of area. . . .	50
209			
210	4.7	The $\phi$ muon distributions from data and signal events of Z decaying in $\Upsilon(1S, 2S, 3S) + \gamma$ after Group I of selection cuts, where on left are presenting the trailing muons and on right are the leading muons. The plots are normalized to the unit of area. . . .	51
211			
212	4.8	The $p_T$ photon distributions from data and signal events for Z decaying in $\Upsilon(1S, 2S, 3S) + \gamma$ Group I of selection cuts. The plots normalized to the unit of area. . . . .	51
213			
214	4.9	The $\eta$ photon distributions from data and signal events of Z decaying in $\Upsilon(1S, 2S, 3S) + \gamma$ after Group I of selection cuts. The plot is normalized to the unit of area. . . . .	51
215			
216	4.10	The $\phi$ photon distributions from data and signal events of Z decaying in $\Upsilon(1S, 2S, 3S) + \gamma$ after Group I of selection cuts. The plot is normalized to the unit of area. . . . .	52
217			
218	4.11	The $p_T$ distributions for the reconstructed $\Upsilon(1S, 2S, 3S)$ in the left and for Z in the right from data and signal events for Z decaying in $\Upsilon(1S, 2S, 3S) + \gamma$ after Group I of selection cuts. The plots are normalized to the unit of area. . . . .	52
219			
220	4.12	The $\eta$ distributions for $\Upsilon(1S, 2S, 3S)$ in the left and for Z in the right from data and signal events for Z decaying in $\Upsilon(1S, 2S, 3S) + \gamma$ after Group I of selection cuts. The plots are normalized to the unit of area. . . . .	52
221			

237	4.13 The $\phi$ distributions for $\Upsilon(1S, 2S, 3S)$ in the left and for Z in the right from data and signal events for Z decaying in $\Upsilon(1S, 2S, 3S) + \gamma$ after Group I of selection cuts. The plots are normalized to the unit of area. . . . .	53
238		
239		
240	4.14 The $\Delta R$ distributions between the photon and the leading muon (left) and the trailing muon (right) for for Z decaying in $\Upsilon(1S, 2S, 3S) + \gamma$ from data and signal events after Group I of selection cuts. The plots are normalized to the unit of area. . . . .	53
241		
242		
243	4.15 Left: The $\Delta R$ distributions between reconstructed dimuon ( $\mu\mu$ ) system and the photon. Right: absolute value of the $\Delta\phi$ between the leading muon and the photon for for Z decaying in $\Upsilon(1S, 2S, 3S) + \gamma$ from data and signal events after Group I of selection cuts. The plots are normalized to the unit of area. . . . .	53
244		
245		
246		
247	4.16 The ratio for the transverse momentum of the reconstructed Upsilon and the reconstructed Z mass ( $p_T^{\mu\mu}/M_{\mu\mu\gamma}$ - left) and the ratio for the transverse energy of the reconstructed Photon and the reconstructed Z mass ( $E_T^{\mu\mu}/M_{\mu\mu\gamma}$ - right) distribution for Z decaying in $\Upsilon(1S, 2S, 3S) + \gamma$ from data and signal events after Group I of selection cuts. The plots are normalized to the unit of area. . . . .	54
248		
249		
250		
251		
252	4.17 The dimuon mass distribution of the reconstructed $\Upsilon(1S, 2S, 3S)$ from data and signal events for Z decaying after Group I of selection cuts. The plot is normalized to the number of events. "Signal" stands for the $Z \rightarrow \Upsilon(1S, 2S, 3S) + \gamma$ sample (scaled by a factor of $\times 100$ ) and "Background" corresponds to the peaking background ( $Z \rightarrow \mu\mu\gamma_{FSR}$ ) sample (scaled by a factor of x3). . . . .	54
253		
254		
255		
256		
257	4.18 The $p_T$ muon distributions from data and signal events for Higgs decaying in $\Upsilon(1S, 2S, 3S) + \gamma$ after Group I of selection cuts, where on left are presenting the trailing muons and on right are the leading muons. The plots are normalized to the unit of area. . . .	54
258		
259		
260	4.19 The $\eta$ muon distributions from data and signal events of Higgs decaying in $\Upsilon(1S, 2S, 3S) + \gamma$ after Group I of selection cuts, where on left are presenting the trailing muons and on right are the leading muons. The plots are normalized to the unit of area. . . .	55
261		
262		
263	4.20 The $\phi$ muon distributions from data and signal events of Higgs decaying in $\Upsilon(1S, 2S, 3S) + \gamma$ after Group I of selection cuts, where on left are presenting the trailing muons and on right are the leading muons. The plots are normalized to the unit of area. . . .	55
264		
265		
266	4.21 The $p_T$ photon distributions from data and signal events for Higgs decaying in $\Upsilon(1S, 2S, 3S) + \gamma$ Group I of selection cuts. The plot is normalized to the unit of area. . . . .	55
267		
268		
269	4.22 The $\eta$ photon distributions from data and signal events of Higgs decaying in $\Upsilon(1S, 2S, 3S) + \gamma$ after Group I of selection cuts. The plot is normalized to the unit of area. . . . .	56
270		
271	4.23 The $\phi$ photon distributions from data and signal events of Higgs decaying in $\Upsilon(1S, 2S, 3S) + \gamma$ after Group I of selection cuts. The plot is normalized to the unit of area. . . . .	56
272		
273	4.24 The $p_T$ distributions for $\Upsilon(1S, 2S, 3S)$ in the left and for Higgs in the right from data and signal events for Higgs decaying in $\Upsilon(1S, 2S, 3S) + \gamma$ after Group I of selection cuts. The plots are normalized to the unit of area. . . . .	56
274		
275		
276	4.25 The $\eta$ distributions for $\Upsilon(1S, 2S, 3S)$ in the left and for Higgs in the right from data and signal events for Higgs decaying in $\Upsilon(1S, 2S, 3S) + \gamma$ after Group I of selection cuts. The plots are normalized to the unit of area. . . . .	57
277		
278		

279	4.26 The $\phi$ distributions for $\Upsilon(1S, 2S, 3S)$ in the left and for Higgs in the right from data 280 and signal events for Higgs decaying in $\Upsilon(1S, 2S, 3S) + \gamma$ after Group I of selection 281 cuts. The plots are normalized to the unit of area. . . . .	57
282	4.27 The $\Delta R$ distributions between the photon and the leading muon (left) and the trailing 283 muon (right) for Higgs decaying in $\Upsilon(1S, 2S, 3S) + \gamma$ from data and signal events 284 after Group I of selection cuts. The plots are normalized to the unit of area. . . . .	57
285	4.28 Left: The $\Delta R$ distributions between reconstructed dimuon ( $\mu\mu$ ) system and the 286 photon. Right: absolute value of the $\Delta\phi$ between the leading muon and the photon 287 for for Higgs decaying in $\Upsilon(1S, 2S, 3S) + \gamma$ from data and signal events after Group 288 I of selection cuts. The plots are normalized to the unit of area. . . . .	58
289	4.29 The ratio for the transverse momentum of the reconstructed Upsilon and the recon- 290 structed Higgs mass ( $p_T^{\mu\mu}/M_{\mu\mu\gamma}$ - left) and the ratio for the transverse energy of the 291 reconstructed Photon and the reconstructed Higgs mass ( $E_T^{\mu\mu}/M_{\mu\mu\gamma}$ - right) distribu- 292 tion for Higgs decaying in $\Upsilon(1S, 2S, 3S) + \gamma$ from data and signal events after Group 293 I of selection cuts. The plots are normalized to the unit of area. . . . .	58
294	4.30 The dimuon mass distribution of the reconstructed $\Upsilon(1S, 2S, 3S)$ from data and signal 295 events for Higgs decaying after Group I of selection cuts. This plot is normalized the 296 expected number of events. The plot is normalized to the number of events. "Signal" 297 stands for the $H \rightarrow \Upsilon(1S, 2S, 3S) + \gamma$ sample (scaled by a factor of $\times 60000$ ) and 298 "Background" corresponds to the peaking background (Higgs Dalitz Decay) sample 299 (scaled by a factor of $\times 400$ ). . . . .	58
300	4.31 The $p_T$ muon distributions from data and signal events for Z decaying in $\Upsilon(1S, 2S, 3S)$ 301 $+ \gamma$ after Group I of selection cuts, where on left are presenting the trailing muons 302 and on right are the leading muons. The plots are normalized to the number of 303 events. Signal sample is scaled by a factor of $\times 100$ . . . . .	59
304	4.32 The $\eta$ muon distributions from data and signal events of Z decaying in $\Upsilon(1S, 2S, 3S)$ 305 $+ \gamma$ after Group I of selection cuts, where on left are presenting the trailing muons 306 and on right are the leading muons. The plots are normalized to the number of 307 events. Signal sample is scaled by a factor of $\times 100$ . . . . .	60
308	4.33 The $\phi$ muon distributions from data and signal events of Z decaying in $\Upsilon(1S, 2S, 3S)$ 309 $+ \gamma$ after Group I of selection cuts, where on left are presenting the trailing muons 310 and on right are the leading muons. The plots are normalized to the number of 311 events. Signal sample is scaled by a factor of $\times 100$ . . . . .	60
312	4.34 The $p_T$ photon distributions from data and signal events for Z decaying in $\Upsilon(1S, 2S, 3S)$ 313 $+ \gamma$ all (Group I+II) selection cuts. The plot is normalized to the number of events. 314 Signal sample is scaled by a factor of $\times 100$ . . . . .	60
315	4.35 The $\eta$ photon distributions from data and signal events of Z decaying in $\Upsilon(1S, 2S, 3S)$ 316 $+ \gamma$ after all (Group I+II) selection cuts. The plot is normalized to the number of 317 events. Signal sample is scaled by a factor of $\times 100$ . . . . .	61
318	4.36 The $\phi$ photon distributions from data and signal events of Z decaying in $\Upsilon(1S, 2S, 3S)$ 319 $+ \gamma$ after all (Group I+II) selection cuts. The plot is normalized to the number of 320 events. Signal sample is scaled by a factor of $\times 100$ . . . . .	61

321	4.37 The $p_T$ distributions for $\Upsilon(1S, 2S, 3S)$ in the left and for Z in the right from data 322 and signal events for Z decaying in $\Upsilon(1S, 2S, 3S) + \gamma$ after all (Group I+II) selection 323 cuts. The plots are normalized to the number of events. Signal sample is scaled by 324 a factor of $\times 100$ ). . . . . .	61
325	4.38 The $\eta$ distributions for $\Upsilon(1S, 2S, 3S)$ in the left and for Z in the right from data and 326 signal events for Z decaying in $\Upsilon(1S, 2S, 3S) + \gamma$ after all (Group I+II) selection 327 cuts. The plots are normalized to the number of events. Signal sample is scaled by 328 a factor of $\times 100$ ). . . . . .	62
329	4.39 The $\phi$ distributions for $\Upsilon(1S, 2S, 3S)$ in the left and for Z in the right from data and 330 signal events for Z decaying in $\Upsilon(1S, 2S, 3S) + \gamma$ after all (Group I+II) selection 331 cuts. The plots are normalized to the number of events. Signal sample is scaled by 332 a factor of $\times 100$ ). . . . . .	62
333	4.40 The $\Delta R$ distributions between the photon and the leading muon (left) and the trailing 334 muon (right) for $\Upsilon(1S, 2S, 3S)$ from data and signal events for Z decaying after all 335 (Group I+II) selection cuts. The plots are normalized to the number of events. Signal 336 sample is scaled by a factor of $\times 100$ ). . . . . .	62
337	4.41 The ratio for the transverse momentum of the reconstructed Upsilon and the re- 338 constructed Z mass ( $p_T^{\mu\mu}/M_{\mu\mu\gamma}$ - left) and the ratio for the transverse energy of the 339 reconstructed Photon and the reconstructed Z mass ( $E_T^{\mu\mu}/M_{\mu\mu\gamma}$ - right) distribution 340 for $\Upsilon(1S, 2S, 3S)$ from data and signal events for Z decaying after all (Group I+II) 341 selection cuts. The plots are normalized to the number of events. Signal sample is 342 scaled by a factor of $\times 100$ ). . . . . .	63
343	4.42 The $p_T$ muon distributions from data and signal events for Higgs decaying in $\Upsilon(1S, 2S, 3S)$ 344 $+ \gamma$ after Group I of selection cuts, where on left are presenting the trailing muons 345 and on right are the leading muons. The plots are normalized to the number of 346 events. Signal sample is scaled by a factor of $\times 600000$ ). . . . . .	63
347	4.43 The $\eta$ muon distributions from data and signal events of Higgs decaying in $\Upsilon(1S, 2S, 3S)$ 348 $+ \gamma$ after Group I of selection cuts, where on left are presenting the trailing muons 349 and on right are the leading muons. The plots are normalized to the number of 350 events. Signal sample is scaled by a factor of $\times 600000$ ). . . . . .	63
351	4.44 The $\phi$ muon distributions from data and signal events of Higgs decaying in $\Upsilon(1S, 2S, 3S)$ 352 $+ \gamma$ after Group I of selection cuts, where on left are presenting the trailing muons 353 and on right are the leading muons. The plots are normalized to the number of 354 events. Signal sample is scaled by a factor of $\times 600000$ ). . . . . .	64
355	4.45 The $p_T$ photon distributions from data and signal events for Higgs decaying in 356 $\Upsilon(1S, 2S, 3S) + \gamma$ all (Group I+II) selection cuts. The plot is normalized to the 357 number of events. Signal sample is scaled by a factor of $\times 600000$ ). . . . . .	64
358	4.46 The $\eta$ photon distributions from data and signal events of Higgs decaying in $\Upsilon(1S, 2S, 3S)$ 359 $+ \gamma$ after all (Group I+II) selection cuts. The plot is normalized to the number of 360 events. Signal sample is scaled by a factor of $\times 600000$ ). . . . . .	64

361	4.47 The $\phi$ photon distributions from data and signal events of Higgs decaying in $\Upsilon(1S, 2S, 3S)$		
362	+ $\gamma$ after all (Group I+II) selection cuts. The plot is normalized to the number of		
363	events. Signal sample is scaled by a factor of c). . . . .	65	
364	4.48 The $p_T$ distributions for $\Upsilon(1S, 2S, 3S)$ in the left and for Higgs in the right from		
365	data and signal events for Higgs decaying in $\Upsilon(1S, 2S, 3S) + \gamma$ after all (Group I+II)		
366	selection cuts. The plots are normalized to the number of events. Signal sample is		
367	scaled by a factor of $\times 600000$ ). . . . .	65	
368	4.49 The $\eta$ distributions for $\Upsilon(1S, 2S, 3S)$ in the left and for Higgs in the right from data		
369	and signal events for Higgs decaying in $\Upsilon(1S, 2S, 3S) + \gamma$ after all (Group I+II)		
370	selection cuts. The plots are normalized to the number of events. Signal sample is		
371	scaled by a factor of $\times 600000$ ). . . . .	65	
372	4.50 The $\phi$ distributions for $\Upsilon(1S, 2S, 3S)$ in the left and for Higgs in the right from data		
373	and signal events for Higgs decaying in $\Upsilon(1S, 2S, 3S) + \gamma$ after all (Group I+II)		
374	selection cuts. The plots are normalized to the number of events. Signal sample is		
375	scaled by a factor of $\times 600000$ ). . . . .	66	
376	4.51 The $\Delta R$ distributions between the photon and the leading muon (left) and the trailing		
377	muon (right) for $\Upsilon(1S, 2S, 3S)$ from data and signal events for Higgs decaying after		
378	all (Group I+II) selection cuts. The plots are normalized to the number of events.		
379	Signal sample is scaled by a factor of $\times 600000$ ). . . . .	66	
380	4.52 The ratio for the transverse momentum of the reconstructed Upsilon and the re-		
381	constructed Higgs mass ( $p_T^{\mu\mu}/M_{\mu\mu\gamma}$ - left) and the ratio for the transverse energy		
382	of the reconstructed Photon and the reconstructed Higgs mass ( $E_T^{\mu\mu}/M_{\mu\mu\gamma}$ - right)		
383	distribution for $\Upsilon(1S, 2S, 3S)$ from data and signal events for Higgs decaying after		
384	all (Group I+II) selection cuts. The plots are normalized to the number of events.		
385	Signal sample is scaled by a factor of $\times 600000$ ). . . . .	66	
386	4.53 Data and MC of the R9 variable, before and after the reweighting. Barrel (left) and		
387	Endcap (right). . . . .	67	
388	4.54 Peaking background for the $Z \rightarrow \Upsilon(1S, 2S, 3S) + \gamma$ analysis. $\mu\mu$ mass distribution		
389	(left) and $\mu\mu\gamma$ invariant mass distribution (right). From top to bottom categories:		
390	Inclusive, EB High R9, EB Low R9, EE. . . . .	71	
391	4.55 $\Upsilon$ control sample fit with Chebychev 1 <sup>st</sup> order for the background support and 3		
392	gaussian for the three $\Upsilon(1S, 2S, 3S)$ peaks. . . . .	72	
393	4.56 $Z \rightarrow \Upsilon(1S, 2S, 3S) + \gamma$ Background Modeling: $\mu\mu$ distribution. Inclusive (top left);		
394	EB High R9 (top right), EB Low R9 (bottom left), EE (bottom right). The pdfs		
395	projections are plotted with respect to the overall best choice of the statistica test. .	75	
396	4.57 $Z \rightarrow \Upsilon(1S, 2S, 3S) + \gamma$ Background Modeling: $\mu\mu\gamma$ distribution. Inclusive (top left);		
397	EB High R9 (top right), EB Low R9 (bottom left), EE (bottom right). The plotted		
398	<i>pdfs</i> corresponds to the best choice by the statistical test for each family. The signal		
399	region, from 80 GeV to 100 GeV was blinded. . . . .	75	
400	4.58 Peaking Background for the $H \rightarrow \Upsilon(1S, 2S, 3S) + \gamma$ analysis. $m_{\mu\mu}$ invariant mass		
401	distribution (left) and $m_{\mu\mu\gamma}$ invariant mass distribution (right). . . . .	76	

402	4.59 $H \rightarrow \Upsilon(1S, 2S, 3S) + \gamma$ Background Modeling: $m_{\mu\mu}$ distribution. The <i>pdfs</i> projections 403 are plotted with respect to the overall best choice of the statistical test. . . . .	76
404	4.60 $H \rightarrow \Upsilon(1S, 2S, 3S) + \gamma$ Background Modeling: $\mu\mu\gamma$ distribution. The plotted <i>pdfs</i> 405 corresponds to the best choice by the statistical test for each family. The signal 406 region, from 115 GeV to 135 GeV was blinded. . . . .	76
407	4.61 Signal Modeling for the $Z \rightarrow \Upsilon(1S, 2S, 3S) + \gamma$ analysis for Inclusive category. $m_{\mu\mu}$ 408 mass distribution (left) and $m_{\mu\mu\gamma}$ mass distribution (right). From top to bottom: 409 $\Upsilon(1S)$ , $\Upsilon(2S)$ , $\Upsilon(3S)$ . . . . .	78
410	4.62 Signal Modeling for the $Z \rightarrow \Upsilon(1S, 2S, 3S) + \gamma$ analysis for EB High R9 category. 411 $m_{\mu\mu}$ mass distribution (left) and $m_{\mu\mu\gamma}$ mass distribution (right). From top to bottom: 412 $\Upsilon(1S)$ , $\Upsilon(2S)$ , $\Upsilon(3S)$ . . . . .	79
413	4.63 Signal Modeling for the $Z \rightarrow \Upsilon(1S, 2S, 3S) + \gamma$ analysis for EB Low R9 category. 414 $m_{\mu\mu}$ mass distribution (left) and $m_{\mu\mu\gamma}$ mass distribution (right). From top to bottom: 415 $\Upsilon(1S)$ , $\Upsilon(2S)$ , $\Upsilon(3S)$ . . . . .	80
416	4.64 Signal Modeling for the $Z \rightarrow \Upsilon(1S, 2S, 3S) + \gamma$ analysis for EE category. $m_{\mu\mu}$ mass 417 distribution (left) and $m_{\mu\mu\gamma}$ mass distribution (right). From top to bottom: $\Upsilon(1S)$ , 418 $\Upsilon(2S)$ , $\Upsilon(3S)$ . . . . .	81
419	4.65 Signal Modeling for the $H \rightarrow \Upsilon(1S, 2S, 3S) + \gamma$ . $m_{\mu\mu}$ mass distribution (left) and 420 $m_{\mu\mu\gamma}$ mass distribution (right). From top to bottom: $\Upsilon(1S)$ , $\Upsilon(2S)$ , $\Upsilon(3S)$ . . . . .	82
421	4.66 Examples of the toy datasets fit ( $M_{\mu\mu}$ ), for the Z decay analysis, after the toy dataset 422 refit, for 1S, 2S and 3S (left to right), with $\mu_{true}$ equals to 20, 50, 100, 1000 (top to 423 bottom). The red lines corresponds to the background model (B), the green lines to 424 signal model (S), the blue lines to the total (S+B) and the dots is the toy dataset. . . . .	87
425	4.67 Examples of the toy datasets fit ( $M_{\mu\mu\gamma}$ ), for the Z decay analysis, after the toy dataset 426 refit, for 1S, 2S and 3S (left to right), with $\mu_{true}$ equals to 20, 50, 100, 1000 (top to 427 bottom). The red lines corresponds to the background model (B), the green lines to 428 signal model (S), the blue lines to the total (S+B) and the dots is the toy dataset. . . . .	88
429	4.68 Examples of the toy datasets fit ( $M_{\mu\mu}$ ), for the Higgs decay analysis, after the toy 430 dataset refit, for 1S, 2S and 3S (left to right), with $\mu_{true}$ equals to 100000, 200000, 431 300000, 1000000 (top to bottom). The red lines corresponds to the background model 432 (B), the green lines to signal model (S), the blue lines to the total (S+B) and the 433 dots is the toy dataset. . . . .	89
434	4.69 Examples of the toy datasets fit ( $M_{\mu\mu\gamma}$ ), for the Higgs decay analysis, after the toy 435 dataset refit, for 1S, 2S and 3S (left to right), with $\mu_{true}$ equals to 100000, 200000, 436 300000, 1000000 (top to bottom). The red lines corresponds to the background model 437 (B), the green lines to signal model (S), the blue lines to the total (S+B) and the 438 dots is the toy dataset. . . . .	90
439	4.70 Distribution of pulls ( $\frac{\mu_{fit} - \mu_{true}}{\sigma_{fit}}$ ), for the Z decay analysis, after the toy dataset refit, 440 for 1S, 2S and 3S (left to right), with $\mu_{true}$ equals to 20, 50, 100, 1000 (top to bottom). . . . .	91
441	4.71 Distribution of pulls ( $\frac{\mu_{fit} - \mu_{true}}{\sigma_{fit}}$ ), for the Higgs decay analysis, after the toy dataset 442 refit, for 1S, 2S and 3S (left to right), with $\mu_{true}$ equals to 100000, 200000, 300000, 443 1000000 (top to bottom). . . . .	92

444	5.1 Example of $f(\tilde{q}_\mu \mu, \hat{\theta}_\mu^{\text{obs}})$ $f(\tilde{q}_\mu \mu = 0, \hat{\theta}_{\mu=0}^{\text{obs}})$ distributions generated with toy MC. Source: [128]. . . . .	95
445		
446	5.2 Example of $f(\tilde{q}_\mu \mu, \hat{\theta}_\mu^{\text{obs}})$ $f(\tilde{q}_\mu \mu = 0, \hat{\theta}_{\mu=0}^{\text{obs}})$ distributions generated with toy MC. In the figure, $q$ must be read as $\tilde{q}$ . The green area shows the $p_{s+b}$ defined in 5.7, while the yellow one shows $p_b$ defined in 5.8. Source: [125]. . . . .	96
447		
448		
449	6.1 The Avalanche production process inside a RPC gap. (Top) The initial process and the secondary electron/ion generation. (Bottom) The overall charge distribution of an Avalanche between the electrodes. Source: [132]. . . . .	100
450		
451		
452	6.2 Streamer formation process. The distorted electric field around the high positive charge concentration enhances the ionization process, initiating secondary avalanches. Source: [132]. . . . .	101
453		
454		
455	6.3 RPC chamber on installed on station RE+4 of CMS Endcap. Source: [134]. . . . .	102
456		
457	6.4 R- $\phi$ (left) and R-Z (right) projections of the barrel Muon System. . . . .	103
458		
459	6.5 R-Z projections of the endcap Muon System (positive Z side). This is the same configuration for the 36 $\phi$ sectors. . . . .	104
460		
461		
462	6.6 RPC efficiencies (per chamber) over Run2 Integrated Luminosity for Barrel (left) and Endcap (right). Red lines indicates technical stops (TS) while grey ones indicates Year-End-Technical stops (YETS). The drop in the efficiency around $110 \text{ pb}^{-1}$ is related to a known operation mistake. Source: [145]. . . . .	105
463		
464		
465	6.7 RPC cluster size (CLS - per chamber) over Run2 Integrated Luminosity for Barrel (left) and Endcap (right). Red lines indicates technical stops (TS) while grey ones indicates Year-End-Technical stops (YETS). The drop in the cluster size around $110 \text{ pb}^{-1}$ is related to a known operation mistake. Source: [145]. . . . .	105
466		
467	6.8 Ohmic current history of W+0, RE+1, RE+4 and RE-4. The blank regions, from time to time, corresponds to technical stops (TS), when the detector is off. Source: [145].	106
468		
469	6.9 (a) Luminosity delivered by the LHC, recorded one by CMS and the certified (vali- dated), from the 22nd of April, 2016 to the 27th of October, 2016. (b) Efficiency of the certification process for each subsystem, from the 22nd of April, 2016 to the 27th of October, 2016. Total CMS efficiency is above 90%. Source: [146] . . . . .	107
470		
471		
472		
473	6.10 Upgrade of the RPC online software. . . . .	108
474		
475	6.11 Example of the updated screens, using Trigger Supervisor 5. . . . .	109
476		
477	6.12 $\eta$ projection of the Muon System subdetectors. In purple, is labeled the iRPCS to be installed during the CMS upgrade. . . . .	109
478		
479		
480	6.13 FEB configured 8 channels modes. Group should be understood as wire pad. Left: Logical diagram for OR2. Right: Logical diagram for AND2. . . . .	111
481		
482	6.14 FEB configured 2 channels modes. Left: Logical diagram for OR8. Group should be understood as wire pad. Right: Logical diagram for OR4AND2. . . . .	111
483		
484	6.15 Left: Setup mounted for commissioning. Two MWPC chamber on the top (chambers A and B) and two (chambers C and D) on the bottom with a RPC R&D in the middle. Right: Rack with all the services for the operation of these chambers. . . . .	112
485		

484	6.16	Coincidence rate of two chambers with respect to an arbitrary distance between 485       the two top planes. Measured in 10 minutes, for 2 logical combinations (OR8 and 486       OR4AND2). Applied high voltage: 2.65 kV. Threshold: 7 pC. Active area: readout 487       of 160 mm x 160 mm per chamber. . . . .	113
488	6.17	Individual rates (chambers A, B, C and D) and coincidence rates for two chambers 489       (A AND B, C AND D), for without $\gamma$ source (blue), a shielded $\gamma$ source (orange) and 490       an unshielded $\gamma$ source (green). Source sitting on top of chamber A. Applied high 491       voltage: 2.65 kV. Threshold: 7 pC. Active area: readout of 160 mm x 320 mm per 492       chamber. Logical combination: AND2 . . . . .	114
493	6.18	Left: Proposed adapter the chamber patch panel which make it possible to replace 494       a tripolar by a jupiter HV connector. Right: Try out of the proposed HV connector 495       replacement. . . . .	116
496	6.19	RPC Front-end board (FEB) used in the barrel chambers. . . . .	117
497	6.20	RPC FEB Commissioning Analyzer. . . . .	118

# List of Tables

499	2.1	Relative strength (with respect to the strong force) and effective range of action for the four fundamentals interactions. . . . .	5
500	2.2	Summary of cross section and branching ratio for $H/Z \rightarrow \Upsilon(1S, 2S, 3S) + \gamma \rightarrow \mu^+ \mu^- + \gamma$ analysis. The effective cross-section will be discussed in section 4.1.2. . . . .	20
501	2.3	Observed upper limits, by the ATLAS experiment, on the branching fractions for the Higgs and Z decays (last result). Detailed comparisons with the results obtained in this study will be presented in chapter 5. . . . .	22
502	2.4	Observed upper limits, by CMS, on the branching fractions for the Higgs and Z decays. The number are compatible with the ones obtained by ATLAS. The results presented for different polarization scenarios of the $J/\Psi$ . . . . .	23
503	4.1	Datasets simulated (MC) for 2016 conditions. Assuming that $\sigma(pp \rightarrow H)$ , taking into consideration all the simulated Higgs production modes, is $55.13\text{ pb}$ [99] and $\sigma(pp \rightarrow Z \rightarrow \mu\mu)$ is $57094.5\text{ pb}$ , including the next-to-next-to-leading order (NNLO) QCD contributions, and the next-to-leading order (NLO) electroweak corrections from fewz 3.1 [100] calculated using the NLO PDF set NNPDF3.0, with the phase space selection in invariant mass of the dimuon system of $m_{\mu\mu} > 50\text{ GeV}$ . For the Higgs Dalitz $\sigma$ , we consider only the gluon fusion contribution ( $\sigma_{ggF} = 48.6\text{ pb}$ ) [99]. The Higgs Dalitz Decay $BR_{SM}$ and the $Z \rightarrow \mu\mu\gamma_{FSR}$ were obtained with MCFM 6.6 [101] (as in the CMS search for Higgs Dalitz Decay in at $\sqrt{s} = 8\text{ TeV}$ [102]) and with MADGRAPH 5 _MC@NLO, respectively. The $BR_{\Upsilon(1S,2S,3S) \rightarrow \mu\mu}^{PDG} = (2.48, 1.93, 2.18) \times 10^{-2}$ is quoted from Particle Data Group report (PDG) [13]. The "Effective $\sigma$ " for the signal samples is $\sigma(pp \rightarrow Z(H)) \times BR_{SM} \times BR_{\Upsilon(nS) \rightarrow \mu\mu}^{PDG}$ . . . . .	42
504	4.2	Summary of the impact of reweighted of polarization contribution using several scenarios. . . . .	43
505	4.3	Conditions for a muon to pass the strict tracker requirements. . . . .	48
506	4.4	Number of events for the Z decay, before and after the full selection, per categorization scenarios. . . . .	68
507	4.5	Number of events for the H decay, before and after the full selection. . . . .	68
508	4.6	Modeling for each background source and mass component. . . . .	69
509	4.7	Modeling for each signal source and mass component. . . . .	77
510	4.8	A summary table of systematic uncertainties in the Z boson decaying in $\Upsilon(1S, 2S, 3S) + \gamma$ , affecting the final yields of the MC samples. . . . .	85
511	4.9	A summary table of systematic uncertainties in the Higgs boson decaying in $\Upsilon(1S, 2S, 3S) + \gamma$ , affecting the final yields of the MC samples. . . . .	86

533	4.10 A summary table of systematic uncertainties in the Z (H) decaying in $\Upsilon(1S, 2S, 3S) +$	
534	$\gamma$ , affecting the signal fits. . . . .	86
535	5.1 Summary table for the limits on branching ratio of $Z \rightarrow \Upsilon(1S, 2S, 3S)\gamma$ and $H \rightarrow$	
536	$\Upsilon(1S, 2S, 3S)\gamma$ decays. . . . .	97
537	5.2 Summary table for the limits on branching ratio of $Z \rightarrow \Upsilon(1S, 2S, 3S)\gamma$ , for the two	
538	possible categorization scenarios. . . . .	97

# 539 1 Introduction

540 The Standard Model (SM) have been proven successful over the last decades by its accordance  
 541 with results from many collider experiments, the Large Electron–Positron Collider (LEP) [1] and  
 542 its experiments created the experimental conditions to the discovery of the electroweak bosons,  $W^\pm$   
 543 and  $Z$ . The Tevatron experiments (D0 and CDF) allowed the discovery of the top quark. These  
 544 were 3 of the four heaviest components of the SM. The missing piece was the, so called, Higgs  
 545 Boson, or any other explanation to the mass of the other SM particles.

546 In 2012, during CMS' Run1, at center-of-mass energy  $\sqrt{s} = 13$  TeV, researchers from CMS [2] and  
 547 ATLAS [3], two collaborations with experiments located at the Large Hadron Collider (LHC), a 27  
 548 km long circular proton-proton collider build and operated by CERN, announced the discovery a  
 549 new particle [4, 5], with characteristics compatibles with the Brout-Englert-Higgs boson, completing  
 550 the SM picture proposed up to fifty years ago. In 2013, Francois Englert and Peter Higgs were  
 551 awarded with the Noble Prize for "*for the theoretical discovery of a mechanism that contributes to  
 552 our understanding of the origin of mass of subatomic particles, and which recently was confirmed  
 553 through the discovery of the predicted fundamental particle, by the ATLAS and CMS experiments at  
 554 CERN's Large Hadron Collider*" [6].

555 On top of the success of the Higgs program at CMS, there is much to be understood, e.g. pin down  
 556 the coupling constants of the Higgs boson with all three generations of quarks and leptons, its mass  
 557 and its full width, evaluate non-zero CP-odd components in Higgs interactions, investigate double  
 558 Higgs production and its self-coupling constant and possible extensions of the SM close to the Higgs  
 559 sector and explore rare decays of Higgs. The former one, specially rare decays involving quarkonia,  
 560 such as  $H \rightarrow M\gamma$ , where  $M$  is a meson state, are a very good scenario to investigate the Higgs  
 561 interaction with other SM particles other than the direct decay. This one would be overwhelmed  
 562 by the immense background coming from QCD events. The same analogy can be extended to the  
 563  $Z$  boson, which also serves as a benchmark for the Higgs study.

564 The present study corresponds to  $35.86 fb^{-1}$  of data taken by CMS during 2016, during the Run2,  
 565 at center-of-mass energy  $\sqrt{s} = 13$  TeV, in which an upper limit on the branching fraction for  
 566  $H/Z \rightarrow \Upsilon(1S, 2S, 3S)(\rightarrow \mu\mu) + \gamma$  is determined.

567 Because of its narrow resolution, muons play a special role not only for this study, but for CMS,  
 568 in general. Not only the Higgs studies heavily depends of muonic final states (for decay channels,  
 569 such as  $H \rightarrow \mu\mu$  and  $H \rightarrow ZZ \rightarrow 4l$  and identification of the production modes), but also muon  
 570 final states are very important to a whole broad of physics process accessible at CMS/LHC. The  
 571 Figure 1.1 presents the the distribution of dimuon invariant mass reconstructed from different double  
 572 muon triggers, with different requirements in pseudorapidity and transverse momentum. It is clear

573 how the muons at CMS broaden the set of interesting process giving access to light quark hadrons  
 574 to high transverse momentum phenomena.

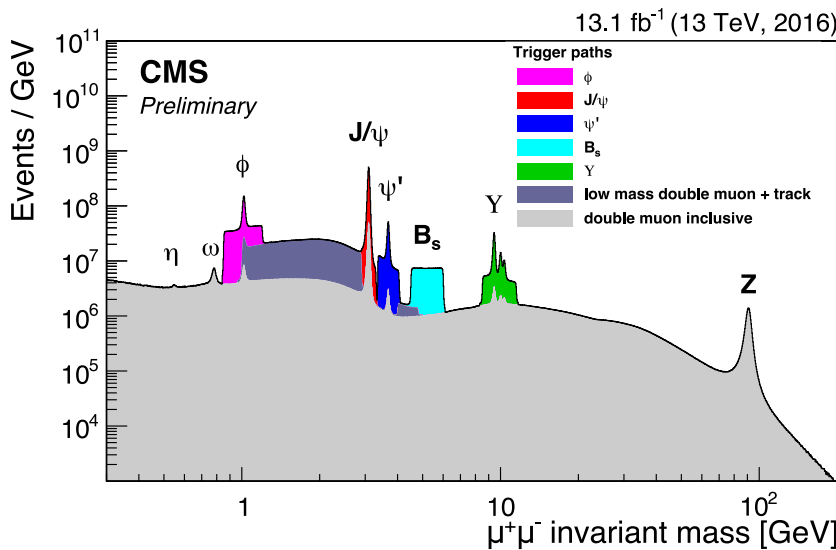


Figure 1.1: Dimuon mass distribution collected with various dimuon triggers. The light gray continuous distribution represents events collected with inclusive dimuon triggers with high  $p_T$  thresholds. The dataset corresponding to an integrated luminosity of  $13.1 \text{ fb}^{-1}$  was collected during the 25 ns LHC running period at 13 TeV in 2016. Source: [7].

575 In this scenario, a contribution to the muon system of CMS is a meaningfully one to the col-  
 576 laboration. In this document it is described the contributions given to Resistive Plate Chamber  
 577 (RPC) subdetector, including its commissioning, instrumentation for its upgrade, operation and  
 578 maintenance.

579 This document is organized as follows: Chapter 1 is this introduction. Chapter 2 is devoted to  
 580 a review of the theoretical foundations of this study and the motivations for the study of Rare  
 581 Z and Higgs decays involving quarkonia. Chapter 3 is a review of the collider and experimental  
 582 setup, LHC and CMS respectively. Chapter 4 is a detailed description of the data sample and the  
 583 applied analysis procedure, as well as the statistical modeling and the branching fraction upper limit  
 584 extraction. Chapter 5 is a reviews of the Resistive Plate Chamber technology for muon detection  
 585 at CMS and the details of the contributions given to this subdetector.

586 Wherever figures and tables' sources are not provided, the source is the author himself.

587 In this document, the convention of natural units is implicitly used: the vacuum speed of light ( $c$ ),  
 588 the reduced Planck constant ( $\hbar$ ) and electric permittivity ( $\epsilon_0$ ) are normalized to unity. In this way,  
 589 SI units are:

- 590 • mass ( $[m]$ ) = GeV,
- 591 • energy ( $[E]$ ) = GeV,
- 592 • momemtum ( $[p]$ ) = GeV,
- 593 • mass ( $[m]$ ) = GeV,
- 594 • time ( $[t]$ ) = 1/GeV,

- 595      • length ( $[s]$ ) = 1/GeV.

596      The Einstein summation convention is also followed. In the notation,  $y = A^i B_i$  stands for  $y =$   
597       $\sum_{i=0}^n A^i B_i = A^1 B_1 + A^2 B_2 + A^3 B_3 + \dots + A^n B_n$ .

DRAFT

DRAFT

## 598 2 Standard Model and rare Z and Higgs 599 decays to quarkonia

### 600 2.1 Standard Model and Local Gauge Invariance

601 Physics understands matter and how it interacts in terms of two components: fundamental forces  
 602 and elementary particles. From the weakest to the strongest, the fundamental forces are: Gravita-  
 603 tional, Weak, Electromagnetic and Strong. All share common characteristics like, being mediated  
 604 by particles <sup>1</sup>, being relevant within some effective range and have a associate a charge-like quan-  
 605 tity (i.e. an intrinsic characteristic of the object) that defines whether or not, particles might be  
 606 subjected to a specific interaction.

607 Along with the fundamental interactions, the Standard Model [8–11] (or simply *SM*) defines every  
 608 existing matter in the Universe as a set of fundamental quantum objects, with properties that pre-  
 609 scribes their interaction. Those objects are said to be fundamental since, in the context of the SM,  
 610 they are the smallest possible components of matter. We shall refer to them as *Fundamental Parti-*  
*611 cles*. There four of those mediating particles (force carriers), gluon ( $g$  - for the strong interaction),  
 612 photon ( $\gamma$  - for the electromagnetic interaction), Z (neutral) and  $W^\pm$  (for weak interaction), all of  
 613 them being vector bosons (spin 1). Besides the interaction mediators, described at Table 2.1, the  
 614 fundamental particles are divided in two groups (*quarks* and *leptons*), with three generations, each.  
 615 These are not force carriers, but elementary particles, endowed with charge-like characteristics that  
 616 allow them to interact by exchange the vector bosons. Those are the building blocks of Matter in  
 617 our Universe.

618 Figure 2.1 summarizes their properties. Table 2.1 presents the relative strength and effective range,  
 619 for each one of the four fundamental interactions. It is important to stress that, the gravitational  
 620 force is not study subject of the Standard Model.

Table 2.1: Relative strength (with respect to the strong force) and effective range of action for the four fundamentals interactions.

	Mediator	Relative Strength	Effective Range
Gravitational	Graviton	$10^{-41}$	$\infty$
Weak	W and Z	$10^{-16}$	$10^{-18}$ m
Electromagnetic	Photon	$10^{-3}$	$\infty$
Strong	Gluon	1	$10^{-15}$ m

<sup>1</sup>There is no evidence of the existence of the Graviton (force carrier associated to the gravitational force), even though, it is theorized by models that wish to comprehend gravity in a quantum perspective.

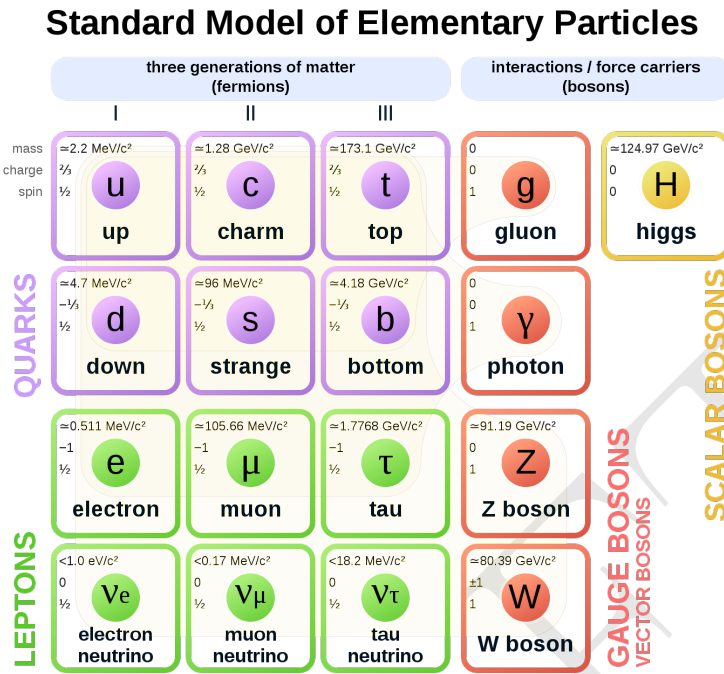


Figure 2.1: Elementary particles of the Standard Model, with their masses charges and spin. Those particles can be divided in two classes: boson (the interaction/force carriers) and the fermions, which are divided in three generations. Source: [12].

621 There are six quarks, up and down ( $u$  and  $d$  - first generation), charm and strange ( $c$  and  $s$  - second  
622 generation), top and bottom ( $t$  and  $b$  - third generation), in increasing invariant mass order of the  
623 generations. Since they interact through all the three fundamental forces of the SM, they are said  
624 to possess electrical charge (for the electromagnetic interaction), flavour (for the weak interaction)  
625 and color (for the strong). Their generational counterparts, the leptons, don't interact via strong  
626 force, that is why they are said to have only flavour and electric charge. The leptons are electron  
627 and electron neutrino ( $e$  and  $\nu_e$  - first generation), muon and muon neutrino ( $\mu$  and  $\nu_\mu$  - second  
628 generation) and tau and tau neutrino ( $\tau$  and  $\nu_\tau$  - third generation). The neutrinos, within the  
629 SM, are massless, even though, experimental measurements have shown that they actually have  
630 mass [13]. Neutrinos are also electrically neutral, meaning that they only interact through weak  
631 interactions.

632 Figure 2.1 also presents the Higgs Boson ( $H$ ) which is part of the SM and shall be discussed later.

### 633 2.1.1 Local Gauge Invariance

634 Within the Standard Model, the theoretical basis that describe the fundamental interactions are  
635 derived from a common principle: the local gauge invariance. According to Salam and Ward [14]:

636 "Our basic postulate is that it should be possible to generate strong, weak and electro-  
637 magnetic interaction terms [...], by making local gauge transformations on the kinetic-  
638 energy terms in the free Lagrangian for all particles."

639 Taking the Quantum Electrodynamics (QED) as an example: the quantum field theory that de-  
 640 scribes the electromagnetic interactions, consider the Dirac equation, in the covariant form, for a  
 641 particle with mass  $m$ , charge  $-e$  and spin  $1/2$ , i.e. a electron:

$$(i\gamma^\mu \partial_\mu + m)\psi(x) = 0, \quad (2.1)$$

642 where  $\psi(x)$  is a spinor, describing the wave-function and  $\gamma^\mu$  are gamma-matrices. This equation  
 643 can be obtained from the lagrangian  $\mathcal{L}$ <sup>2</sup> of a free particle, in the form of

$$\mathcal{L}_0 = i\bar{\psi}(x)\gamma^\mu \partial_\mu \psi(x) - m\bar{\psi}\psi(x), \quad (2.2)$$

644 when applied to the Euler-Lagrange equation.

645 It is clear that, the Dirac Equation (2.1) and its lagrangian (2.2) are invariant under a global phase  
 646 transformation.

$$\psi(x) \rightarrow \psi'(x) = \exp(-ie\alpha)\psi(x), \quad (2.3)$$

647 where  $\alpha$  is a constant (global phase shift).

648 The same is not true when  $\alpha$  is not a constant, but actually a local phase transformation, a gauge  
 649 transform.

$$\psi(x) \rightarrow \psi'(x) = \exp(-ie\alpha(x))\psi(x) \quad (2.4)$$

650 In this case, the derivative of  $\alpha(x)$  will introduce a new term that would break the invariance. To  
 651 recover it, the covariant derivative operator should be modified as follows:

$$\partial_\mu \rightarrow D_\mu = \partial_\mu - ieA_\mu. \quad (2.5)$$

652 This modification introduces the concept of the gauge field  $A_\mu$ , associated to a particle of spin 1  
 653 and zero mass, the photon. This term should transform under gauge, in the following manner:

$$A_\mu \rightarrow A'_\mu = A_\mu - \partial_\mu \alpha(x). \quad (2.6)$$

654 Modifications 2.5 and 2.6 are sufficient not only to make the free particle Dirac Equation and its  
 655 lagrangian gauge transformation invariant (Equations 2.7 and 2.8 ), but also it naturally gives rise  
 656 to an interaction term associated to the gauge field  $A_\mu$ .

$$(i\gamma^\mu \partial_\mu + m)\psi(x) = -e\gamma_\mu A_\mu(x)\psi(x) \quad (2.7)$$

---

<sup>2</sup>Even though, the  $\mathcal{L}$  actually represents the lagrangian density, in this document we shall refer to it as simply lagrangian.

$$\begin{aligned}\mathcal{L} \rightarrow \mathcal{L}' &= i\bar{\psi}'(x)\gamma^\mu D_\mu\psi'(x) - m\bar{\psi}'\psi'(x) \\ \mathcal{L}' &= \mathcal{L}_0 + e\bar{\psi}(x)\gamma^\mu A_\mu\psi(x) = \mathcal{L}\end{aligned}\tag{2.8}$$

657 Interesting to notice that the  $\mathcal{L}_0$  term, on 2.8, corresponds to the electron kinetic energy plus its  
 658 mass contribution (the free particle lagrangian), while the second corresponds to the interaction of  
 659 the electron ( $\psi(x)$ ) and the electromagnetic field. On this basis,  $e$  is said to be the generator of the  
 660 electromagnetic four-potential,  $A_\mu$ . One could add the energy contribution of the electromagnetic  
 661 field itself, by adding a term like:

$$\mathcal{L}_{EM} = -\frac{1}{4}F_{\mu\nu}F^{\mu\nu},\tag{2.9}$$

where:

$$F_{\mu\nu} = \partial_\mu A_\nu - \partial_\nu A_\mu\tag{2.10}$$

662 is the electromagnetic field tensor.

663 It can be proven that applying 2.10 on the Euler-Lagrange equations, this will give us the Maxwell's  
 664 Equations for the vacuum,  $\partial_\mu F^{\mu\nu} = 0$ <sup>3</sup>. One could also expect that a field mass contribution in as  
 665 below, could be introduced, as well.

$$\frac{1}{2}m_{photon}A_\mu A^\mu\tag{2.11}$$

666 This one would break the gauge invariance, therefore we can imply that the photon should be  
 667 massless.

668 The QED is said to be a gauge theory with the symmetry group  $U(1)$ . The  $U(1)$  description comes  
 669 from Lie Algebra, where 2.5 and 2.6 are transformations of gauge  $\alpha$  (in one dimension) to which  
 670 the system is symmetric (invariant), then unitary and generated by a  $1 \times 1$  matrix ( $e$ ).

### 671 2.1.2 The Standard Model

672 Taking profit of the Local Gauge Invariance as path to introduce interactions in a quantum field  
 673 theory (QFT), such as for the QED, the Standard Model can be defined as a QFT of the gauge  
 674 group  $SU_C(3) \times SU_L(2) \times U_Y(1)$ . All the experimental results we have, so far (Section 2.2), give us  
 675 support to this definition.

676 In this context there are 8 spin 1 bosons (called gluons) for the  $SU_C(3)$  component, which corre-  
 677 sponds to the strong interaction, plus 4 bosons,  $W^\pm$ ,  $Z$  and the photon for the other components  
 678 (weak and electromagnetic interactions).

679 Hadrons are defined as colorless particles that interact strongly. They are bound states of quarks,  
 680 which also interact via strong force and have non-neutral color. Hadrons are divided in mesons

---

<sup>3</sup>A non-vacuum covariant form of the Maxwell's Equations would be  $\partial_\mu F^{\mu\nu} = j^\nu$ .

681 (spin integer) and barions (spin non-integer). Leptons are those particles that do not interact via  
 682 gluons.

683 **Quantum Chromodinamics**

684 Quantum Chromodynamics (QCD) is the  $SU_C(3)$  component of the SM, where  $SU$  stands for special  
 685 unitary group, to which the  $\det(e^{i\lambda_i}) = 1$ , where  $\lambda_i$  are the Gell-Mann matrices (the 8 generators  
 686 of the  $SU(3)$ ). It corresponds to the field of gluons, responsible for the strong interaction acting  
 687 on a charge-like degree of freedom: colour ( $c$ ). Gluons follow the same fashion as photons, they  
 688 are massless and have spin 1, but contrary to electromagnetism, the QCD is a non-abelian gauge  
 689 theory. This means that the force carriers (gluons) can interact with each other (self-coupling). In  
 690 other words, gluons are charged (coloured). In a more formal manner, the generators of this group  
 691 are non-commutative, as follows.

$$[T_a, T_b] = \left[ \frac{\lambda_a}{2}, \frac{\lambda_b}{2} \right] = i \sum_{c=1}^8 f_{ab}^c \lambda_c, \quad (2.12)$$

692 where  $f_{ab}^c$  are antisymmetric structure constants.

693 From a experimental perspective, the idea of colour begins with the observation of  $\Lambda^{++}$  [15]. It  
 694 could be only be composed by three up quarks, which would break Pauli Exclusion Principle <sup>4</sup>. This  
 695 observation demanded the inclusion of another degree of freedom, the colour, typically refereed as  
 696 RED, BLUE, GREEN and its anti-colours.

697 The QCD lagrangian for a quark of colour  $c$ , just the QED lagrangian for a electron of charge  $-e$ ,  
 698 is <sup>5</sup>:

$$\mathcal{L}_{QCD} = \bar{\psi}_c(x) (i\gamma^\mu D_\mu - m) \psi_c(x) - \frac{G_{\mu\nu}^c G_c^{\mu\nu}}{4}, \quad (2.13)$$

where

$$D_\mu = \partial_\mu - ig_s T_c G_\mu^c \quad (2.14)$$

and

$$G_{\mu\nu}^c = \partial_\mu G_\nu^c - \partial_\nu G_\mu^c - g_s f_{ab}^c G_\mu^a G_\nu^b \quad (2.15)$$

699 This lagrangian is local gauge invariant when the strength tensor 2.15 as:

$$G_\mu^c \rightarrow G_\mu^{c'} = G_\mu^c - \frac{1}{g_s} \partial_\mu \alpha_c(x) - f_{ab}^c \alpha_a(x) G_\mu^b \quad (2.16)$$

700 Coloured particles, such as quarks and gluons, are subjected to the phenomenon of Colour Con-  
 701 finement, which prohibits the direct observation of these particles. These can only be observed in  
 702 colourless bound states (hadrons). A isolated quark or gluon will immediately interact with the

<sup>4</sup>Two or more fermion can not be in the same quantum state.

<sup>5</sup>The total QD lagrangian would the sum over all possible states.

vacuum and initiates a hadronization process until a set of stable colourless particle is produced. As a consequence of the Colour Confinement and the self-coupling property of gluons, a bound state of gluons, Glueballs [16], is possible, even though there are no experimental clear evidences of its existence. This is one of the few open topics in the SM.

QCD is a perturbation theory which demands renormalization <sup>6</sup>. In a qualitative way, one could imagine that, as larger the distance on interaction is, more sea vacuum gluon pairs can contribute to the net colour charge, due to the self-coupling, increasing the total interaction strength. To cope the Colour Confinement and the self-coupling, one would redefine the the strong coupling constant as  $g_s = \sqrt{4\pi\alpha_s}$  (from 2.14, 2.15 and 2.16), where  $\alpha_s(Q^2) \propto \frac{\Lambda_{QCD}^2}{\ln Q^2}$ . In this situation, the coupling strength is related to the transferred momentum  $Q^2$ , in such a way that, in a highly energetic interaction (high  $Q^2$ , hence short distance) the coupling is weaker and the quarks and gluons involved, behave like a quasi-free particles, allowing the use of perturbation theory. This effect is known as Asymptotic Freedom, and its scale have already been measured by the LHC experiments [13].

## Electroweak Theory

The  $SU_L(2) \times U_Y(1)$  represents the Electroweak component of the SM. It is the unification of the Weak and Electromagnet interaction, under the same theory. Here two new degrees of freedom are introduced,  $L$  and  $Y$ . The former one is related to the chirality of  $SU(2)$  and the latter is the weak hypercharge. The generators of groups are the Pauli Matrices ( $T_i$ ) <sup>7</sup>, form the  $SU_L(2)$  and the electromagnetic generator structure for  $U_Y(1)$  (but for  $Y$ , instead of  $-e$ , as before). Since:

$$\begin{aligned}[T_a, T_b] &= i\epsilon^{abc}T_c, \\ [T_a, Y] &= 0\end{aligned}\tag{2.17}$$

where  $\epsilon^{abc}$  is the Levi-Civita tensor,  $SU_L(2)$  is also a non-abelian group.

The connection between electric charge  $Q$  and the weak charge is  $Y = Q - T_3$ , as such, QED ( $U_{EM}(1)$ ), as defined in Section 2.1.1 is derived from  $U_Y(1)$ .

In the Electroweak Theory, fermions can have left-handed or right-handed components of their wave-functions, according to their chirality. Left-handed components transform as doublets of  $(T, T_3)$  with eigenvalues  $(1/2, \pm 1/2)$  under  $SU_L(2)$  and the right-handed components transform as singlets ( $T = 0$ ). Weak interactions act only on left-handed fermions. That is the reason for the  $L$  subscript in the electroweak symmetry group definition.

<sup>6</sup>A techniques to deal with infinites that might arrive when calculating quantities in a QFT. In summary the total probability for the theory is required to re-sum to unity.

<sup>7</sup>The usual  $\sigma_i$  representation for the Pauli Matrices usually is reserved for the  $SU_{spin}(2)$  group.

---

**731 Standard Model Lagrangian and the Scalar Sector****732 Spontaneous Symmetry break and the Higgs Boson****733 2.2 SM and Higgs results**

734 The Standard Model have been proven extremely successful in describing what it is proposed to  
735 do. The discovery of the two highest invariant mass particles of the SM, the top quark [17, 18], by  
736 the CDF and 0 collaboration, at FERMILAB, and the Higgs Boson [4, 5], by CMS and ATLAS,  
737 at CERN, fill the two missing pieces of the SM puzzle, presented at Figure 2.1. In general, SM  
738 measurements presents very good agreement between theory and experiment, even when the Higgs  
739 boson is taken into account, once its mass has been established, the subsequent results tend to  
740 be found restricted within the expectations and constrained by the statistics and experimental  
741 sensitivity.

742 In this section, we shall briefly review some of the most relevant SM results from LHC, with special  
743 focus to  $Z$  and Higgs boson, subjects of the study.

**744 2.2.1 Standard Model vector bosons at CMS**

745 The success of the Standard Model relies mostly on its excellent agreement between its predictions  
746 and the measurements, even though there are still many open questions on fundamental particle  
747 physics [19], such as: How can we explain the number of fundamental particles known so far? Why  
748 matter and antimatter appear in the Universe in different proportions? What is the astrophysical  
749 dark matter? How could we unify the fundamental interactions? How to quantize gravity?

750 The Figures 2.2b, 2.2a and 2.3 presents a summary of relevant CMS results on SM measurements.  
751 The former one presents the ratio between the observed and expected cross section ( $\sigma_{exp}/\sigma_{theo}$ )  
752 for different di-boson production at NNLO calculations and pure electroweak processes, while the  
753 later have a summary of cross section measurements made by CMS. When theory and experiment  
754 agreement is not exact, one has to take into account the experimental limitations of one experiment,  
755 such as CMS and the many possible electroweak phenomena to be studied.

756 The open questions above are not subjected to the SM scope, but even within the SM there still  
757 relevant precision measurements [21] that are important to understand the validity of the SM and  
758 what other questions lies about the SM, at the threshold of the LHC experiments precision.

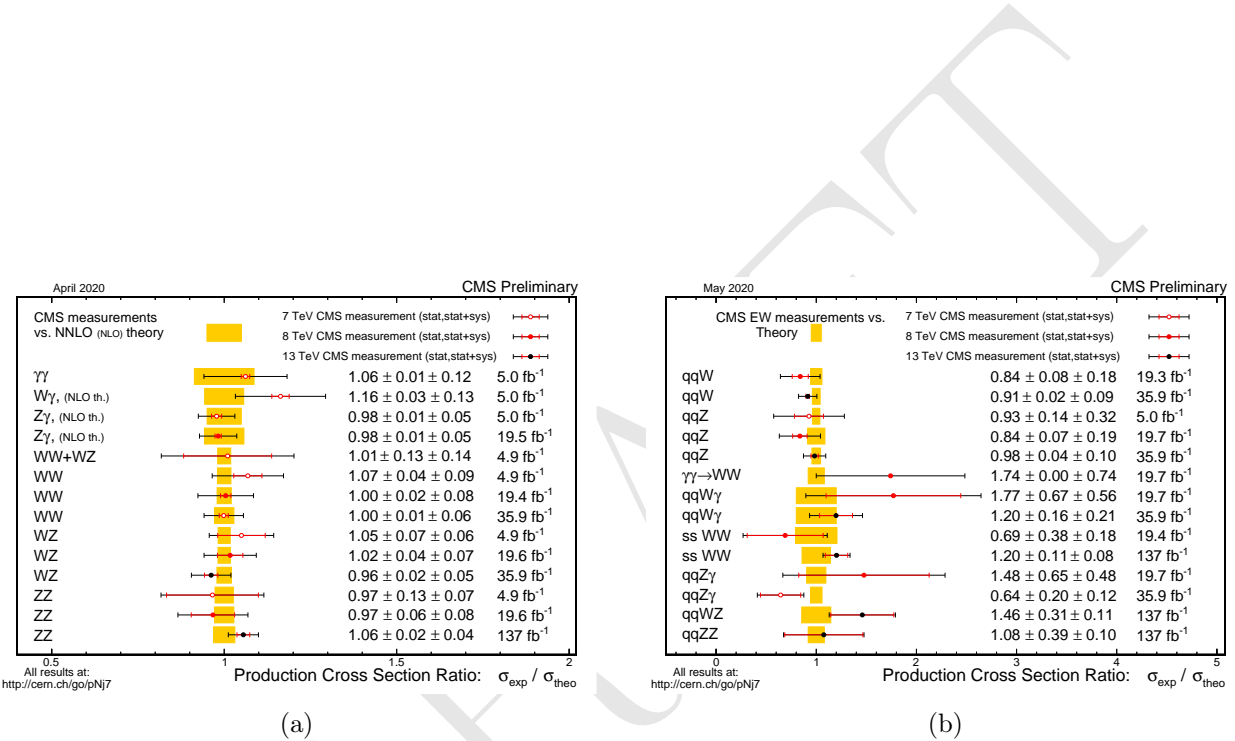


Figure 2.2: (a) Di-boson cross section ratio comparison to theory: Theory predictions updated to latest NNLO calculations where available compared to predictions in the CMS papers and preliminary physics analysis summaries. Source: [20]. (b) Summary of the cross sections of pure Electroweak (EWK) interactions among the gauge bosons presented as a ratio compared to theory. Source: [20].

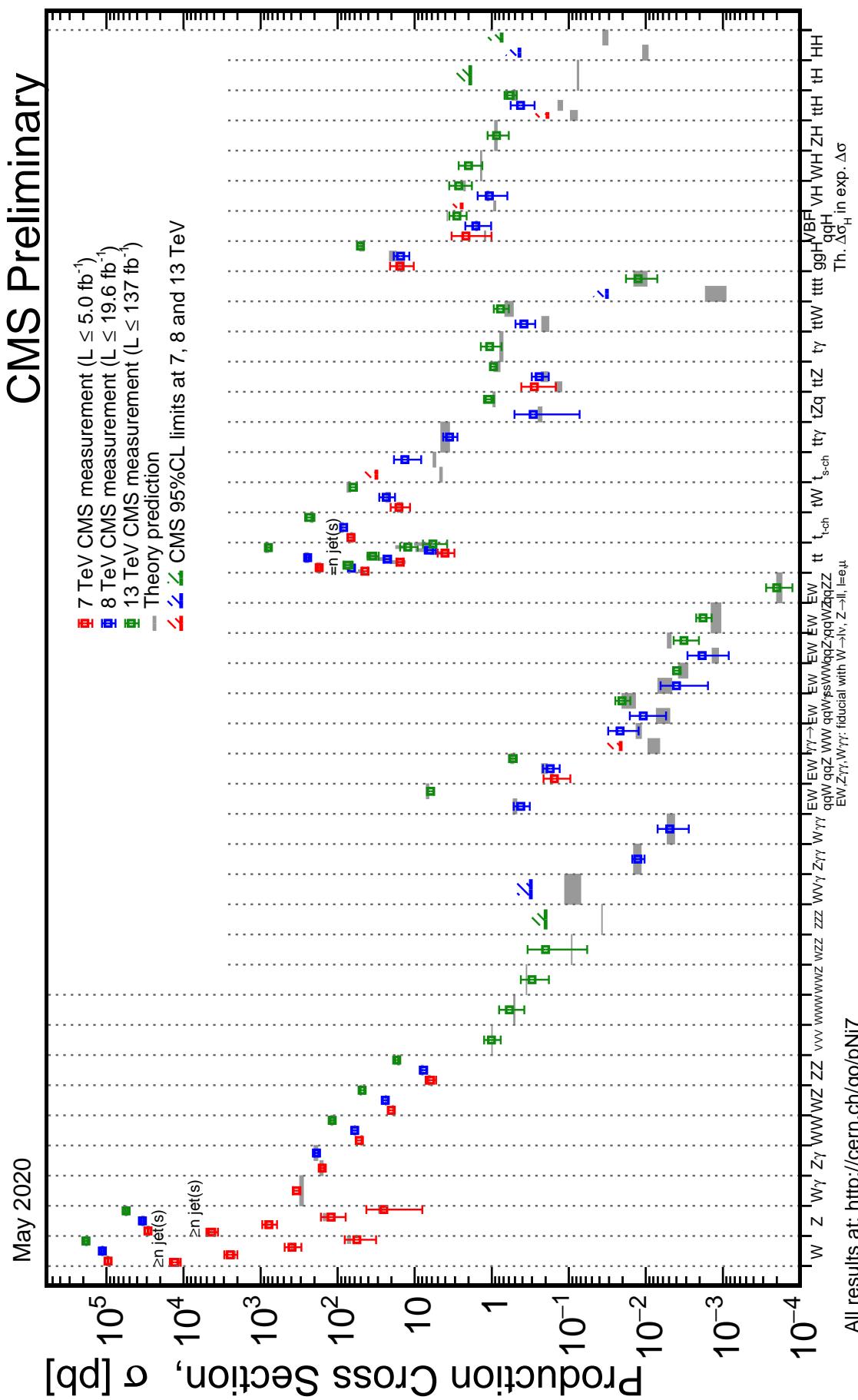


Figure 2.3: Summary of the cross section measurements of Standard Model processes at CMS. Source: [20].

### 759 2.2.2 Higgs boson at CMS

760 The Higgs may be produced at LHC proton-proton collisions by the following process, called  
 761 **Production Modes.** *state-of-art* SM cross section predictions were computed by the "LHC Higgs  
 762 Cross Section Working Group" [22] and are presented as a function of the Higgs mass is pre-  
 763 sented at Figure 2.4a and examples of leading order Feynmann diagrams of them are presented at  
 764 Figure 2.5, for the highest cross section production modes.

765 The **Gluon Fusion - ggF** - is the result of a gluon-gluon interaction which is mediated by a heavy  
 766 quark loop. Each quark contributing is suppressed by  $1/m_q^2$ . It is by far the one with highest cross  
 767 section. Its final state is composed only by a Higgs boson, which makes it harder to identify, since  
 768 there are no other auxiliary final state particle to tag it. In this decay, QCD radiative corrections  
 769 are very important and have been included the results of Figure 2.4a up to N3LO (next-to-next-  
 770 to-next-to-leading order, while electroweak corrections are computed up to NNLO. The **Associated**  
 771 **Vector Boson Production - VH** - a SM vector boson (Z or W) irradiate a Higgs. Due to its  
 772 clear electroweak signature (a final state with a Higgs and a vector boson), this production mode  
 773 enhances the signal, when the Higgs decay has a large contribution from QCD background, e.g.  
 774  $H \rightarrow b\bar{b}$ . This process is also called Higgs-Strahlung.

775 The third process is the **Vector Boson Fusion - VBFH** - in which the two quarks from the  
 776 initial state scatter by the emission a pair of vector bosons (ZZ or  $W^\pm W^\mp$ ). Those would interact  
 777 (fuse) and produce a Higgs in the final, associated with two back-to-back jets, from the initial state  
 778 quarks. The **Associated  $t\bar{t}$  Production - ttH** - and **Associated  $b\bar{b}$  Production - bbH** are very  
 779 similar process (especially in the scale of  $\sqrt{s} = 13$  TeV, where their cross sections almost match),  
 780 where the coupling of the heavy quark to the Higgs boson, contrary to what happens in the ggF  
 781 production, it is not with a virtual state of then.

782 The **Associated Single Top Production - tH** - is the production mode with the smallest cross  
 783 section, due to its destructive interference with other process. Without loss of generality, it is not  
 784 considered in this study.

785 The Higgs allowed **Decay Channel**, in the context of the Standard Model, is also a closet set,  
 786 which have also been subject of study of the "LHC Higgs Cross Section Working Group" [22].  
 787 Figure 2.4b presents their expected branching ratios.

788 The largest branching fraction is the decay to a  $b\bar{b}$  pair, which is, at  $\sqrt{s} = 13$  TeV, more than  
 789 the double of the next channel. The large cross section does not imply in being the most sensible  
 790 channel for the Higgs observation. One has to take into account the experimental sensitivity to this  
 791 final state (which rely on b-tagging techniques) and its enormous QCD background. Tagging on  
 792 an specific production modes is usually explored in this kind of study [24] to enhance the signal  
 793 to background ratio. Similar to  $b\bar{b}$ , decays to other SM dileptons are also usually studied, such as  
 794 dimuons [25],  $\tau\tau$  [26] and  $c\bar{c}$  [27].

795 Other decays include the  $VV$  state, where  $V$  is a electroweak vector boson ( $Z$  [28],  $W^\pm$  [29] and  
 796  $\gamma$  [30]). Even tough the branching fraction for these ones are relatively smaller, they offer a clear  
 797 signature for event selection, with reduced QCD background. It is important to notice that  $H \rightarrow Z\gamma$

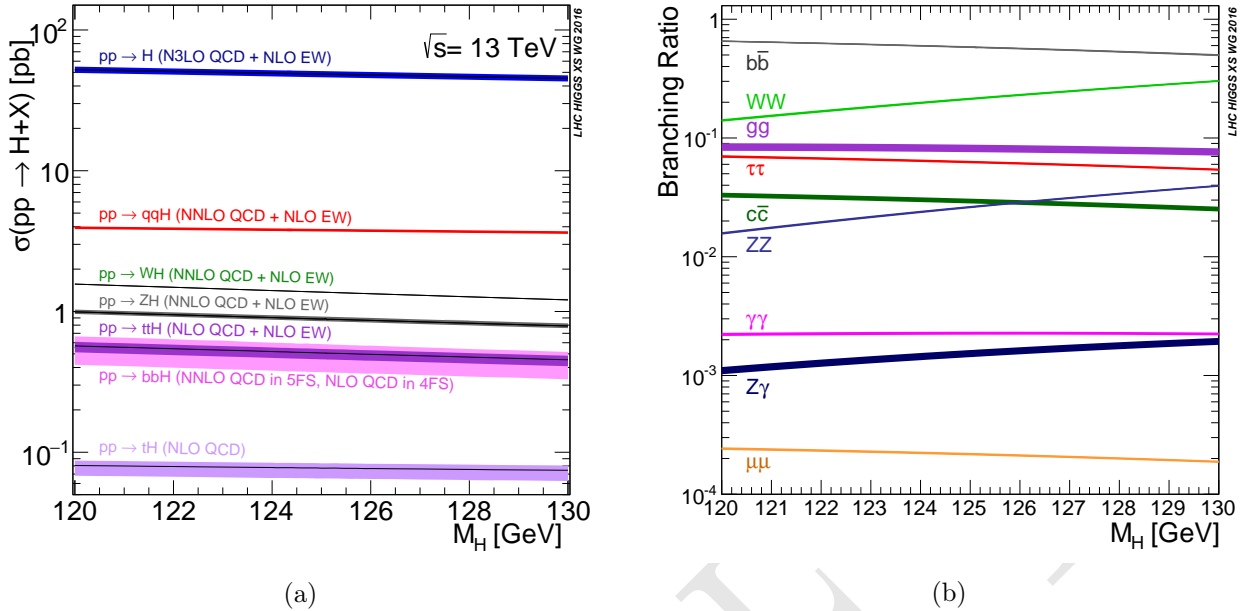


Figure 2.4: (a) Standard Model Higgs boson production cross sections at  $\sqrt{s} = 13$  TeV as a function of Higgs boson mass. The  $tH$  production cross section accounts for  $t$ -channel and  $s$ -channel only (no  $tWH$  production). The VBF process is indicated here as  $qqH$ . The theoretical uncertainties are indicated as shaded bands around the lines. Source: [22]. (b) Standard Model Higgs boson decay branching ratios for different decay channels. The theoretical uncertainties are indicated as shaded bands around the lines. Source: [22].

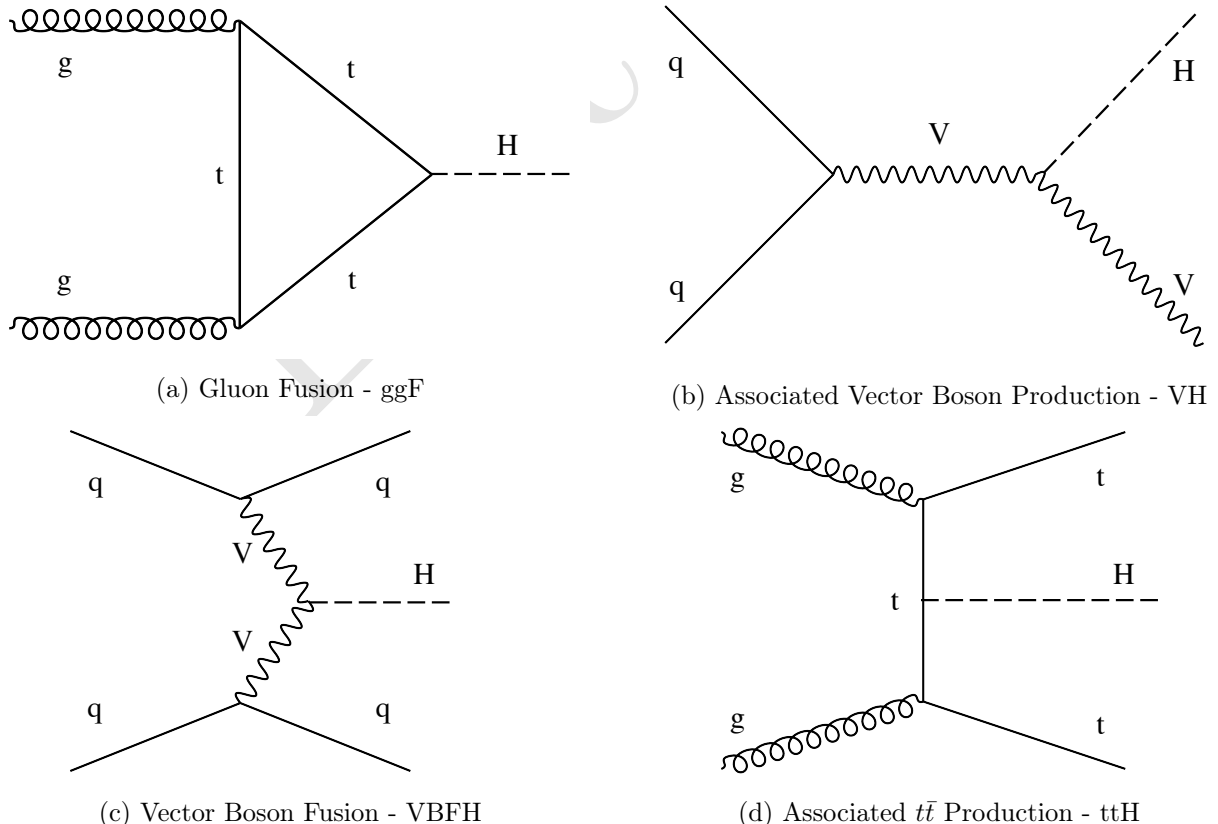


Figure 2.5: Example of leading order Standard Model Higgs boson production model diagrams. Source: [23].

also play a role in this decay mode. CMS (and ATLAS) has a very good sensitivity for leptonic final states of these bosons and for a direct measurement of photons, with resolutions to the order of 1% for the Higgs. Other channels will have resolutions larger than 10% [13].

Gluonic Higgs decays ( $H \rightarrow gg$ ) are allowed in the Standard Model, but they would be overwhelmed by the QCD background. This is considered to be measurable only in the context of a  $e^+e^-$  detector [31].

As already mentioned on Section ??, the Higgs have been found at CMS and ATLAS in 2012, with Run1 data at  $\sqrt{s} = 7$  and 8 TeV, by investigating the  $H \rightarrow ZZ \rightarrow 4l$  and  $H \rightarrow \gamma\gamma$  decays. Figures 2.6a and 2.6b present the reconstructed final state invariant masses that lead to its discovery. Since then, a broad program have been carried out by both, ATLAS and CMS, to extend the understanding of the Higgs boson to all accessible decays, production modes and also its properties and differential cross section.

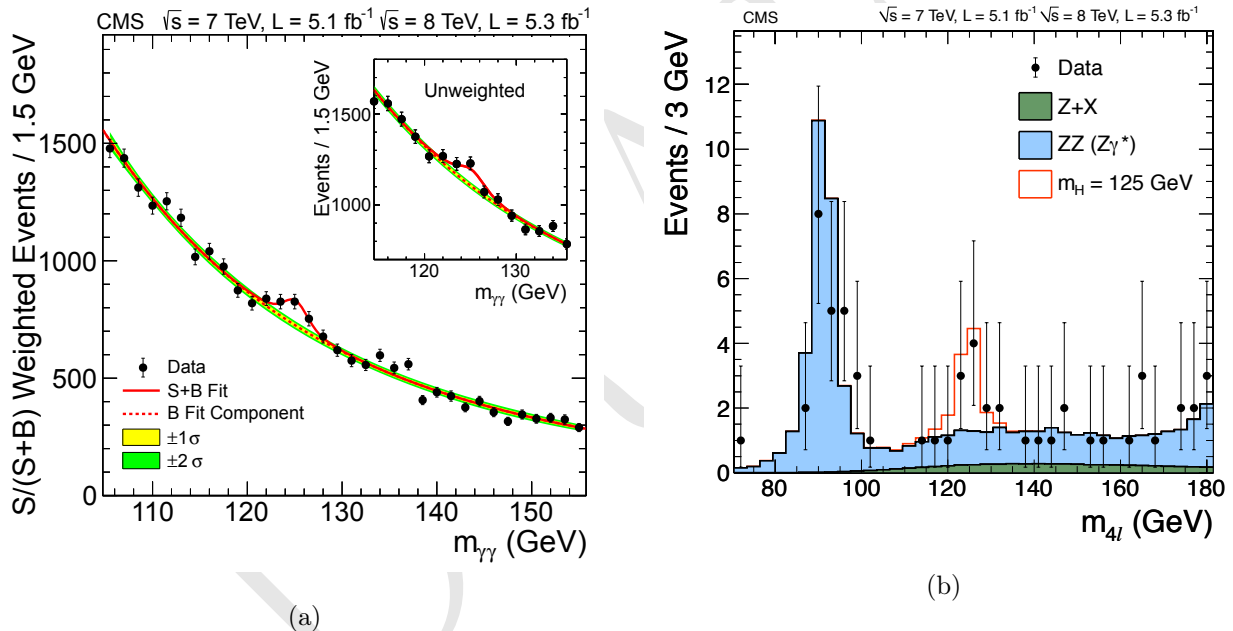


Figure 2.6: (a) The diphoton invariant-mass distribution for the 7 and 8 TeV datasets (points), with each event weighted by the predicted  $S/(S + B)$  ratio of its event class. The solid and dotted lines give the results of the signal-plus-background and background-only fit, respectively. The light and dark bands represent the  $\pm 1$  and  $\pm 2$  standard deviation uncertainties respectively on the background estimate. The inset shows the corresponding unweighted invariant-mass distribution around  $m_{\gamma\gamma} = 125$  GeV. Source: [4]. (b) Distribution of the observed four-lepton invariant mass from the combined 7 and 8 TeV data for the  $H \rightarrow ZZ \rightarrow 4\ell$  analysis (points). The prediction for the expected  $Z+X$  and  $ZZ(Z\gamma^*)$  background are shown by the dark and light histogram, respectively. The open histogram gives the expected distribution for a Higgs boson of mass 125 GeV. Source: [4].

A complete list of Higgs publications and public result from CMS can be found at [32, 33]. With the Higgs measurements being carried out per decay channel, a important effort of combination of these results in performed independently by each collaboration, as well as joint combinations. Some of the Higgs boson measurements by CMS are summarized.

814 The signal strength modifier is the ratio of the measured cross section or branching ratio over the  
 815 expected one.

$$\mu^i = \frac{\sigma^i}{\sigma_{SM}^i} \quad \mu^f = \frac{\mathcal{B}^i}{\mathcal{B}_{SM}^i}, \quad (2.18)$$

816 where  $\sigma^i$  and  $\mathcal{B}^i$  stand for the measured cross section and branching ratio of a certain production  
 817 mode or decay channel, respectively. Figure 2.7 presents the most updated measurements of  $\mu^i$  and  
 818  $\mu^f$  during Run2. The overall combined strength modifier is  $\mu = 1.02^{+0.07}_{-0.06}$  [34], for  $m_H = 125.09$   
 819 GeV, which shows very good agreement with the SM expectation.

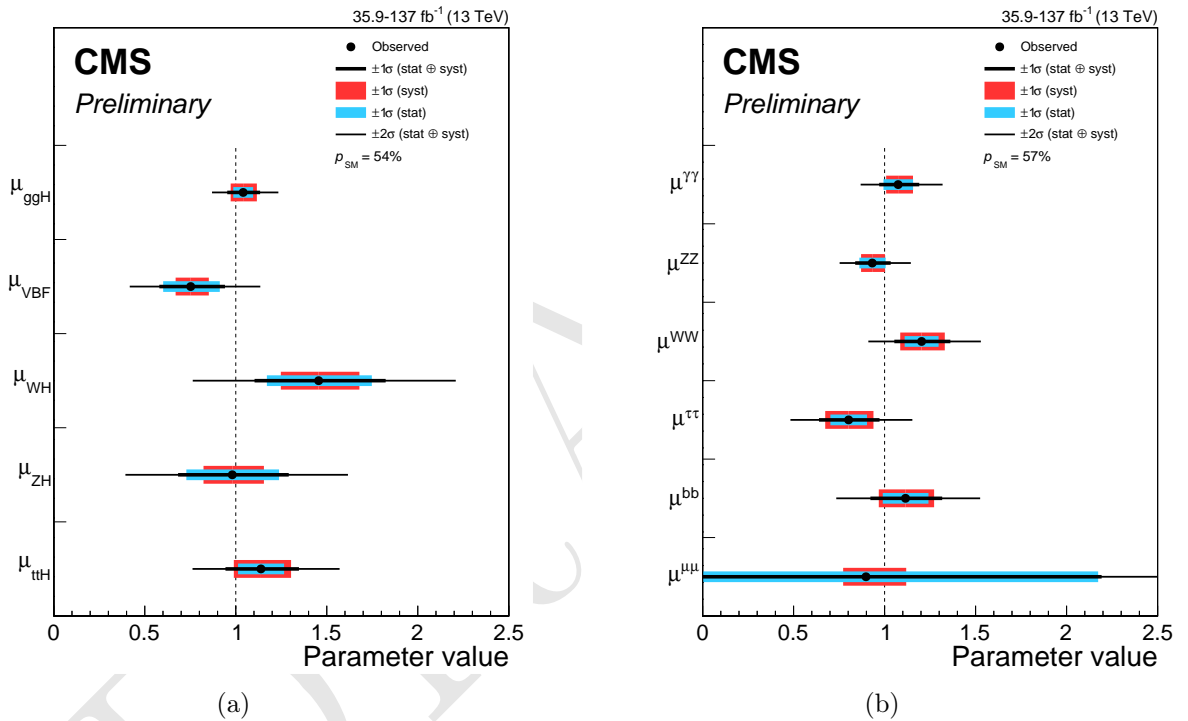


Figure 2.7: Signal strength modifiers for the production modes, (a)  $\mu^i$ , and for the decay channels, (b)  $\mu^f$ . The thick (thin) black lines report the  $1\sigma$  ( $2\sigma$ ) confidence intervals. The thick blue and red lines report the statistical and systematic components of the  $1\sigma$  confidence intervals. Source: [34].

820 The Higgs mass was also subject of many study, here we quote the results on Figure 2.8 [30], for  
 821 Run1 and partial Run2 datasets, for both  $H \rightarrow ZZ \rightarrow 4l$  and  $H \rightarrow \gamma\gamma$  decays. The combined  
 822 measurement is  $m_H = 125.38 \pm 0.14$  GeV. This is the *state-of-art* value for the Higgs mass.

823 Other properties studied comprehends its quantum numbers. The Landau-Yang theorem [35, 36]  
 824 rules out the spin-1 possibility, based on its observation on the  $\gamma\gamma$  channel. All the tests conducted,  
 825 so far, support the  $J^P = 0^+$  hypothesis [37].

826 A recent very relevant Higgs result published by CMS is the evidence of the  $H \rightarrow \mu\mu$  decay [25]. In  
 827 this paper it is reported an excess on data, with respect to the background only hypothesis, with  
 828  $3\sigma$  of significance. This is the first evidence of the Higgs coupling to second generation fermions.  
 829 Figure 2.9a presents a weighted invariant mass distribution of the dimuon system ( $m_{\mu\mu}$ ) for all the  
 830 categories included in this analysis.

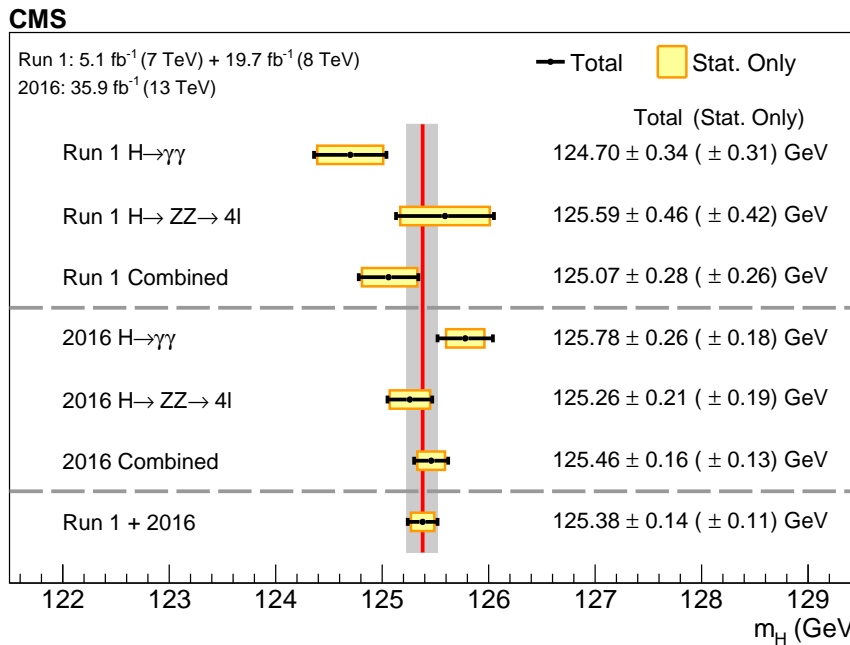


Figure 2.8: A summary of the measured Higgs boson mass in the  $H \rightarrow ZZ \rightarrow 4l$  and  $H \rightarrow \gamma\gamma$  decay channels, and for the combination of the two is presented here. The statistical (wider, yellow-shaded bands), and total (black error bars) uncertainties are indicated. The (red) vertical line and corresponding (grey) shaded column indicate the central value and the total uncertainty of the Run 1 + 2016 combined measurement, respectively. Source: [30].

831 The same note also updates the coupling constant modifier by combining the new results for  $H \rightarrow \mu\mu$   
 832 with previous Higgs results from Run2 [34]. The measured parameters are presented at Figure 2.9b  
 833 and they also present very good agreement with the SM prediction, where the coupling constants  
 834 to fermions is proportional to the fermion mass ( $M_f$ ), while for electroweak boson, it is proportional  
 835 to the square of the boson mass ( $M_V$ ). The fit results are scaled to the reduced coupling strength  
 836 modifiers, defined as  $y_V = \sqrt{\kappa_V} \frac{m_V}{\nu}$  and  $y_f = \kappa_f \frac{m_F}{\nu}$ , where  $\nu$  is the vacuum expectation value of  
 837 the Higgs field of 246.22 GeV.

### 838 2.3 Rare Z and Higgs decays to quarkonia

839 The rare decays of the Higgs boson [4, 5] to a quarkonium state and a photon provide a unique  
 840 sensitivity to the magnitude of the Yukawa couplings of the Higgs boson to quarks [38–40]. These  
 841 couplings are difficult to access on hadronic collisions through direct decay of Higgs in quark-  
 842 antiquark, due to the immense background from QCD [41].

843 Among the channels available to explore Yukawa’s couplings of light quarks [39, 40] are those with  
 844 heavy-quarkonia. The rare modes of decay of the Z boson have attracted attention focused on  
 845 establishing its sensitivity to New Physics [42], being configured as an alternative environment to  
 846 investigate the Yukawa couplings of the Higgs boson.

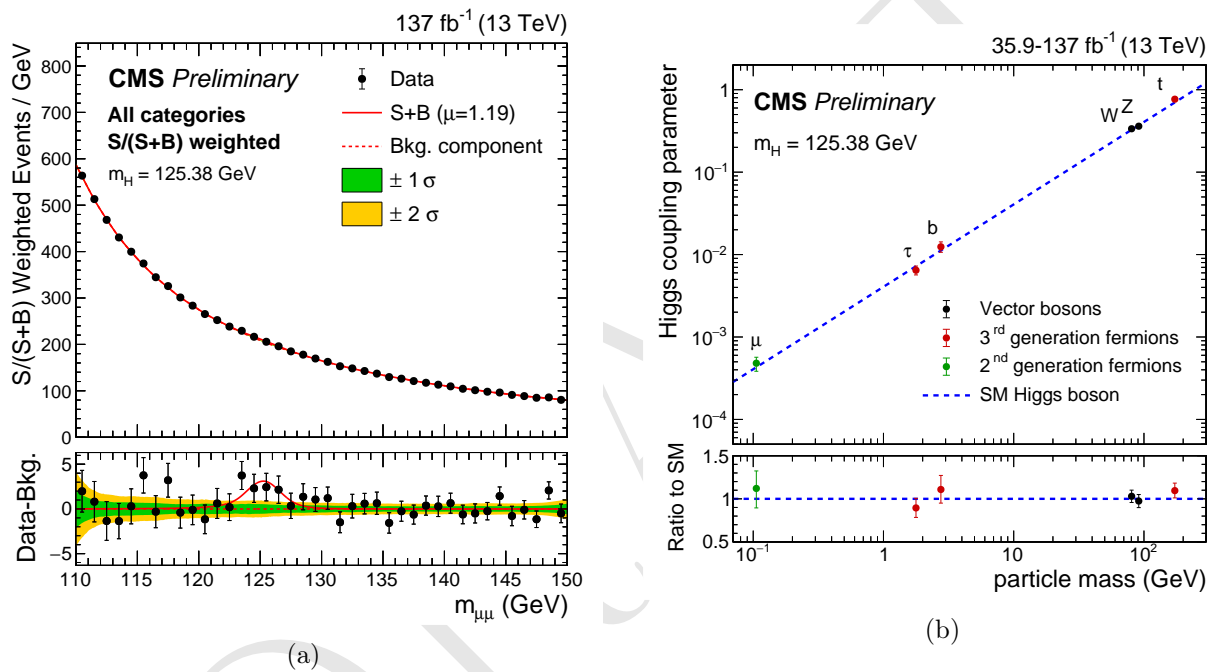


Figure 2.9: (a) The  $m_{\mu\mu}$  distribution for the weighted combination of all event categories used in the analysis. The upper panel is dominated by the gluon-gluon fusion categories with many data events but relatively small  $S/(S + B)$ . The lower panel shows the residuals after background subtraction, with the best-fit SM  $H \rightarrow \mu\mu$  signal contribution with  $m_H = 125.38$  GeV indicated by the red line. The measured signal strength is  $1.19^{+0.41}_{-0.39}(\text{stat})^{+0.17}_{-0.16}(\text{sys})$ . Source: [25]. (b) The best-fit estimates for the reduced coupling modifiers extracted for fermions and weak bosons from the resolved  $\kappa$ -framework model compared to their corresponding prediction from the SM. The error bars represent 68% CL intervals for the measured parameters. The lower panel shows the ratios of the measured coupling modifiers values to their SM predictions. Source: [25].

Also, the exclusive rare decays of vector bosons ( $Z$ ,  $W$ ) provide a favorable environment for testing the factorization of QCD, thus allowing an approach in a context where the power of corrections are definitely under control. The main focus of this kind of analysis are the hadronic radioactive decays,  $Z \rightarrow M\gamma$ , where  $M$  can be a pseudoscalar or a vector meson ( $J/\psi, \phi, \Upsilon_n$ ).

They offer the perfect way to explore some of the leading order properties of the light-cone distribution amplitudes (LCDAs) [43] of several mesons, but they present a difficulty, considering that in the LHC energy scale the branching ratio of these processes is very small. There are theoretical predictions [44, 45] that point out a branching ratio for several decay channels in the Standard Model, as shown in the Table 2.2.

Table 2.2: Summary of cross section and branching ratio for  $H/Z \rightarrow \Upsilon(1S, 2S, 3S) + \gamma \rightarrow \mu^+ \mu^- + \gamma$  analysis. The effective cross-section will be discussed in section 4.1.2.

Physics Processes	Branching Ratio ( $\text{BR}_{SM}$ ):
$H \rightarrow \Upsilon(1S) + \gamma$	$5.22 \times 10^{-9}$
$H \rightarrow \Upsilon(2S) + \gamma$	$1.42 \times 10^{-9}$
$H \rightarrow \Upsilon(3S) + \gamma$	$9.10 \times 10^{-10}$
$Z \rightarrow \Upsilon(1S) + \gamma$	$4.88 \times 10^{-8}$
$Z \rightarrow \Upsilon(2S) + \gamma$	$2.44 \times 10^{-8}$
$Z \rightarrow \Upsilon(3S) + \gamma$	$1.88 \times 10^{-8}$

Recent studies on exclusive Higgs boson decays [46–48] in final states containing a simple vector meson and a photon have caused interest in these physics topics. It was proposed to use these decays as a possible way to explore non-standard Yukawa couplings of the Higgs boson. Such measures are quite challenging in the LHC environment. The observation of hadronic decays of vector bosons provides could provide a new frontier for the nature of heavy quarkonia production in hadronic collisions.

Along the same lines, the simple exploration of rare SM decays, even in scenarios where anomalous couplings are, in principle, ruled out by direct measurements [49], as in the case of this analysis ( $H \rightarrow \Upsilon(nS) + \gamma$ ), are still important as a stress test of the SM and as reference for future measurements. Specially the later one, when you consider that the small predicted cross sections from Table 2.2, most probably, would imply that an observation of this decay would be unlikely even in the HL-LHC [50].

This measurement is sensitive to the direct and indirect production (Figure 2.10). The *direct* process consists in the decay of boson (Higgs or  $Z$ ) to a quark anti-quark pair, in which, one of the quarks radiates a photon and the pair hadronizes to a meson (a  $\Upsilon(nS)$ , for this study), while in *indirect* process, the decay happens to a  $\gamma\gamma^*(Z)$ , with the subsequent decay of the  $\gamma^*(Z)$  to a quark anti-quark that hadronizes.

Clearly, only the direct process is sensible to the Yukawa coupling of the boson with the quarks, but, since both processes are indistinguishable in their final state, the in direct process needs to be taken into account. In this study, a dimuon final state is used to tag the  $\Upsilon(nS)$ .

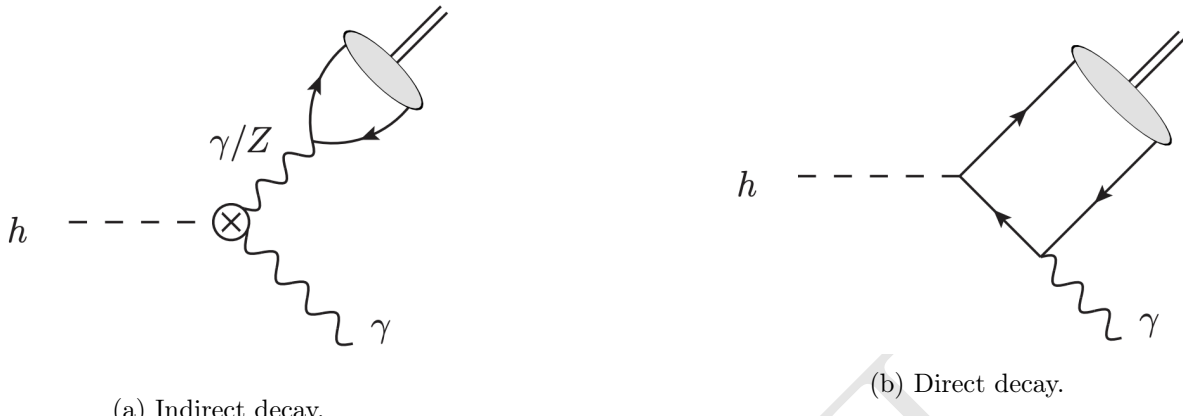


Figure 2.10: Example of leading order diagrams for the indirect and direct production mechanisms. In these diagrams, the  $h$  can also be understood as a  $Z$  or a Higgs boson.

Even though there is different theoretical predictions for the cross section of this process and its twin brother ( $H \rightarrow J/\Psi + \gamma$ ), each one taking into account different levels of complexity, the 2013 paper [38], from G. Bodwin, F. Petriello, S. Stoynev and M. Velasco, summarizes very well and in a simpler manner, the most relevant phenomenological results on these decays. For the decay to  $J/Psi + \gamma$ , the quantum interference with the indirect amplitude, enhances the directed production, leading to a larger, and potentially observable, cross section. This is not true for the  $\Upsilon(nS) + \gamma$  decay, since the interference is destructive, diminishing the cross sections.

Another interesting aspect of this study is that, for both  $Hc\bar{c}$  and  $Hb\bar{b}$  direct coupling measurements are not sensible to the sign of the Yukawa coupling, while the presence of the indirect process in the  $H \rightarrow M + \gamma$  ( $M$  standing for  $J/Psi$  or  $\Upsilon(nS)$ ) decays resolve this ambiguity.

Finally, since the  $\Upsilon(nS) + \gamma$  decay has a much smaller cross section, because of the destructive quantum interference between direct and indirect production mechanisms, a small deviation in the  $Hb\bar{b}$  Yukawa coupling, can lead a large increase in the expected branching ratio, making this channel sensible any non-Standard Model process that might interfere in this final state. This becomes clear when we look to Figure 2.11.

## 2.4 Recent results

The ATLAS experiment [3] already have two results on this decays [51, 52]. The first one corresponds to data taken from 2015, while the former one, corresponds to data from 2016 (the same data taking period to which this study refers).

The what concerns the most updated result, the study corresponded to  $36.1 \text{ fb}^{-1}$  at  $\sqrt{s} = 13 \text{ TeV}$  and no significant excess was found by the experiment. Upper limits for the were obtained, assuming the Standard Model branching fractions predictions, at 95% confidence level, according to table 2.3.

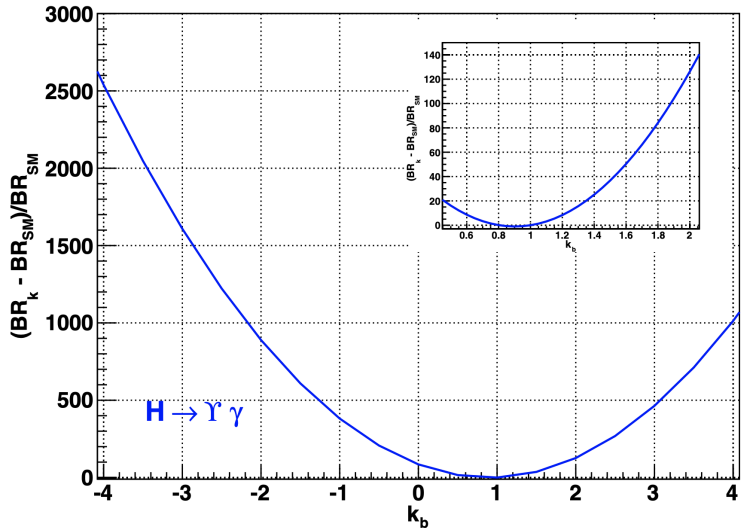


Figure 2.11: Expected relative variation of the branching ratio for the  $H \rightarrow \Upsilon(nS) + \gamma$  to  $k_b$ , where  $k_b = g(Hb\bar{b})/g(Hb\bar{b})_{SM}$  is the ratio for the observed and expected Yukawa coupling on  $Hb\bar{b}$ . Source: [38]

Table 2.3: Observed upper limits, by the ATLAS experiment, on the branching fractions for the Higgs and Z decays (last result). Detailed comparisons with the results obtained in this study will be presented in chapter 5.

Decay	$\mathcal{B}F$ at 95% CL
$H \rightarrow J/\Psi + \gamma$	$< 4.5 \times 10^{-4}$
$H \rightarrow \Psi(2S) + \gamma$	$< 2.0 \times 10^{-3}$
$H \rightarrow \Upsilon(1S) + \gamma$	$< 4.9 \times 10^{-4}$
$H \rightarrow \Upsilon(2S) + \gamma$	$< 5.9 \times 10^{-4}$
$H \rightarrow \Upsilon(3S) + \gamma$	$< 5.7 \times 10^{-4}$
$Z \rightarrow J/\Psi + \gamma$	$< 2.3 \times 10^{-6}$
$Z \rightarrow \Psi(2S) + \gamma$	$< 4.5 \times 10^{-6}$
$Z \rightarrow \Upsilon(1S) + \gamma$	$< 2.8 \times 10^{-6}$
$Z \rightarrow \Upsilon(2S) + \gamma$	$< 1.7 \times 10^{-6}$
$Z \rightarrow \Upsilon(3S) + \gamma$	$< 4.8 \times 10^{-6}$

899 It is worth it to mention that the ATLAS papers present a broader analysis, including the decays  
 900 to  $J/\Psi + \gamma$  and  $\Psi(2S) + \gamma$ .

901 CMS [53] also have a result on  $J/\Psi + \gamma$  and  $\Psi(2S) + \gamma$  decay channel, of the Higgs and Z boson [54].  
 902 The observed upper limit on the branching fraction for these decays are presented in table 2.4.

Table 2.4: Observed upper limits, by CMS, on the branching fractions for the Higgs and Z decays. The number are compatible with the ones obtained by ATLAS. The results presented for different polarization scenarios of the  $J/\Psi$ .

Channel	Polarization	$\mathcal{B}F$ at 95% CL
$Z \rightarrow J/\Psi + \gamma$	Unpolarized	$< 1.4 \times 10^{-6}$
	Transverse	$< 1.5 \times 10^{-6}$
	Longitudinal	$< 1.2 \times 10^{-6}$
$H \rightarrow J/\Psi + \gamma$	Transverse	$< 7.6 \times 10^{-4}$

903 No result on the Z and Higgs decays to  $\Upsilon(nS) + \gamma$  have been published by CMS, yet.

904 The results presented here, are a subset of a broader topic related to the rare decays of Standard  
 905 Model (SM) boson, involving quarkonia. Sticking only to CMS results, we can cite:

- 906 • Search for Higgs and Z boson decays to  $J/\psi$  or  $\Upsilon$  pairs in proton-proton collisions at  $\sqrt{s} =$   
 907    13 TeV [55].
- 908 • Observation of the  $Z \rightarrow \psi\ell^+\ell^-$  decay in pp collisions at  $\sqrt{s} = 13$  TeV [56]. This one specifically,  
 909    is the first observation a such decay, involving a Z boson.
- 910 • Search for decays of the 125 GeV Higgs boson into a Z boson and a  $\rho$  or  $\phi$  meson [57].

DRAFT

# 911 3 Experimental Setup

912 This chapter describes the experimental setup used in this study, for the sake of brevity, it is provided  
913 a brief descriptions of the Large Hadron Collider (LHC), the Compact Muons Solenoid (CMS), and  
914 its subdetectors, and the process of high-level physics objects processing and reconstruction.

## 915 3.1 The Large Hadron Collider

916 The Large Hadron Collider (LHC) is the world largest and powerful particle accelerator for protons  
917 and heavy-ions ever build. It is located in a complex of other accelerator operated by the European  
918 Organization for Nuclear Research (CERN), in the border of between Switzerland and France.  
919 The LHC is built in the same 26.7 km extension tunnel with depth varying from 45 m to 170  
920 m below the surface (the LHC plane is tilted 1.4% for construction reasons), once used by Large  
921 Electron–Positron Collider. The CERN complex is a composition of many accelerators, for proton  
922 and heavy-ions, used to provide beams of particles for smaller experiments and as a sequence of  
923 injectors for the LHC. Figure 3.1 presents the many components of the LHC complex of accelerators.  
924 A detailed description of the LHC can be found at [58–61].

925 A LHC section is composed of two vacuum pipes, in which the bunch of particles travels in opposite  
926 directions. This means that both beams are magnetically coupled by the same super-conducting  
927 magnetic system, saving space and allowing the use of the pre-built LEP tunnel. The particle  
928 acceleration is made by Resonant Cavities [63]. Those cavities apply to each beam a set of radio-  
929 frequencies (RF) used to transfer energy by means of a 2 MV electric potential per cavity, at a  
930 revolution frequency of 400.789 MHz. The acceleration is applied to bunches of particles. The  
931 bunch configuration depends of the injection mode (configurable), but a typical  $pp$  injection would  
932 be composed by 2808 bunches of  $1.1 \times 10^{11}$  protons each. Proper timing of the bunches injection  
933 and the RF is a key factor for an efficient energy transfer inside the RF cavities. The cavities also  
934 are operated in low temperatures of 4.5 K, to ensure superconducting properties and reduce energy  
935 losses.

936 The nominal time spacing between each bunch (bunch crossing - BX) is 25 ns. This defines the  
937 clock frequency of the LHC at  $f_{LHC} = 400$  MHz. This frequency is propagated to all experiments  
938 and used as a reference for timing and synchronization.

939 In certain positions, called the interaction points (IP), those two bunches are allowed to cross, possi-  
940 bility the particle collisions. The experiments on the LHC are located in those interaction points.  
941 ATLAS (A Toroidal LHC ApparatuS) [3] and CMS (Compact Muon Solenoid, better explained in

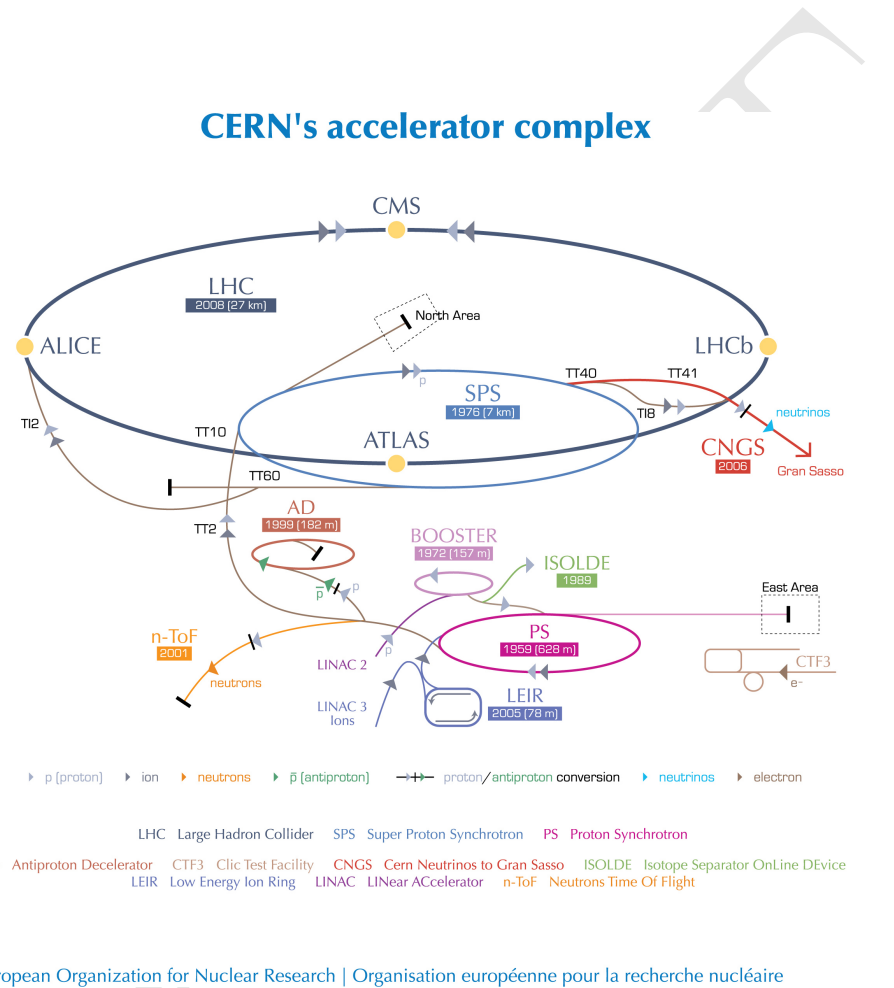


Figure 3.1: The LHC is the last ring (dark grey line) in a complex chain of particle accelerators. The smaller machines are used in a chain to help boost the particles to their final energies and provide beams to a whole set of smaller experiments. Source: [62].

the next section), at P1 and P5, respectively, are so called general proposes experiments, with focus on different aspects of a particle interactions in the LHC energy scale, including extensive test of known Standard Model process (in high and low transverse momentum regime), including the Higgs sector and Heavy Flavour Physics (phenomena involving the hadrons composed by  $c$  and  $b$  quarks), exploration of Beyond Standard Model (BSM) phenomena, as well as an competitive program in heavy-ions collisions. The LHCb (Large Hadron Collider beauty) [64] is a experiment devoted, mostly, to precision measurements of CP violation and rare decays of  $B$  hadrons. The ALICE (A Large Ion Collider Experiment) [65] experiment is dedicated to the study of  $p$ - $Pb$  and  $Pb$ - $Pb$  collisions and processes such as QCD, strongly interacting matter and the quark-gluon plasma at extreme values of energy density and temperature.

The number of events of a certain kind  $i$ , per unit of time, is given by Equation 3.1.

$$\frac{dN^i}{dt} = \sigma^i \mathcal{L}, \quad (3.1)$$

where  $\sigma^i$  is the cross-section for a certain process  $i$  and  $\mathcal{L}$  is the instantaneous luminosity delivered by the LHC.

In order to accumulate as much statistics as possible, in the shortest amount of time (for the most efficiently use of the resources available, including person-power), the luminosity is a key factor in the exploration of the collisions. This is dependent of the number of particles per bunch, number of bunches per beam, revolution frequency, form factors of the bunches, crossing angles at the interaction points and correction factors to address relativistic and electromagnetic associated phenomena. For  $pp$  collisions, the LHC aims peak luminosities of, for ATLAS and CMS, around  $2 \times 10^{34} \text{ cm}^{-2} \text{ s}^{-1}$ . For future upgrades of the LHC (called HL-LHC [66]), the peak luminosity might increase 10 times, allowing an accumulated luminosity <sup>1</sup> of  $3000 \text{ fb}^{-1}$ .

The LHC can collide protons with center-of-mass energy  $\sqrt{s}$  up to 14 TeV. Different energy configurations have been used so far, historically increasing the energy. For the operation cycle used in this study (Run2, from 2015 to 2018), the machine was producing collisions at  $\sqrt{s} = 13 \text{ TeV}$ . For the next operation cycle (Run3), to start in 2022, it is expected that the LHC might reach the 14 TeV energy values.

## 3.2 The Compact Muon Solenoid - CMS

The Compact Muon Solenoid (CMS) is a multiple purpose experiment used to investigated  $pp$  as well as lead-lead collisions at the LHC. It is operated by the CMS Collaborations, composed by around 5000 researches and 20 institutes <sup>2</sup>. The CMS is located in the city of Cessy, France, 100 below the surface. The CMS apparatus has an overall length of 22m, a diameter of 15m, and weighs 14 000 tonnes. A detailed description of the CMS detector, can be found in [2]. Figure 3.2 presents a sketch of CMS and its subdetectors.

<sup>1</sup>Accumulated (or integrated) luminosity is defined as  $L = \int \mathcal{L} dt$ .

<sup>2</sup>It is important to stress that CMS is a collaboration of institutes, not researches.

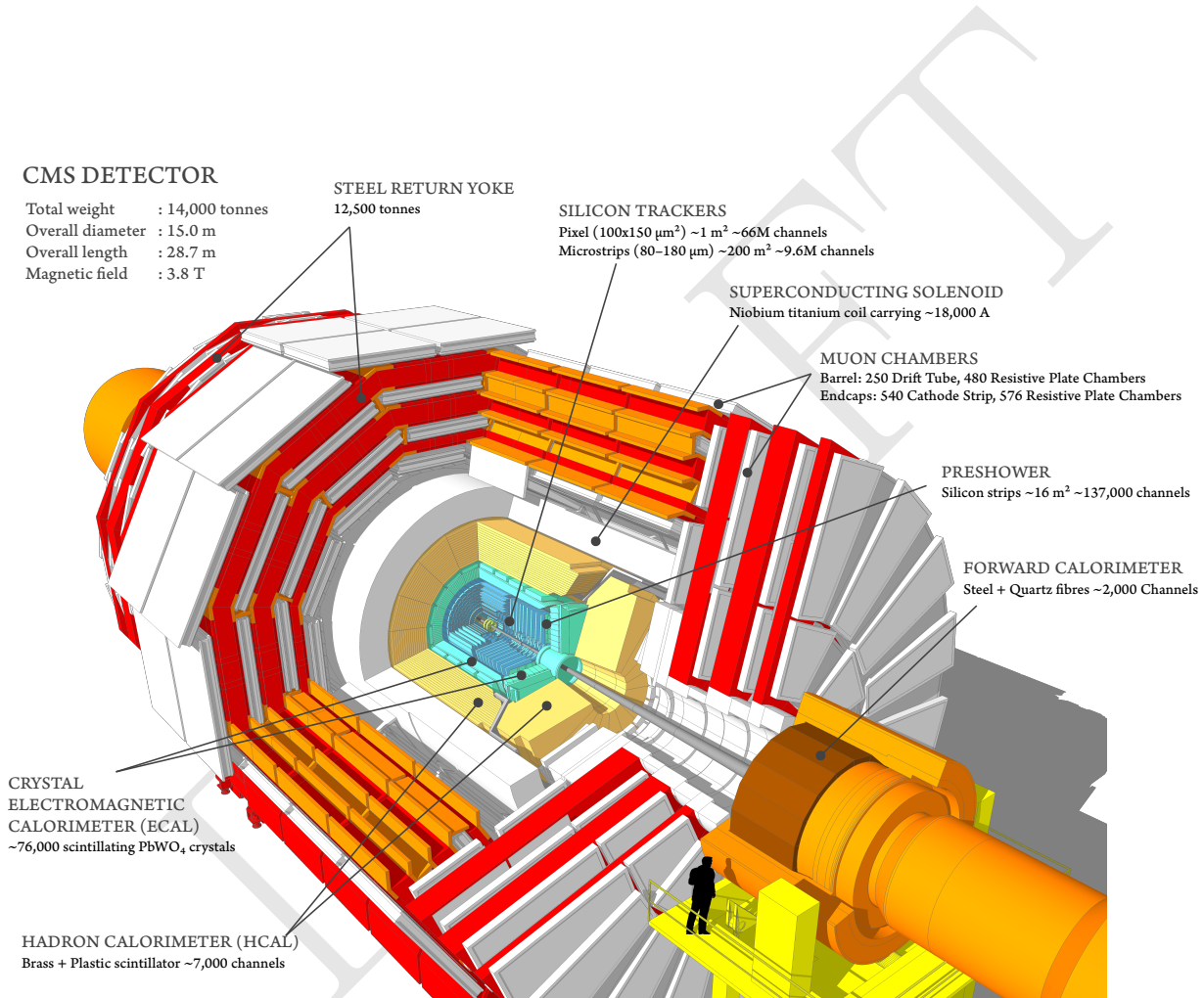


Figure 3.2: Overview of the CMS experiment and its subdetectors. Source: [67].

975 The central feature of the CMS apparatus is a superconducting solenoid of 6 m internal diameter,  
 976 providing a magnetic field of 3.8 T. Within the solenoid volume are a silicon pixel and strip tracker,  
 977 a lead tungstate crystal electromagnetic calorimeter (ECAL), and a brass and scintillator hadron  
 978 calorimeter (HCAL), each composed of a barrel and two endcap sections. Forward calorimeters ex-  
 979 tend the pseudorapidity coverage provided by the barrel and endcap detectors. Muons are detected  
 980 in gas-ionization chambers embedded in the steel flux-return yoke outside the solenoid.

981 The following sections describes the subdetectors, mentored above, and the CMS coordinate system,  
 982 as well as some important variables.

### 983 3.2.1 Coordinate system

984 CMS uses a right-handed coordinate system, with the origin at the nominal interaction point, the  
 985  $x$  axis pointing to the centre of the LHC ring, the  $y$  axis pointing up (perpendicular to the LHC  
 986 plane), and the  $z$  axis along the anticlockwise-beam direction. The polar angle  $\theta$  is measured from  
 987 the positive  $z$  axis and the azimuthal angle  $\phi$  is measured in the  $x$ - $y$  plane.

988 It is important to define some key variables for CMS, in this study. The rapidity is defined as in  
 989 Equation 3.2, bellow.

$$y = \frac{1}{2} \ln \left( \frac{E + p_z}{E - p_z} \right), \quad (3.2)$$

990 where  $E$  is the energy of the object and  $p_z$  is the momentum ov the objects along the  $z$  direction.  
 991 The difference between the rapidity of two objects is known for being a lorentz invariant under a  
 992 boost.

993 A usually more suitable variable is the pseudorapidity, which is the rapidity in the relativistic limit  
 994 of  $E \gg m$ .

$$\eta = -\ln \left[ \tan \left( \frac{\theta}{2} \right) \right], \quad (3.3)$$

995 where  $\theta$  is the angle between the transverse plane to the beam line ( $x$ - $y$  plane) and the positive  $z$   
 996 direction. The convenience of using the pseudorapidity is its direct connection with the geometry  
 997 of the event by the  $\theta$  angle.

998 Spatial distance, at CMS, usually is measured based on the  $\eta$ - $\phi$  space. In this sense the distance  
 999  $\Delta R$  between two objects is defined as:

$$\begin{aligned} \Delta R &= \sqrt{(\Delta\eta)^2 + (\Delta\phi)^2} \\ &= \sqrt{(\eta_1 - \eta_2)^2 + (\phi_1 - \phi_2)^2} \end{aligned} \quad (3.4)$$

1000 One last important variable is the transverse momentum component, computed as in Equation 3.5

$$\begin{aligned} p_T &= \sqrt{p_x^2 + p_y^2} \\ &= |\mathbf{p}| \cos(\theta) \end{aligned} \quad (3.5)$$

### 1001 3.3 Tracker

1002 The tracker is the closest subdetector to the interaction point, with 5.8 m length and 2.5 m  
 1003 diameter cylinder. The silicon tracker measures charged particles within the pseudorapidity range  
 1004  $|\eta| < 2.5$ . The challenge of this subdetector is to cope with the high efficiency demanded for the  
 1005 secondary vertices identification for long lived particles and initial momentum measurement, the  
 1006 required radiation hardness for being close to the interaction point and the expected resolution  
 1007 demanded to deal with the high multiplicity of a  $pp$  collisions, specially in the high pileup <sup>3</sup> regime.  
 1008 It consists of 1440 silicon pixel and 15 148 silicon strip detector modules, as in Figure 3.3. For  
 1009 non-isolated particles of  $1 < p_T < 10$  GeV and  $|\eta| < 1.4$ , the track resolutions are typically 1.5% in  
 1010  $p_T$  and 25–90 (45–150)  $\mu\text{m}$  in the transverse (longitudinal) impact parameter [68].

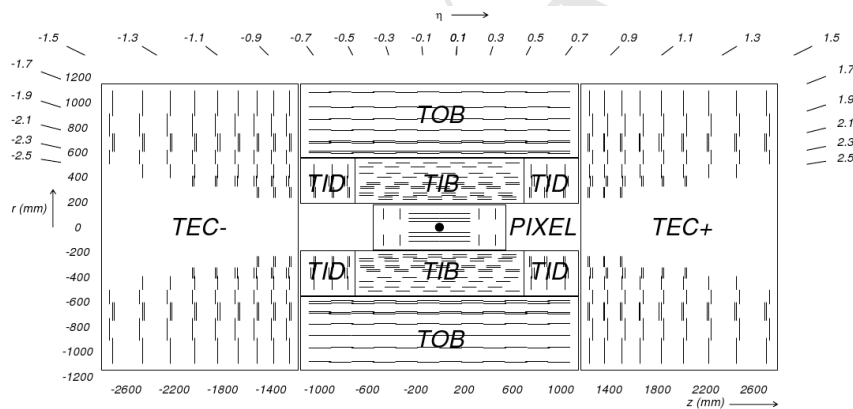


Figure 3.3: Schematic cross section through the CMS tracker. Each line represents a detector module. Double lines indicate back-to-back modules which deliver stereo hits. Source: [2].

1011 The pixel detector consists of 3 layers <sup>4</sup> on the barrel region and 4 layers on the endcap <sup>5</sup>. The pixel  
 1012 is located in a region of 20 cm from the beam pipe.

1013 Each pixel sensor has 100 by  $150 \mu\text{m}^2$ . The silicon strips detector covers a area of  $\approx 200\text{m}^2$  with  
 1014  $9.3 \times 10^6$  channels. It is the largest silicon detector covered area ever built. It is divided in Tracker  
 1015 Inner Barrel (TIB), with length of 130 cm covering the central part of the detector, the Tracker

<sup>3</sup>Each LHC collision recorded by CMS, is composed not by a single  $pp$  interaction, but by bunches of protons crossing each other. In this case, a hard interaction is actually surrounded by many soft interaction between adjacent protons. The extra activity produced in these interactions, and caught by the detector, is called **pileup** and has its signal mixed with the hard one.

<sup>4</sup>After 2017, the pixel received one more layer, but this irrelevant to the context of this study, since the data analyzed was collected during 2016.

<sup>5</sup>From 2017, another layer on each side was added.

- 1016 Inner Disks (TID) at the inner endcap, both are surrounded by the Tracker Outer Barrel (TOB)  
 1017 on the barrel, and the Tracker Endcap (TEC).  
 1018 The tracker is essential for a proper muon measurement in this study.

1019 **3.4 Electromagnetic Calorimeter**

1020 The Electromagnetic Calorimeter (ECAL) is responsible for absorb (and measure) the energy of  
 1021 photons and electrons produced as final state particles of the collisions. The ECAL consists of  
 1022 75 848 lead tungstate ( $PbWO_4$ ) crystals, which provide coverage in pseudorapidity  $|\eta| < 1.48$  in a  
 1023 barrel region (EB,  $2.2 \times 2.2 cm^2$  and a length of 23 cm) and  $1.48 < |\eta| < 3.0$  in two endcap regions  
 1024 (EE,  $2.86 \times 2.86 cm^2$  front cross section and 22 cm long). Preshower detectors consisting of two  
 1025 planes of silicon sensors interleaved with a total of  $3X_0$  of lead are located in front of each EE  
 1026 detector [69], as shown in Figure 3.4.

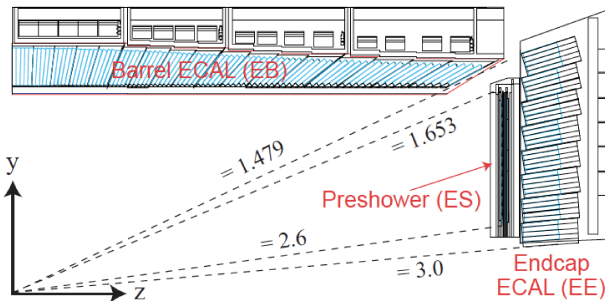


Figure 3.4: Longitudinal section view of the ECAL and its components. Source: [2].

1027 When a electron (or photon) enters the high density region of the lead tungstate crystals ( $8.3 g/cm^3$ ),  
 1028 it initiates a cascade effect of pair production and photon emission via bremsstrahlung. The intensity  
 1029 of light produce is proportional to the energy of the particle adsorbed. With radiation length <sup>6</sup> of  
 1030 0.89 cm and a small Molière radius (2.2 cm) the ECAL was built with compact size and its fine  
 1031 granularity. The preshower, located in front of the endcap ECAL (EE), is used to distinguish from  
 1032 high momentum photons and pair of photons coming from  $\pi^0$  decays, highly boosted, in such a way  
 1033 that they would be indistinguishable one from the other. Its first layer is composed oh the lead  
 1034 tungstate crystal, followed by silicon strip sensor, that allow to measure the shape of the initiated  
 1035 cascade on the first layer and correlate this with the source of the radiation.

1036 Each ECAL crystal is isolated by a carbon fiber layer and it is connected to two photodetectors  
 1037 with a gain of 50. Their signal is collected by a ADC (Analog to Digital Converter) which catches  
 1038 the charge from the photodetectors and convert it to a digital signal.

1039 In the barrel section of the ECAL, an energy resolution of about 1% is achieved for unconverted  
 1040 or late-converting photons that have energies in the range of tens of GeV. The remaining barrel  
 1041 photons have a resolution of about 1.3% up to a pseudorapidity of  $|\eta| = 1$ , rising to about 2.5% at  
 1042  $|\eta| = 1.4$ . In the endcaps, the resolution of unconverted or late-converting photons is about 2.5%,

<sup>6</sup>Distance an electron or a photon travels until its energy is reduced by a factor of  $1/e$ .

1043 while the remaining endcap photons have a resolution between 3 and 4% [70]. When combining  
 1044 information from the entire detector, the jet energy resolution amounts typically to 15% at 10 GeV,  
 1045 8% at 100 GeV, and 4% at 1 TeV, to be compared to about 40%, 12%, and 5% obtained when the  
 1046 ECAL and Hadronic Calorimeter (HCAL) alone are used.

1047 Due to its responsibility on photon and electrons identification, the ECAL had a very important  
 1048 role on the Higgs observation, specially concerning its relation with the  $\gamma\gamma$  and 4-leptons finals  
 1049 states of the discovery.

### 1050 3.5 Hadronic Calorimeter

1051 The Hadronic Calorimeter (HCAL) is devoted to absorb and measure the energy of final states  
 1052 hadrons. Together with the ECAL, it plays a key role on the jet reconstruction and missing energy  
 1053 measurement. It is the last subdetector until the magnet coil and, as much as possible, tries to cover  
 1054 the largest pseudorapidity region in order to enhance the missing transverse energy identification. It  
 1055 is composed by layers of brass and steel, interleaved with plastic scintillators, with 3.7 mm thickness  
 1056 each, in order to leave as much as possible space for the absorptive materials. This allows, once a  
 1057 hadron hit the material, the formation of hadronic cascades. These cascades are detected by the  
 1058 scintillators which emits light proportional to the amount of energy deposited.

1059 The HCAL is divided in 4 components, the HB (barrel) 9 m long in the central region

1060 In the region  $|\eta| < 1.74$ , the HCAL cells have widths of 0.087 in pseudorapidity and 0.087 in azimuth  
 1061 ( $\phi$ ), corresponding to 5 to 10 interaction lengths. In the  $\eta$ - $\phi$  plane, and for  $|\eta| < 1.48$ , the HCAL  
 1062 cells map on to  $5 \times 5$  arrays of ECAL crystals to form calorimeter towers projecting radially outwards  
 1063 from close to the nominal interaction point. For  $|\eta| > 1.74$ , the coverage of the towers increases  
 1064 progressively to a maximum of 0.174 in  $\Delta\eta$  and  $\Delta\phi$ . Within each tower, the energy deposits in  
 1065 ECAL and HCAL cells are summed to define the calorimeter tower energies, which are subsequently  
 1066 used to provide the energies and directions of hadronic jets. Figure 3.5 shows a longitudinal view  
 1067 of the HCAL.

1068 Jets are reconstructed offline from the energy deposits in the calorimeter towers, clustered using the  
 1069 anti- $k_T$  algorithm [71, 72] with a distance parameter of 0.4. In this process, the contribution from  
 1070 each calorimeter tower is assigned a momentum, the absolute value and the direction of which are  
 1071 given by the energy measured in the tower, and the coordinates of the tower. The raw jet energy  
 1072 is obtained from the sum of the tower energies, and the raw jet momentum by the vectorial sum of  
 1073 the tower momenta, which results in a nonzero jet mass. The raw jet energies are then corrected to  
 1074 establish a relative uniform response of the calorimeter in  $\eta$  and a calibrated absolute response in  
 1075 transverse momentum  $p_T$ .

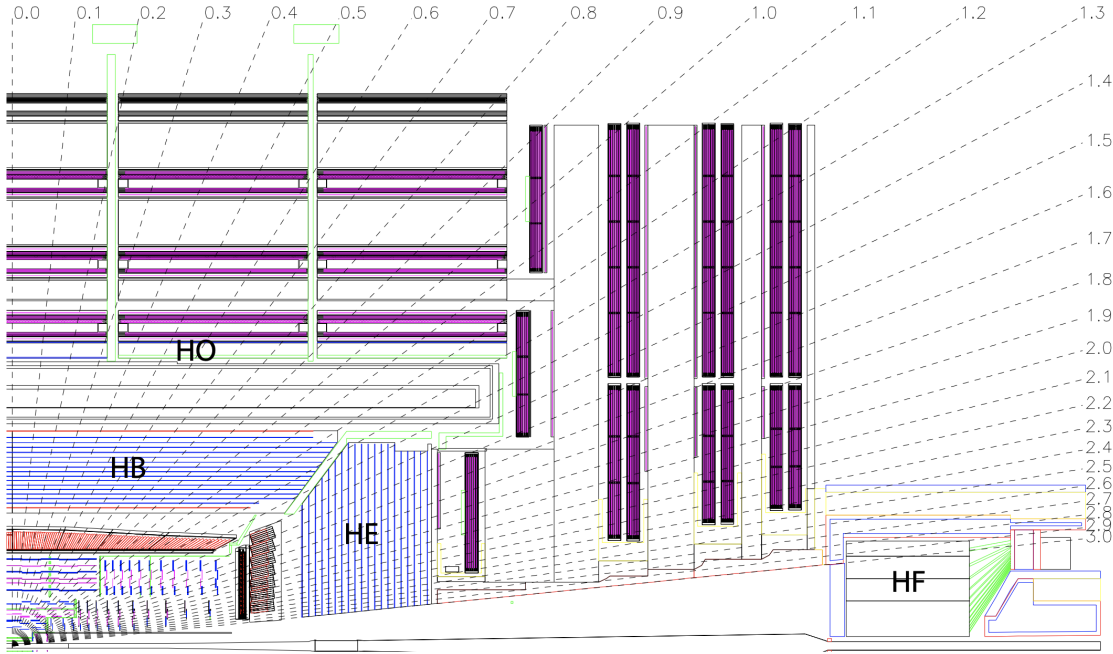


Figure 3.5: Longitudinal section view of the HCAL and its components. The barrel calorimeter (HB) covers the central region, inside the solenoid, the outer calorimeter covers also the central region, but it is positioned on the outside the solenoid. The endcap calorimeter (HE) covers the forward region and it is complemented by the forward calorimeter (HF), which uses Cherenkov light detectors made of radiation-hard quartz fibers. Source: [2].

## 1076 3.6 Muon System

1077 Muons at CMS [73] are measured in the pseudorapidity range  $|\eta| < 2.4$ , with detection planes  
1078 made using three technologies: drift tubes, cathode strip chambers, and resistive plate chambers,  
1079 as presented in Figure 3.6. The single muon trigger efficiency exceeds 90% over the full  $\eta$  range,  
1080 and the efficiency to reconstruct and identify muons is greater than 96%. Matching muons to tracks  
1081 measured in the silicon tracker results in a relative transverse momentum resolution, for muons with  
1082  $p_T$  up to 100 GeV, of 1% in the barrel and 3% in the endcaps. The  $p_T$  resolution in the barrel is  
1083 better than 7% for muons with  $p_T$  up to 1 TeV [74].

1084 The muon detection system has around 1 million channels. For Run3, the muon system is be-  
1085 ing expanded and upgraded, by the inclusion of new chamber with the Gas Electron Multiplier  
1086 (GEM) [76] technology.

### 1087 3.6.1 Drift Tubes

1088 The Drift Tubes (DT) [77] is a gaseous detector (85% Ar and 15% CO<sub>2</sub>) installed in the central  
1089 region of CMS (Barrel), covering the region of  $|\eta| < 1.2$ . The barrel is divided in 5 wheels, along  $z$ ,  
1090 W+2, W+1, W0, W-1 and W-2. Each will is composed by four concentric stations along  $r$ , MB 1  
1091 to MB4, and each station is divided in 12 sectors along  $\phi$ , S01 to S12. In total, there are 205 DT

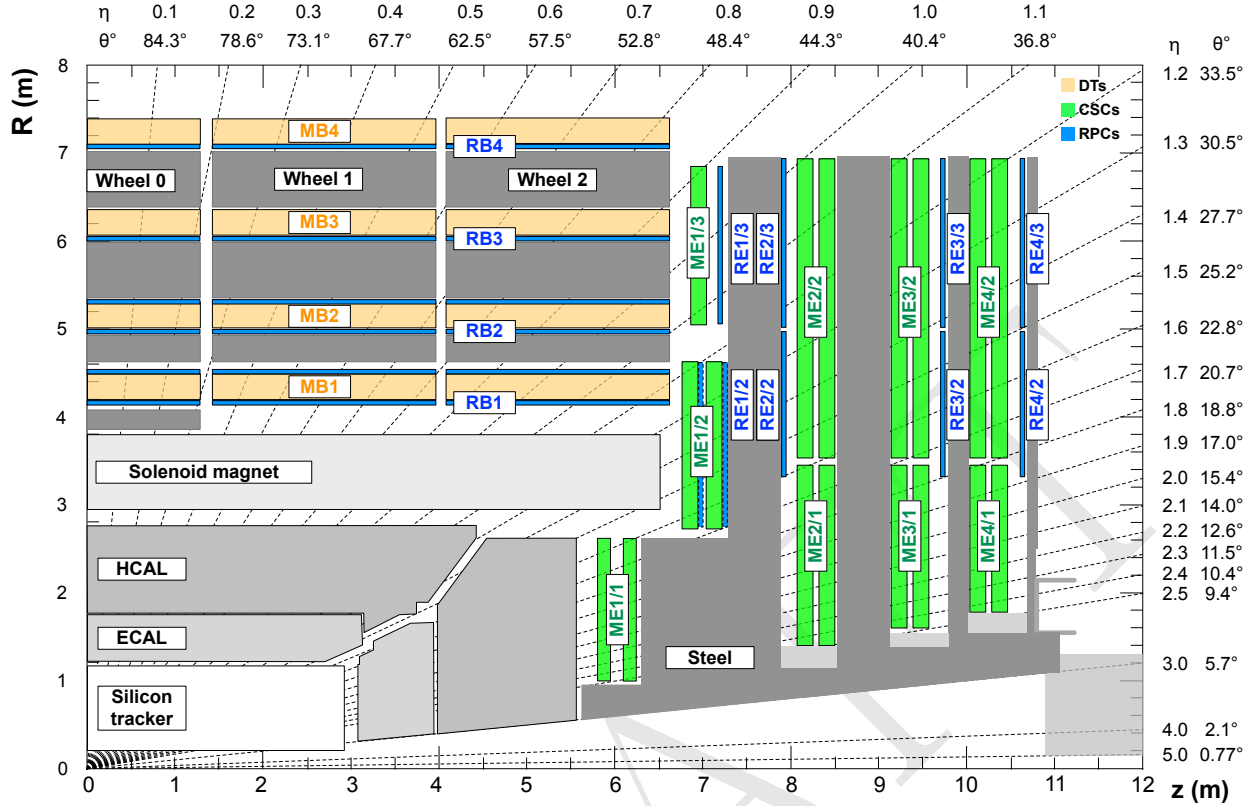


Figure 3.6: Longitudinal section view of the ECAL and its components. Source: [75].

1092 chambers. Each tube has  $50 \mu\text{m}$  tick (diameter) gold-plated stainless steel wire, as well as, kept at  
 1093 positive voltage, and aluminum electrodes. The signal is read on the golden wire only.

1094 The tubes are arranged in layers and occupy the whole length of the chamber. The tubes are  
 1095 arranged in coaxial layers. Each set of three layers, forms a Super-Layer (SL).The first and the  
 1096 last SL are aligned in the, so called,  $r - \phi$  direction, while the middle one, in the  $r - z$  direction,  
 1097 transversal to the previous one. This arrangement give the DTs, the possibility to measure the  
 1098 passage of a muon in  $\eta$  and  $\phi$  direction, with a resolution of  $100 \mu\text{m}$ .

### 1099 3.6.2 CSC

1100 The Cathode Strip Chamber (CSC) is also a gaseous detector (50% CO<sub>2</sub>, 40% Ar, and 10% CF<sub>4</sub>) of  
 1101 the Muon System which covers the endcap region, up to  $|\eta| < 2.4$  composed by wires perpendicular  
 1102 to  $\eta$  (radial measurement) and strips along  $\eta$ , the former operating at 3.9 to 3.6 kV. With 8.4 to 16  
 1103 mm strip width and a wire-distance of 2.5 to 3.16 mm depending on their location, they provide a  
 1104 75 to 150  $\mu\text{m}$  resolution.

1105 They are installed in four layers (or disk) on each side of CMS, with each disk divided in up to  
 1106 three rings.

1107 **3.6.3 RPC**

- 1108 The Resistive Plate Chambers (RPC) is the only muon detection technology present in both barrel  
1109 and endcap. It has very good timing resolution and it is used mostly for triggering.  
1110 Due to the particularities of the study, especially the contributions given to the RPC project of  
1111 CMS, Chapter 6 is devoted exclusively to this subdetector.

1112 **3.7 Trigger and Data Acquisition**

1113 The LHC collides protons at 40 MHz. To process and save this amount of information would be  
1114 unmanageable. To deal with the high rate of readouts generated by the collisions and nuclear back-  
1115 ground (around 950 TB/s) CMS uses a two-tiered trigger system [78]. The first level (L1), composed  
1116 of custom hardware processors, uses information from the calorimeters and muon detectors, in the  
1117 form of the so called trigger-primitives, to select events at a rate of around 100 kHz within a time  
1118 interval of less than 4  $\mu$ s. The L1 trigger relies on the processing of the optical links, coming  
1119 CMS subdetector by FPGAs (Field Programmable Gate Array) processors. This combination of  
1120 technologies allows the maximum speed in the readout information processing.

1121 The second level, known as the high-level trigger (HLT), consists of a farm of processors running a  
1122 version of the full event reconstruction software optimized for fast processing, and reduces the event  
1123 rate to around 1 kHz before data storage.

1124 Both triggers systems are designed to quickly identify the events <sup>7</sup> that have a specific set of  
1125 signatures of interesting physics, to the context of CMS. As an example, events with characteristics  
1126 of the historically widely studied soft-diffraction, are mostly (but not fully) discarded.

1127 Once a event is read by CMS, it is categorized in one or many of the defined "triggers". Each trigger  
1128 is composed by a minimum sets of requirements, e.g. a single isolated muon trigger is defined as "at  
1129 least one muon, well isolated from any other detector relevant activity, above a minimum transverse  
1130 momentum threshold". If a event falls into a L1 trigger definition and passes the prescaling <sup>8</sup> of  
1131 that trigger, a "L1 Accept" (L1A) optical signal is propagated to all subdetectors readout hardware  
1132 and the information is injected into the Data Acquisition (DAQ) system and saved at the local  
1133 computing cluster, the HLT. This decision process takes around 3.2  $\mu$ s. Saved events are processed  
1134 by an optimized version of the Particle-Flow algorithm and if it again falls into one the the HLT  
1135 triggers paths (definitions) it is saved for future analysis.

1136 **3.8 Particle Flow Algorithm**

1137 The global event reconstruction (also called particle-flow event reconstruction [79]) aims to re-  
1138 construct and identify each individual particle in an event, with an optimized combination of all

<sup>7</sup>A Event can be understood the set of information from the detector channels, extracted in one readout cycle.

<sup>8</sup>Each trigger has its prescaling. For example, a prescaling 30 means that only once every 30 times that this trigger is activated, the event will in be processed and forwarded into the data acquisition chain.

subdetector information. In this process, the identification of the particle type (photon, electron, muon, charged hadron, neutral hadron) plays an important role in the determination of the particle direction and energy. Photons ( $e/\gamma$  coming from  $Z$  decays or from electron bremsstrahlung) are identified as ECAL energy clusters not linked to the extrapolation of any charged particle trajectory to the ECAL. Electrons are identified as a primary charged particle track and potentially many ECAL energy clusters corresponding to this track extrapolation to the ECAL and to possible bremsstrahlung photons emitted along the way through the tracker material. Muons are identified as tracks in the central tracker consistent with either a track or several hits in the muon system, and associated with calorimeter deposits compatible with the muon hypothesis. Charged hadrons are identified as charged particle tracks neither identified as electrons, nor as muons. Finally, neutral hadrons are identified as HCAL energy clusters not linked to any charged hadron trajectory, or as a combined ECAL and HCAL energy excess with respect to the expected charged hadron energy deposit. Figure 3.7 show the identification process for each high-level physics object, as previously described.

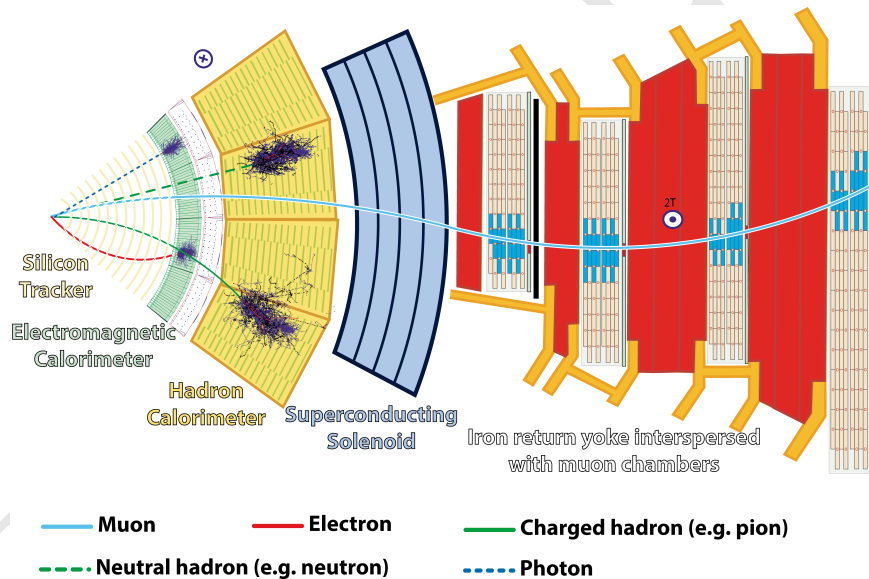


Figure 3.7: The figure illustrates how the information from each subdetector is used in order to identify the different high-level objects in the Particle-Flow algorithm. Source: [79].

The energy of photons is obtained from the ECAL measurement. The energy of electrons is determined from a combination of the track momentum at the main interaction vertex, the corresponding ECAL cluster energy, and the energy sum of all bremsstrahlung photons attached to the track. The energy of muons is obtained from the corresponding track momentum. The energy of charged hadrons is determined from a combination of the track momentum and the corresponding ECAL and HCAL energies, corrected for the response function of the calorimeters to hadronic showers. Finally, the energy of neutral hadrons is obtained from the corresponding corrected ECAL and HCAL energies.

The candidate vertex with the largest value of summed physics-object  $p_T^2$  is taken to be the primary  $pp$  interaction vertex. For each event, hadronic jets are clustered from these reconstructed particles using the infrared and collinear safe anti- $k_T$  algorithm [71, 72] with a distance parameter of 0.4. Jet

momentum is determined as the vectorial sum of all particle momenta in the jet, and is found from simulation to be, on average, within 5 to 10% of the true momentum over the whole  $p_T$  spectrum and detector acceptance. Additional proton-proton interactions within the same or nearby bunch crossings (pileup) can contribute additional tracks and calorimetric energy depositions to the jet momentum. To mitigate this effect, charged particles identified to be originating from pileup vertices are discarded and an offset correction is applied to correct for remaining contributions. Jet energy corrections are derived from simulation to bring the measured response of jets to that of particle level jets on average. In situ measurements of the momentum balance in dijet, photon + jet,  $Z + \text{jet}$ , and multijet events are used to account for any residual differences in the jet energy scale between data and simulation [80]. The jet energy resolution amounts typically to 15–20% at 30 GeV, 10% at 100 GeV, and 5% at 1 TeV [80]. Additional selection criteria are applied to each jet to remove jets potentially dominated by anomalous contributions from various subdetector components or reconstruction failures.

Anomalous high- $p_T^{\text{miss}}$  events can be due to a variety of reconstruction failures, detector malfunctions or non collisions backgrounds. Such events are rejected by event filters that are designed to identify more than 85–90% of the spurious high- $p_T^{\text{miss}}$  events with a mistagging rate less than 0.1% [81].

Hadronic decays of top quarks are identified using the ratio between 3-subjettiness and 2-subjettiness [82],  $\tau_{32} = \tau_3/\tau_2$ , and the groomed jet mass. The groomed jet mass is calculated after applying a modified mass-drop algorithm [83, 84], known as the *soft drop* algorithm [85], to anti- $k_T$  jets with a distance parameter of 0.8 and parameters  $\beta = 0$ ,  $z_{\text{cut}} = 0.1$ , and  $R_0 = 0.8$ . The variables are calibrated in a top quark-antiquark enriched sample [86].

In the barrel section of the ECAL, an energy resolution of about 1% is achieved for unconverted or late-converting photons in the tens of GeV energy range. The remaining barrel photons have a resolution of about 1.3% up to a pseudorapidity of  $|\eta| = 1$ , rising to about 2.5% at  $|\eta| = 1.4$ . In the endcaps, the resolution of unconverted or late-converting photons is about 2.5%, while the remaining endcap photons have a resolution between 3 and 4% [70].

The electron momentum is estimated by combining the energy measurement in the ECAL with the momentum measurement in the tracker. The momentum resolution for electrons with  $p_T \approx 45$  GeV from  $Z \rightarrow ee$  decays ranges from 1.7% to 4.5%. It is generally better in the barrel region than in the endcaps, and also depends on the bremsstrahlung energy emitted by the electron as it traverses the material in front of the ECAL [69].

Muons have their momentum computed by curvature of their tracks in the muon system solo or the matched track in the muon system and the tracker.

DRAFT

## <sub>1197</sub> 4 Physics Analysis

<sub>1198</sub> The analysis here presented corresponds to the search for rare decays of  $H \rightarrow \Upsilon + \gamma$ , where the  
<sub>1199</sub>  $\Upsilon$  might appear in the states  $1S$ ,  $2S$  or  $3S$ , and shall decay to a pair of muons (from here on,  
<sub>1200</sub> called dimuon system) and the  $\gamma$  will be identified as a offline reconstructed photon. The decay  
<sub>1201</sub> to the dimuon channel offers a very efficient triggering for this process, characteristic of CMS. The  
<sub>1202</sub> analogous process of the  $Z$  boson decays to the same channel is also studied, as a benchmark for  
<sub>1203</sub> the Higgs decay.

<sub>1204</sub> The main process contributing to the accessible phase space of these decays are described in Fig-  
<sub>1205</sub> ure 4.1, in which the different process are represented in a diagram for the reconstructed invariant  
<sub>1206</sub> masses of the muon-muon-photon system ( $\mu\mu\gamma$  - horizontal axis) and the muon-muon system ( $\mu\mu$   
<sub>1207</sub> - vertical axis). The vicinity of the  $H/Z$  mass and  $\Upsilon$  mass regions are represented in the midpoint  
<sub>1208</sub> for each axis. The backgrounds can be divided in **Resonant** and **Non-Resonant** backgrounds.  
<sub>1209</sub> The Non-Resonant might come from two sources, a Full Combinatorial background is composed by  
<sub>1210</sub> the combination of two non-correlated muons with a photon in the final state of the event. This is  
<sub>1211</sub> expected to be spread all over the phase space and in the diagram, it is represented by the color blue.  
<sub>1212</sub> The  $\Upsilon + \gamma$  Combinatorial background is a combination of two correlated muons (e.g.: the decay of  
<sub>1213</sub> a  $\Upsilon$  to a dimuon muon system) combined with a photon from a secondary process (e.g.: Multiple  
<sub>1214</sub> Particle Interaction - MPI, pileup, a jet mis-identified as a photon). This should be concentrated  
<sub>1215</sub> in the region around the  $\Upsilon(1S, 2S, 3S)$  and it is represented by the gray region.

<sub>1216</sub> The Resonant background is composed by the processes where the boson (Higgs or Z) decays to  
<sub>1217</sub> a  $\mu\mu\gamma$  final state without going trough the the intermediate meson state. For the Z decays, this  
<sub>1218</sub> background is modeled based on a Drell-Yan to dimuon decays, with a final state radiated (FSR)  
<sub>1219</sub> photon ( $Z \rightarrow \mu\mu\gamma_{FSR}$ ), while for the Higgs decay, a Higgs Dalitz decay ( $H \rightarrow \mu\mu\gamma$ ) is used. The  
<sub>1220</sub> Resonant background (also called Peaking Background) is represented in the diagram by the region  
<sub>1221</sub> in yellow. The Signal is represented by the red region on the diagram.

<sub>1222</sub> Around these representations, the a 2-dimensional model of the reconstructed invariant masses  
<sub>1223</sub> ( $m_{\mu\mu\gamma}$  and  $m_{\mu\mu}$ ) is constructed for each contributing process and tested against the collected data  
<sub>1224</sub> by the experiment, by means of a unbinned maximum likelihood fit. No significant excess above  
<sub>1225</sub> the background-only model is observed and a upper limit of the signal branch fraction is extracted.  
<sub>1226</sub> The following sections describes the data and simulated samples used in this analysis, the event  
<sub>1227</sub> selection applied in order to enhance the signal to background ratio and the process to construct  
<sub>1228</sub> the statistical models used in the upper limits extraction.

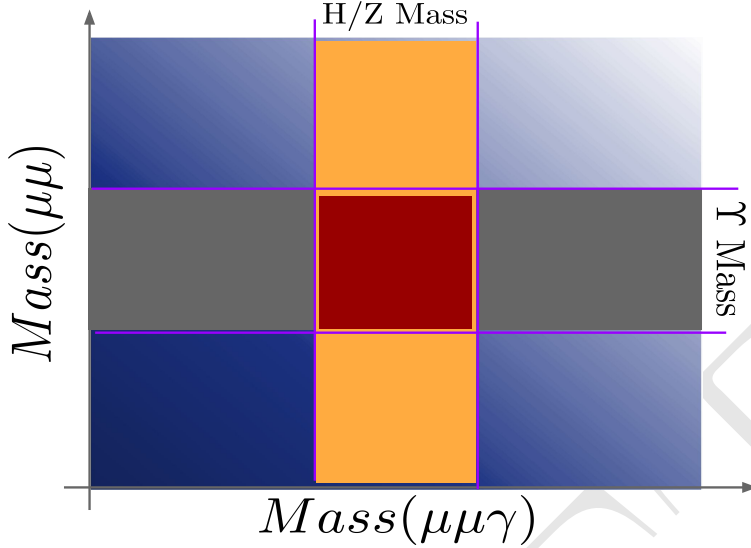


Figure 4.1: A diagram for the reconstructed invariant mass of the  $\mu\mu\gamma$  final state. The blue and gray regions represent the Full Combinatorial and  $\Upsilon + \gamma$  Combinatorial contributions, respectively, while the yellow and red regions represent the Resonant background and the signal region.

## 1229 4.1 Datasets and simulated events

### 1230 4.1.1 Data samples

1231 The data sample used in this analysis consists of the 2016 13 TeV run with 25 ns bunch separation  
1232 recorded by CMS. This data sample is composed only by events that were certified from all CMS  
1233 subsystems and reconstruction specialist as good for physics analysis.

1234 This data sample corresponds to  $35.86 \text{ fb}^{-1}$  of integrated luminosity [87].

### 1235 4.1.2 Simulated datasets

1236 Data simulation at CMS is done by the use of Monte Carlo (from here on, simply called MC)  
1237 simulations generates pseudo-random events, constrained by the physics of the related process to  
1238 which we are interested, including the effect of the produced particles interacting with the detector.  
1239 The simulation starts with the **hard-scattering** process, at parton (constituents of the proton)  
1240 level, done usually, by matrix element generators, which impose to the incoming and outgoing  
1241 partons, the dynamics of the simulated process, according to some pre-defined theoretical model.  
1242 Along the hard interaction simulation, the **fragmentation** process takes place. Since the the matrix  
1243 element generator provide information on the parton level, it is necessary to extract the momentum  
1244 distribution of the parton as a function of the  $Q^2$  (transferred momentum) of the process. To do  
1245 so, MC generators use the PDFs (parton distribution functions) to sample those values, accordingly.  
1246 The matrix element formalism also allows the simulation of the process, taking into account, different  
1247 orders of perturbations, like NLO (next-to-leading order), NNLO (next-to-next-to-leading order),  
1248 and so on.

1249 After the hard-scattering, the **showering** process simulates the radiation emission by gluons and  
 1250 quarks in the initial and final states. Along the hard interaction, the other proton constituents  
 1251 may also interact through soft interaction. This part of the simulation is called **multiple parton**  
 1252 **interaction** (MPI). The last components of the simulation is the **hadronization** and the **decay**  
 1253 **of heavy hadrons and leptons**. The former one, imposes the QCD confinement to low energy  
 1254 quarks and gluons<sup>1</sup>, while the latter one, implements specific models to decays heavy hadrons and  
 1255 leptons, like  $B$  hadrons and taus.

1256 Usually, different generators are used to simulate a process. Each specialized in one or more steps.

1257 A summary of the signal and background MC samples used is presented in Table 4.1. These  
 1258 simulated data are comparable with the proton-proton collision using 2016 data conditions and the  
 1259 **pileup**<sup>2</sup> events are added to the simulated event in this step. The pileup events distribution used is  
 1260 modeled as a Poisson pdf (probability distribution function) with mean of 23 events, as recommended  
 1261 by CMS. Detector response in the MC samples is simulated using a detailed description of the CMS  
 1262 detector, based on GEANT4 [88].

1263 The signal MC samples are simulated for the Higgs bosons decaying to  $\Upsilon(nS)(\rightarrow \mu\mu) + \gamma$  channels  
 1264 with POWHEG v2.0 [89–91], at next-to-leading order (NLO) of Feynman graphs computation, for  
 1265 the following production modes: gluon-gluon fusion (ggF), vector boson fusion (VBF), associated  
 1266 production (VH) and associated top production (ttH), with cross-section summarized at table 4.1.  
 1267 A extensive review of these production modes can be found at [92]. The PYTHIA 8 generator [93,  
 1268 94] is used for hadronization and fragmentation with underlying event tune CUETP8M1 [95]. The  
 1269 parton distribution functions (pdf) NNPDF3.0 [96] are used.

1270 For Z decaying to  $\Upsilon(nS)(\rightarrow \mu\mu) + \gamma$  channels, the signal samples are simulated with MADGRAPH 5  
 1271 \_MC@NLO 2.6.0 matrix element generator [97] at next leading order and the PYTHIA 8 generator [93,  
 1272 94] for hadronization and fragmentation with underlying event tune CUETP8M1 [95].

1273 The Drell-Yan process,  $pp \rightarrow Z \rightarrow \mu\mu\gamma_{FSR}$ , results in the same final state as the signal. This  
 1274 process exhibits a peak in the three-body invariant mass,  $m_{\mu\mu\gamma}$ , at the Z boson mass,  $m_Z$ , and it is  
 1275 a resonant background for this channel, therefore referred to as a Peaking Background.

1276 It is taken into account when deriving the upper limit on the branching fraction for  $Z \rightarrow \Upsilon(nS) +$   
 1277  $\gamma \rightarrow \mu\mu + \gamma$ . The MADGRAPH 5 \_MC@NLO 2.6.0 matrix element generator [97] at leading order,  
 1278 interfaced with PYTHIA 8.226 for parton showering and hadronization with tune CUETP8M1 [95],  
 1279 is used to generate a sample of these resonant background events. The photons in these events are

---

<sup>1</sup>QCD forbids coloured objects to exist in non-asymptotic states. They must decays to more complex systems, until they form stable colorless states.

<sup>2</sup>Each LHC collision recorded by CMS, is composed not by a single  $pp$  interaction, but by bunches of protons crossing each other. In this case, a hard interaction is actually surrounded by many soft interaction between adjacent protons. The extra activity produced in these interactions, and caught by the detector, is called **pileup** and has its signal mixed with the hard one. Since, during the data taking, the number of pileup interactions varies according to the instantaneous luminosity, the MC are mixed some soft interaction only sample, called Minimum Bias. The number of mixed soft interaction (pileup events) is governed by a Poisson distribution with a pre-defined mean. The MC samples are then reweighted to match the same distribution of primary vertexes for the corresponding Data. Systematics related to this procedure will be discussed later.

1280 all produced as final-state radiation from the  $Z \rightarrow \mu\mu$  decay and therefore the  $m_{\mu\mu\gamma}$  distribution  
 1281 peaks at the Z boson mass and there is no continuum contribution.

1282 Similarly, the Higgs boson Dalitz decay [98],  $H \rightarrow \gamma^*\gamma \rightarrow \mu\mu + \gamma$ , is a Peaking Background  
 1283 (resonant) to  $H \rightarrow \Upsilon(nS) \rightarrow \mu\mu + \gamma$ . It is simulated at NLO with MADGRAPH 5 \_MC@NLO  
 1284 2.6.0 matrix element generator [97] at next-to-leading order and the PYTHIA 8 generator [93, 94] for  
 1285 hadronization and fragmentation with underlying event tune CUETP8M1 [95]. This Higgs Dalitz  
 1286 Decay sample, was generated only for the ggF production mode, but its cross-section was rescaled  
 1287 to the full Higgs cross-section. This process will present a small contribuition of selected events, so  
 1288 this approximation should be sufficient for the Higgs Peaking Background modeling.

1289 There are also background processes that do not give resonance peaks in the three-body invariant  
 1290 mass spectrum. They are modeled from data, as it will be explained latter in more details.

Table 4.1: Datasets simulated (MC) for 2016 conditions. Assuming that  $\sigma(pp \rightarrow H)$ , taking into consideration all the simulated Higgs production modes, is  $55.13 \text{ pb}$  [99] and  $\sigma(pp \rightarrow Z \rightarrow \mu\mu)$  is  $57094.5 \text{ pb}$ , including the next-to-next-to-leading order (NNLO) QCD contributions, and the next-to-leading order (NLO) electroweak corrections from fewz 3.1 [100] calculated using the NLO PDF set NNPDF3.0, with the phase space selection in invariant mass of the dimuon system of  $m_{\mu\mu} > 50 \text{ GeV}$ . For the Higgs Dalitz  $\sigma$ , we consider only the gluon fusion contribution ( $\sigma_{\text{ggF}} = 48.6 \text{ pb}$ ) [99]. The Higgs Dalitz Decay  $BR_{SM}$  and the  $Z \rightarrow \mu\mu\gamma_{FSR}$  were obtained with MCFM 6.6 [101] (as in the CMS search for Higgs Dalitz Decay in at  $\sqrt{s} = 8 \text{ TeV}$  [102]) and with MADGRAPH 5 \_MC@NLO, respectively. The  $BR_{\Upsilon(1S,2S,3S) \rightarrow \mu\mu}^{PDG} = (2.48, 1.93, 2.18) \times 10^{-2}$  is quoted from Particle Data Group report (PDG) [13]. The "Effective  $\sigma$ " for the signal samples is  $\sigma(pp \rightarrow Z(H)) \times BR_{SM} \times BR_{\Upsilon(nS) \rightarrow \mu\mu}^{PDG}$ .

Physics Processes	Branching Ratio ( $BR_{SM}$ )	Effective $\sigma$ (in pb)	Generator	Sample Type
$H \rightarrow \Upsilon(1S) + \gamma$	$5.22 \times 10^{-9}$	$7.14 \times 10^{-9}$	POWHEG 2.0	Signal
$H \rightarrow \Upsilon(2S) + \gamma$	$1.42 \times 10^{-9}$	$1.51 \times 10^{-9}$	POWHEG 2.0	Signal
$H \rightarrow \Upsilon(3S) + \gamma$	$9.10 \times 10^{-10}$	$1.10 \times 10^{-9}$	POWHEG 2.0	Signal
$Z \rightarrow \Upsilon(1S) + \gamma$	$4.88 \times 10^{-8}$	$6.80 \times 10^{-5}$	MADGRAPH 5	Signal
$Z \rightarrow \Upsilon(2S) + \gamma$	$2.44 \times 10^{-8}$	$2.69 \times 10^{-5}$	MADGRAPH 5	Signal
$Z \rightarrow \Upsilon(3S) + \gamma$	$1.88 \times 10^{-8}$	$2.34 \times 10^{-5}$	MADGRAPH 5	Signal
H Dalitz Decay	$3.83 \times 10^{-5}$	$2.13 \times 10^{-3}$	MADGRAPH 5	Peaking Background
$Z \rightarrow \mu\mu\gamma_{FSR}$	—	$7.93 \times 10^{-2}$	MADGRAPH 5	Peaking Background

1291 The number of simulated events is rescaled by the Effective  $\sigma$ , from table 4.1, in order to match  
 1292  $35.86 \text{ fb}^{-1}$  of integrated luminosity, from the recorded data. Being  $N = \sigma \mathcal{L}$ ,  $N$  in the number of  
 1293 events for a process,  $\sigma$  is the cross-section and  $\mathcal{L}$  is the integrated luminosity, the reweighting factor,  
 1294 for a simulated sample is:

$$w_{MC} = \frac{\sigma \mathcal{L}}{N_{sim}}, \quad (4.1)$$

1295 where  $N_{sim}$  is the number of simulated events for a specific process.

1296 The simulated sample are also corrected by the data pileup distribution, since the pileup distribution  
 1297 of MC is different from the pileup distribution of data. The way to correct the MC is to assign a

1298 weight to each bin of the MC pileup distribution, with respect to the data. The rescaling is defined  
1299 as the ratio between normalized pileup (PU) distribution for Data and MC.

$$w_{PU}(n) = \frac{P_{PU}^{Data}(n)}{P_{PU}^{Sim}(n)}, \quad (4.2)$$

1300 where  $n$  is the number of interaction per bunch crossing (pileup).

## 1301 4.2 Contribution of the $\Upsilon(nS)$ polarisation

1302 Measurements of quarkonium polarization observables may yield information about quarkonium  
1303 production mechanisms that are not available from the study of unpolarized cross sections alone.  
1304 The three polarization states of a  $J = 1$  quarkonium can be specified in terms of a particular  
1305 coordinate system in the rest frame of the quarkonium. This coordinate system is often called the  
1306 "spin-quantization frame".

1307 In a hadron collider,  $\Upsilon(1S, 2S, 3S)$  are reconstructed through their electromagnetic decays into  
1308 a lepton pair. The information about the polarization of the quarkonium state is encoded in the  
1309 angular distribution of the leptons. This angular distribution is usually described in the quarkonium  
1310 rest frame with respect to a particular spin-quantization frame [103]. The polarization of the  
1311  $\Upsilon(1S, 2S, 3S)$  is not simulated for signal MC sample and we only apply a reweighting scale factor to  
1312 each event and so we can emulate the polarization effects [104]. Figure 4.2 present the distributions  
1313 of  $\cos \Theta$  of  $\Upsilon \rightarrow \mu\mu$ , where  $\Theta$  is the angle between the positive muon and the  $\Upsilon$  in the Z (Higgs) rest-  
1314 frame. At Table 4.2 we show the the analytical functions used to describe the extremes scenarios  
1315 (Unpolarized, Transverse Polarization and Longitudinal Polarization) reweighting, presented in this  
1316 analysis.

1317 It is worth stating that, for the Higgs decay, on the Transverse Polarization is considered. For  
1318 the Z decay, because of its spin nature, the Unpolarized scenario is used as the nominal one, and  
1319 the effects of the two other extremes (Transverse Polarization and Longitudinal Polarization) are  
1320 quoted as systematics.

Table 4.2: Summary of the impact of reweighted of polarization contribution using several scenarios.

$J_Z$	Polarisation Scenario	Analytic Description
$\pm 1$	Transverse	$3/4 \times (1 + (\cos \Theta)^2)$
0	Longitudinal	$3/2 \times (1 - (\cos \Theta)^2)$

## 1321 4.3 Kinematical studies using MC generator

1322 Using the PYTHIA 8.226 generator, the Monte Carlo signals are produced for Higgs (Z) boson events  
1323 decaying in  $(\Upsilon(1S, 2S, 3S)) + \gamma$ , which are highly boosted. Observing the kinematic generator level  
1324 distributions in Figure 4.3 for Z boson and Figure 4.4 for Higgs boson, we could conclude that the

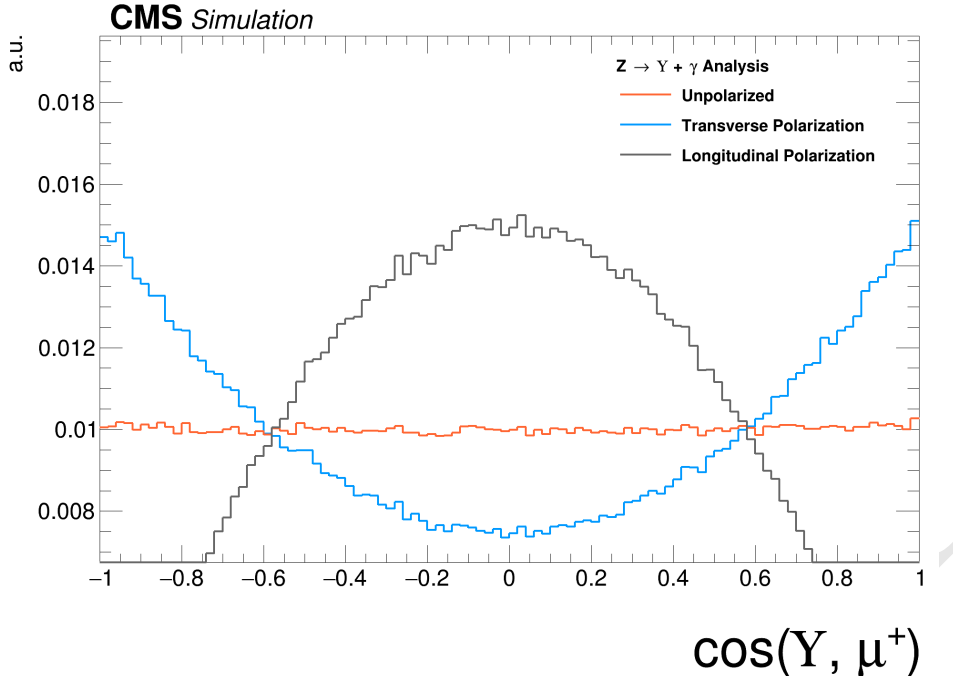


Figure 4.2: Distributions of  $\cos\theta$  of  $\Upsilon \rightarrow \mu\mu$  and  $\gamma^* \rightarrow \mu\mu$ . The orange distribution is the  $Z \rightarrow \Upsilon(1S, 2S, 3S) + \gamma$  sample before reweighting (Unpolarized); the blue and gray distributions are  $Z \rightarrow \Upsilon(1S, 2S, 3S)$  sample after reweighting, for the Transverse and Longitudinal Polarization.

1325 high- $E_T$  (transverse energy, with respect to the beam line) photon will be back-to-back to the  $\Upsilon$   
 1326 particles being possible to apply an isolation selection to identify a photon in this kinematic topology.  
 1327 Also, we can observe those transverse momenta of the leading/trailing  $p_T$  (transverse momentum,  
 1328 with respect to the beam line) muon <sup>3</sup> and the photon and distances  $\Delta R = \sqrt{\Delta\eta^2 + \Delta\phi^2}$  between  
 1329 the two muons and between the muons and the photon are a good variable that can be used to  
 1330 discriminate the contribution between signal and background events. The leading muon transverse  
 1331 momentum can be greater than 45(30) GeV and trailing muon is greater than 10(20) GeV in Higgs( $Z$ )  
 1332 decay.  $\Delta R$  distributions of the two muons and between the muons and the photon in the both cases  
 1333 show that the two muons are very close and the photon is back-to-back in relation of dimuon system.  
 1334 Another feature of this kinematic topology is that the production vertex between muons produced  
 1335 in  $\Upsilon$  decaying events and the high- $E_T$  photon is very well defined.

<sup>3</sup>In this study we define leading muon and the muon, decaying from the  $\Upsilon$ , with highest  $p_T$ . Trailing muon is the one with the second hight  $p_T$ .

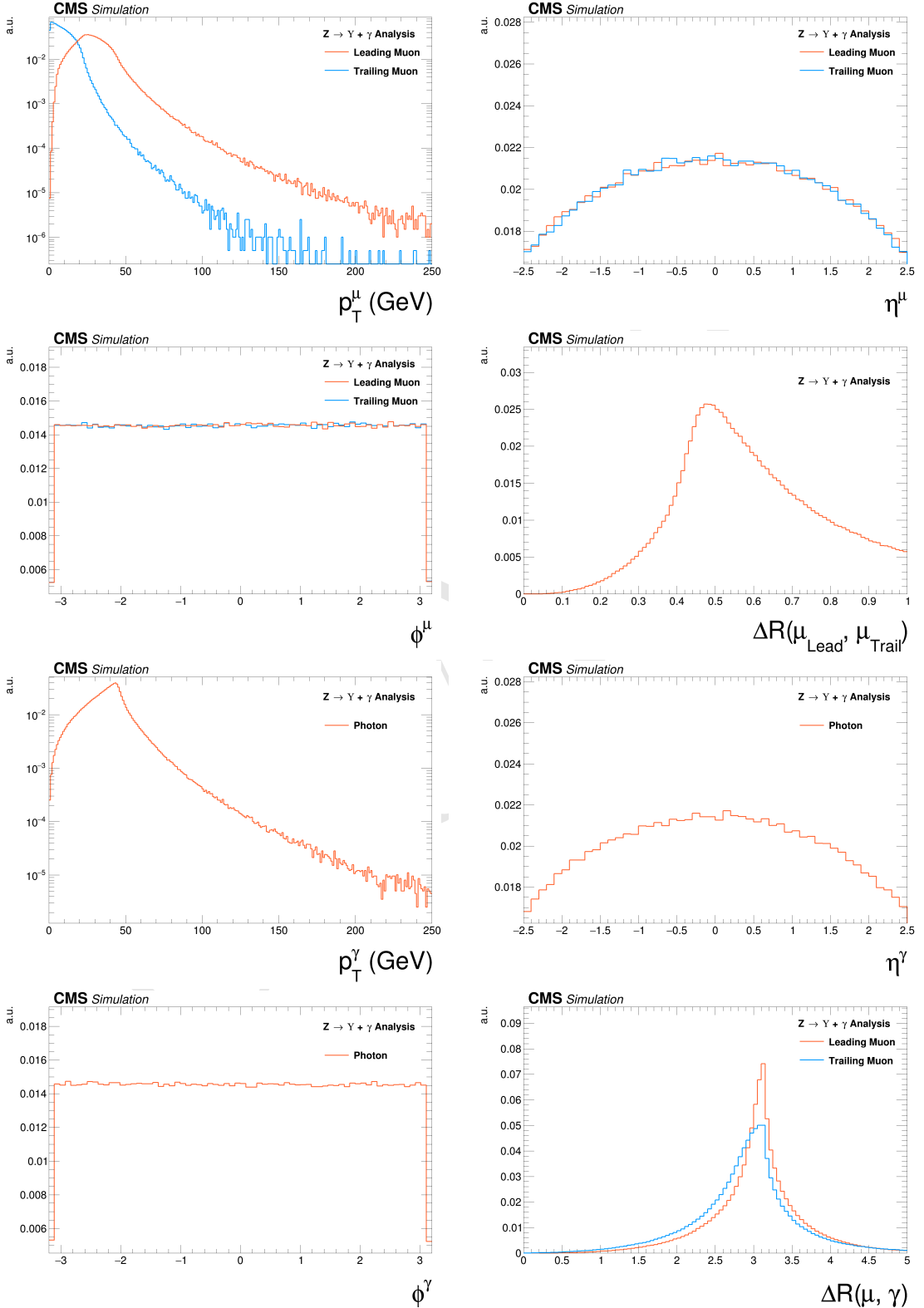


Figure 4.3: Generator level distributions of main variables for  $Z \rightarrow \Upsilon(1S, 2S, 3S) + \gamma$ : Transverse momenta of the leading/trailing  $p_T$  muon and the photon, pseudorapidity ( $\eta$ ) and  $\phi$  of the muons and the photon, distances  $\Delta R$  between the two muons and between the muons and the photon. All the distributions shown in the figure are normalized to the unity of area.

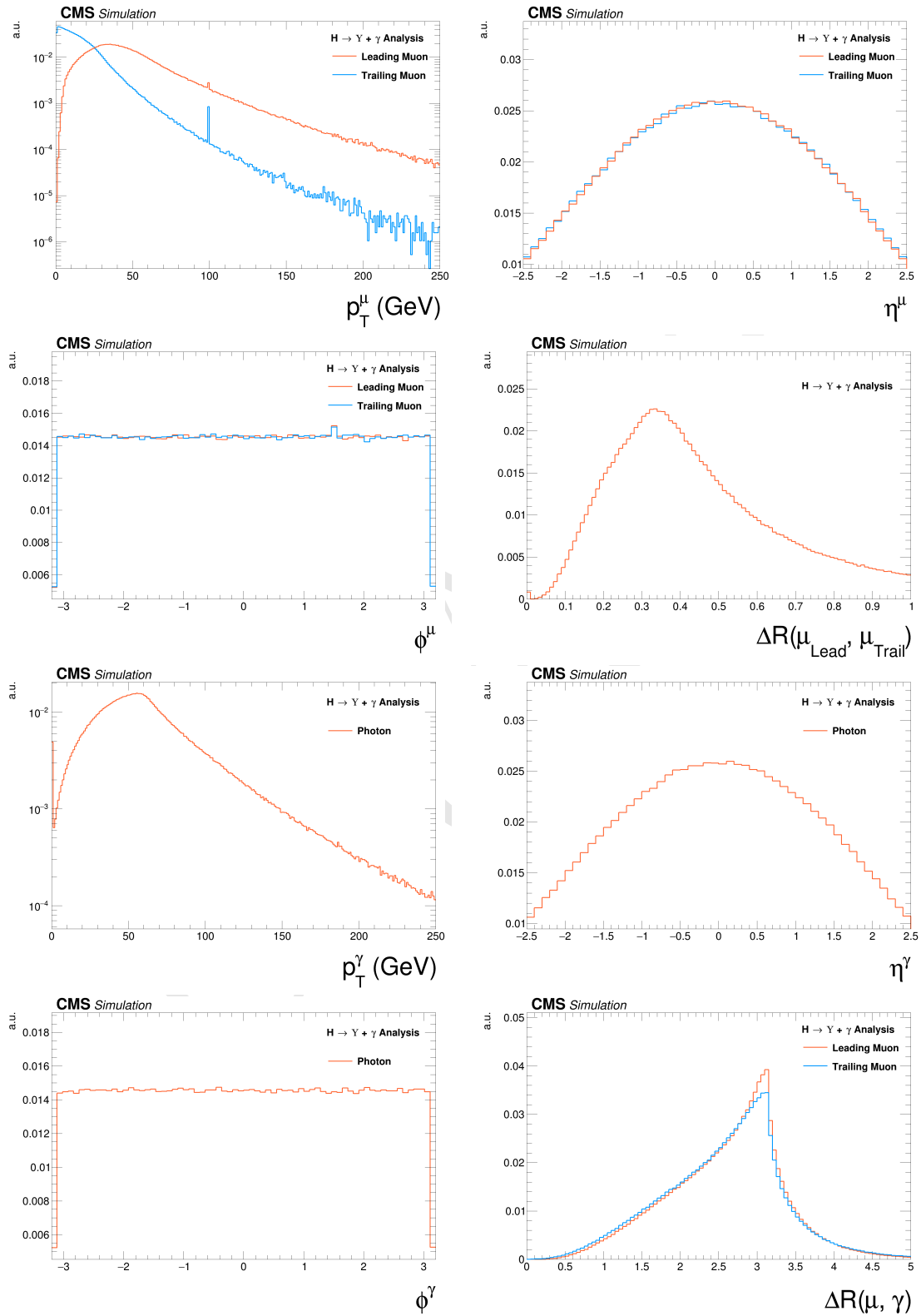


Figure 4.4: Generator level distributions of main variables for  $H \rightarrow \Upsilon(1S, 2S, 3S) + \gamma$  : Transverse momenta of the leading/trailing  $p_T$  muon and the photon, pseudorapidity ( $\eta$ ) and  $\phi$  of the muons and the photon, distances  $\Delta R$  between the two muons and between the muons and the photon. All the distributions shown in the figure are normalized to the unity of area.

## 1336 4.4 Event selection

1337 The event selection is divided in two steps. At first, a set of cuts related to trigger and physics object  
 1338 (muons and photons) selection is applied. High level physics objects at CMS are reconstructed based  
 1339 of the Particle Flow (PF) algorithm [105]. This selection is called, within this analysis, Group I.  
 1340 For the events that pass the Group I selection, another set of cuts is applied, this time focusing on  
 1341 kinematical (phase space) event selection, in order to enhance the signal to background ratio. This  
 1342 later set is called, within this analysis, Group II. After full selection, three exclusive categories are  
 1343 defined, based on the photon's  $\eta$  region and its energy spread shape within the ECAL cells (R9).  
 1344 After the full selection, a background and signal modeling process is applied, based on the invariant  
 1345 mass distributions, which will be explained in the next section.

## 1346 4.5 Trigger and physics object selection (Group I)

### 1347 4.5.1 Trigger

1348 In this study, the same trigger requirements are applied to both data and simulated samples. For  
 1349 the first trigger level (L1), events are selected if they present at least one muon with transverse  
 1350 momentum greater than 5 GeV and an isolated <sup>4</sup> photon or electron with transverse momentum  
 1351 greater than 18 GeV (at L1, there is no differentiation between photons and electrons). At the  
 1352 software level of the trigger system (HLT), the events are required to have at least one muon with  
 1353 transverse momentum greater than 17 GeV and a photon with transverse momentum greater than  
 1354 30 GeV.  
 1355 In order to compensate any difference in the trigger performance between simulated and data sam-  
 1356 ples, for every selected MC a proper scale factor is applied, based on the the  $p_T$  of the reconstructed  
 1357 muon and photon. These scale factor computed by the ratio between efficiency of the trigger for  
 1358 the Data sample over the efficiency for a MC sample. These efficiencies are calculated with the  
 1359 tag-and-probe method, exploring the the resonance of a final state composted by two muon and  
 1360 one photon in the vicinity of the  $Z$  boson invariant mass. To this final state, a selections was  
 1361 applied to ensure that the photon comes from a Final State Radiation process, allowing us to use  
 1362 the tag-and-probe method.  
 1363 Considering the similarity of this analysis with the  $H/Z \rightarrow J/\psi + \gamma$  analysis [54], not only in therm  
 1364 of data samples, but also for triggering and physics object selection, the same scale factors were  
 1365 applied. More details are given in the same paper.

---

<sup>4</sup>The concept of isolation will be detailed later, but in summary, it means a object which has very small activity (above a certain threshold of energy/momentum) around it. In hadron-hadron collider, isolation is a characteristics of hard interactions.

1366 **4.5.2 Muon Identification**

1367 Ahead of any selection, a standard CMS "Ghost Cleaning" procedure is applied to all reconstructed  
1368 muons in order to avoid that a single physical muon is reconstructed as two or more. For this  
1369 procedure, reconstructed muons sharing 50% or more segments in the system are arbitrated.

1370 After the cleaning, a muon is chosen when it passes a two step identification: the **Loose ID** and  
1371 the **Tight ID**. Below the muon identification procedure is summarized .

1372 For the Loose ID, each muon is required to:

- 1373 • have transverse momentum greater than 5 GeV, in order to cope with Particle Flow require-  
1374 ments;
- 1375 • be within the muon system acceptance:  $|\eta| < 2.4$ ;
- 1376 • to have a three dimensional impact parameter uncertainty smaller than 4;
- 1377 • to have transverse distance smaller than 0.5 cm ( $d_{xy} < 0.5$ ), with respect to the primary  
1378 vertex (PV);
- 1379 • to have longitudinal distance greater than 1.0 cm ( $d_z < 1$ ), with respect to the primary vertex  
1380 (PV).

1381 Muons reconstructed only in the muon system, without a correspondence with the tracker, are  
1382 rejected. The last three requirements of the Loose ID are imposed in order to suppress muons from  
1383 in-flight decays.

1384 The primary vertex itself, is determined as the reconstructed vertex with the biggest sum of  $p_T^2$  in  
1385 the event. This sum is performed, considering all the charged PF candidates clustered by the jet  
1386 finding algorithms [71, 72] and the MET, which is defined as the  $p_T$  vector sum of all the charged  
1387 and neutral PF candidates associated to that vertex.

1388 For the Tight ID, muons with transverse momentum  $p_T < 200$  GeV, are required to have been  
1389 reconstructed with the Particle Flow (PF) algorithm. If they have  $p_T > 200$  GeV, they should re-  
1390 constructed with the Particle Flow (PF) algorithm or satisfy the strict tracker requirements (defined  
1391 in table 4.3).

Table 4.3: Conditions for a muon to pass the strict tracker requirements.

Requirement	Technical definition
Muon station matching	Muon is matched to segments in at least two stations in the muon system
Good $p_T$ measurement	$\frac{p_T}{\sigma_{p_T}} < 0.3$
Vertex compatibility ( $x - y$ )	$d_{xy} < 2$ mm
Vertex compatibility ( $z$ )	$d_z < 5$ mm
Pixel hits	At least one pixel hit
Tracker hits	Hits in at least six tracker layers

1392 To mitigate spurious signal in the detector that would mimic a muon, the leading muon (the one  
 1393 with highest  $p_T$ ) is required to be isolated within a cone of radius  $\Delta R = \sqrt{\Delta\eta^2 + \Delta\phi^2} < 0.3$  in  
 1394 the  $\eta - \phi$  plane. The isolation is evaluated in terms of  $\mathcal{I}^\mu < 0.35$ , defined as:

$$\mathcal{I}^\mu \equiv \left( \sum p_T^{\text{charged}} + \max \left[ 0, \sum p_T^{\text{neutral}} + \sum p_T^\gamma - p_T^{\text{PU}}(\mu) \right] \right) / p_T^\mu. \quad (4.3)$$

1395 The  $\sum p_T^{\text{charged}}$  is the scalar sum of the transverse momenta of charged hadrons originating from the  
 1396 chosen primary vertex of the event. The  $\sum p_T^{\text{neutral}}$  and  $\sum p_T^\gamma$  are the scalar sums of the transverse  
 1397 momenta for neutral hadrons and photons, respectively. Since the isolation variable is particularly  
 1398 sensitive to energy deposits from pileup interactions, a  $p_T^{\text{PU}}(\mu)$  contribution is subtracted, where  
 1399  $p_T^{\text{PU}}(\mu) \equiv 0.5 \times \sum_i p_T^{\text{PU},i}$ , where  $i$  runs over the momenta of the charged hadron PF candidates  
 1400 not originating from the primary vertex, and the factor of 0.5 corrects for the different fraction of  
 1401 charged and neutral particles in the cone.

1402 One should keep in mind that this muon identification is the same as the one used by the  $H \rightarrow$   
 1403  $ZZ^* \rightarrow 4l$  [106]. This was done in order to keep in phase with other Higgs analysis inside the  
 1404 collaboration. After the muon identification, an appropriate scale factor is applied to the MC  
 1405 events based on the leading muon  $p_T$  and  $\eta$ , in order to correct any possible discrepancy between  
 1406 data and simulated samples. The scale factors were taken from the  $H \rightarrow ZZ^* \rightarrow 4l$  analysis.

1407 In order to cope with trigger requirements, the leading muon should have  $p_T > 20$  GeV and the  
 1408 trailing muon  $p_T > 4$  GeV.

### 1409 4.5.3 Photon Identification

1410 For the photon identification and selection, standard CMS . The Multivariate (MVA) Photon iden-  
 1411 tification is used with a working point of 90%, together with a electron veto procedure, to avoid  
 1412 misidentification of electrons as photons. Kinematically, the photons are requested to have trans-  
 1413 verse energy, with respect to the beam line,  $E_T > 33$  GeV and reconstructed within the CMS  
 1414 acceptance for photons  $|\eta_{SC}| < 2.5^5$ , excluding the Electromagnetic Calorimeter (ECAL) Barrel-  
 1415 Endcap intersections.

1416 The threshold of 33 GeV for the photon transverse energy is driven by the trigger requirements.  
 1417 The selecte photon, per event, is the one with highest  $E_T$ .

### 1418 4.5.4 Kinematical distributions

1419 The selection described so far, is called Group I. The plots shown below are related to selected  
 1420 events after this set.

1421 Figures 4.5 to 4.10 presents the  $p_T$ ,  $\eta$  and  $\phi$  distributions for the leading muon, trailing muon and  
 1422 the photon, for the Z decaying in  $\Upsilon(1S, 2S, 3S) + \gamma$ .

<sup>5</sup>SC stands for Super Cluster of the reconstructed photon. It is the set of cell in the Electromagnetic Calorimeter used for the photon observation.

Figures 4.11 to 4.13 presents the  $p_T$ ,  $\eta$  and  $\phi$  distributions for reconstructed  $\Upsilon(nS)$  ( $\mu\mu$  system) and the reconstructed boson ( $\mu\mu\gamma$  system).

Figures 4.14 to 4.17 presents the  $\Delta R = \sqrt{\Delta\eta^2 + \Delta\phi^2}$  between the photon and the muons, the  $\Delta R$  distributions between reconstructed dimuon ( $\mu\mu$ ) system and the photon, the absolute value of the  $\Delta\phi$  between the leading muon and the photon, the ratio for the transverse momentum of the reconstructed Upsilon and the reconstructed Z mass ( $p_T^{\mu\mu}/M_{\mu\mu\gamma}$ ), the ratio for the transverse energy of the reconstructed Photon and the reconstructed Z mass ( $E_T^{\mu\mu}/M_{\mu\mu\gamma}$ ) and dimuon mass distribution of the reconstructed  $\Upsilon(nS)$ .

Figures 4.18 to 4.30 present the same variables, but for the Higgs decaying in  $\Upsilon(1S, 2S, 3S) + \gamma$  channel.

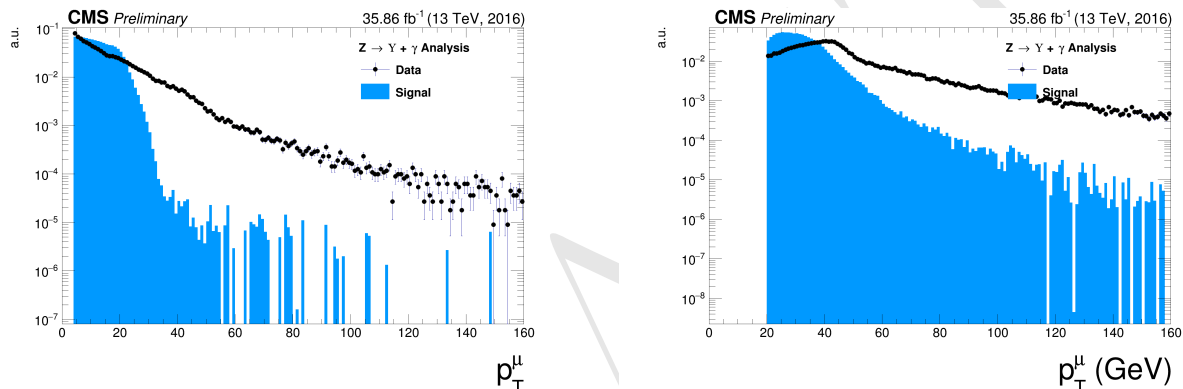


Figure 4.5: The  $p_T$  muon distributions from data and signal events for Z decaying in  $\Upsilon(1S, 2S, 3S) + \gamma$  after Group I of selection cuts, where on left are presenting the trailing muons and on right are the leading muons. The plots are normalized to the unit of area.

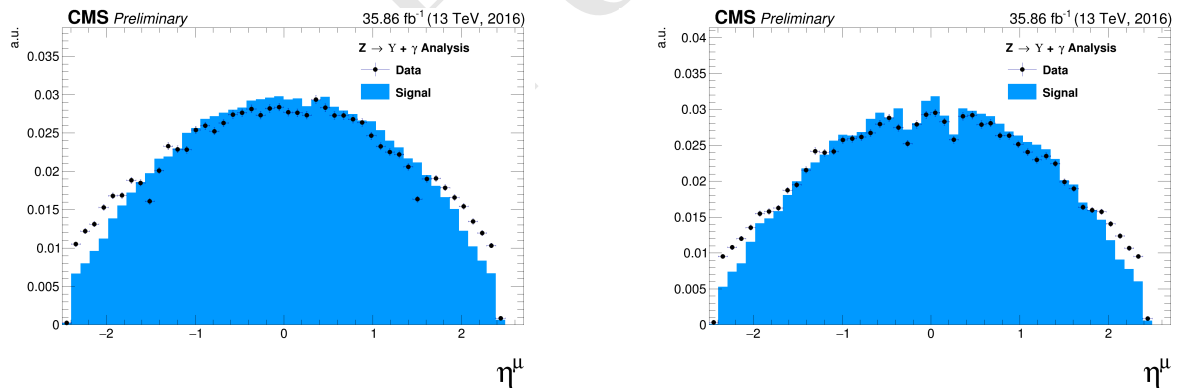


Figure 4.6: The  $\eta$  muon distributions from data and signal events of Z decaying in  $\Upsilon(1S, 2S, 3S) + \gamma$  after Group I of selection cuts, where on left are presenting the trailing muons and on right are the leading muons. The plots are normalized to the unit of area.

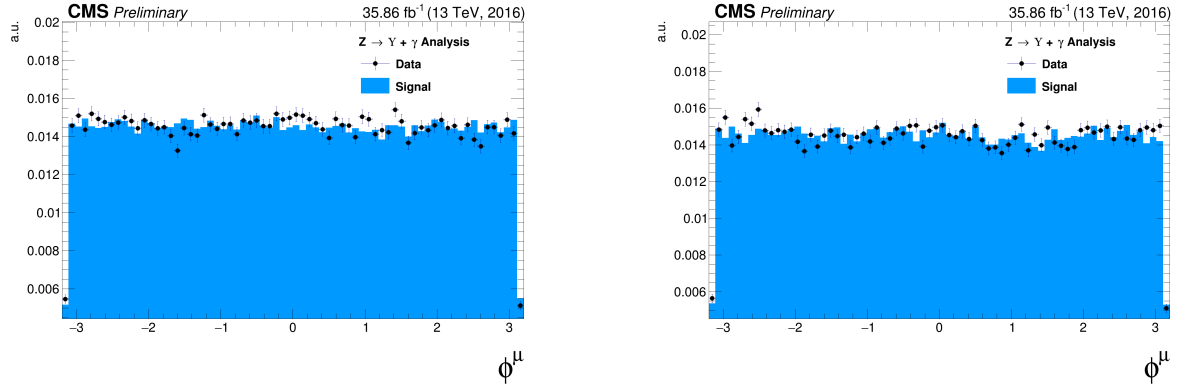


Figure 4.7: The  $\phi$  muon distributions from data and signal events of  $Z$  decaying in  $\Upsilon(1S, 2S, 3S) + \gamma$  after Group I of selection cuts, where on left are presenting the trailing muons and on right are the leading muons. The plots are normalized to the unit of area.

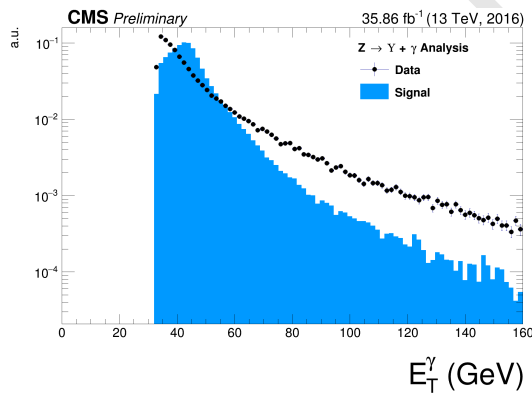


Figure 4.8: The  $p_T$  photon distributions from data and signal events for  $Z$  decaying in  $\Upsilon(1S, 2S, 3S) + \gamma$  Group I of selection cuts. The plots normalized to the unit of area.

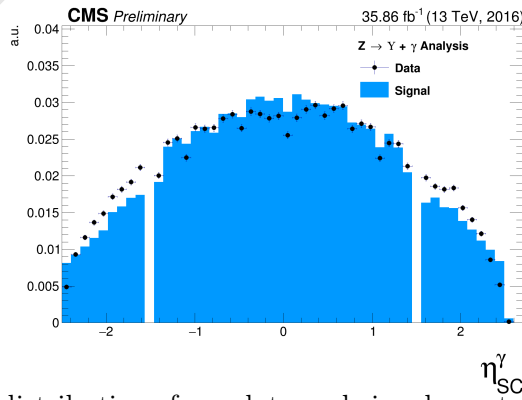


Figure 4.9: The  $\eta$  photon distributions from data and signal events of  $Z$  decaying in  $\Upsilon(1S, 2S, 3S) + \gamma$  after Group I of selection cuts. The plot is normalized to the unit of area.

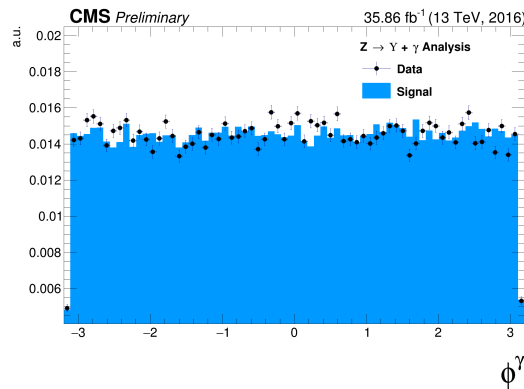


Figure 4.10: The  $\phi$  photon distributions from data and signal events of Z decaying in  $\Upsilon(1S, 2S, 3S) + \gamma$  after Group I of selection cuts. The plot is normalized to the unit of area.

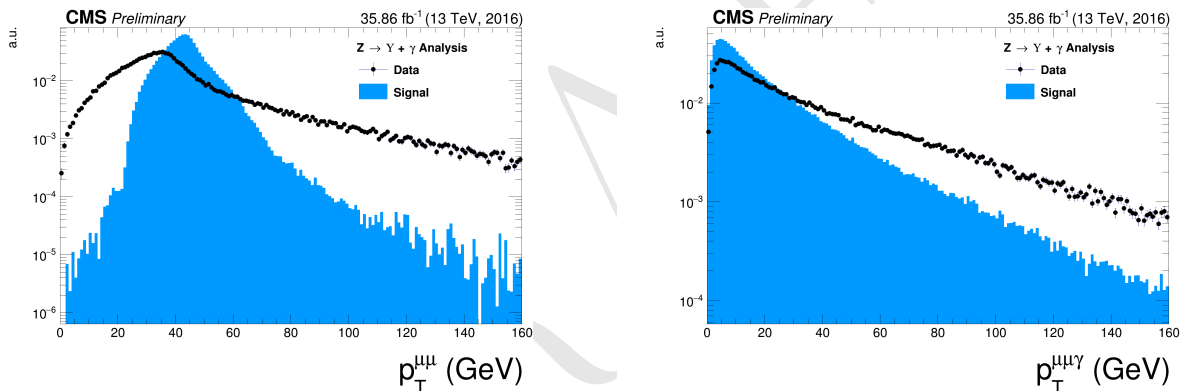


Figure 4.11: The  $p_T$  distributions for the reconstructed  $\Upsilon(1S, 2S, 3S)$  in the left and for Z in the right from data and signal events for Z decaying in  $\Upsilon(1S, 2S, 3S) + \gamma$  after Group I of selection cuts. The plots are normalized to the unit of area.

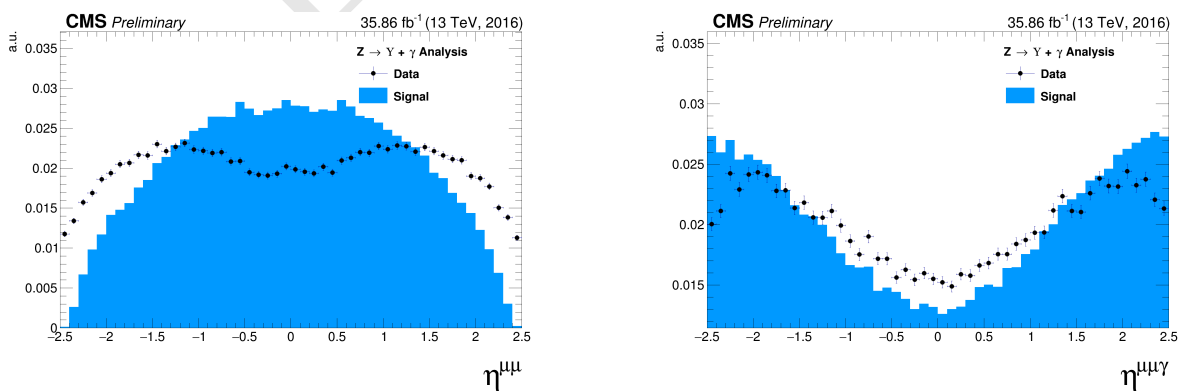


Figure 4.12: The  $\eta$  distributions for  $\Upsilon(1S, 2S, 3S)$  in the left and for Z in the right from data and signal events for Z decaying in  $\Upsilon(1S, 2S, 3S) + \gamma$  after Group I of selection cuts. The plots are normalized to the unit of area.

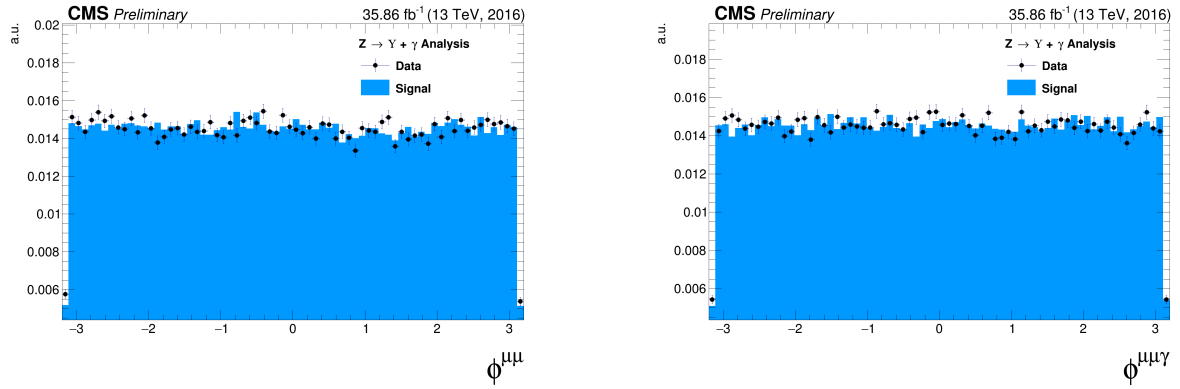


Figure 4.13: The  $\phi$  distributions for  $\Upsilon(1S, 2S, 3S)$  in the left and for  $Z$  in the right from data and signal events for  $Z$  decaying in  $\Upsilon(1S, 2S, 3S) + \gamma$  after Group I of selection cuts. The plots are normalized to the unit of area.

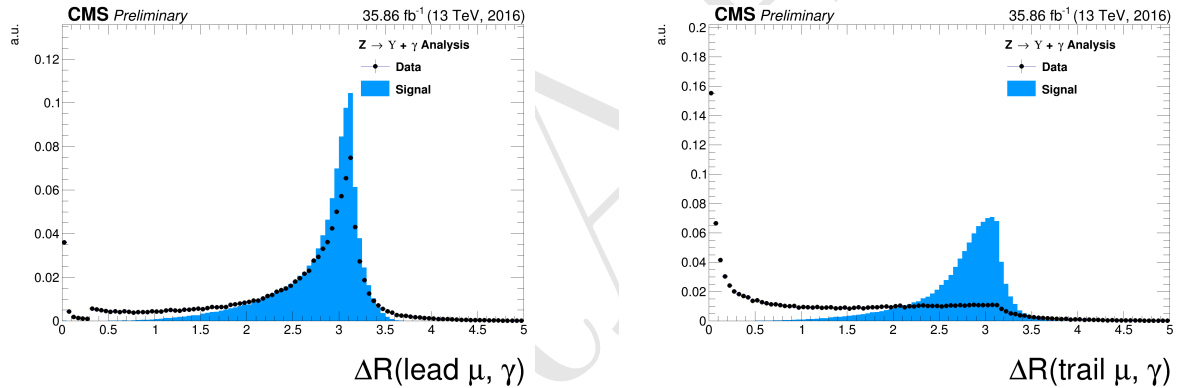


Figure 4.14: The  $\Delta R$  distributions between the photon and the leading muon (left) and the trailing muon (right) for for  $Z$  decaying in  $\Upsilon(1S, 2S, 3S) + \gamma$  from data and signal events after Group I of selection cuts. The plots are normalized to the unit of area.

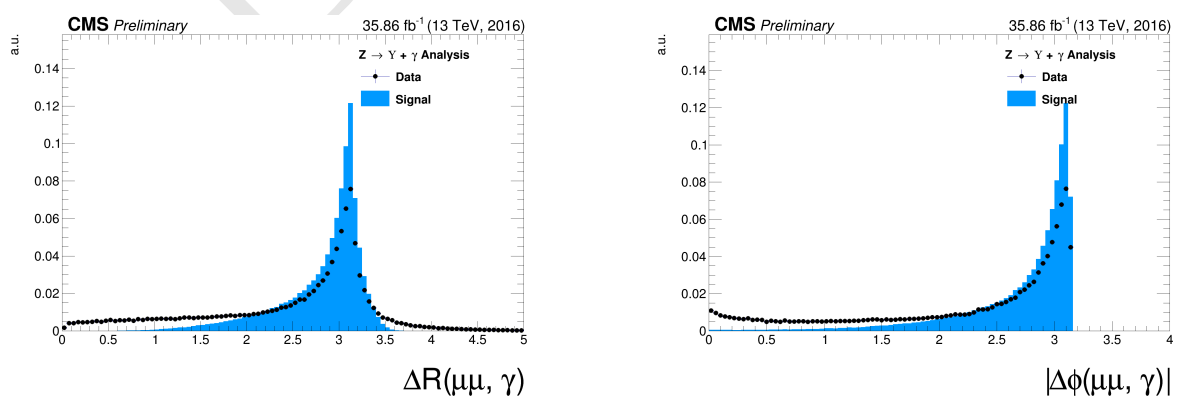


Figure 4.15: Left: The  $\Delta R$  distributions between reconstructed dimuon ( $\mu\mu$ ) system and the photon. Right: absolute value of the  $\Delta\phi$  between the leading muon and the photon for for  $Z$  decaying in  $\Upsilon(1S, 2S, 3S) + \gamma$  from data and signal events after Group I of selection cuts. The plots are normalized to the unit of area.

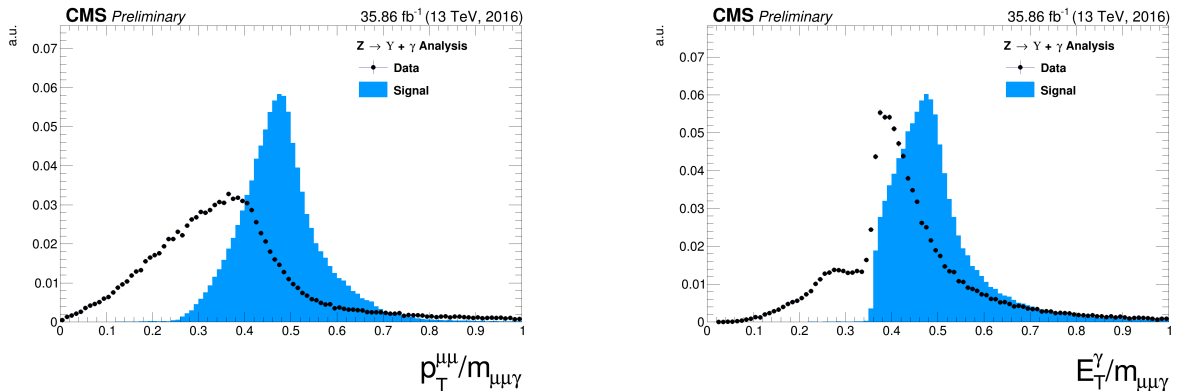


Figure 4.16: The ratio for the transverse momentum of the reconstructed Upsilon and the reconstructed Z mass ( $p_T^{\mu\mu}/M_{\mu\mu\gamma}$  - left) and the ratio for the transverse energy of the reconstructed Photon and the reconstructed Z mass ( $E_T^\gamma/M_{\mu\mu\gamma}$  - right) distribution for Z decaying in  $\Upsilon(1S, 2S, 3S) + \gamma$  from data and signal events after Group I of selection cuts. The plots are normalized to the unit of area.

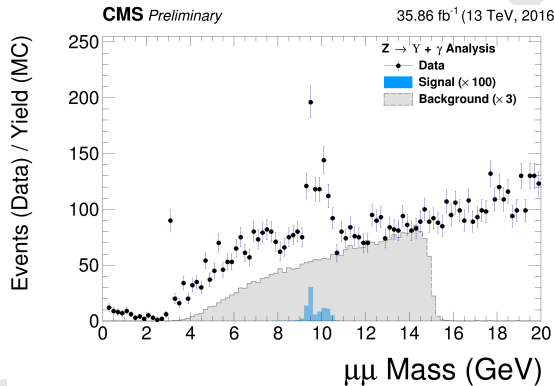


Figure 4.17: The dimuon mass distribution of the reconstructed  $\Upsilon(1S, 2S, 3S)$  from data and signal events for Z decaying after Group I of selection cuts. The plot is normalized to the number of events. "Signal" stands for the  $Z \rightarrow \Upsilon(1S, 2S, 3S) + \gamma$  sample (scaled by a factor of  $\times 100$ ) and "Background" corresponds to the peaking background ( $Z \rightarrow \mu\mu\gamma_{FSR}$ ) sample (scaled by a factor of  $\times 3$ ).

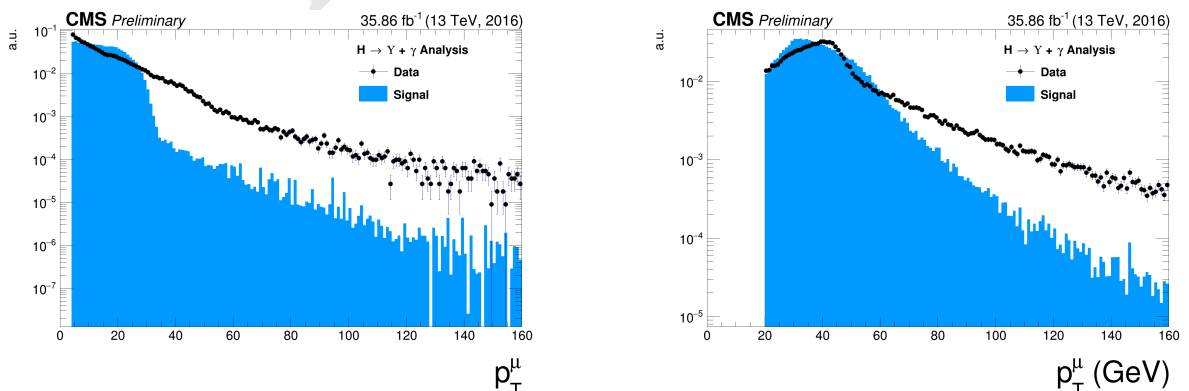


Figure 4.18: The  $p_T$  muon distributions from data and signal events for Higgs decaying in  $\Upsilon(1S, 2S, 3S) + \gamma$  after Group I of selection cuts, where on left are presenting the trailing muons and on right are the leading muons. The plots are normalized to the unit of area.

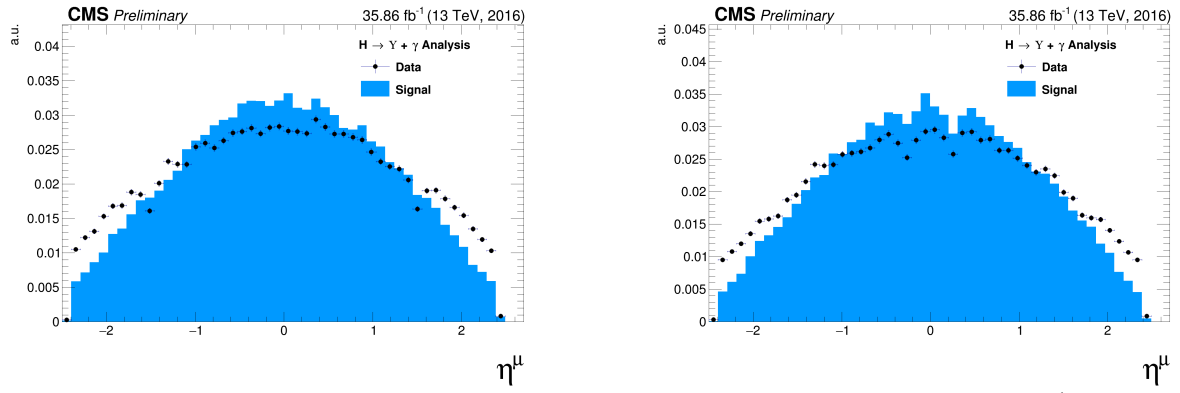


Figure 4.19: The  $\eta$  muon distributions from data and signal events of Higgs decaying in  $\Upsilon(1S, 2S, 3S) + \gamma$  after Group I of selection cuts, where on left are presenting the trailing muons and on right are the leading muons. The plots are normalized to the unit of area.

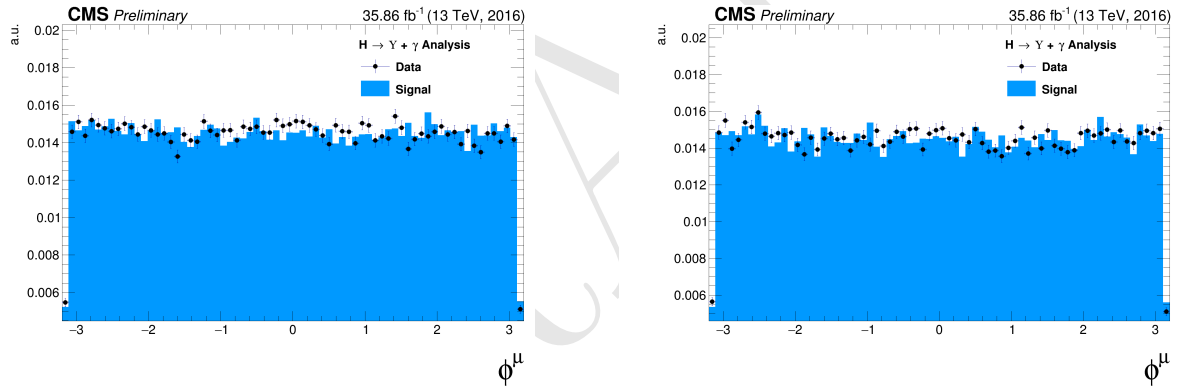


Figure 4.20: The  $\phi$  muon distributions from data and signal events of Higgs decaying in  $\Upsilon(1S, 2S, 3S) + \gamma$  after Group I of selection cuts, where on left are presenting the trailing muons and on right are the leading muons. The plots are normalized to the unit of area.

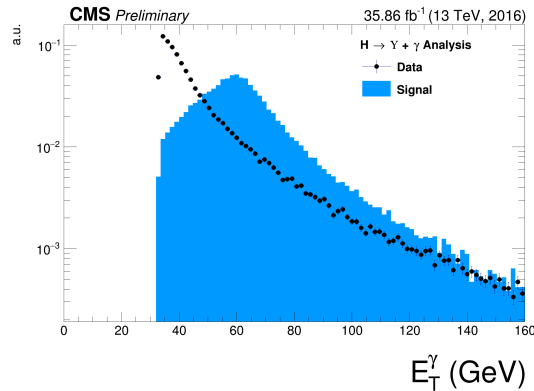


Figure 4.21: The  $p_T$  photon distributions from data and signal events for Higgs decaying in  $\Upsilon(1S, 2S, 3S) + \gamma$  Group I of selection cuts. The plot is normalized to the unit of area.

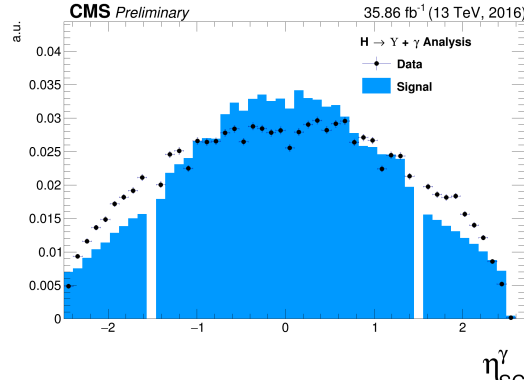


Figure 4.22: The  $\eta$  photon distributions from data and signal events of Higgs decaying in  $\Upsilon(1S, 2S, 3S) + \gamma$  after Group I of selection cuts. The plot is normalized to the unit of area.

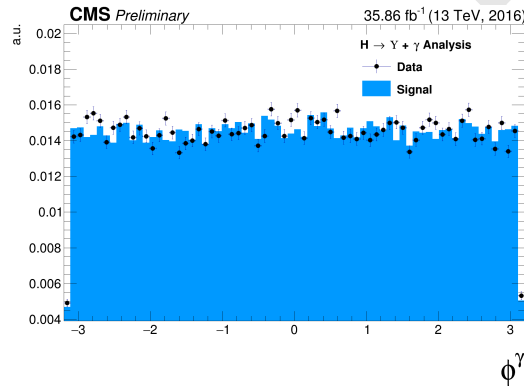


Figure 4.23: The  $\phi$  photon distributions from data and signal events of Higgs decaying in  $\Upsilon(1S, 2S, 3S) + \gamma$  after Group I of selection cuts. The plot is normalized to the unit of area.

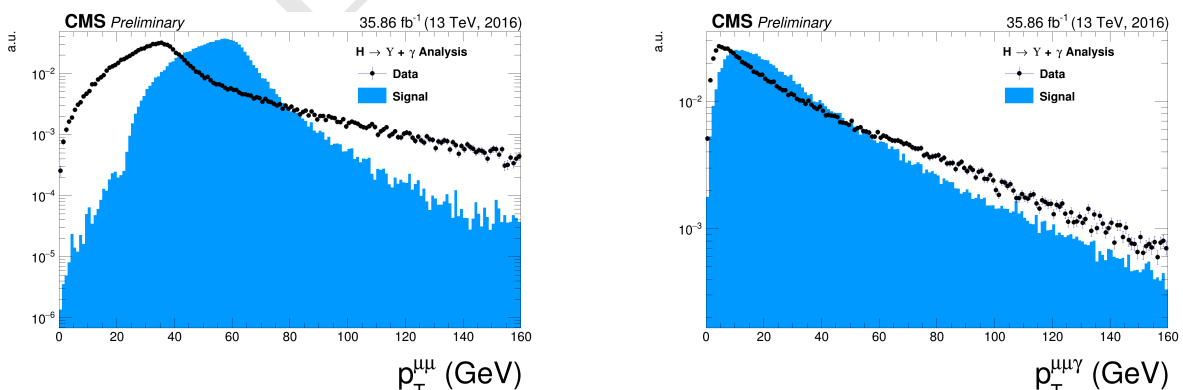


Figure 4.24: The  $p_T$  distributions for  $\Upsilon(1S, 2S, 3S)$  in the left and for Higgs in the right from data and signal events for Higgs decaying in  $\Upsilon(1S, 2S, 3S) + \gamma$  after Group I of selection cuts. The plots are normalized to the unit of area.

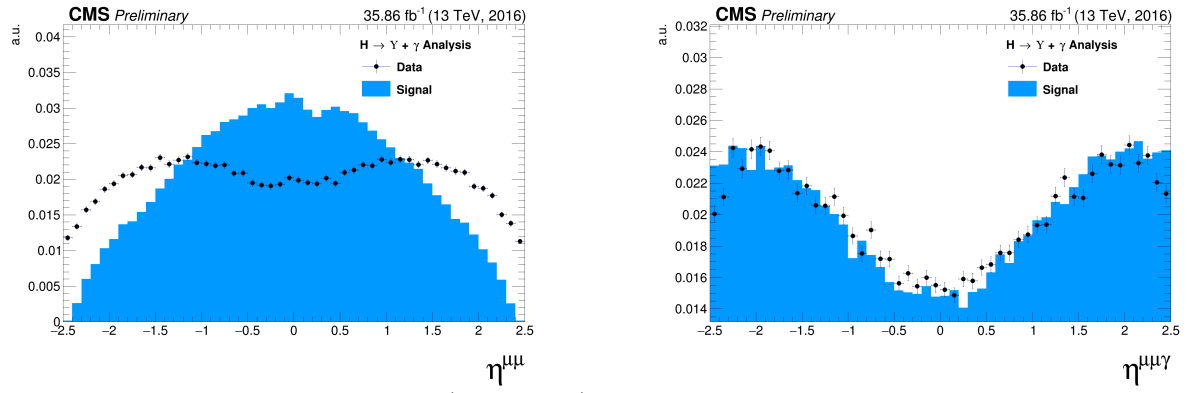


Figure 4.25: The  $\eta$  distributions for  $\Upsilon(1S, 2S, 3S)$  in the left and for Higgs in the right from data and signal events for Higgs decaying in  $\Upsilon(1S, 2S, 3S) + \gamma$  after Group I of selection cuts. The plots are normalized to the unit of area.

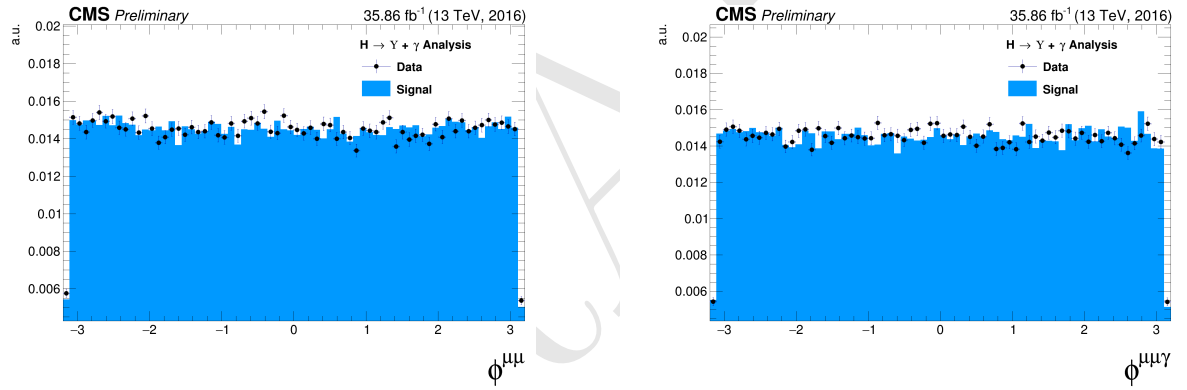


Figure 4.26: The  $\phi$  distributions for  $\Upsilon(1S, 2S, 3S)$  in the left and for Higgs in the right from data and signal events for Higgs decaying in  $\Upsilon(1S, 2S, 3S) + \gamma$  after Group I of selection cuts. The plots are normalized to the unit of area.

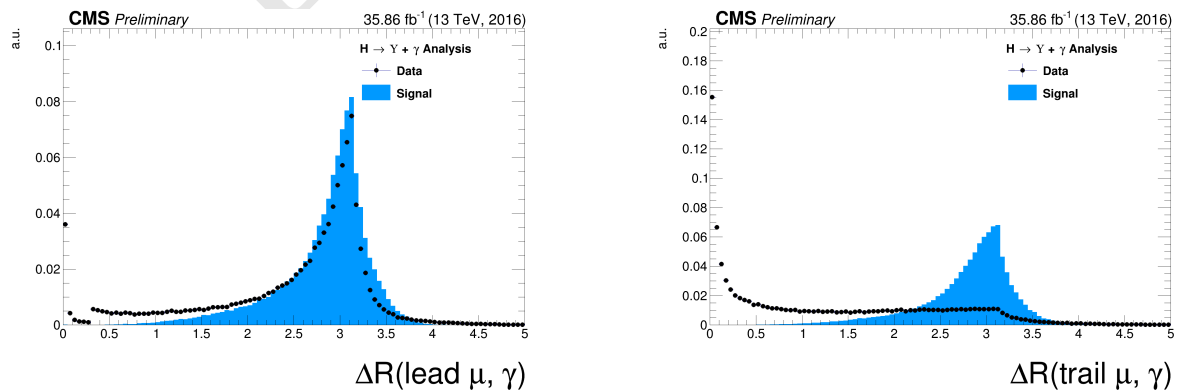


Figure 4.27: The  $\Delta R$  distributions between the photon and the leading muon (left) and the trailing muon (right) for Higgs decaying in  $\Upsilon(1S, 2S, 3S) + \gamma$  from data and signal events after Group I of selection cuts. The plots are normalized to the unit of area.

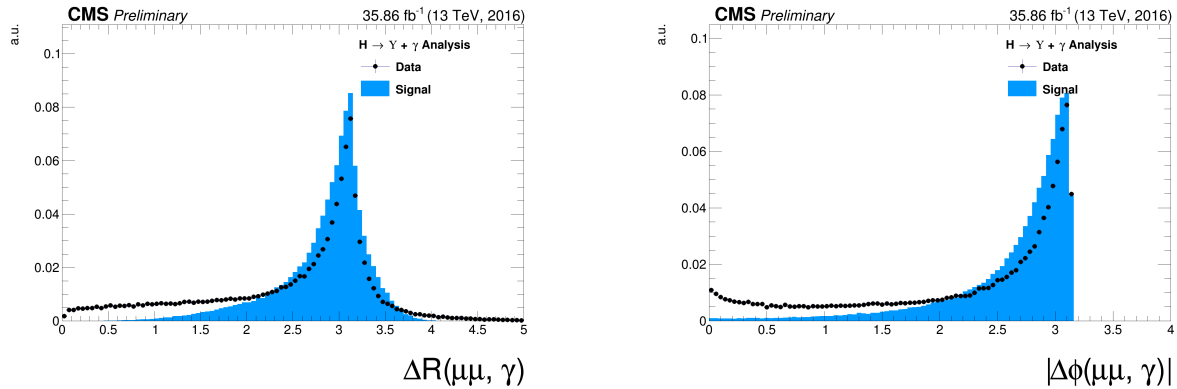


Figure 4.28: Left: The  $\Delta R$  distributions between reconstructed dimuon ( $\mu\mu$ ) system and the photon. Right: absolute value of the  $\Delta\phi$  between the leading muon and the photon for for Higgs decaying in  $\Upsilon(1S, 2S, 3S) + \gamma$  from data and signal events after Group I of selection cuts. The plots are normalized to the unit of area.

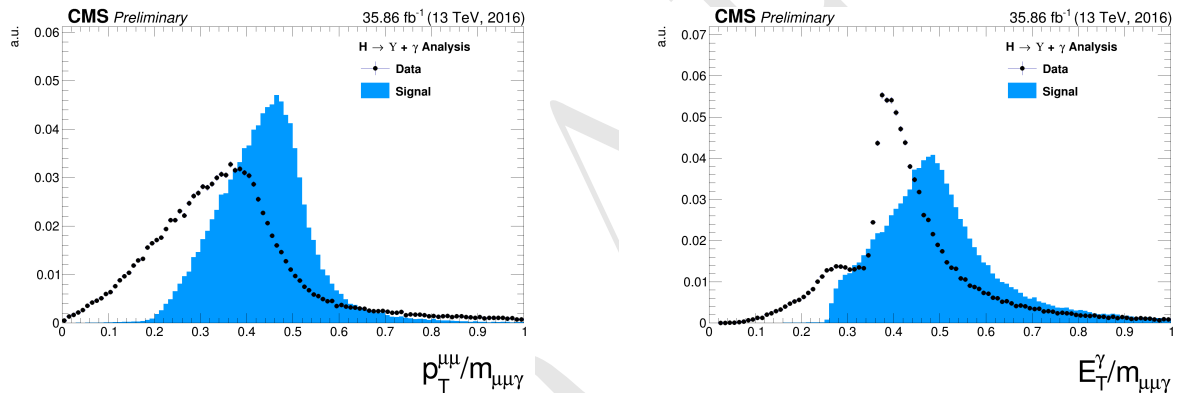


Figure 4.29: The ratio for the transverse momentum of the reconstructed Upsilon and the reconstructed Higgs mass ( $p_T^{\mu\mu} / M_{\mu\mu\gamma}$  - left) and the ratio for the transverse energy of the reconstructed Photon and the reconstructed Higgs mass ( $E_T^\gamma / M_{\mu\mu\gamma}$  - right) distribution for Higgs decaying in  $\Upsilon(1S, 2S, 3S) + \gamma$  from data and signal events after Group I of selection cuts. The plots are normalized to the unit of area.

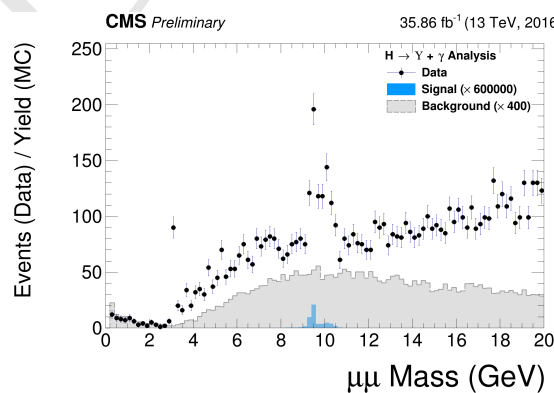


Figure 4.30: The dimuon mass distribution of the reconstructed  $\Upsilon(1S, 2S, 3S)$  from data and signal events for Higgs decaying after Group I of selection cuts. This plot is normalized the expected number of events. "Signal" stands for the  $H \rightarrow \Upsilon(1S, 2S, 3S) + \gamma$  sample (scaled by a factor of  $\times 600000$ ) and "Background" corresponds to the peaking background (Higgs Dalitz Decay) sample (scaled by a factor of  $\times 400$ ).

## 4.6 Kinematical selection (Group II)

After all Trigger and Object Identification cuts, described in before (**Group I**), a set of kinematical cuts are applied in order to improve the signal to background relation. They are

- $\Delta R(\text{leading } \mu, \gamma) > 1;$
- $\Delta R(\text{trailing } \mu, \gamma) > 1;$
- $\Delta R(\mu\mu, \gamma) > 2;$
- $|\Delta\phi(\text{leading } \mu, \gamma)| > 1.5;$
- $8.4 \text{ GeV} < M_{\mu\mu} < 11.1 \text{ GeV};$
- $E_T^\gamma/M_{\mu\mu\gamma} > 35/91.2 \text{ for the Z decay or } 35/125 \text{ for the Higgs decay};$
- $p_T^{\mu\mu}/M_{\mu\mu\gamma} > 35/91.2 \text{ for the Z decay or } 35/125 \text{ for the Higgs decay.}$

The choice of these thresholds were based on the visual inspection of the distributions (besides the invariant mass distribution of the dimuon system  $M_{\mu\mu}$ , which needs to be defined around the  $v(1S, 2S, 3S)$  mass) and to keep this analysis in phase with other similar analysis within CMS.

Below it is shown the same set of plot shown before, but this time, taking into account the full selection (**Group I+II**).

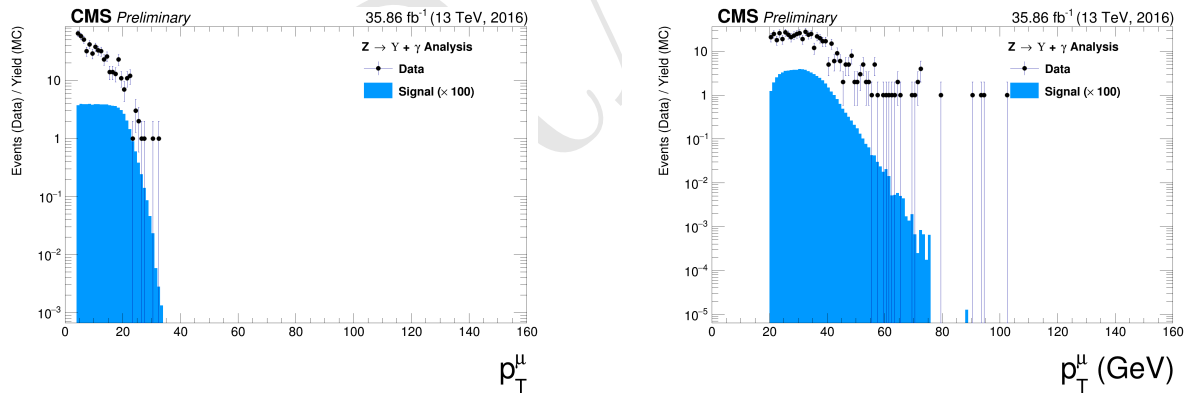


Figure 4.31: The  $p_T$  muon distributions from data and signal events for Z decaying in  $\Upsilon(1S, 2S, 3S) + \gamma$  after Group I of selection cuts, where on left are presenting the trailing muons and on right are the leading muons. The plots are normalized to the number of events. Signal sample is scaled by a factor of  $\times 100$ .

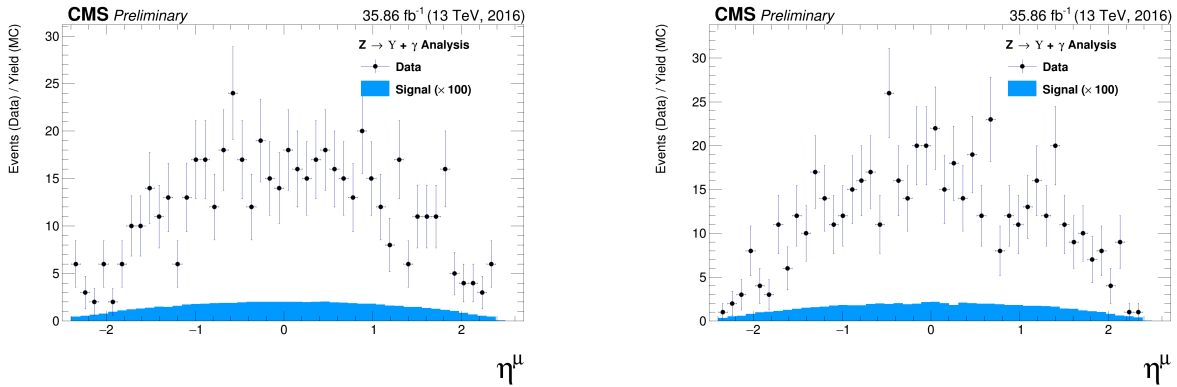


Figure 4.32: The  $\eta$  muon distributions from data and signal events of Z decaying in  $\Upsilon(1S, 2S, 3S) + \gamma$  after Group I of selection cuts, where on left are presenting the trailing muons and on right are the leading muons. The plots are normalized to the number of events. Signal sample is scaled by a factor of  $\times 100$ .

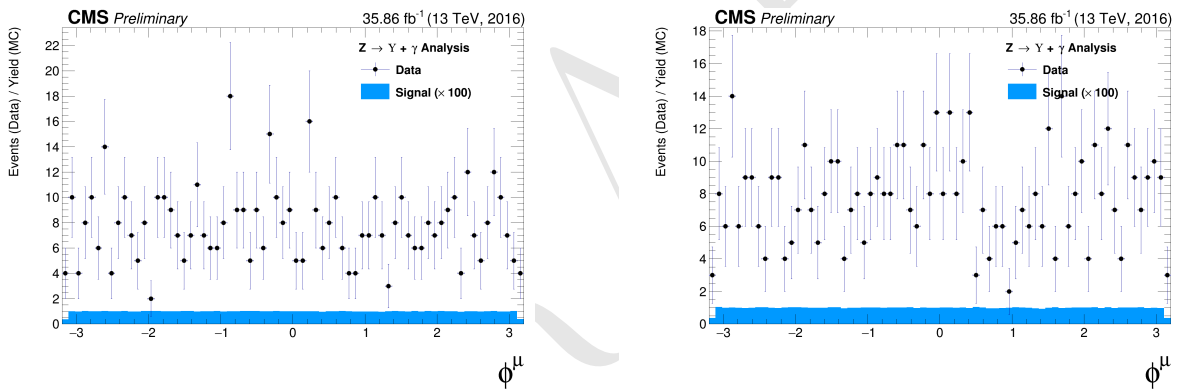


Figure 4.33: The  $\phi$  muon distributions from data and signal events of Z decaying in  $\Upsilon(1S, 2S, 3S) + \gamma$  after Group I of selection cuts, where on left are presenting the trailing muons and on right are the leading muons. The plots are normalized to the number of events. Signal sample is scaled by a factor of  $\times 100$ .

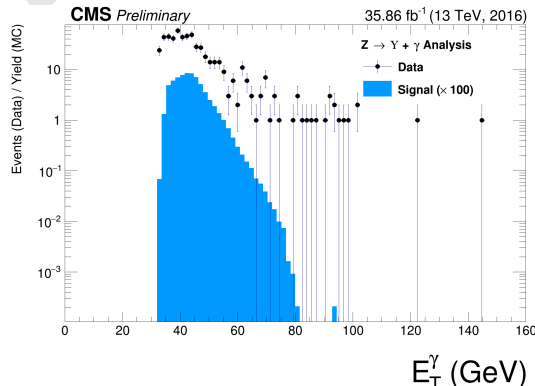


Figure 4.34: The  $p_T$  photon distributions from data and signal events for Z decaying in  $\Upsilon(1S, 2S, 3S) + \gamma$  all (Group I+II) selection cuts. The plot is normalized to the number of events. Signal sample is scaled by a factor of  $\times 100$ .

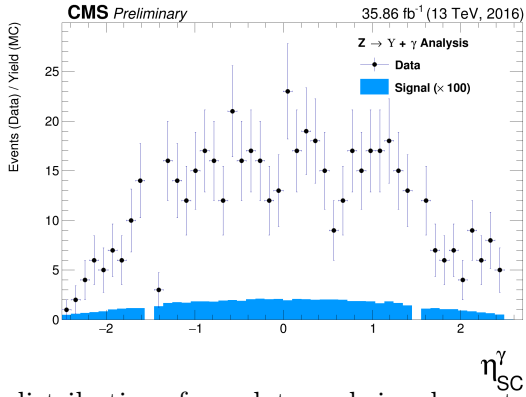


Figure 4.35: The  $\eta$  photon distributions from data and signal events of  $Z$  decaying in  $\Upsilon(1S, 2S, 3S) + \gamma$  after all (Group I+II) selection cuts. The plot is normalized to the number of events. Signal sample is scaled by a factor of  $\times 100$ .

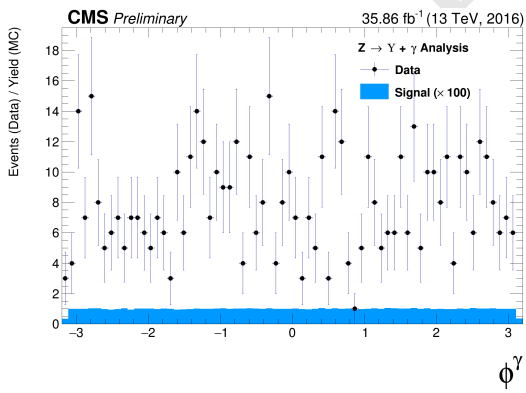


Figure 4.36: The  $\phi$  photon distributions from data and signal events of  $Z$  decaying in  $\Upsilon(1S, 2S, 3S) + \gamma$  after all (Group I+II) selection cuts. The plot is normalized to the number of events. Signal sample is scaled by a factor of  $\times 100$ .

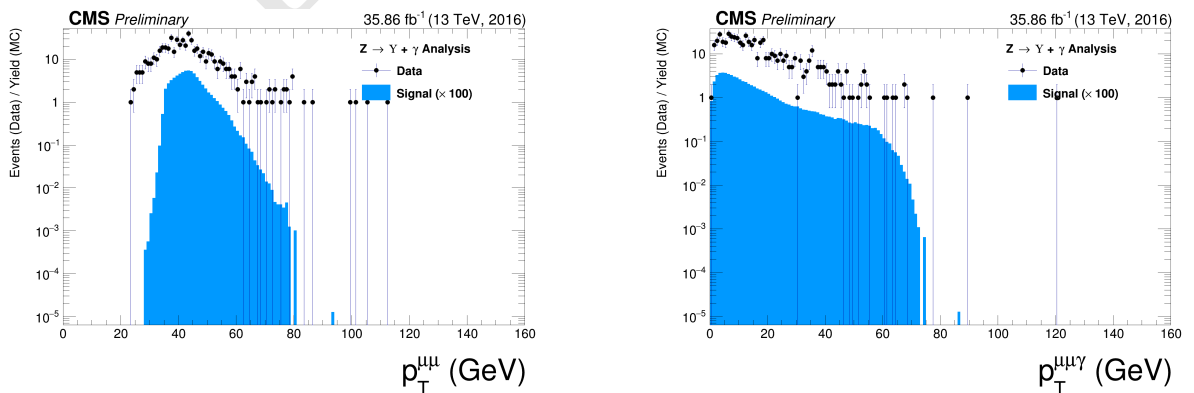


Figure 4.37: The  $p_T$  distributions for  $\Upsilon(1S, 2S, 3S)$  in the left and for  $Z$  in the right from data and signal events for  $Z$  decaying in  $\Upsilon(1S, 2S, 3S) + \gamma$  after all (Group I+II) selection cuts. The plots are normalized to the number of events. Signal sample is scaled by a factor of  $\times 100$ .

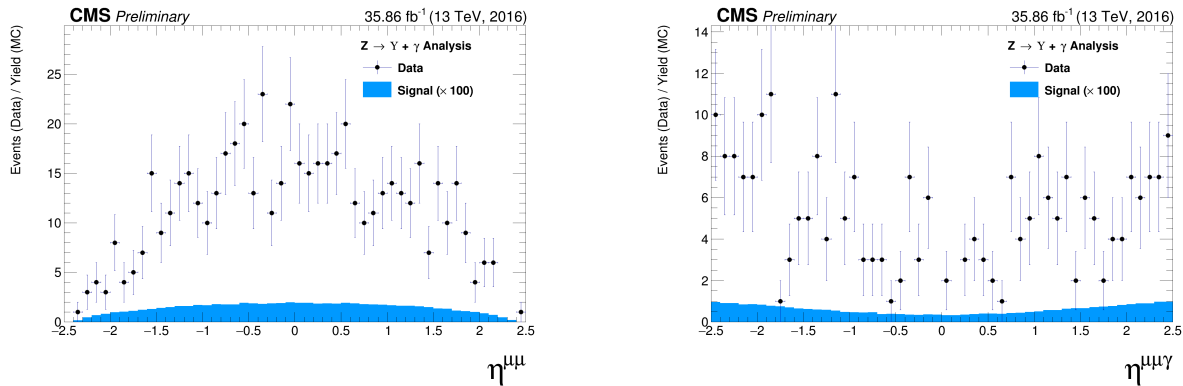


Figure 4.38: The  $\eta$  distributions for  $\Upsilon(1S, 2S, 3S)$  in the left and for  $Z$  in the right from data and signal events for  $Z$  decaying in  $\Upsilon(1S, 2S, 3S) + \gamma$  after all (Group I+II) selection cuts. The plots are normalized to the number of events. Signal sample is scaled by a factor of  $\times 100$ .

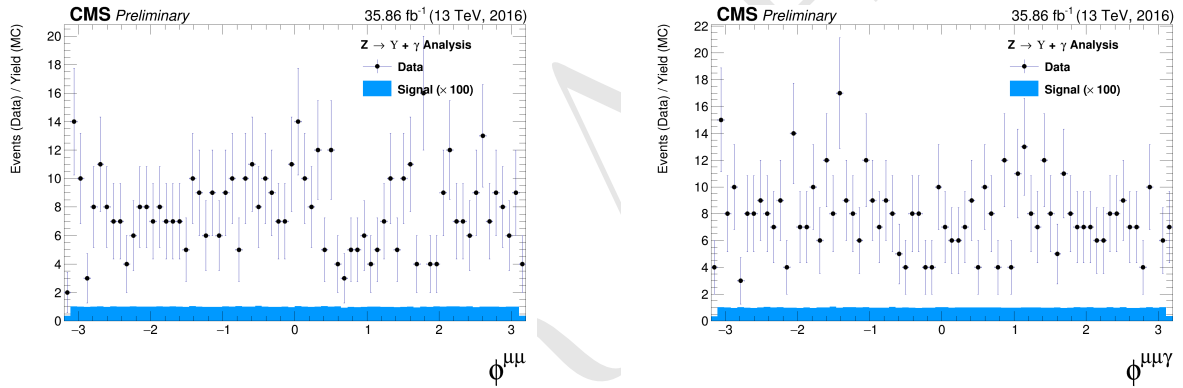


Figure 4.39: The  $\phi$  distributions for  $\Upsilon(1S, 2S, 3S)$  in the left and for  $Z$  in the right from data and signal events for  $Z$  decaying in  $\Upsilon(1S, 2S, 3S) + \gamma$  after all (Group I+II) selection cuts. The plots are normalized to the number of events. Signal sample is scaled by a factor of  $\times 100$ .

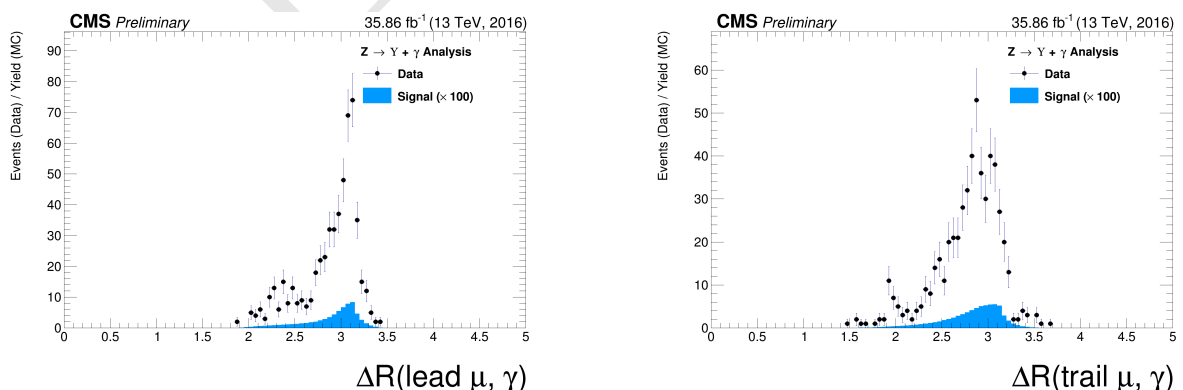


Figure 4.40: The  $\Delta R$  distributions between the photon and the leading muon (left) and the trailing muon (right) for  $\Upsilon(1S, 2S, 3S)$  from data and signal events for  $Z$  decaying after all (Group I+II) selection cuts. The plots are normalized to the number of events. Signal sample is scaled by a factor of  $\times 100$ .

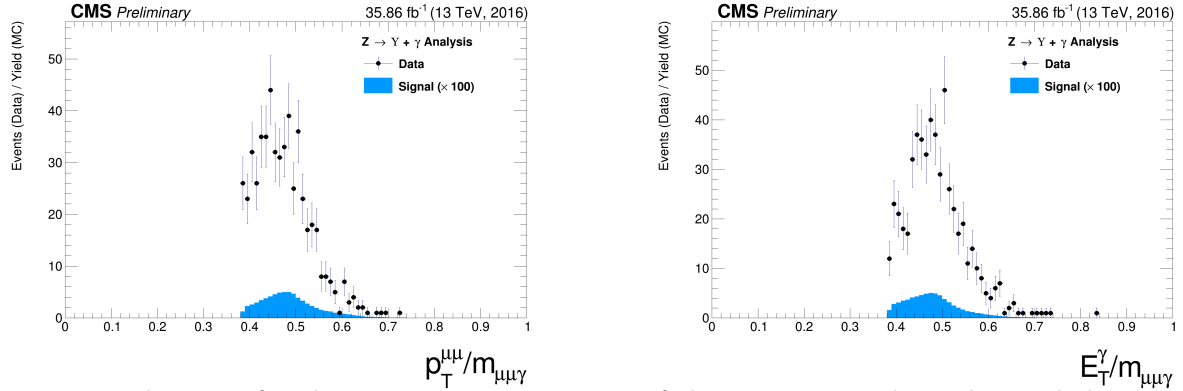


Figure 4.41: The ratio for the transverse momentum of the reconstructed Upsilon and the reconstructed Z mass ( $p_T^{\mu\mu}/M_{\mu\mu\gamma}$  - left) and the ratio for the transverse energy of the reconstructed Photon and the reconstructed Z mass ( $E_T^{\mu\mu}/M_{\mu\mu\gamma}$  - right) distribution for  $\Upsilon(1S, 2S, 3S)$  from data and signal events for Z decaying after all (Group I+II) selection cuts. The plots are normalized to the number of events. Signal sample is scaled by a factor of  $\times 100$ .

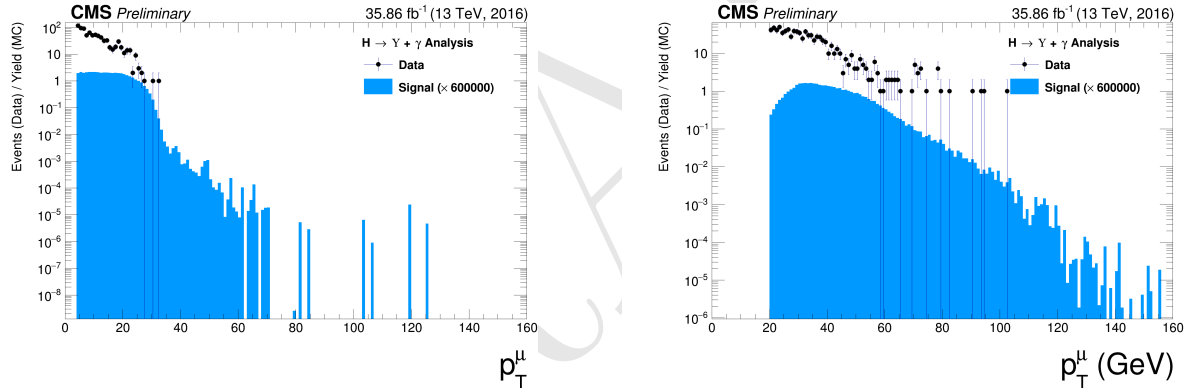


Figure 4.42: The  $p_T$  muon distributions from data and signal events for Higgs decaying in  $\Upsilon(1S, 2S, 3S) + \gamma$  after Group I of selection cuts, where on left are presenting the trailing muons and on right are the leading muons. The plots are normalized to the number of events. Signal sample is scaled by a factor of  $\times 600000$ .

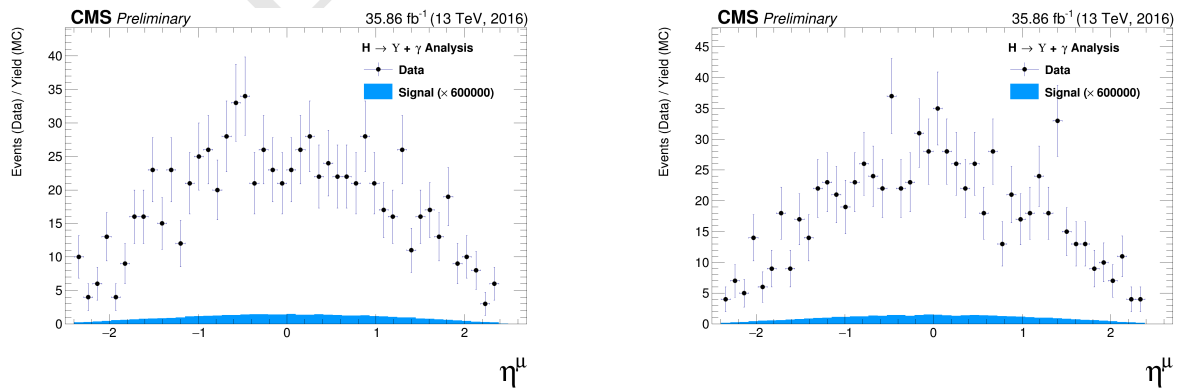


Figure 4.43: The  $\eta$  muon distributions from data and signal events of Higgs decaying in  $\Upsilon(1S, 2S, 3S) + \gamma$  after Group I of selection cuts, where on left are presenting the trailing muons and on right are the leading muons. The plots are normalized to the number of events. Signal sample is scaled by a factor of  $\times 600000$ .

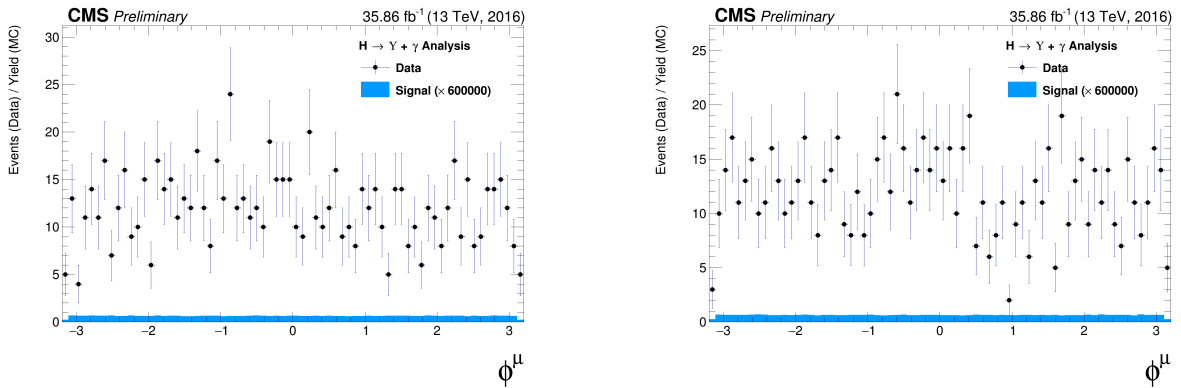


Figure 4.44: The  $\phi$  muon distributions from data and signal events of Higgs decaying in  $\Upsilon(1S, 2S, 3S) + \gamma$  after Group I of selection cuts, where on left are presenting the trailing muons and on right are the leading muons. The plots are normalized to the number of events. Signal sample is scaled by a factor of  $\times 600000$ .

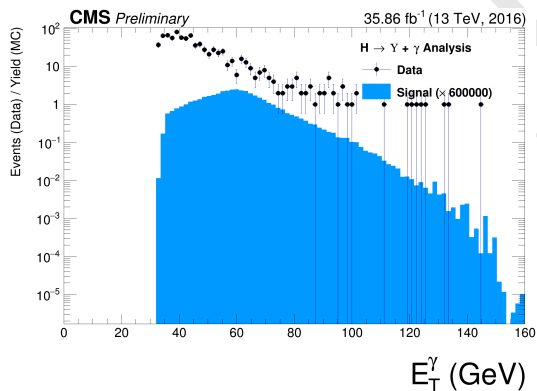


Figure 4.45: The  $p_T$  photon distributions from data and signal events for Higgs decaying in  $\Upsilon(1S, 2S, 3S) + \gamma$  all (Group I+II) selection cuts. The plot is normalized to the number of events. Signal sample is scaled by a factor of  $\times 600000$ .

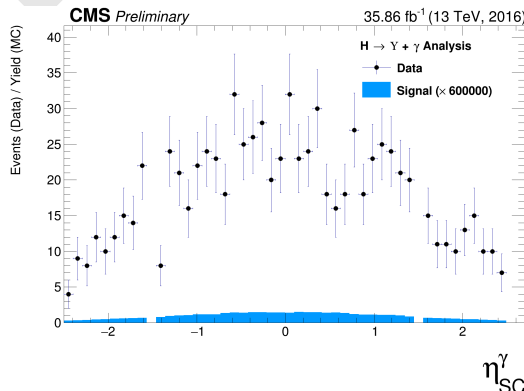


Figure 4.46: The  $\eta$  photon distributions from data and signal events of Higgs decaying in  $\Upsilon(1S, 2S, 3S) + \gamma$  after all (Group I+II) selection cuts. The plot is normalized to the number of events. Signal sample is scaled by a factor of  $\times 600000$ .

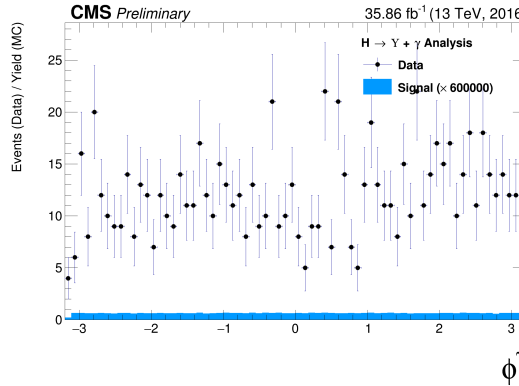


Figure 4.47: The  $\phi$  photon distributions from data and signal events of Higgs decaying in  $\Upsilon(1S, 2S, 3S) + \gamma$  after all (Group I+II) selection cuts. The plot is normalized to the number of events. Signal sample is scaled by a factor of  $c$ .

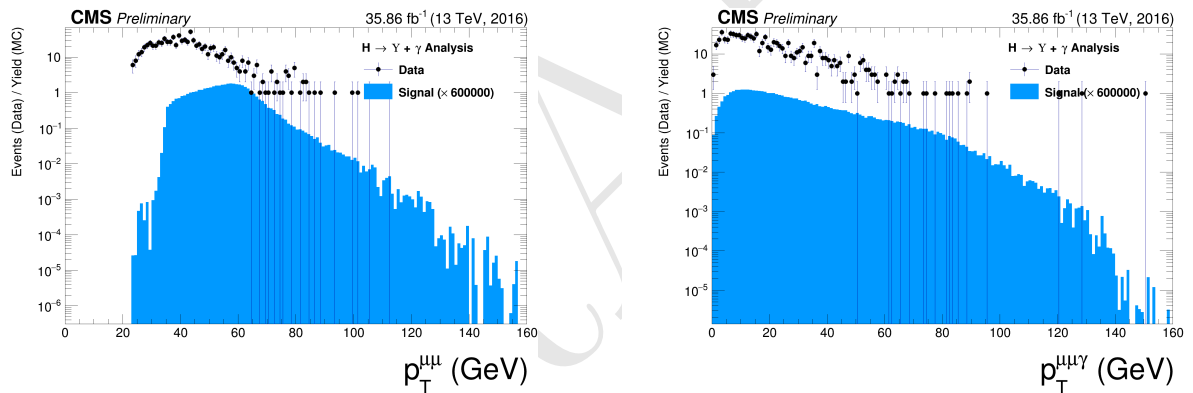


Figure 4.48: The  $p_T$  distributions for  $\Upsilon(1S, 2S, 3S)$  in the left and for Higgs in the right from data and signal events for Higgs decaying in  $\Upsilon(1S, 2S, 3S) + \gamma$  after all (Group I+II) selection cuts. The plots are normalized to the number of events. Signal sample is scaled by a factor of  $\times 600000$ .

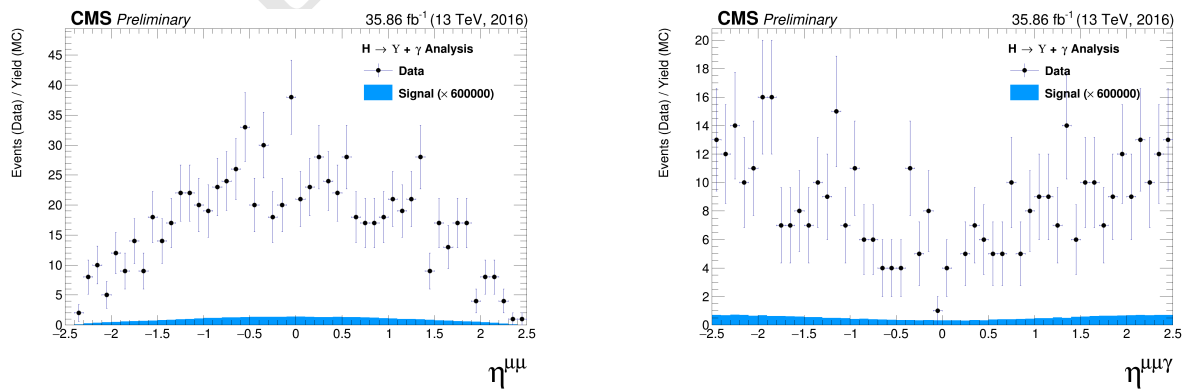


Figure 4.49: The  $\eta$  distributions for  $\Upsilon(1S, 2S, 3S)$  in the left and for Higgs in the right from data and signal events for Higgs decaying in  $\Upsilon(1S, 2S, 3S) + \gamma$  after all (Group I+II) selection cuts. The plots are normalized to the number of events. Signal sample is scaled by a factor of  $\times 600000$ .

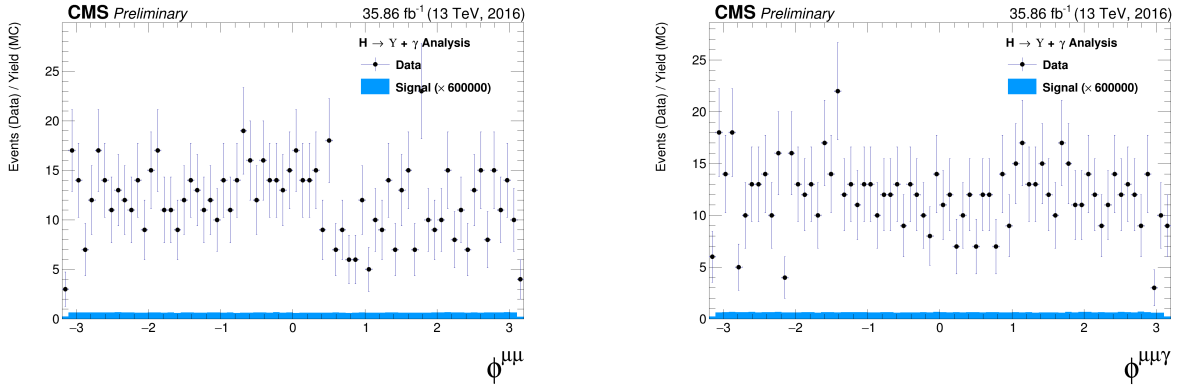


Figure 4.50: The  $\phi$  distributions for  $\Upsilon(1S, 2S, 3S)$  in the left and for Higgs in the right from data and signal events for Higgs decaying in  $\Upsilon(1S, 2S, 3S) + \gamma$  after all (Group I+II) selection cuts. The plots are normalized to the number of events. Signal sample is scaled by a factor of  $\times 600000$ .

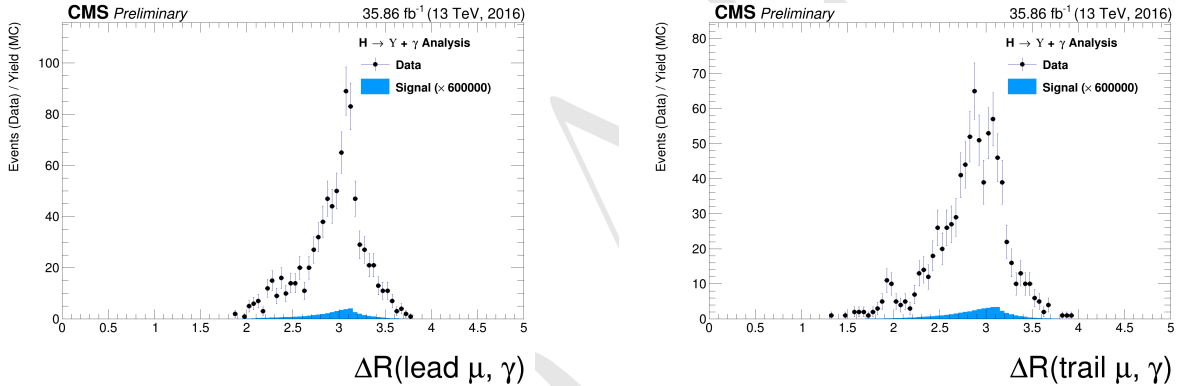


Figure 4.51: The  $\Delta R$  distributions between the photon and the leading muon (left) and the trailing muon (right) for  $\Upsilon(1S, 2S, 3S)$  from data and signal events for Higgs decaying after all (Group I+II) selection cuts. The plots are normalized to the number of events. Signal sample is scaled by a factor of  $\times 600000$ .

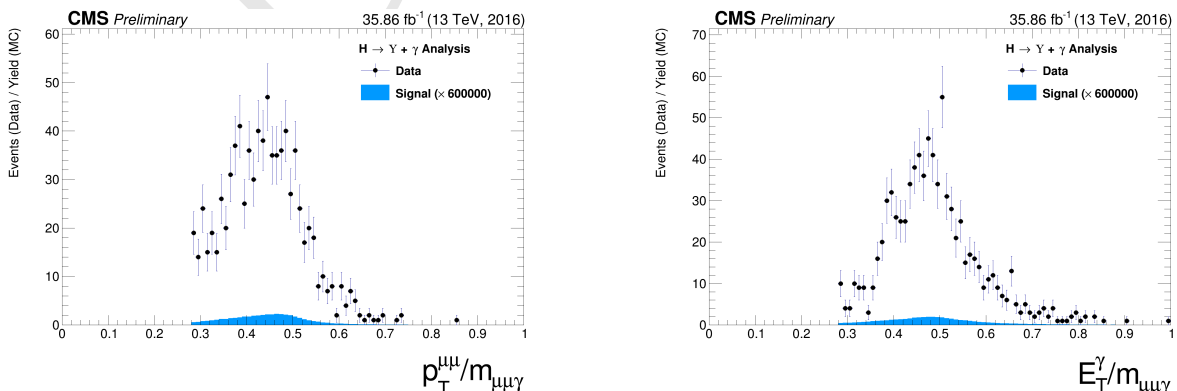


Figure 4.52: The ratio for the transverse momentum of the reconstructed Upsilon and the reconstructed Higgs mass ( $p_T^{\mu\mu} / M_{\mu\mu\gamma}$  - left) and the ratio for the transverse energy of the reconstructed Photon and the reconstructed Higgs mass ( $E_T^\gamma / m_{\mu\mu\gamma}$  - right) distribution for  $\Upsilon(1S, 2S, 3S)$  from data and signal events for Higgs decaying after all (Group I+II) selection cuts. The plots are normalized to the number of events. Signal sample is scaled by a factor of  $\times 600000$ .

## <sup>1448</sup> 4.7 Event categorization and yields

<sup>1449</sup> In order to increase the sensibility of the analysis, a categorization procedure was applied. They  
<sup>1450</sup> are based on the  $\eta$  and R9 distribution of the reconstructed photon.

<sup>1451</sup> The photon R9 is a shower shape variable defined as the fraction of energy deposited in the 5x5  
<sup>1452</sup> square surrounding the Super Cluster seed of the reconstructed photon. A photon that convert  
<sup>1453</sup> before reaching the ECAL tend to have lower values of R9, in comparison with unconverted photons.  
<sup>1454</sup> Converted photons have wider energy resolution and are more likely to be misidentified.

<sup>1455</sup> Selected events with the photon reconstructed inside the barrel and with  $R9 > 0.94$  are categorized  
<sup>1456</sup> as "EB High R9"<sup>6</sup>, selected events with the photon reconstructed inside the barrel and with  
<sup>1457</sup>  $R9 < 0.94$  are categorized as "EB Low R9" and selected events with the photon reconstructed  
<sup>1458</sup> inside the endcap, regardless of its R9 value, categorized as "EE". This categorization is done in  
<sup>1459</sup> view of increase the analysis sensitivity.

<sup>1460</sup> This categorization is implemented only for the Z decay. The Higgs does not present enough  
<sup>1461</sup> statistics to make it profitable, so only the inclusive one is used.

### <sup>1462</sup> 4.7.1 R9 reweighting

<sup>1463</sup> As spotted by the  $H \rightarrow \gamma\gamma$  at  $\sqrt{13}$  TeV analysis [107], there is a disagreement in the R9 distribution  
<sup>1464</sup> of photons in Data and MC. In order to mitigate this difference, a transformation factor is extracted  
<sup>1465</sup> and applied to the reconstructed photons before the categorization.

<sup>1466</sup> The same approach of the  $H \rightarrow \gamma\gamma$  analysis is applied, in which the nominal photon selection of this  
<sup>1467</sup> analysis (see section 4.5.3) is used to select photons on Data and MC. Then the two distributions  
<sup>1468</sup> are remapped and the transformation factors are extracted.

<sup>1469</sup> Figure 4.53 show the R9 distribution before and after the reweighting, for the Barrel and the Endcap.

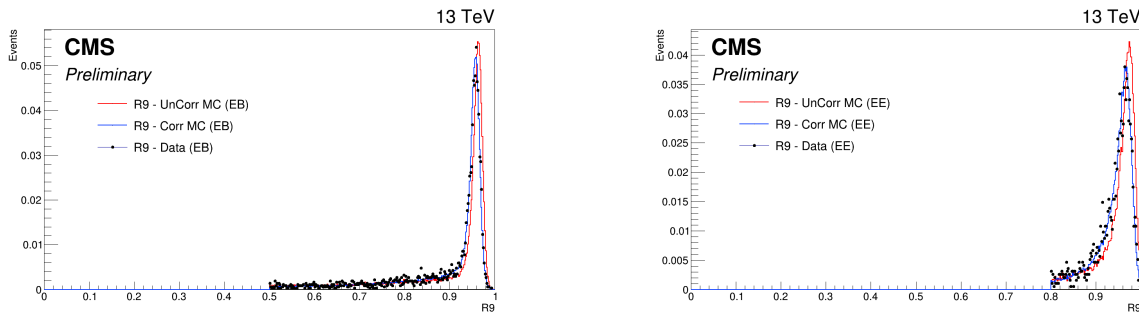


Figure 4.53: Data and MC of the R9 variable, before and after the reweighting. Barrel (left) and Endcap (right).

<sup>6</sup>EB stands for Electromagnetic Barrel

### 4.7.2 Event counting and yields

Tables 4.4 and 4.5 show the total number of events before and after the full selection. Two things are important to notice.

Table 4.4: Number of events for the Z decay, before and after the full selection, per categorization scenarios.

	Data	Signal			$Z \rightarrow \mu\mu\gamma_{FSR}$
		$Z \rightarrow \Upsilon(1S) + \gamma$	$Z \rightarrow \Upsilon(2S) + \gamma$	$Z \rightarrow \Upsilon(3S) + \gamma$	
Total (before selection)	169.84 M	3.54	1.4	1.22	$3.33 \times 10^3$
Inclusive	447	0.393	0.157	0.136	176
EB High R9	197	0.172	0.0682	0.0597	78
EB Low R9	146	0.129	0.0519	0.0448	58.5
EE	104	0.0916	0.0365	0.032	39.8

Table 4.5: Number of events for the H decay, before and after the full selection.

	Data	Signal			$H \rightarrow \gamma\gamma^*$
		$H \rightarrow \Upsilon(1S) + \gamma$	$H \rightarrow \Upsilon(2S) + \gamma$	$H \rightarrow \Upsilon(3S) + \gamma$	
Total (before selection)	169.84 M	0.000257	$5.43 \times 10^{-5}$	$3.93 \times 10^{-5}$	136
Inclusive	231	$5.23 \times 10^{-5}$	$1.2 \times 10^{-5}$	$8.96 \times 10^{-6}$	1.22

The signal selection efficiency is between 20% and 21% for all  $\Upsilon$  states and categories.

When one compares the fraction of selected peaking background, with respect to the selected data events for the Higgs decay (1.22/231), the fraction obtained ( $\sim 0.3\%$ ) is irrelevant. On the other hand, the same fraction for the Z decay (176/447) is far from irrelevant ( $\sim 39\%$ )<sup>7</sup>. The same relation is not found in the  $H/Z \rightarrow J/\psi + \gamma$  analysis [54], where both decays (Higgs and Z) show neglectable estimations of peaking background contribution to data. The very same behavior was found by ATLAS [51]. It can be explained by the relatively larger cross-section of the Z peaking background ( $Z \rightarrow \mu\mu\gamma_{FSR}$ ), with respect to the Higgs peaking background (Higgs Dalitz Decay). For the  $J/\psi$  channel, it is not an issue since its cross-section is way larger than the peaking background. The figures 4.17 and 4.30 help to clarify these affirmations, for the Z and Higgs decay, respectively. One can easily see how clear the  $J/\psi$  peak is in both decays and how minor the Higgs Dalitz Decay contributions is to the  $\Upsilon$  peak, with respect to the  $Z \rightarrow \mu\mu\gamma_{FSR}$  contribution. It is important to keep in mind the different scaling of the peaking background distributions, x3 for the Z and  $\times 100$  for the Higgs. The peaking background to the data due to  $Z \rightarrow \Upsilon(1S, 2S, 3S) + \gamma$  channel is the main motivation to use a 2-dimensional modeling fitting of the signal and background events, in order to add one more layer of differentiation between many backgrounds contributions which will be detailed in the next section.

<sup>7</sup>It is worth to keep in mind that this is a estimation based on MC

## 1490 4.8 Background modeling

1491 The background modeling proposed for this analysis is a two dimensional unbinned maximum  
 1492 likelihood fit on the  $\mu\mu$  and the  $\mu\mu\gamma$  invariant mass distributions. It is considered and modeled, as  
 1493 briefly discussed in 4.1.2, three kinds of backgrounds:

- 1494 • **Full Combinatorial:** any combination of two muon and one photon that pass all the object  
 1495 reconstruction and event selection criteria.
  - 1496 •  **$\Upsilon$  Combinatorial:** a  $\Upsilon(1S, 2S, 3S)$ , that decays to a dimuon system, combined with a  
 1497 misidentified photon (misreconstructed, pileup photon, etc.), that pass all the object recon-  
 1498 struction, identification and event selection criteria.
  - 1499 • **Peaking background:** a Z (or Higgs) that decays straight to a  $\mu\mu\gamma$ , that pass all the object  
 1500 reconstruction and event selection criteria, without passing through any intermediate state.  
 1501 The main contributions considered for this background are  $Z \rightarrow \mu\mu\gamma_{FSR}$  (a Z decaying to a  
 1502 dimuon system with one of the muons irradiating a photon) or a Higgs Dalitz Decay.
- 1503 All of them will be modeled from data, with some inputs from the MC (simulated) samples, as  
 1504 explained below. For both invariant mass spectra ( $\mu\mu$  and  $\mu\mu\gamma$ ) the full combinatorial background  
 1505 is expected to behave like a non-peaking distribution. The same behavior is expected for the  $\mu\mu\gamma$   
 1506 mass distribution of the  $\Upsilon$  Combinatorial background and for the  $\mu\mu$  mass distribution of the  
 1507 peaking background.
- 1508 On the other hand, the  $\mu\mu$  distribution of the  $\Upsilon$  Combinatorial background and the  $\mu\mu\gamma$  mass  
 1509 distribution for the peaking background are expected to behave like a peaking distribution, centered  
 1510 around the  $\Upsilon(1S, 2S, 3S)$  invariant mass (9.46 GeV, 10.02 GeV and 10.35 GeV) [13] and the Z boson  
 1511 invariant mass (91.2 GeV) [13], respectively . Table 4.6 summarizes the background modeling  
 1512 proposed for this analysis.

Table 4.6: Modeling for each background source and mass component.

	$m_{\mu\mu}$	$m_{\mu\mu\gamma}$
<b>Peaking background</b>	Bernstein 1 <sup>st</sup> order	Crystal Ball (Higgs decay) Double Crystal Ball (Z decay)
<b><math>\Upsilon</math> Combinatorial</b>	3 Gaussians (one for each $\Upsilon$ state)	
<b>Full Combinatorial</b>	Chebychev 1 <sup>st</sup> order	Polynomial

1513 For the  $Z \rightarrow \Upsilon(1S, 2S, 3S) + \gamma$  analysis, the peaking background model parameters are extracted  
 1514 by performing a simultaneous 2-dimensional fit over the invariant masses,  $m_{\mu\mu}$  and  $m_{\mu\mu\gamma}$ , of the  
 1515 simulated  $Z \rightarrow \mu\mu\gamma_{FSR}$  MC sample of events that passes the selection described in Section 4.4, as in  
 1516 figure 4.54. Once the parameters are extracted, they are fixed and the *pdf* (Probability Distributions  
 1517 Function) of the 2-Dimensional modeling is stored, leaving only the normalization of the *pdf* as a  
 1518 parameter free to float (this will be determined from data).

1519 In order to describe the 2-dimensional invariant mass distribution of the Peaking Background, as  
 1520 stated in Table 4.6, the  $m_{\mu\mu}$  component is described by a Bernstein polynomial of 1<sup>st</sup> order [108],  
 1521 which is used here just a representation of a linear function. The  $m_{\mu\mu\gamma}$  component is described

1522 by Double Crystal Ball function [109]. A Crystal Ball function is a *pdf* composed by a gaussian  
 1523 distribution and a power-law tail to the left, before certain threshold. The Crystal Ball function was  
 1524 named after the Crystal Ball Collaboration (first to use this *pdf*) and it is widely used in high-energy  
 1525 physics to describe mass distributions that incorporate FSR (final state radiation) effects, via the  
 1526 power-law tail. A Double Crystal Ball is a Crystal Ball function with the power-law tail on both  
 1527 sides.

1528 A Crystal Ball function is defined as:

$$CB(x; \alpha, n, \bar{x}, \sigma) = N \cdot \begin{cases} \exp\left(-\frac{(x-\bar{x})^2}{2\sigma^2}\right), & \text{for } \frac{x-\bar{x}}{\sigma} > -\alpha \\ A \cdot (B - \frac{x-\bar{x}}{\sigma})^{-n}, & \text{for } \frac{x-\bar{x}}{\sigma} \leq -\alpha \end{cases}, \quad (4.4)$$

1529 where,

$$\begin{aligned} A &= \left(\frac{n}{|\alpha|}\right)^n \cdot \exp\left(-\frac{|\alpha|^2}{2}\right), \\ B &= \frac{n}{|\alpha|} - |\alpha|, \\ N &= \frac{1}{\sigma(C + D)}, \\ C &= \frac{n}{|\alpha|} \cdot \frac{1}{n-1} \cdot \exp\left(-\frac{|\alpha|^2}{2}\right), \\ D &= \sqrt{\frac{\pi}{2}} \left(1 + \operatorname{erf}\left(\frac{|\alpha|}{\sqrt{2}}\right)\right), \end{aligned}$$

1530 and  $\operatorname{erf}$  is the error function.

1531 For the three gaussian functions fits, which represent the three  $\Upsilon$  states (1S, 2S and 3S) from the  $\Upsilon$   
 1532 Combinatorial background in the  $m_{\mu\mu}$  component, we use a  $\Upsilon$  control sample in order to extract the  
 1533 fit parameters, including the relative normalization between each  $\Upsilon$  state. This sample is composed  
 1534 by dimuon candidates obtained from data, by selecting the events that passes the same trigger and  
 1535 dimuon selection of the nominal selection and with  $p_T^{\mu\mu} > 35$  GeV (this cut is done in order to  
 1536 keep this selected dimuon candidates compatibles with the  $p_T^{\mu\mu}/M_{\mu\mu\gamma}$  cut applied in the nominal  
 1537 selection). No selection or cuts in the photon are required.

1538 This control sample is fitted with a Chebychev 1<sup>st</sup> order (linear polynomial) for the background  
 1539 support and 3 gaussian with the following constraints:

- 1540 • the mean of each state should be the ones in the PDG [13], but allowed to shift by a float and  
 1541 common (the same for all states) value.
- 1542 • the sigma should be based on the 1S fit of the MC. All other sigma should be the result of  
 1543 the 1S sigma times the state mass over the 1S mass ( $\sigma_{2S,3S} = \frac{m_{2S,3S}}{m_{1S}} \sigma_{1S}$ ).

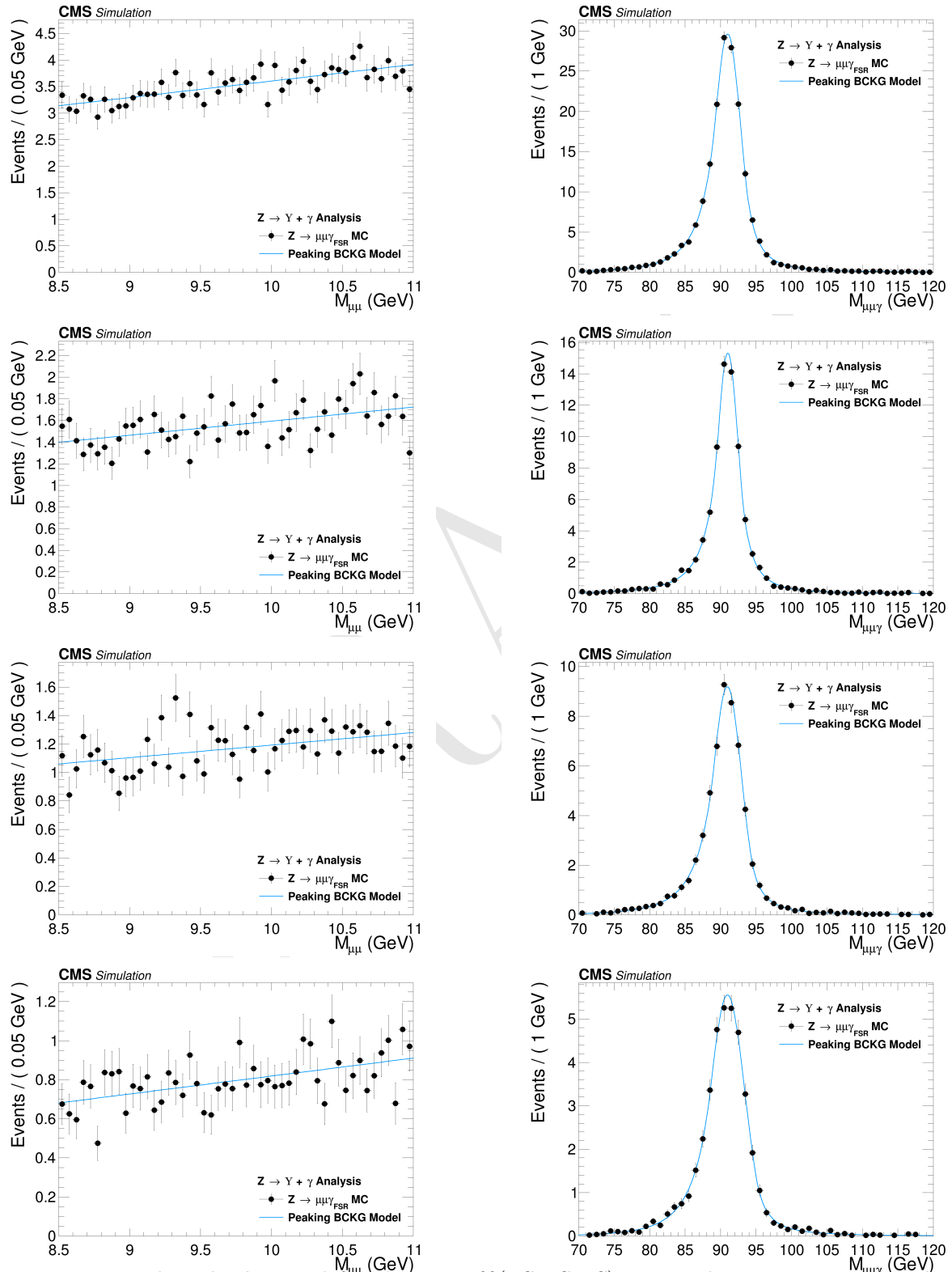


Figure 4.54: Peaking background for the  $Z \rightarrow \Upsilon(1S, 2S, 3S) + \gamma$  analysis.  $\mu\mu$  mass distribution (left) and  $\mu\mu\gamma$  invariant mass distribution (right). From top to bottom categories: Inclusive, EB High R9, EB Low R9, EE.

1544 The idea behind this fit is that scale and resolution (mean and sigma, respectively, of the gaussians)  
 1545 over a sample without a photon selection should be the same as over a sample with photon selection,  
 1546 since these are detector only dependent effects. The fact that we exclude the photon from this control  
 1547 sample, improves the statistics and gives a better measurement of these variables.

1548 The fit of the  $\Upsilon$  control sample if shown in figure 4.55.

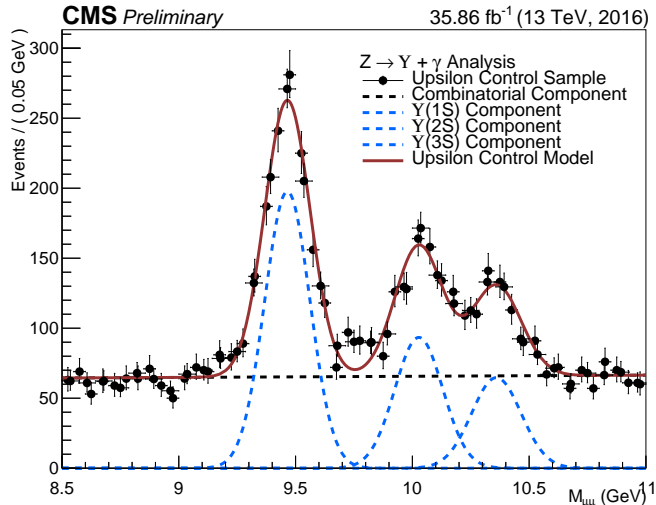


Figure 4.55:  $\Upsilon$  control sample fit with Chebychev 1<sup>st</sup> order for the background support and 3 gaussian for the three  $\Upsilon(1S, 2S, 3S)$  peaks.

1549 Once determined, the fit parameters are fixed, they are used to compose the 2-Dimensional *pdf*. The  
 1550  $m_{\mu\mu}$  component of the full combinatorial background is derived fully from the data fit (described  
 1551 below). In the same sense, the  $m_{\mu\mu\gamma}$  component of the full combinatorial and the  $\Upsilon(nS)$  Combin-  
 1552 atorial backgrounds are also fully derived from the data, but following a more complex procedure: a  
 1553 composition with the *pdf* components described above, plus a statistical test, to avoid overfitting  
 1554 within a Discrete Profiling (or "Envelope Method"), as described in [110] and also implemented  
 1555 in [107].

1556 The statistical test consists of, for each category, different orders of a set of polynomial *pdfs* families  
 1557 are tested: a sums of exponentials, sum of polynomials (in the Bernstein basis), a Laurent series  
 1558 and a sums of power-law functions.

- Sums of exponentials:

$$f_N(x) = \sum_{i=1}^N p_{2i} e^{p_{2i+1}x},$$

- Sums of polynomials (in the Bernstein basis):

$$f_N(x) = \sum_{i=0}^N p_i b_{(i,N)}, \text{ where } b_{(i,N)} := \binom{N}{i} x^i (1-x)^{N-i},$$

- Laurent series:

$$f_N(x) = \sum_{i=1}^N p_i x^{-4+\sum_{j=1}^i (-1)^j(j-1)},$$

- Sums of power-law functions:

$$f_N(x) = \sum_{i=1}^N p_{2i} x^{-p_{2i+1}},$$

1559 where for all  $k$ , the  $p_k$  are a set of floating parameters in the fit.

1560 Twice difference in the negative log-likelihood ( $NLL$ ) between the  $N^{th}$  and the  $(N+1)^{th}$  order of  
1561 the same polynomial ( $\Delta NLL = 2 \times (NLL_N - NLL_{N+1})$ ) is expected to follow a  $\chi^2$  distribution  
1562 with  $M$  degrees of freedom, where  $M$  is the increase in degrees of freedom when going from  $N^{th}$  to  
1563  $(N+1)^{th}$ . This can be shown with the help of the Wilks' theorem [111].

1564 Starting from the lowest order possible, the best choice of order, for each family, is determined when  
1565 a increase in the order of the polynomial, does not brings a significant improvement in the quality  
1566 of the fit. Since a model with more fit parameters (higher order polynomials) will always perform,  
1567 if not the same, better than a simpler one, an optimal choice of the polynomial order, will be the  
1568 one right before the model becomes too flexible for the data.

1569 Consider a  $p$ -value defined as:

$$\begin{aligned} p\text{-value} &= \int_{\Delta NLL}^{\infty} \chi_M^2(\Delta) d\Delta \\ &= P(\chi_M^2 > \Delta NLL), \end{aligned} \tag{4.5}$$

1570 In the same spirit as the Wilks' theorem, this is the  $p$ -value for a likelihood ratio test between a  
1571 null hypotheses and an alternative model, where the null hypotheses is the  $N^{th}$  order and  $(N+1)^{th}$   
1572 order is the alternative one.

$$\begin{aligned} \Delta NLL &= 2 \times (NLL_N - NLL_{N+1}) \\ &= -2 \times \log\left(\frac{\mathcal{L}_N}{\mathcal{L}_{N+1}}\right), \end{aligned} \tag{4.6}$$

1573 where  $\mathcal{L}_N$  is the likelihood for the  $N^{th}$  polynomial order.

1574 The alternative will present a statistically significant improvement, with respect to the null hypothe-  
1575 ses, if the  $p$ -value is smaller than 0.05, since the probability of obtaining, by chance, considering  
1576 the null hypotheses is true, a even higher  $\Delta NLL$  is less than 5%. This will give support to chose  
1577  $(N+1)^{th}$  over  $N^{th}$ .

1578 If the  $p$ -value is greater than 0.05 a higher order is not supported, since the probability of obtaining  
1579 a  $\Delta NLL$  greater than the one observed is statistically significant (more than 5%). A higher  $\Delta NLL$

means that another data sample, collected and analyzed with strictly the same conditions, would have a probability of more than 5% of giving a better fit improvement than the one observed, again assuming that the null hypotheses is true. This is an indication of overfitting, since the improvements are likely to come from just statistical fluctuations. When testing the  $(N+1)^{th}$  order and this condition is reached, the optimal order should be the  $N^{th}$ .

At first, before any fit to data, the 2-Dimensional model is composed by the five components, as described in Table 4.6 (in which the  $m_{\mu\mu\gamma}$  modeling for the Full Combinatorial Background and the  $\Upsilon$  combinatorial are shared), then, the statistical test described before is ran for each family. It is important to stress that before the statistical test all the other fitting parameters have been fixed. This leaves only the normalizations of the model components and the polynomial coefficients free to float.

Once the optimal order for each *pdf* family is obtained, the composed *pdf* with each choice from statistical test is saved in the same model, providing a discrete variable that indexes the different polynomial *pdf* families. This method is called Discrete Profiling (or "*Envelope Method*") and it allows the analysis algorithm to treat the choice of the *pdf* as a systematics and incorporate its effect in the extracted upper limits. This model, with different choices of polynomial families is called envelope.

The implementation, used in the analysis, of the statistical test and the Discrete Profiling is based on the same algorithm used by the  $H \rightarrow \gamma\gamma$  Run II analysis. An extensive documentation on these methods can be found in  $H \rightarrow \gamma\gamma$  analysis note and physics analysis summary [112, 113] and in the specific reference of the Discrete Profiling [110]. The figures 4.56 and 4.57 show the projection for the  $\mu\mu$  and  $\mu\mu\gamma$  distribution after the statistical test.

For the  $H \rightarrow \Upsilon(1S, 2S, 3S) + \gamma$  analysis, the same procedure is implemented, except for the peaking background modeling. Since the MC prediction for the contribution of the background is too small, according to the comparison between the final selected events for data and the Higgs Dalitz Decay sample, in order to avoid fitting over statistical fluctuations of the data sample, the Peaking Background, for the Higgs channel, is fully modeled from the MC sample, including its normalization, as shown in figure 4.58, hence it is not included the the statistical test, neither in the final background modeling envelope.

The results of the background modeling for the Full Combinatorial and  $\Upsilon$  Combinatorial, can be found at Figures 4.59 and 4.60, for the  $\mu\mu$  and  $\mu\mu\gamma$  distribution, respectively. It is worth to remember that, for the Higgs channel, we are not implementing any categorization.

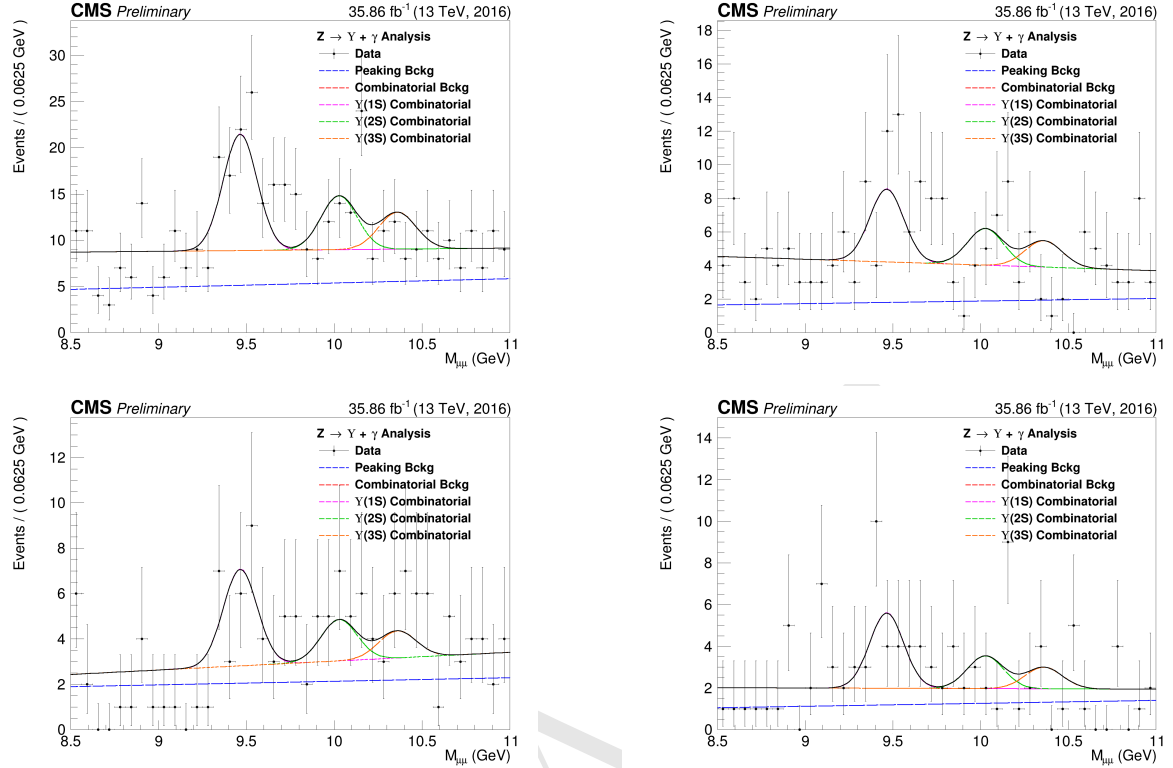


Figure 4.56:  $Z \rightarrow \Upsilon(1S, 2S, 3S) + \gamma$  Background Modeling:  $\mu\mu$  distribution. Inclusive (top left); EB High R9 (top right), EB Low R9 (bottom left), EE (bottom right). The pdfs projections are plotted with respect to the overall best choice of the statistica test.

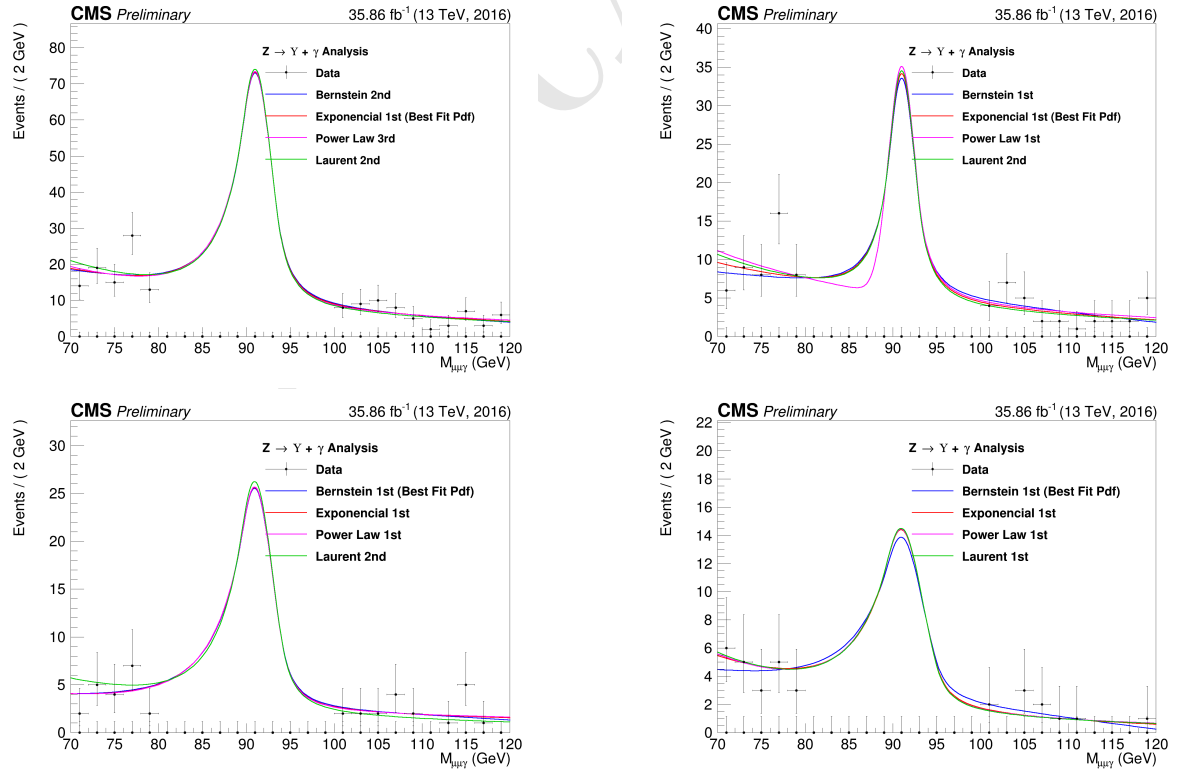


Figure 4.57:  $Z \rightarrow \Upsilon(1S, 2S, 3S) + \gamma$  Background Modeling:  $\mu\mu\gamma$  distribution. Inclusive (top left); EB High R9 (top right), EB Low R9 (bottom left), EE (bottom right). The plotted pdfs corresponds to the best choice by the statistical test for each family. The signal region, from 80 GeV to 100 GeV was blinded.

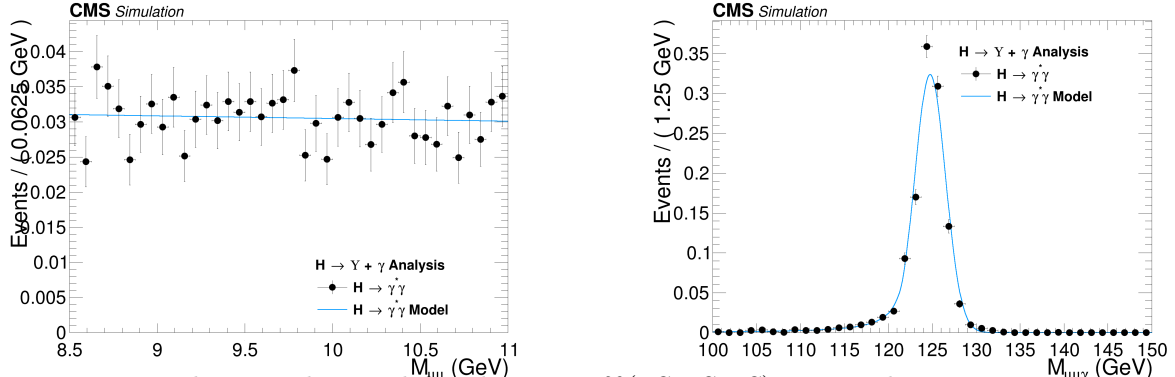


Figure 4.58: Peaking Background for the  $H \rightarrow \Upsilon(1S, 2S, 3S) + \gamma$  analysis.  $m_{\mu\mu}$  invariant mass distribution (left) and  $m_{\mu\mu\gamma}$  invariant mass distribution (right).

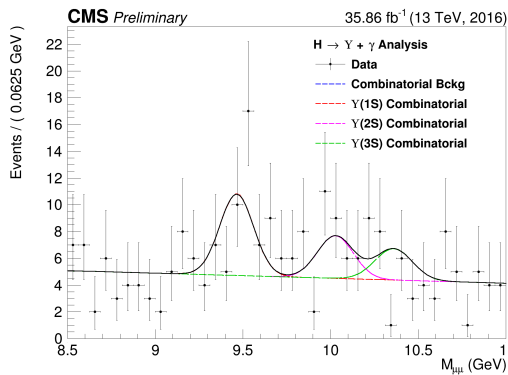


Figure 4.59:  $H \rightarrow \Upsilon(1S, 2S, 3S) + \gamma$  Background Modeling:  $m_{\mu\mu}$  distribution. The  $pdfs$  projections are plotted with respect to the overall best choice of the statistical test.

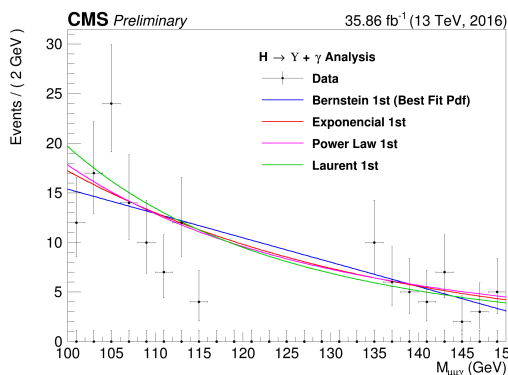


Figure 4.60:  $H \rightarrow \Upsilon(1S, 2S, 3S) + \gamma$  Background Modeling:  $\mu\mu\gamma$  distribution. The plotted  $pdfs$  corresponds to the best choice by the statistical test for each family. The signal region, from 115 GeV to 135 GeV was blinded.

## 1612 4.9 Signal modeling

1613 Along the same lines as the background modeling (Section 4.8), the signal modeling is implemented  
1614 as a two dimensional unbinned maximum likelihood fit on the  $m_{\mu\mu}$  and the  $m_{\mu\mu\gamma}$  invariant masses  
1615 distributions, but this time, only using the signal simulated MC samples 4.1.2. Since, for the two  
1616 spectra, it is expected a peak-like distribution, one centered in the Z (or Higgs) boson mass and the  
1617 other centered in the  $\Upsilon$  mass, two also peak-like analytics *pdfs* were chosen to compose the signal  
1618 model. The modeling is summarized in table 4.7.

Table 4.7: Modeling for each signal source and mass component.

	$m_{\mu\mu}$	$m_{\mu\mu\gamma}$
$Z \rightarrow \Upsilon(1S, 2S, 3S) + \gamma$	Double Crystal Ball	Double Crystal Ball
$H \rightarrow \Upsilon(1S, 2S, 3S) + \gamma$	Double Crystal Ball	Crystal Ball + Gaussian with the same mean

1619 The projections of the modeling for the Z boson decay channel analysis can be found at figures 4.61,  
1620 4.62, 4.63 and 4.64, for Inclusive, EB High R9, EB Low R9 and EE, respectively. The projection  
1621 on the modeling for the Higgs boson signal can be found at Figure 4.65. A deeper discussion on the  
1622 systematics uncertainties associated to them, will be presented in the next section.

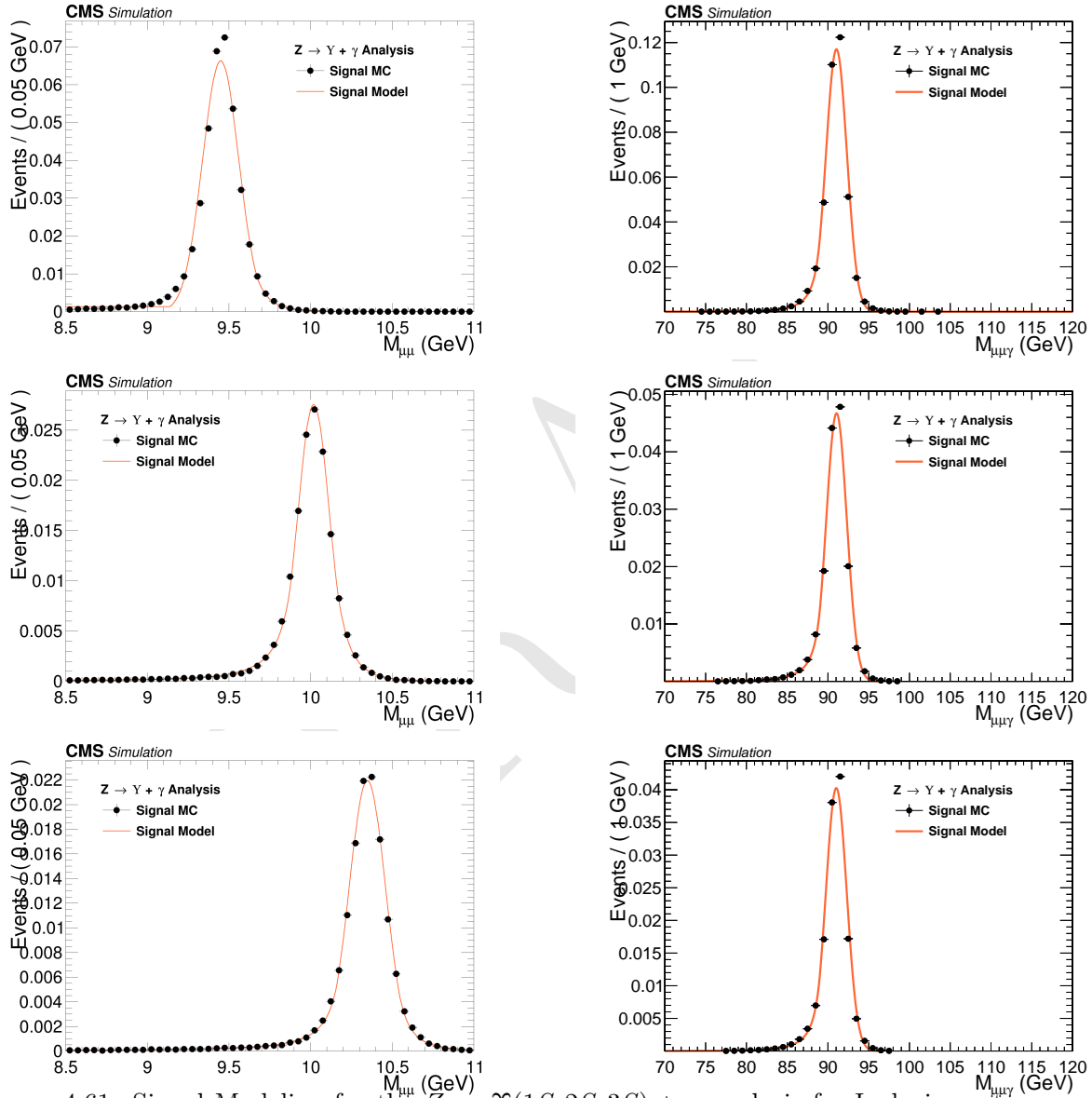


Figure 4.61: Signal Modeling for the  $Z \rightarrow \Upsilon(1S, 2S, 3S) + \gamma$  analysis for Inclusive category.  $m_{\mu\mu}$  mass distribution (left) and  $m_{\mu\mu\gamma}$  mass distribution (right). From top to bottom:  $\Upsilon(1S)$ ,  $\Upsilon(2S)$ ,  $\Upsilon(3S)$ .

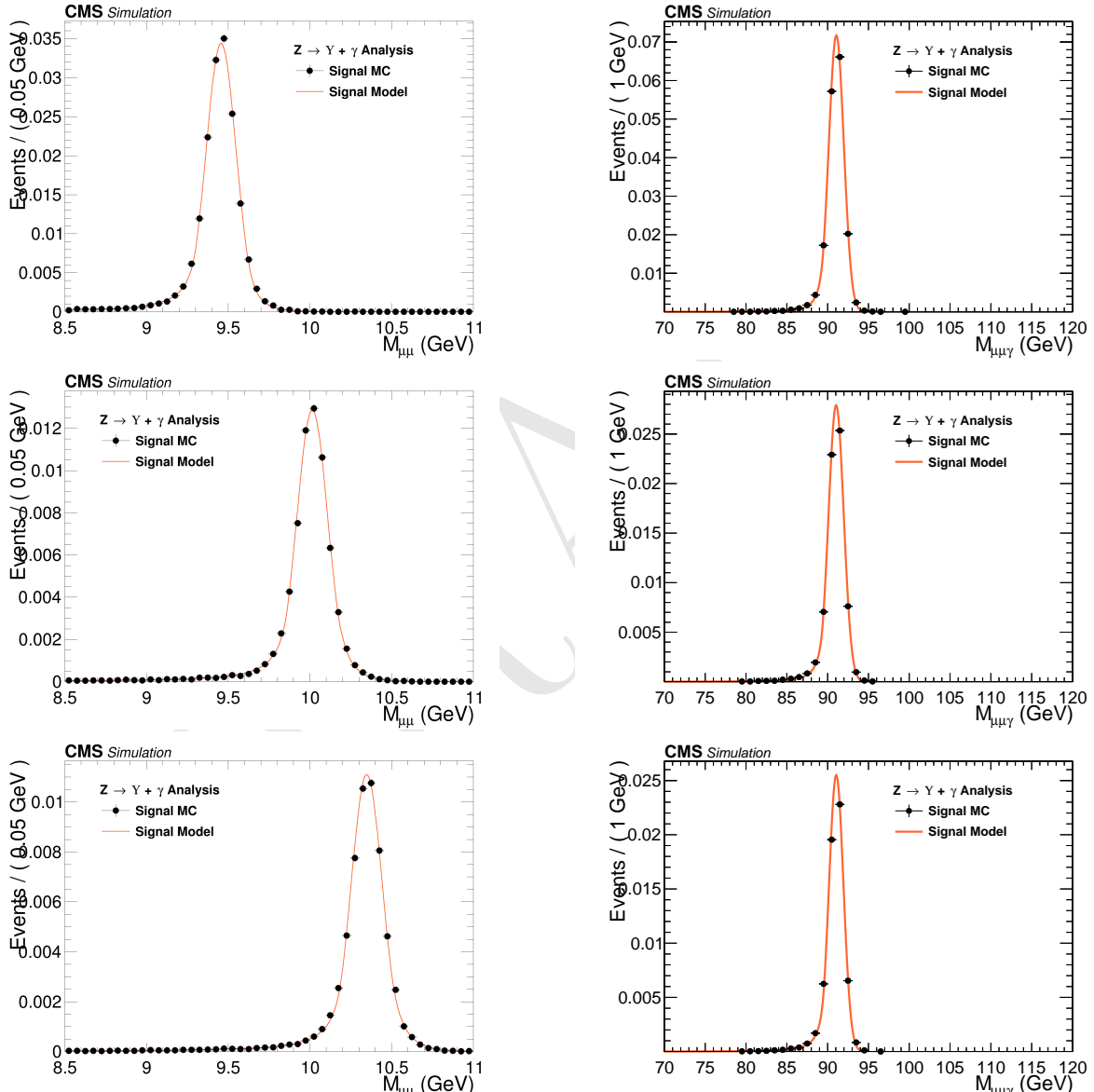


Figure 4.62: Signal Modeling for the  $Z \rightarrow \Upsilon(1S, 2S, 3S) + \gamma$  analysis for EB High R9 category.  $m_{\mu\mu}$  mass distribution (left) and  $m_{\mu\mu\gamma}$  mass distribution (right). From top to bottom:  $\Upsilon(1S)$ ,  $\Upsilon(2S)$ ,  $\Upsilon(3S)$ .

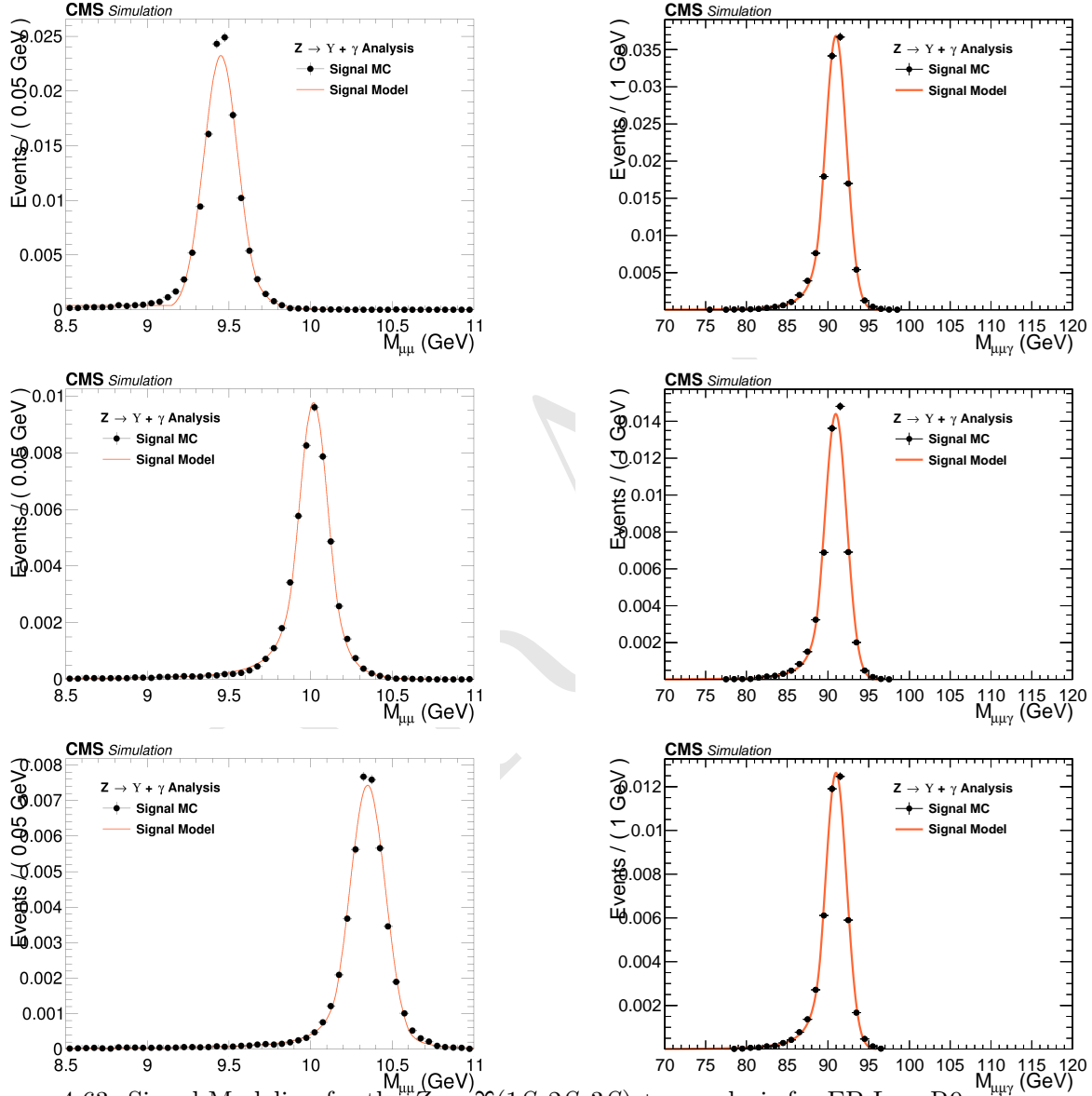


Figure 4.63: Signal Modeling for the  $Z \rightarrow \Upsilon(1S, 2S, 3S) + \gamma$  analysis for EB Low R9 category.  $m_{\mu\mu}$  mass distribution (left) and  $m_{\mu\mu\gamma}$  mass distribution (right). From top to bottom:  $\Upsilon(1S)$ ,  $\Upsilon(2S)$ ,  $\Upsilon(3S)$ .

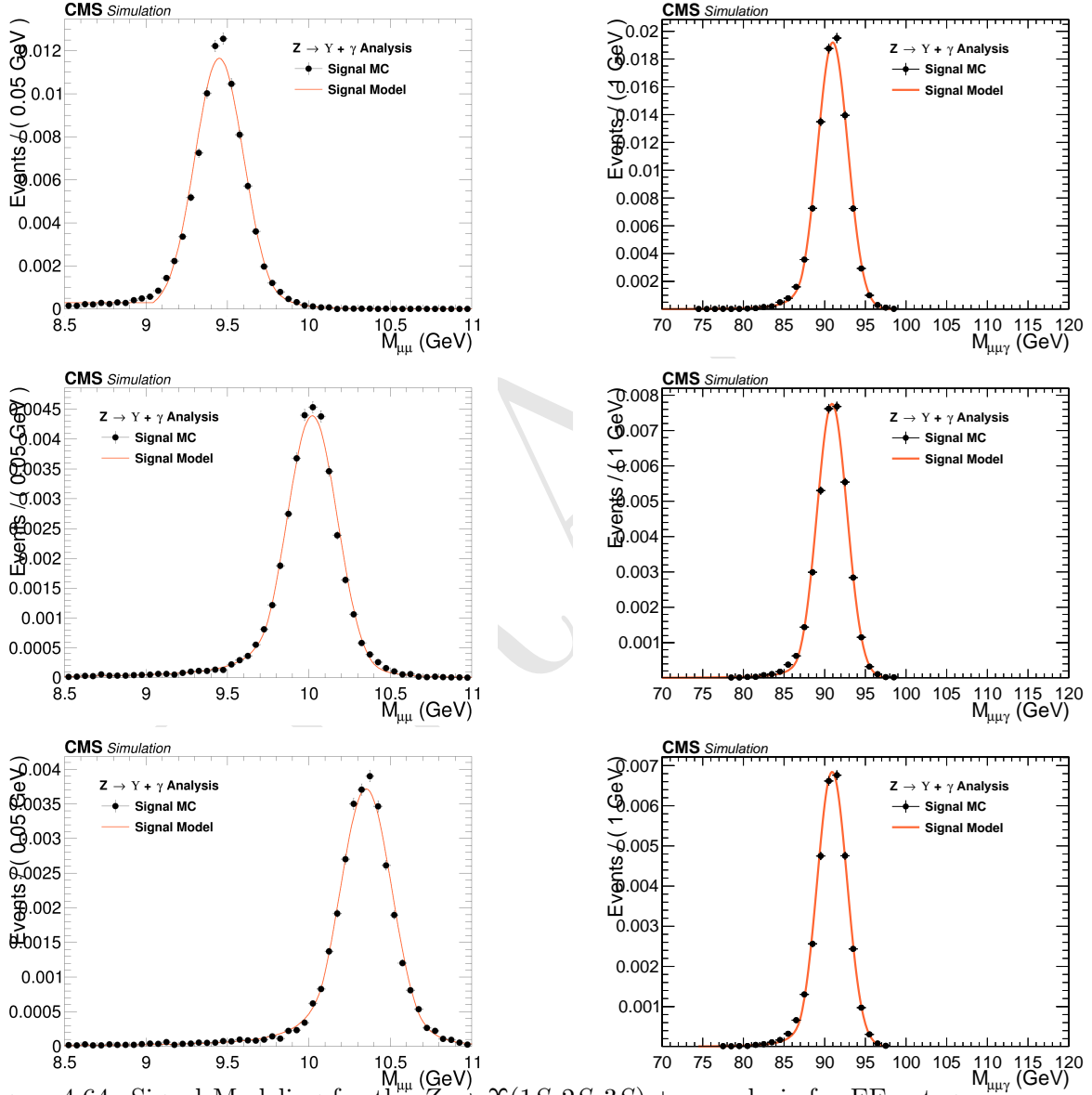


Figure 4.64: Signal Modeling for the  $Z \rightarrow \Upsilon(1S, 2S, 3S) + \gamma$  analysis for EE category.  $m_{\mu\mu}$  mass distribution (left) and  $m_{\mu\mu\gamma}$  mass distribution (right). From top to bottom:  $\Upsilon(1S)$ ,  $\Upsilon(2S)$ ,  $\Upsilon(3S)$ .

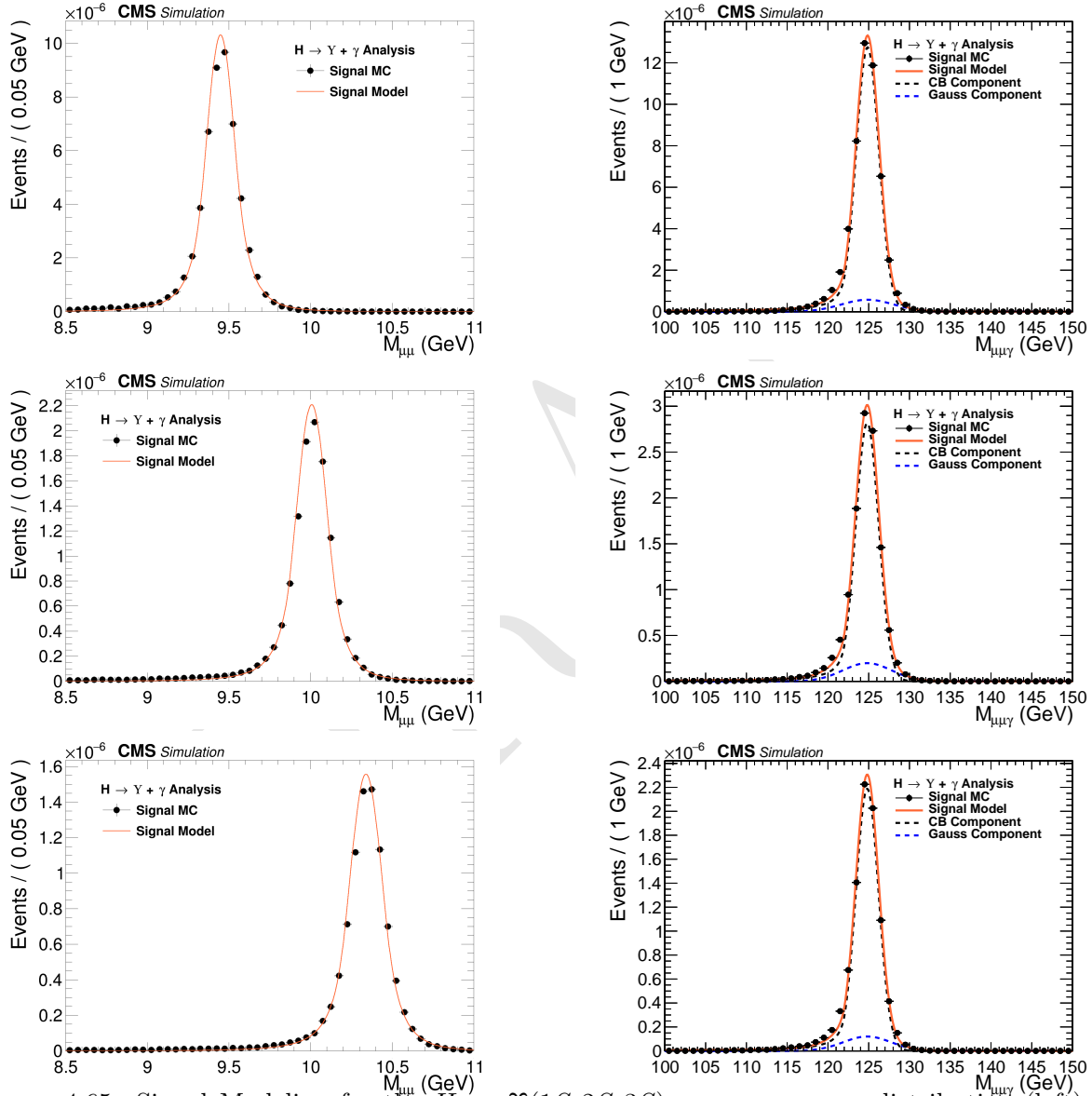


Figure 4.65: Signal Modeling for the  $H \rightarrow \Upsilon(1S, 2S, 3S) + \gamma$ .  $m_{\mu\mu}$  mass distribution (left) and  $m_{\mu\mu\gamma}$  mass distribution (right). From top to bottom:  $\Upsilon(1S)$ ,  $\Upsilon(2S)$ ,  $\Upsilon(3S)$ .

## 1623 4.10 Systematic uncertainties

- 1624 Two sources of systematics are considered: the ones that affect the predicted yields<sup>8</sup> and the ones  
 1625 that affect the shape of the pdfs used to compose the signal and background model.
- 1626 Those that affect the predicted yields, presented in Section 4.7.2, it is considered integrated lu-  
 1627 minosity measurement [87], the pileup description in the Monte-Carlo simulations, the corrections  
 1628 applied to the simulated events in order to compensate for the differences in performance of the some  
 1629 selection criteria, such as trigger, object reconstruction and identification, the  $\Upsilon$  polarization and  
 1630 the theoretical uncertainties, such as the effects of the *parton density functions* (PDF) to the signal  
 1631 cross section [22, 96, 114], the variations of the renormalization and factorization scales [115–119],  
 1632 and the prediction of the decay branching ratios.
- 1633 For the systematics on the signal modeling, it is considered possible imprecisions of the momentum  
 1634 scale and resolution. They are measured on how they affect the mean ( $\mu$ ) and the standard deviation  
 1635 ( $\sigma$ ) of the signal model. For the background modeling, since it is derived from data, the choice of  
 1636 the *pdf* (Probability distribution function) is the only systematic uncertainties considered. It is  
 1637 treated by the Discrete Profiling method, as described in section 4.8.
- 1638 The two kinds of systematics uncertainties are described in details below.

### 1639 4.10.1 Uncertainties on the predicted yields

- 1640 The theoretical sources of uncertainties includes: parton distribution functions uncertainties, strong  
 1641 coupling constant ( $\alpha_s$ ) uncertainty and uncertainty on the  $H \rightarrow \gamma\gamma$  branching fraction (used to derive  
 1642 the Higgs Dalitz Decays cross-section). The values for these theoretical uncertainties are taken from  
 1643 the Higgs Combination Group [99] and also from [118, 120].
- 1644 An uncertainty value of 2.5% is used on the integrated luminosity of the data samples, as recom-  
 1645 mended by CMS [87]. To evaluate the impact of the pileup reweighting in the final result, the The  
 1646 total inelastic cross section of 69.2  $mb$  is varied by  $\pm 4.6\%$  and the analysis is ran with these extreme  
 1647 values. The systematic uncertainty quoted is the maximum difference in the yields with respect to  
 1648 nominal value, as recommended by CMS.
- 1649 The impact of the trigger scale factor is evaluated by running this analysis with  $\pm 1\sigma$  on the  
 1650 Trigger Efficiency Scale factors (section 4.5.1). The systematic uncertainty quoted is the maximum  
 1651 difference in the yields with respect to nominal value.
- 1652 For the final state object identification and isolation associated uncertainty, the scale factors, pro-  
 1653 vided by CMS, to match the performance of MC and Data samples are varied in  $\pm 1\sigma$ . The  
 1654 systematic uncertainty quoted is the maximum difference in the yields with respect to nominal  
 1655 value. This procedure is applied on the scale factors for the Photon MVA ID and the Electron Veto  
 1656 (section 4.5.3) and for Muon Identification and Isolation(section 4.5.2).

---

<sup>8</sup>Number of events, per process, after full selection and corrected by the expected SM cross sections.

Finally, the  $\Upsilon$  Polarization is assessed applying the extremes scenarios of the  $\Upsilon$  polarization (Transverse and Longitudinal Polarization to the signal samples (section 4.2). The systematic uncertainty quoted is the maximum difference in the yields with respect to nominal (Unpolarized) yield. This procedure is applied only for the Z decay. For the Higgs decay, the only polarization considered is the transverse polarization.

The effect of all systematic uncertainties in the signal and peaking background yields are summarized on table 4.8, for the Z decay and table 4.9, for the Higgs decay. Clearly, the main contribution to the systematics uncertainties on the yields is Polarization of the  $\Upsilon(nS)$  (only for the Z decay), around 15%.

#### 4.10.2 Uncertainties that affect the signal fits

Smearing and scaling corrections are applied on simulated events since the resolution of Monte Carlo is better than that on data and the detector might not catch all the possible differences in the detector performance, with respect to the data observation. They need to be estimated and included on the systematics. The corrections are:

- **Muon Momentum Scale and Resolution:** extracted by running the analysis with different setups of the official CMS Muon scaling and smearing package [121]. The deviations, with respect to the default correction are summed in quadrature. Once the nominal parameters (mean or sigma) are obtained, the default corrections are shifted by  $\pm 1\sigma$  and the fits are re-done, with the parameters of interest free to float and all others fixed. The systematic uncertainty quoted is the maximum difference of the parameter with respect to nominal value.

- **Photon Energy Scale and Resolution:** extracted by running the analysis with different sets of corrections, provided by the CMS <sup>9</sup>. Once the nominal mean is obtained, the sets are changed and the fits are re-done, with the mean free to float and all others parameters fixed. The corrections are shifted by  $\pm 1\sigma$  on each source of systematics (following standard CMS recommendations). The quoted as systematic uncertainty is the quadrature sum of the maximum deviation within each set.

The effective systematic uncertainty associated with the scale and resolution are the quadrature sum of the muon and photon contributions. The effect of all systematic uncertainties in the Signal fits are summarized on table 4.10, for the Z and Higgs decay.

---

<sup>9</sup>CMS has not published, yet, a paper on the Run2 performance of the Photon reconstruction (This document is under internal review process.). Just as a reference, we cite the Run1 paper [122].

Table 4.8: A summary table of systematic uncertainties in the Z boson decaying in  $\Upsilon(1S, 2S, 3S) + \gamma$ , affecting the final yields of the MC samples.

Source	Uncertainty			
	Signal		Peaking Background	
	$Z \rightarrow \Upsilon(1S)\gamma$	$Z \rightarrow \Upsilon(2S)\gamma$	$Z \rightarrow \Upsilon(3S)\gamma$	$Z \rightarrow \mu\mu\gamma_{FSR}$
Integrated luminosity				
All Categories	2.5%			
SM Z boson $\sigma$ (scale)				
All Categories	3.5%		5.0%	
SM Z boson $\sigma$ (PDF + $\alpha_s$ )				
All Categories	1.73%		5.0%	
Pileup Reweighting				
Inclusive	0.65%	0.68%	0.71%	0.62%
EB High R9	1.01%	1.1%	1.04%	1.06%
EB Low R9	0.17%	0.08%	0.13%	0.11%
EE	1.07%	0.98%	1.26%	0.78%
Trigger				
Inclusive	4.45%	4.46%	4.49%	4.71%
EB High R9	3.5%	3.5%	3.52%	3.71%
EB Low R9	3.55%	3.54%	3.58%	3.72%
EE	7.52%	7.58%	7.56%	8.13%
Muon Identification				
Inclusive	4.82%	4.81%	4.8%	4.52%
EB High R9	4.45%	4.45%	4.44%	4.2%
EB Low R9	4.65%	4.62%	4.63%	4.32%
EE	5.75%	5.75%	5.74%	5.44%
Photon Identification				
Inclusive	1.1%	1.1%	1.09%	1.09%
EB High R9	1.1%	1.09%	1.09%	1.11%
EB Low R9	1.1%	1.1%	1.09%	1.08%
EE	1.1%	1.1%	1.1%	1.09%
Electron Veto				
Inclusive	1.02%	1.02%	1.02%	1.03%
EB High R9	1.2%	1.2%	1.2%	1.2%
EB Low R9	1.2%	1.2%	1.2%	1.2%
EE	0.45%	0.45%	0.45%	0.45%
Polarization				
Inclusive	15.36%	14.78%	14.84%	-
EB High R9	15.6%	14.88%	14.87%	-
EB Low R9	15.01%	14.31%	14.4%	-
EE	15.39%	15.27%	15.39%	-

Table 4.9: A summary table of systematic uncertainties in the Higgs boson decaying in  $\Upsilon(1S, 2S, 3S) + \gamma$ , affecting the final yields of the MC samples.

Source	Uncertainty			
	Signal			Peaking Background
	$H \rightarrow \Upsilon(1S)\gamma$	$H \rightarrow \Upsilon(2S)\gamma$	$H \rightarrow \Upsilon(3S)\gamma$	$H \rightarrow \gamma\gamma^*$
Integrated luminosity			2.5%	
SM Higgs $\sigma$ (scale)			+4.6% / -6.7%	
SM Higgs $\sigma$ (PDF + $\alpha_s$ )			3.2%	
SM BR $H \rightarrow \gamma\gamma^*$		-		6.0%
Pileup Reweighting	0.61%	0.68%	0.56%	0.9%
Trigger	5.61%	5.47%	5.5%	6.12%
Muon Identification	4.39%	4.36%	4.34%	4.33%
Photon Identification	1.21%	1.22%	1.22%	1.2%
Electron Veto	1.04%	1.04%	1.04%	1.04%

Table 4.10: A summary table of systematic uncertainties in the Z (H) decaying in  $\Upsilon(1S, 2S, 3S) + \gamma$ , affecting the signal fits.

	Z $\rightarrow \Upsilon(nS) + \gamma$				H $\rightarrow \Upsilon(nS) + \gamma$
	Inclusive	EB High R9	EB Low R9	EE	Inclusive
<b>Mean - Scale</b>					
$\Upsilon(1S)$	Muon Unc.	0.06%	0.05%	0.06%	0.11%
	Photon Unc.	0.21%	0.13%	0.19%	0.26%
	<b>Total Unc.</b>	0.22%	0.14%	0.2%	0.28%
<b>Sigma - Resolution</b>					
	Muon Unc.	1.12%	0.84%	1.55%	1.14%
	Photon Unc.	2.14%	2.48%	1.95%	2.79%
	<b>Total Unc.</b>	2.42%	2.61%	2.49%	3.01%
<b>Mean - Scale</b>					
$\Upsilon(2S)$	Muon Unc.	0.07%	0.05%	0.06%	0.13%
	Photon Unc.	0.25%	0.11%	0.2%	0.19%
	<b>Total Unc.</b>	0.26%	0.12%	0.21%	0.23%
<b>Sigma - Resolution</b>					
	Muon Unc.	1.21%	1.54%	2.65%	1.66%
	Photon Unc.	1.85%	2.67%	3.56%	3.6%
	<b>Total Unc.</b>	2.21%	3.08%	4.44%	3.97%
<b>Mean - Scale</b>					
$\Upsilon(3S)$	Muon Unc.	0.06%	0.06%	0.06%	0.09%
	Photon Unc.	0.22%	0.14%	0.25%	0.17%
	<b>Total Unc.</b>	0.23%	0.15%	0.26%	0.19%
<b>Sigma - Resolution</b>					
	Muon Unc.	1.78%	2.38%	2.1%	2.25%
	Photon Unc.	2.51%	4.14%	2.23%	4.08%
	<b>Total Unc.</b>	3.08%	4.77%	3.07%	4.66%

## 4.11 Modeling Cross checks

In order to test the applicability of the statistical (signal and background) modeling proposed in this study, a cross-check procedure is performed by generating a set of pseudo-experiments (toy datasets) based on the signal plus background model, for each decay channel ( $H/Z \rightarrow \Upsilon(1S, 2S, 3S, ) + \gamma$ ) with some signal injected.

The procedure consists of resampling from the signal plus background a number of events, including some extra (injected signal). The amount of injected signal is controlled by the  $\mu_{true}$  variable, where  $\mu_{true} = X$  means inject  $X$  times the expected signal.

Once generated, the toy dataset is refitted to the signal plus background model and the signal strength ( $\mu_{fit}$ ) and its error  $\sigma_{fit}$  are extracted. This procedure is repeated 10000 times and only for the inclusive category. Figures 4.67, 4.66, 4.69 and 4.68 show examples of those fits for the Higgs and Z decay.

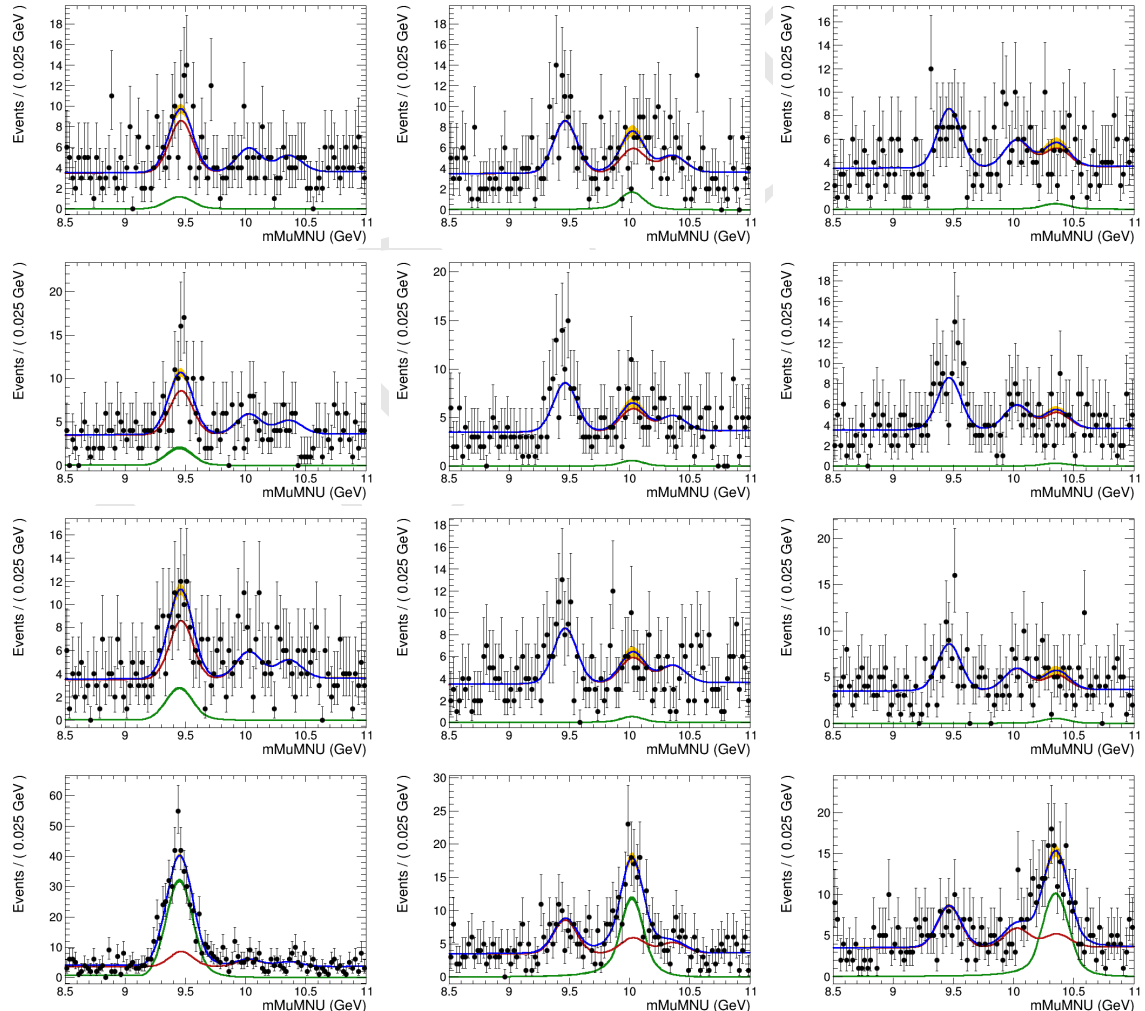


Figure 4.66: Examples of the toy datasets fit ( $M_{\mu\mu}$ ), for the Z decay analysis, after the toy dataset refit, for 1S, 2S and 3S (left to right), with  $\mu_{true}$  equals to 20, 50, 100, 1000 (top to bottom). The red lines corresponds to the background model (B), the green lines to signal model (S), the blue lines to the total (S+B) and the dots is the toy dataset.

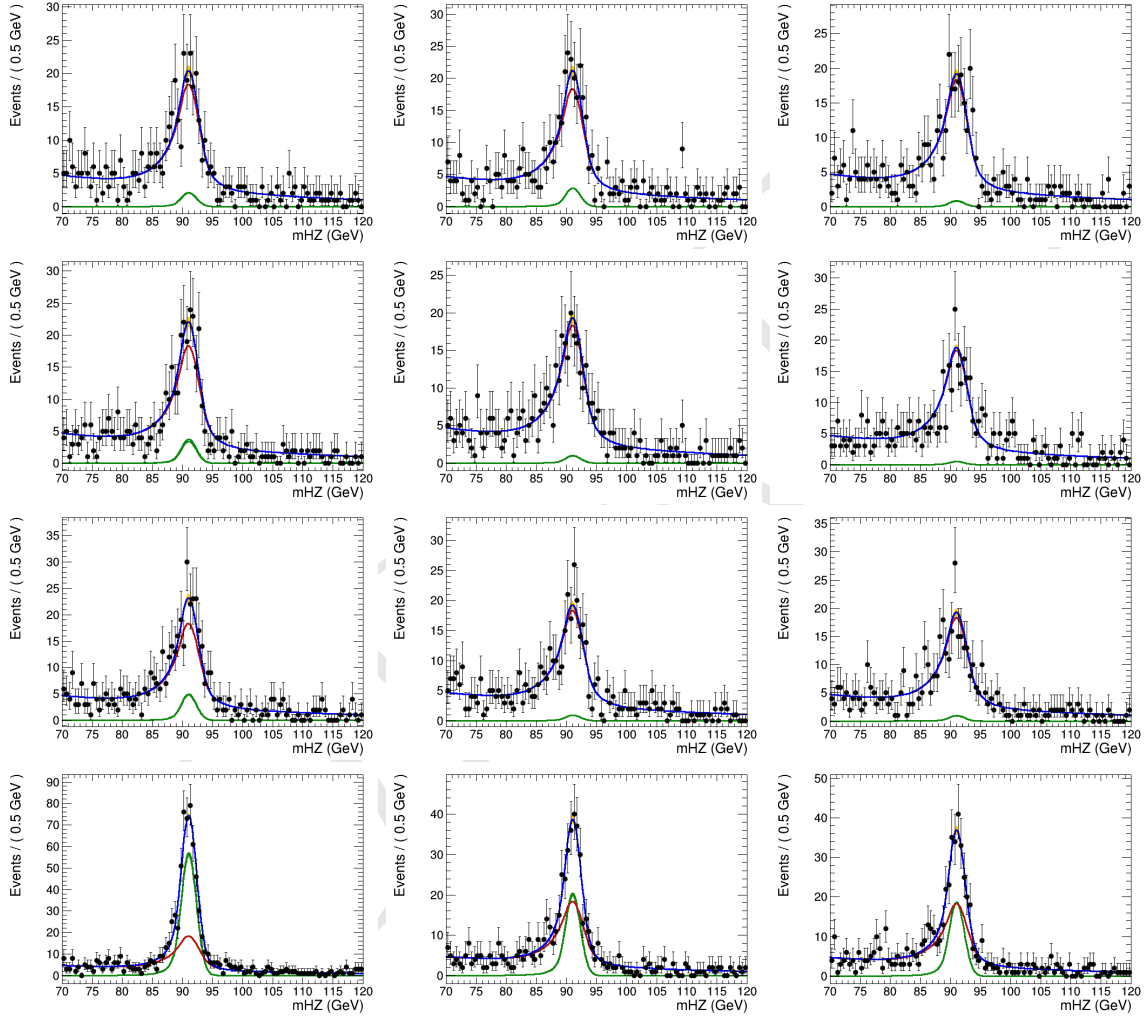


Figure 4.67: Examples of the toy datasets fit ( $M_{\mu\mu\gamma}$ ), for the Z decay analysis, after the toy dataset refit, for 1S, 2S and 3S (left to right), with  $\mu_{true}$  equals to 20, 50, 100, 1000 (top to bottom). The red lines corresponds to the background model (B), the green lines to signal model (S), the blue lines to the total (S+B) and the dots is the toy dataset.

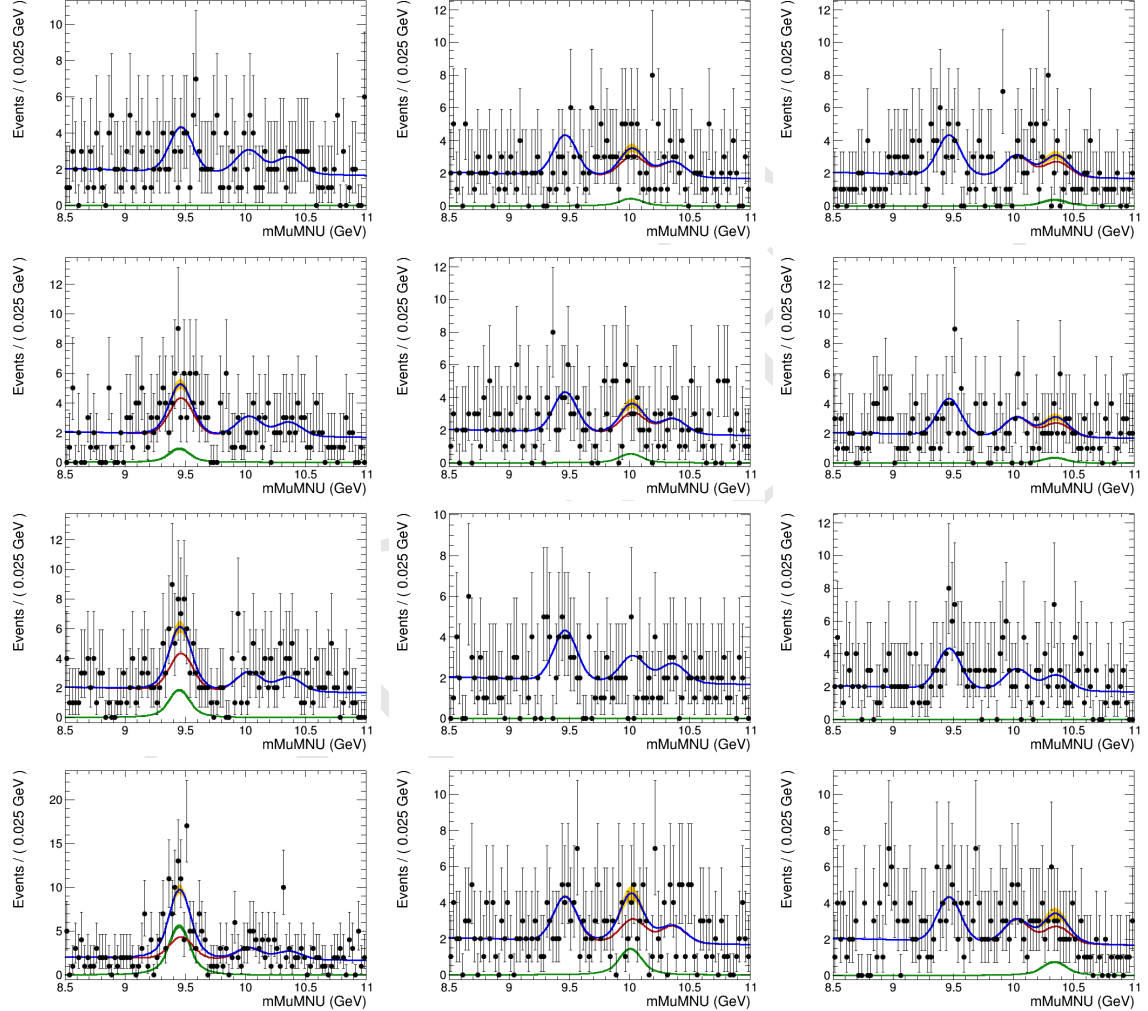


Figure 4.68: Examples of the toy datasets fit ( $M_{\mu\mu}$ ), for the Higgs decay analysis, after the toy dataset refit, for 1S, 2S and 3S (left to right), with  $\mu_{true}$  equals to 100000, 200000, 300000, 1000000 (top to bottom). The red lines corresponds to the background model (B), the green lines to signal model (S), the blue lines to the total (S+B) and the dots is the toy dataset.

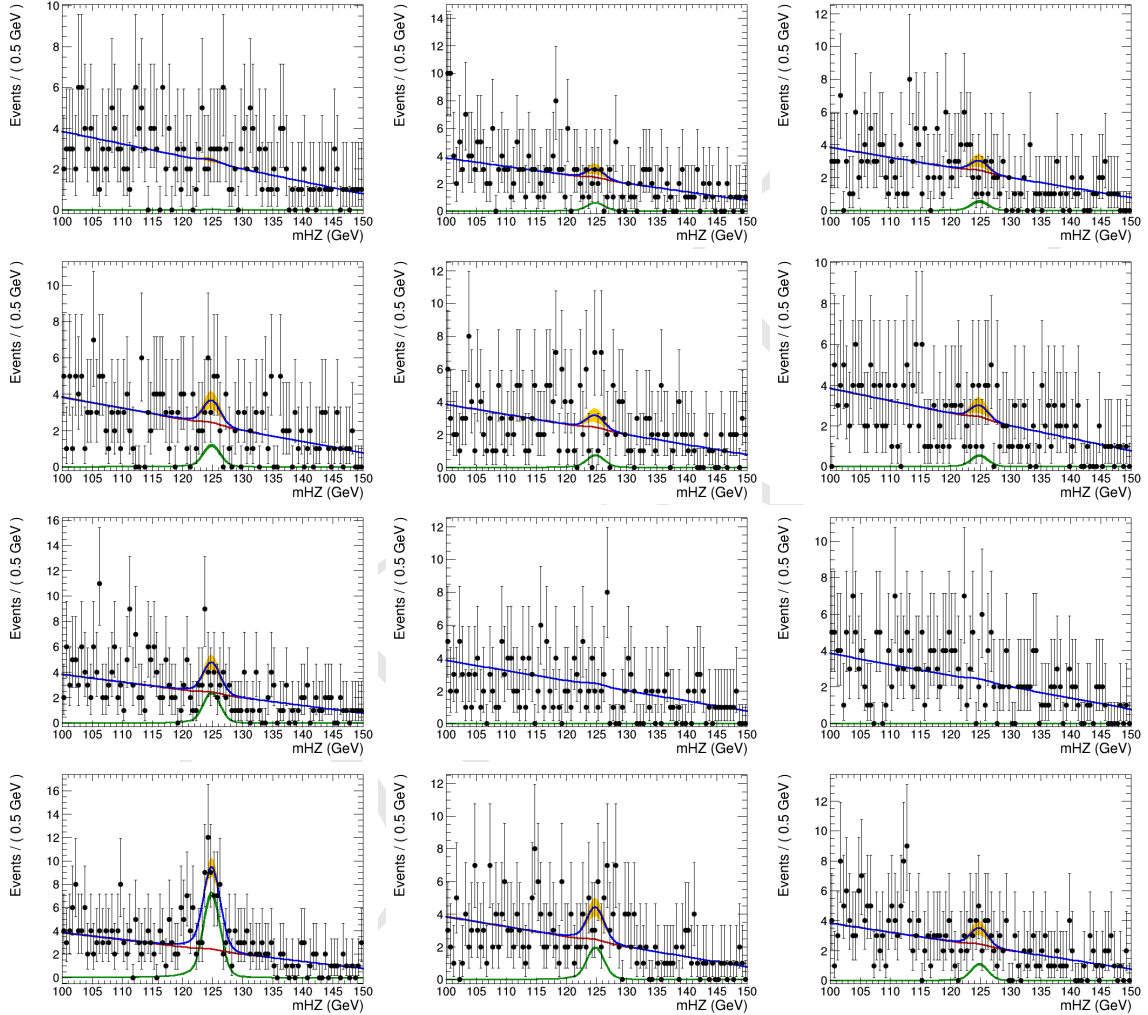


Figure 4.69: Examples of the toy datasets fit ( $M_{\mu\mu\gamma}$ ), for the Higgs decay analysis, after the toy dataset refit, for 1S, 2S and 3S (left to right), with  $\mu_{true}$  equals to 100000, 200000, 300000, 1000000 (top to bottom). The red lines corresponds to the background model (B), the green lines to signal model (S), the blue lines to the total (S+B) and the dots is the toy dataset.

1698 It is expected that the pulls distribution for the fitted signal strength ( $\frac{\mu_{fit} - \mu_{true}}{\sigma_{fit}}$ ) should follow a  
 1699 Gaussian distribution centered in 0 and with  $\sigma$  around 1. Figures 4.70 and 4.71 present those pulls  
 1700 distributions for the Z and Higgs decays, respectively.

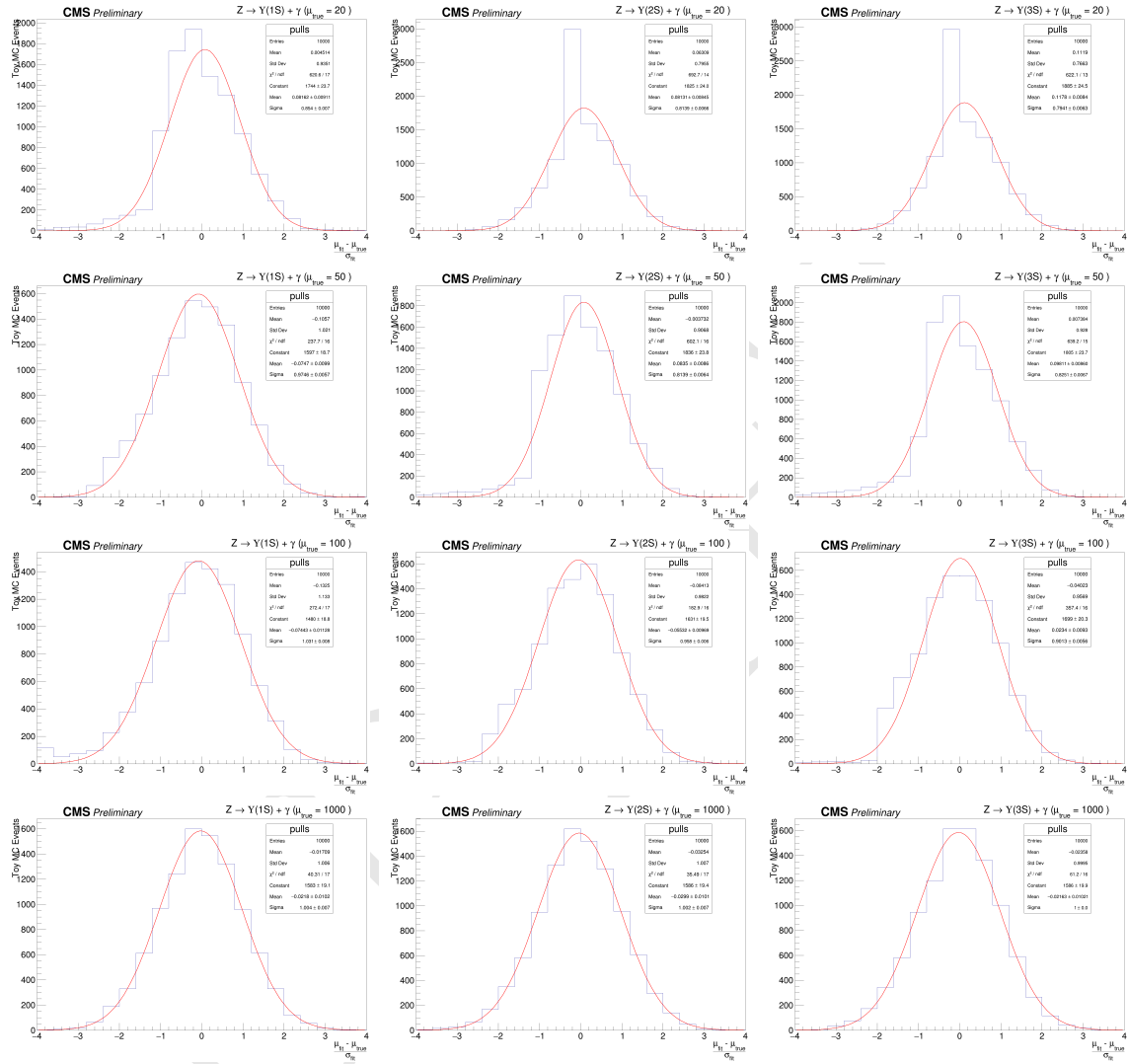


Figure 4.70: Distribution of pulls ( $\frac{\mu_{fit} - \mu_{true}}{\sigma_{fit}}$ ), for the Z decay analysis, after the toy dataset refit, for 1S, 2S and 3S (left to right), with  $\mu_{true}$  equals to 20, 50, 100, 1000 (top to bottom).

1701 As a general conclusion on this cross check, as long as the toy MC generation is able to inject enough  
 1702 signal to be fit, the final modeling of this analysis is able to recover a Gaussian pulls distribution.  
 1703 This, of course, depends on the  $\Upsilon$  state to be considered. For the Z decay, between  $\mu_{true} = 50$   
 1704 and  $\mu_{true} = 100$  (around a hundred of events passing full selection), while for the Higgs decay, it  
 1705 is needed only a few events after full selection, even though it means hundreds of thousands times  
 1706 the expected signal, since the very small cross sections for the decay, as shown in Table 4.1.

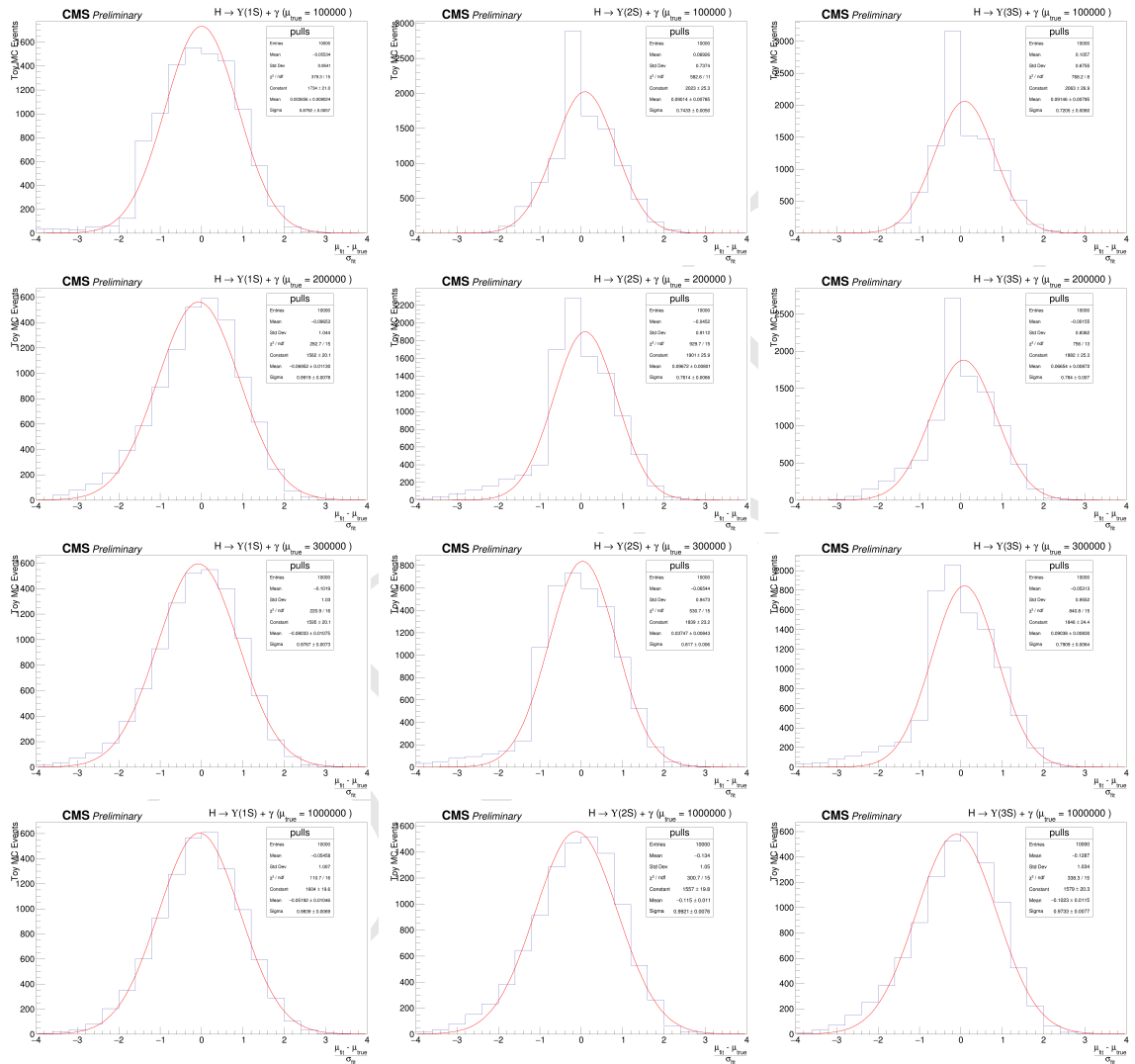


Figure 4.71: Distribution of pulls ( $\frac{\mu_{fit} - \mu_{true}}{\sigma_{fit}}$ ), for the Higgs decay analysis, after the toy dataset refit, for 1S, 2S and 3S (left to right), with  $\mu_{true}$  equals to 100000, 200000, 300000, 1000000 (top to bottom).

## <sup>1707</sup> 5 Results and conclusion

<sup>1708</sup> A two-dimensional (2D) unbinned maximum-likelihood fit to the  $m_{\mu^+\mu^-\gamma}$  and  $m_{\mu^+\mu^-}$  distributions  
<sup>1709</sup> was used to compare the data with background and signal predictions. Search has been performed for  
<sup>1710</sup> a SM Higgs and Z boson decaying into a  $\Upsilon(1S, 2S, 3S)\gamma$ , with  $\Upsilon(1S, 2S, 3S)$  subsequently decaying  
<sup>1711</sup> into  $\mu^+\mu^-$  using data obtained from  $35.9 \text{ fb}^{-1}$  of  $pp$  collisions at  $\sqrt{s} = 13 \text{ TeV}$ .  
<sup>1712</sup> Since no excess has been observed above the background, the  $CL_s$  formalism is applied, in order to  
<sup>1713</sup> establish an upper limit in the branching fractions for each channel.

### <sup>1714</sup> 5.1 The $CL_s$ formalism for upper limits setting at CMS

<sup>1715</sup> The  $CL_s$  formalism [123] consists in a modified frequentist approach to obtain an upper limit for a  
<sup>1716</sup> certain parameter of a model, with respect to the data, when there is no significant excess that could  
<sup>1717</sup> justify an observation. It is based on the profile-likelihood-ratio test statistic [124] and asymptotic  
<sup>1718</sup> approximations [125]. It is a standard upper limit setting procedure for the LHC experiments [126].  
<sup>1719</sup> When searching for non-observed phenomena, it is often usual to derive the results as a function of  
<sup>1720</sup> the signal strength modifier  $\mu$ , which is a free parameter of the full model (signal + background).  
<sup>1721</sup> It can be defined such as, the expectation value for the number of events in a bin <sup>1</sup> is:

$$E[n] = \mu s + b, \quad (5.1)$$

<sup>1722</sup> where,  $s$  and  $b$  are the expected number of signal and background events, respectively.

<sup>1723</sup> The Neyman–Pearson lemma [124] states the likelihood ratio is the optimal test between a null  
<sup>1724</sup> hypothesis and an alternative one (i.e. background-only and signal-plus-background models). On  
<sup>1725</sup> top of this, one could build a likelihood ratio test as:

$$q(\mu) = -2 \ln \left( \frac{\mathcal{L}(\text{data}|\mu s + b)}{\mathcal{L}(\text{data}|b)} \right), \quad (5.2)$$

<sup>1726</sup> where the denominator and numerator defines the likelihoods for the background-only and signal-  
<sup>1727</sup> plus-background models, respectively. This was the hypothesis test used by LEP and Tevatron  
<sup>1728</sup> experiments (the former one, with some modifications to include the nuisances effects).

---

<sup>1</sup>A set of common analysis criteria.

With these two models, i.e. their *pdfs*, one can throw toy MC events in order to construct a distribution of  $q(\mu)$ , namely  $f(q(\mu)|\mu)$ . The *p*-value of  $f(q(\mu)|\mu)$ , as below, can be used to chose between each model.

$$p_\mu = \int_{q(\mu)_{\text{data}}}^{\infty} f(q(\mu)|\mu) dq(\mu), \quad (5.3)$$

where  $q(\mu)_{\text{data}}$  is the observed value of  $q(\mu)$  on data, for a given  $\mu$ .

If  $p_\mu$  is less than  $\alpha$  (usually 0.05 or 0.1) the background-only model can be excluded in favor of the signal-plus-background model. For the propose of a confidence interval estimation, the argument can be reversed and one could look for all the values of  $\mu$  that would not be excluded with Confidence Level (CL)  $1 - \alpha$ .

The problem with this definition is that, when the expected signal strength is very small, e.g. a invariant mass distribution in the TeV scale, the null hypothesis and the alternative one are almost indistinguishable. In this situation, a downward fluctuation of the background might lead us to exclude the alternative hypothesis (signal) in a region of low experimental sensitivity region. Putting in number, if we expect 50 background events and 2 signal events, but we observe 40 events, the signal would be easily excluded.

In order to take this effect into account, a modified frequentist approach for upper limits setting, the  $CL_s$  was proposed during the Higgs search era at LEP. Lets start by considering a profile likelihood ratio [127] as below:

$$\lambda(\mu) = \frac{\mathcal{L}(\text{data}|\mu, \hat{\theta})}{\mathcal{L}(\text{data}|\hat{\mu}, \hat{\theta})}, \quad (5.4)$$

where,  $\mathcal{L}(\text{data}|\mu, \hat{\theta})$  is the profile likelihood function.

Defining  $\mu$  and the investigated signal strength,  $\hat{\theta}$  is the nuisances that maximizes the likelihood for a given  $\mu$  (fixed) while  $\hat{\mu}$  and  $\hat{\theta}$  are the signal strength and nuisances that, overall, maximizes the likelihood. The advantage of the

CMS and ATLAS have a common set of statistical guidelines [128] to ensure the compatibility of the published results. Following these recommendations, the statistics test based on 5.4 is:

$$\tilde{q}_\mu = -2\ln[\lambda(\mu)], \text{ with } 0 \leq \hat{\mu} \leq \mu. \quad (5.5)$$

The left side restriction ( $0 \leq \hat{\mu}$ ) ensure us the proper physical interpretation of  $\mu$  as a positive define signal strength, i.e., the observation a process would, for a given bin, increase the number of events. The right side restriction  $\hat{\mu} \leq \mu$  secure the interpretation of  $\tilde{q}_\mu$ 's *p*-value as a one-sided confidence interval. This is required for a upper limit definition.

The advantage of using the profile likelihood ratio is that, even though it takes into account the effect of nuisances in the likelihood, it is possible to prove that, with the use of Wilk's Theorem [111],

that a statistic test defined as  $\tilde{q}_\mu$ , asymptotically follows a chi-square distribution with one degree of freedom (the signal strength) [125]. Thus,  $\tilde{q}_\mu$  is said to be approximately independent of any nuisance and allow a fast computation of its  $p$ -value without the need of toy MC strategies (which can computationally demanding, depending on the complexity of the models), event though this is not the standard CMS/ATLAS recommendation.

Based on  $\tilde{q}_\mu$ , defined at 5.5, one should compute the  $\tilde{q}_\mu^{\text{obs}}$ , also the  $\hat{\theta}_\mu^{\text{obs}}$  and  $\hat{\theta}_{\mu=0}^{\text{obs}}$ , which corresponds to the observed value of  $\tilde{q}_\mu$  on data, the maximum likelihood estimator for the nuisances assuming some signal strength  $\mu$  and assuming a background-only model, respectively. Then, the distributions of  $f(\tilde{q}_\mu|\mu, \hat{\theta}_\mu^{\text{obs}})$  and  $f(\tilde{q}_\mu|\mu = 0, \hat{\theta}_{\mu=0}^{\text{obs}})$  are generated tossing pseudo-random toy MC. Figure 5.1 presents an example of these two distributions.

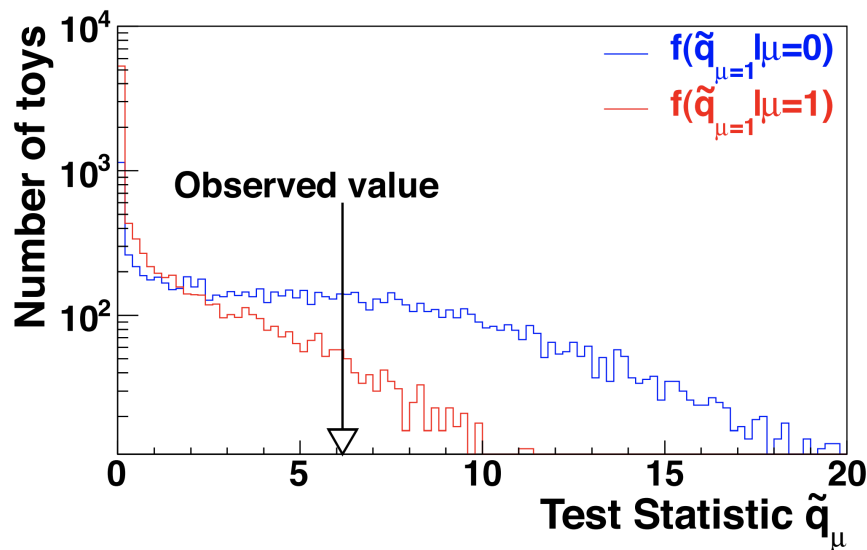


Figure 5.1: Example of  $f(\tilde{q}_\mu|\mu, \hat{\theta}_\mu^{\text{obs}})$   $f(\tilde{q}_\mu|\mu = 0, \hat{\theta}_{\mu=0}^{\text{obs}})$  distributions generated with toy MC. Source: [128].

The  $CL_s$  value is defined as:

$$CL_s(\mu) = \frac{p_{s+b}(\mu)}{1 - p_b}, \quad (5.6)$$

where:

$$p_{s+b}(\mu) = \int_{\tilde{q}_\mu^{\text{obs}}}^{\infty} f(\tilde{q}_\mu|\mu, \hat{\theta}_\mu^{\text{obs}}) d\tilde{q}_\mu \quad (5.7)$$

and

$$p_b = \int_{-\infty}^{\tilde{q}_\mu^{\text{obs}}} f(\tilde{q}_\mu|\mu = 0, \hat{\theta}_{\mu=0}^{\text{obs}}) d\tilde{q}_\mu \quad (5.8)$$

Scanning different values of  $\mu$ , within  $0 \leq \hat{\mu} \leq \mu$ , one would exclude the ones which  $CL_s < \alpha$ . CMS and ATLAS recommends a CL level  $(1 - \alpha)$  of 95%.

1772 The main advantage of the  $CL_s$  approach is that the presence of the denominator  $1 - p_b$  in 5.6  
 1773 penalizes the exclusion of regions in which the experiment is no sensitive. Figure 5.2 helps to  
 1774 illustrate this. One can notice that a small value of  $p_{s+b}$  (yellow area) is balanced by large value  
 1775 of  $p_b$  (green area). When the experimental sensitivity is higher, the two distributions tend to be  
 1776 far away from each other. Thus leading to a smaller compensation factor ( $p_b$ ) and enhancing the  
 1777 chance of a exclusive  $CL_s$  value.

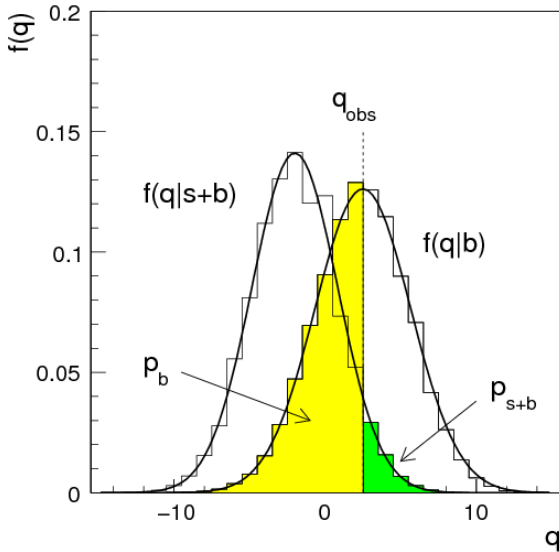


Figure 5.2: Example of  $f(\tilde{q}_\mu | \mu, \hat{\theta}_\mu^{\text{obs}})$   $f(\tilde{q}_\mu | \mu = 0, \hat{\theta}_{\mu=0}^{\text{obs}})$  distributions generated with toy MC. In the figure,  $q$  must be read as  $\tilde{q}$ . The green area shows the  $p_{s+b}$  defined in 5.7, while the yellow one shows  $p_b$  defined in 5.8. Source: [125].

1778 The expected expected upper limit and its  $\pm 1\sigma$  and  $\pm 2\sigma$  are determined by generating a large  
 1779 number of toy mc events, for the background-only model ( $\mu = 0$ ), with nuisances free to float,  
 1780 and for each simulation finding  $\mu_{95\%}$ , which defines the confidence level. Once enough samples are  
 1781 generated, one should scan, from left to right, the cumulative distribution of  $\mu_{95\%}$ . The median  
 1782 defines the expected value and the quantiles for 16%, 84% and 2.5%, 97.5% defines the  $\pm 1\sigma$  and  
 1783  $\pm 2\sigma$ , respectively.

## 1784 5.2 Branching fraction upper limits

1785 The result are summarized on table 5.1.

1786 The observed(expected) exclusion limit at 95% confidence level on the  $\mathcal{B}(Z \rightarrow \Upsilon(1S, 2S, 3S)\gamma) =$   
 1787  $2.9, 2.7, 1.4$  ( $1.6^{+0.8}_{-0.5}, 2.0^{+1.0}_{-0.6}, 1.8^{+1.0}_{-0.6} \times 10^{-6}$ ), and on the  $\mathcal{B}(H \rightarrow \Upsilon(1S, 2S, 3S)\gamma) = 6.9, 7.4, 5.8$   
 1788 ( $7.3^{+4.0}_{-2.4}, 8.1^{+4.6}_{-2.8}, 6.8^{+3.9}_{-2.3} \times 10^{-4}$ ).

1789 As stated before, this analysis was done, for the Z decay, taking into account a mutually excludent  
 1790 categorization of events, based on the reconstructed photon properties ( $\eta_{SC}$  and R9 value), as  
 1791 described in section 4.7.

Table 5.1: Summary table for the limits on branching ratio of  $Z \rightarrow \Upsilon(1S, 2S, 3S)\gamma$  and  $H \rightarrow \Upsilon(1S, 2S, 3S)\gamma$  decays.

95% C.L. Upper Limit			
	$\mathcal{B}(Z \rightarrow \Upsilon\gamma) [\times 10^{-6}]$		
	$\Upsilon(1S)$	$\Upsilon(2S)$	$\Upsilon(3S)$
Expected	$1.6^{+0.8}_{-0.5}$	$2.0^{+1.0}_{-0.6}$	$1.8^{+1.0}_{-0.6}$
Observed	2.9	2.7	1.4
SM Prediction [ $\times 10^{-8}$ ]	4.8	2.4	1.9
	$\mathcal{B}(H \rightarrow \Upsilon\gamma) [\times 10^{-4}]$		
	$\Upsilon(1S)$	$\Upsilon(2S)$	$\Upsilon(3S)$
Expected	$7.3^{+4.0}_{-2.4}$	$8.1^{+4.6}_{-2.8}$	$6.8^{+3.9}_{-2.3}$
Observed	6.9	7.4	5.8
SM Prediction [ $\times 10^{-9}$ ]	5.2	1.4	0.9

<sup>1792</sup> At table 5.2 we present the results obtained when there is no categorization of events (Inclusive  
<sup>1793</sup> category).

Table 5.2: Summary table for the limits on branching ratio of  $Z \rightarrow \Upsilon(1S, 2S, 3S)\gamma$ , for the two possible categorization scenarios.

95% C.L. Upper Limit - $\mathcal{B}(Z \rightarrow \Upsilon\gamma) [\times 10^{-6}]$			
	without categorization		
	$\Upsilon(1S)$	$\Upsilon(2S)$	$\Upsilon(3S)$
Expected	$1.7^{+0.9}_{-0.5}$	$2.1^{+1.1}_{-0.7}$	$1.9^{+1.0}_{-0.6}$
Observed	2.6	2.3	1.2
	with categorization		
	$\Upsilon(1S)$	$\Upsilon(2S)$	$\Upsilon(3S)$
Expected	$1.6^{+0.8}_{-0.5}$	$2.0^{+1.0}_{-0.6}$	$1.8^{+1.0}_{-0.6}$
Observed	2.9	2.7	1.4

<sup>1794</sup> It is worth to remember that the categorization takes places only for the  $Z$  decay. For the Higgs  
<sup>1795</sup> decay, no categorization is imposed.

<sup>1796</sup> By taking, or not, into account any categorization, the numbers presented in both tables (5.1 and  
<sup>1797</sup> 5.2), are compatible within themselves and with the results published by the ATLAS collabora-  
<sup>1798</sup> tion [129].

DRAFT

# <sup>1799</sup> 6 CMS Resistive Plate Chambers - RPC

<sup>1800</sup> In the course of this PhD study, there were a lot of opportunities to work for the RPC project, in  
<sup>1801</sup> the context of the CMS Collaboration. The main activities consists of shifts for the RPC operation  
<sup>1802</sup> and data certification, upgrade and maintenance of the online software, R&D activities for the RPC  
<sup>1803</sup> upgrade and detector maintenance during the LHC Long Shutdown 2 (2019 to 2020).

<sup>1804</sup> In this chapter, it is presented a summary of the Resistive Plate Chamber technology and the  
<sup>1805</sup> contributions to the RPC project at CMS.

## <sup>1806</sup> 6.1 Resistive Plate Chambers

<sup>1807</sup> The seminal paper on the Resistive Plate Chamber (RPC) technology was presented by R. Santonico  
<sup>1808</sup> and R. Cardarelli, in which they described a "dc operated particle detector (...) whose constituent  
<sup>1809</sup> elements are two parallel electrode Bakelite plates between" [130]. The key idea behind the RPC,  
<sup>1810</sup> with respect to other similar gaseous detectors, is the use of two resistive plates as anode and  
<sup>1811</sup> cathode, which makes possible to have a small localized region of dead time, achieving very good  
<sup>1812</sup> time resolution.

<sup>1813</sup> The working principle for RPCs relies on the idea that an ionizing particle crossing the detector, tends  
<sup>1814</sup> to interact with the gap between the two plates (filled with some specific gas mixture) and form a  
<sup>1815</sup> ionizing cascade process, in which the produced charged particles are driven by the strong uniform  
<sup>1816</sup> electrical field produced by the two plates.

<sup>1817</sup> The gas mixture is a key component of a RPC. Even though the first RPCs were produced with  
<sup>1818</sup> a mixture of argon and butane, nowadays RPCs use a mixture of gases that would enhance an  
<sup>1819</sup> ionization caused by the incident particle and quench secondary (background) effects.

<sup>1820</sup> Another feature of the RPCs is its construction simplicity and low cost. This allows the use of RPC to  
<sup>1821</sup> cover larger areas at a reasonable cost.

<sup>1822</sup> An extensive review of the RPC technology and its applications can be found at [131].

### <sup>1823</sup> 6.1.1 Principles and operation modes

<sup>1824</sup> The core of a RPC chamber is a gap made with two parallel high resistivity plates, separated  
<sup>1825</sup> by some regular distance (typically millimeters), filled with a proper gas mixture and under  
<sup>1826</sup> appropriate high voltage (HV) applied on the plates (electrodes, from here on). When an ionizing

1827 particle crosses the gap, there is a high enough chance the the particle will interact with the gas  
 1828 and produce a newly created positive ion and a electron. This pair will travel in opposite directions,  
 1829 according to the electric field from the electrodes. During this process, the electron will gain kinetic  
 1830 energy and inelastically interact with other neighboring atoms/molecules, creating excitations in their  
 1831 energy levels and, potentially, also ionizing them. The secondary ionization electrons will also follow  
 1832 the same curse, creating an **Avalanche** of positive and negative particle/ions traveling towards the  
 1833 electrodes. This process is proportional to the applied electric field. Figure 6.1 illustrates the  
 1834 avalanche production.

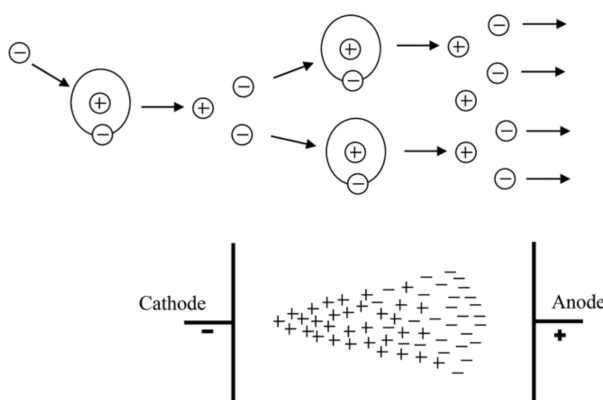


Figure 6.1: The Avalanche production process inside a RPC gap. (Top) The initial process and the secondary electron/ion generation. (Bottom) The overall charge distribution of an Avalanche between the electrodes. Source: [132].

1835 The number of particle composing the avalanche can be expressed as (assuming constant pres-  
 1836 sure) [132]:

$$n_e = n_0 e^{\alpha d} = n_0 A, \quad (6.1)$$

1837 where  $n_0$  is the number of initial electrons initiating the avalanche,  $A$  is the *gas gain*, or *multiplication factor* and  $d$  is the distance since the avalanche creation. This is also known as Townsend theory  
 1838 for discharges and  $\alpha$  is the first Townsend coefficient.  
 1839

1840 When the positive ions bunch reaches the cathode, under certain conditions (if the first ionization  
 1841 energy of the ion is greater than the work function of the cathode), the recombination of the ion  
 1842 with the electrode material might release electrons which will also follow the electric field. The  
 1843 relative probability (with respect to the primary electron emission) of this emission to happen ( $\gamma_+$ )  
 1844 is called the the second Townsend coefficient.

$$n_+ = n_0 A \gamma_+. \quad (6.2)$$

1845 Another process which can occur is the secondary photoelectron productions, described by a similar  
 1846 equation as above:  $n_{pe} = n_0 A \gamma_{ph}$ . This production is mostly related to de-excitation of molecules  
 1847 and atoms in vicinity of the avalanche. The produced photons might initiate new ionization process.

1848 As an alternative to the Townsend theory, Raether, Meek, and Loeb, proposed the *streamer-leader*  
 1849 *theory* [133]. This theory is valid when there is a high enough concentration of ions  
 1850 produced. This critical value is called Raether limit.

$$n_0 A > 10^8 \text{ electrons} \quad (6.3)$$

1851 In this limit, the electric field created by the space distribution is high enough to be same order  
 1852 of the external field. In the vicinity of the head (or tail) of the avalanche the field gets disturbed  
 1853 and intensified. The intensification of the field enhances the ionization effect and give rise to  
 1854 secondary avalanches (photoelectrons). The intensified field also makes the photoelectrons produced  
 1855 travel towards the head (positive ions). Their antikuaption generates more UV radiation and more  
 1856 secondary avalanches. This whole process is called **Streamer**. If no quenching is imposed, the  
 1857 streamer might evolve to a spark, fully discharging on the electrodes. If the concentration of  
 1858 electrons is high enough, the avalanche tail (electrons) might also give rise to a streamer (namely,  
 1859 negative streamer). Figure 6.2 illustrates the different subprocesses related to streamer production.

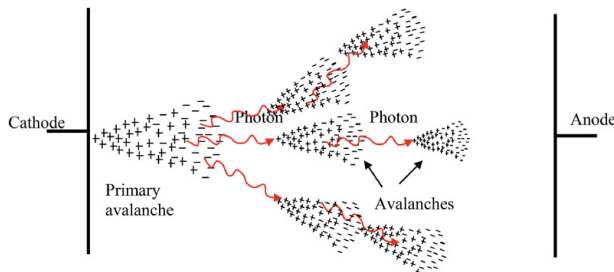


Figure 6.2: Streamer formation process. The distorted electric field around the high positive charge concentration enhances the ionization process, initiating secondary avalanches. Source: [132].

1860 A RPC where most of the charge multiplication process happens in the form of a streamer is said  
 1861 to be working in **Streamer Mode**. The advantage of the of the streamer mode is the high induced  
 1862 charge which is easily caught by non-sensitive readout electronics. On the other hand, the streamer  
 1863 mode, because of its highly associated charge, will have a impact in the rate capability of the  
 1864 detector (the local dead time will be higher).  
 1865 Because of the high background environment of LHC, the CMS RPC operates in **Avalanche Mode**,  
 1866 where de discharge is highly quenched and very well localized. On the other hand, a very sensitive  
 1867 readout electronics is required to cope with the high rate demanded.  
 1868 A good review of electrical discharge on gases can be found at [132].

## 1869 6.2 CMS Resistive Plate Chambers

1870 At CMS, the Resistive Plate Chamber are installed in both the barrel and endcap region, forming  
 1871 a redundant system with the DT (barrel) and CSC (endcap). As described in the CMS Muon  
 1872 Technical Design Report (Muon-TDR) [73], the RPC are composed of 423 Endcap chambers and

1873 633 barrel chambers. Figure 6.3 presents a picture of the CMS RPCs installed on station RE+4 of  
 1874 the Endcap.

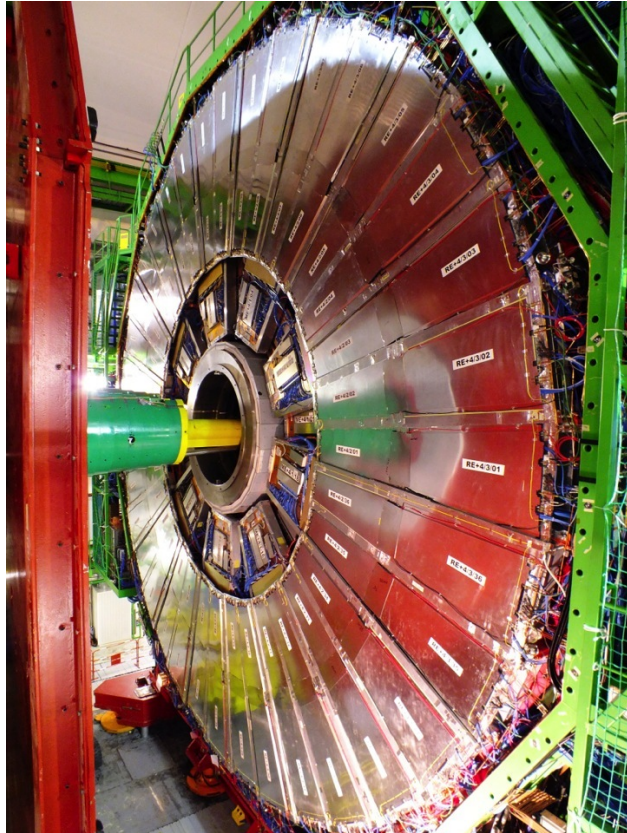


Figure 6.3: RPC chamber on installed on station RE+4 of CMS Endcap. Source: [134].

1875 Each chamber consists of two gas gaps (double gap), 2 mm tick each, made of Bakelite (phenolic  
 1876 resin) with bulk resistivity of  $10^{10} - 10^{11} \Omega m$ . The choice of the bulk resistivity of the electrode has  
 1877 high impact on the rate capability of the detector.

1878 Each gap has its external surface is coated with a thin layer of graphite paint, which acts as  
 1879 conductive material, distributing the applied high-voltage (HV). On top of the graphite a PET  
 1880 film is used for isolation. A sheet of copper strips is sandwiched between the gaps. Everything is  
 1881 wrapped in aluminum case.

1882 The double gap configuration increases the efficiency of the chamber, since the signal is picked up  
 1883 from the OR combination of the two gaps. A chamber with only one gap working, loses around  
 1884 15% of efficiency, even though, this can be recovered by increasing the HV applied during operation  
 1885 mode (working point - WP).

1886 A characteristic that differentiate the CMS RPC from previous RPC application in HEP is  
 1887 the operation mode. A RPC at CMS, operates in avalanche mode, while previous experiments used  
 1888 the streamer mode. Both modes are related to the applied HV, in commitment with the strength of  
 1889 the generated signal, and are capable of generate a well localized signal, which can be picked up by  
 1890 the readout electronics, but the avalanche mode offer a higher rate capability around  $1 \text{ kHz/cm}^2$ ,

1891 while the streamer mode goes up to  $100 \text{ Hz}/\text{cm}^2$ . The high rate capability is a key factor in order  
 1892 to cope with requirements of the LHC luminosity, specially in the high background regions.

1893 Besides the rate capability, the key factors that driven the CMS RPC design were: high efficiency ( $>$   
 1894 95%), low cluster size ( $> 2$ ) for better spatial resolution (this reflects in the momentum resolution)  
 1895 and good timing in order to do the readout of the signal within the 25 ns of a LHC bunch cross  
 1896 (BX) and provide it to the CMS trigger system. These requirements have implications in the choice  
 1897 of material, dimensions, electronics and gas mixture.

1898 In the barrel, along the radial direction, there are 4 muon layers (called stations), MB1 to MB4.  
 1899 MB1 and MB2 is composed of a DT chamber sandwiched between two RPC chambers (RB1 and  
 1900 RB2) with rectangular shape. The stations MB3 and MB4 have only one RPC (RB3 and RB4) are  
 1901 composed by two RPC chambers (named - and + chambers with the increase of  $\phi$ ) attached to one  
 1902 DT chamber, except in sector 9 and 11, where there is only one RPC. RE4, sector 10 is a special  
 1903 case, since it is composed of four chambers (-, -, + and ++). These stations are replicated along  
 1904 the z direction in five different wheels of the CMS (W-2, W-1, W0, W+1 and W+2) and in twelve  
 1905 azimuthally distributed sectors (S1 to S12). Figure 6.4 show the different barrel stations and wheel.

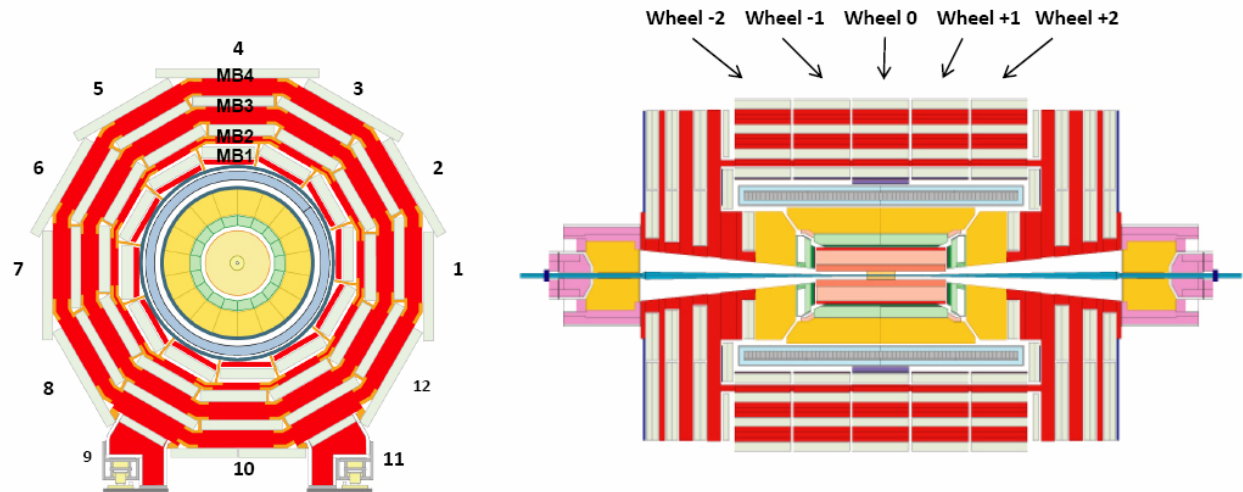


Figure 6.4: R- $\phi$  (left) and R-Z (right) projections of the barrel Muon System.

1906 In the endcap, the RPC chambers have a trapezoidal shape and are distributed in four disks (or  
 1907 stations) each side ( $RE \pm 4$ ,  $RE \pm 3$ ,  $RE \pm 2$ ,  $RE \pm 1$ ), each one with 72 chambers. CMS split up its  
 1908 disks in 3 rings, along the radial direction, and 36 sector in the azimuthal angle. RPCs are present  
 1909 in the two outer rings ( $R2$  and  $R3$ ), in all 36 sectors. The  $RE \pm 4$  are special cases, since these  
 1910 chambers were installed only in 2014, a design choice was made the mechanically attached  $R2$  and  
 1911  $R3$  chambers, each sector, in what is called, a super-module. Figure 6.5 show the different endcap  
 1912 disks.

1913 The length of the strips is chosen, for both barrel and endcap, in such a way to control the area of  
 1914 each strip, in order to reduce the fake muons, due to random coincidence. This has to do with the  
 1915 time-of-flight and signal propagation along the strip. In the barrel, each chamber readout is divided

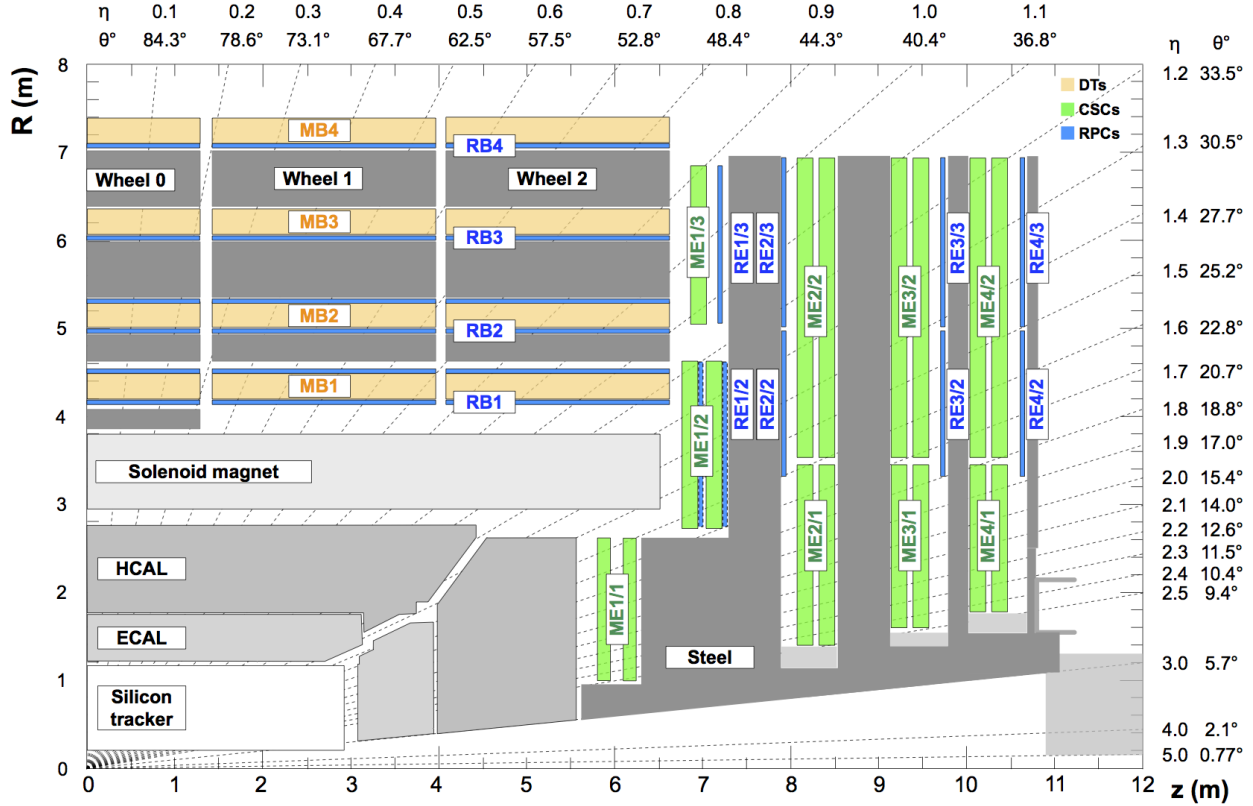


Figure 6.5: R-Z projections of the endcap Muon System (positive Z side). This is the same configuration for the 36  $\phi$  sectors.

in two regions (rolls), called forward and backward (along increasing  $|\eta|$ ) <sup>1</sup>. In the endcap, the strips are divided in 3 regions, called partitions A, B and C (from inside the detector to outside).

The gas mixture used in the CMS RPCs is composed by C2H2F4 (Freon R-134a, tetrafluoroethane), C4H10 (isobutane), SF6 (sulphur hexafluoride) (95.2 : 4.5 : 0.3 ratio) and with controlled humidity of 40% at 20-22 °C. The Freon is used to enhance the ionization and charge multiplication that characterizes the avalanche, while the isobutane is introduced for quenching proposes, in order to reduce the secondary ionizations that could lead to formation of streamers and the SF6 is used to reduce the electron background. The choice of Freon over other gases, i.e. argon-based and helium-based, was motivated by previous studies [135, 136].

Since its R&D, the RPC have shown good performance over aging. This is even historical over previous RPC experiments [137–143]. Even the most recent studies of aging, taking into account future LHC conditions (High-Luminosity LHC - HL-LHC) plus a safety margin of 3 times the expected background ( $600 \text{ Hz/cm}^2$ ) have shown good aging hardness [144].

### 6.2.1 Performance

The RPCs, for the CMS experiment, contribute mainly with triggering inputs, due to its very good time resolution. The important parameters which are monitored to evaluate the RPC performance

<sup>1</sup>Some chamber are divided in three rolls, forward, middle and backward, for trigger propose.

1932 are the efficiency and cluster size. The former is related to the ratio of the registered hits over the  
 1933 number of muons that passed through the chamber, while the former one is the number adjacent  
 1934 strip (minimal readout unit) that were fired (activated) per hit. Figures 6.6 and 6.7 present the  
 1935 historical distribution of efficiency and cluster size as a function of the integrated luminosity collect  
 1936 during Run2.

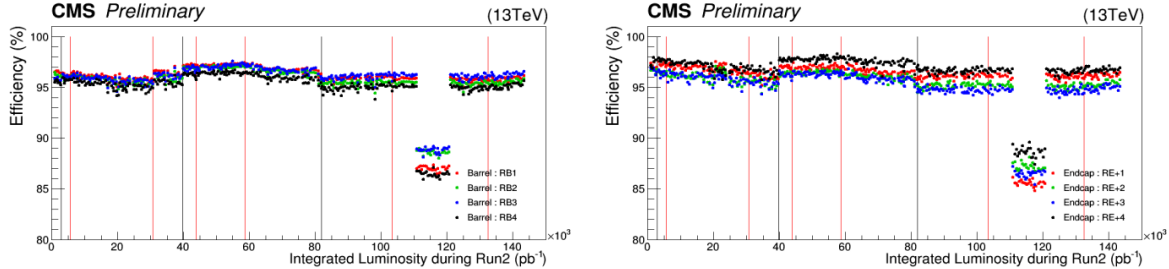


Figure 6.6: RPC efficiencies (per chamber) over Run2 Integrated Luminosity for Barrel (left) and Endcap (right). Red lines indicates technical stops (TS) while grey ones indicates Year-End-Technical stops (YETS). The drop in the efficiency around  $110 \text{ pb}^{-1}$  is related to a known operation mistake. Source: [145].

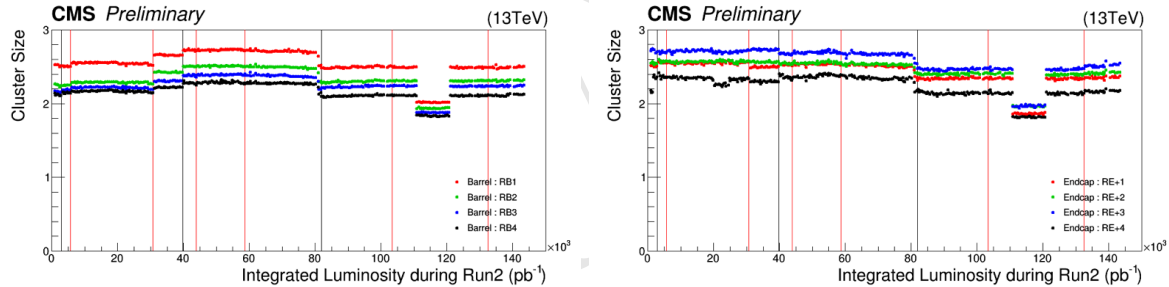


Figure 6.7: RPC cluster size (CLS - per chamber) over Run2 Integrated Luminosity for Barrel (left) and Endcap (right). Red lines indicates technical stops (TS) while grey ones indicates Year-End-Technical stops (YETS). The drop in the cluster size around  $110 \text{ pb}^{-1}$  is related to a known operation mistake. Source: [145].

1937 In general, the RPC system operates with efficiency above 95% and cluster size smaller than 3  
 1938 (a good parameter established during the design phase). The importance of the efficiency is a  
 1939 less complicated concept to catch, on the other hand, the cluster size might not be so straight  
 1940 forward. The optimal regime of RPCs operation at CMS is the avalanche mode, in which the  
 1941 electrical discharge is constrained in a millimeter level size region. Another operation mode is the  
 1942 streamer mode, in which the initial discharge might trigger secondary ones, e.g. by the emission of  
 1943 unquenched photons. A streamer discharge is capable of fire neighbor strips, increasing the cluster  
 1944 size. Operating in avalanche mode is fundamental to keep the RPCs capable of dealing with the  
 1945 high background environment of CMS.

1946 To keep the mean cluster size under control ( $< 3$ ) is important to guarantees enough spatial reso-  
 1947 lution for the measurements (the geometrical position of a hit is the midpoint of the cluster) and  
 1948 ensures that the system has enough rate capability to operate, since a RPC with a high sensitive  
 1949 front-end electronics (necessary for the avalanche mode operation) could be degraded by pileup of

1950 dead time on many channels, including electronics noise, streamers, darks counts and other sources  
 1951 of background.

1952 A third important parameter to be measured and controlled in a RPC system, under the LHC  
 1953 conditions, is the current due to the high voltage applied. This current is known to be proportional  
 1954 to the total charge released in each electrical discharges and to the hit rate on the chamber. The  
 1955 voltage applied is divided, as in a series circuit, between the electrodes and the gap. At increasing  
 1956 background, the current also increases and, since the applied voltage is constant, the voltage across  
 1957 the gap is reduced in favor of the voltage across the electrodes. This reduction of effective voltage  
 1958 on the gas, might have an impact on its gain, imposing a reduction on the detector sensitivity.

1959 Figure 6.8 presents the ohmic currents <sup>2</sup> in different regions of the detector, from 16<sup>th</sup> of April,  
 1960 2018 to 2<sup>nd</sup> of December, 2018. It is clear how the stations subjected to higher background (RE±4  
 1961 - 40 Hz/cm<sup>2</sup>) are subjected to a degrading factor that increases with the luminosity (background  
 1962 rate) and decreases when the detector is powered off. This effect is supposed to be related with  
 1963 the Hydrogen Fluoride (HF) production inside the gap, due to the electrical discharges. HF is a  
 1964 conductivity molecule, which can potentially attach to the internal surface of the gap, reducing  
 1965 the overall resistivity. The HF production can be controlled by properly tuning the gas flow as  
 1966 a function of the background that the chamber is subjected. HF concentration can also lead to  
 1967 permanent degradation of the gap, due to its chemical properties. Keeping the currents levels as  
 1968 low as possible is important for aging proposes.

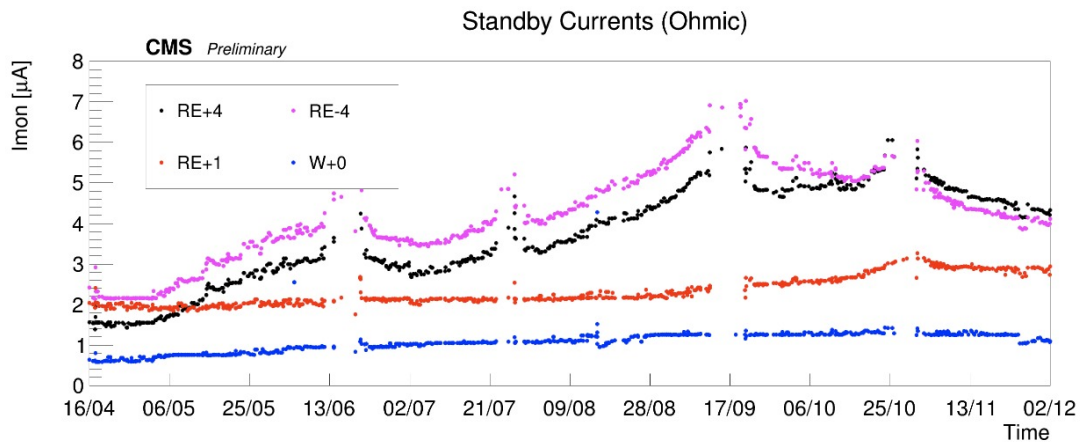


Figure 6.8: Ohmic current history of W+0, RE+1, RE+4 and RE-4. The blank regions, from time to time, corresponds to technical stops (TS), when the detector is off. Source: [145].

1969 A review of the RPC performance during Run2 can be found at [145].

### 1970 6.3 Contribution to the CMS RPC project

1971 During the curse of this study, a head collaboration of our research group and the CMS RPC  
 1972 project was established. Many contributions were given to the project as part of the graduation as a

<sup>2</sup>Current at 6500 V, which is below the typical working point of a CMS RPC (around 9500 V). In this region, no charge multiplication effect take place and chamber current is governed only by Ohm's Law.

<sup>1973</sup> experimental particle physicist, with focus on getting acquaintance with a subsystem technology and  
<sup>1974</sup> give a meaningful collaboration to the detector operation. Those are considered by the community  
<sup>1975</sup> important steps on the student graduation.

<sup>1976</sup> Below it is described the contributions given to the CMS RPC project.

### <sup>1977</sup> 6.3.1 RPC Operation - Shifts and Data Certification

<sup>1978</sup> The first activities done for the CMS RPC project were shifts for data certification of data taken.  
<sup>1979</sup> This certification is done by specialized people for different CMS subsystems and physics objects  
<sup>1980</sup> groups <sup>3</sup>.

<sup>1981</sup> This certification is done in order to ensure the quality of the date recorded based on the well  
<sup>1982</sup> functionality of each system during the data taking and the reconstruction of the physics objects in  
<sup>1983</sup> the expected matter. A certain collection of data (run) is said certificate when all subsystems and  
<sup>1984</sup> object experts agrees on this.

<sup>1985</sup> Figure 6.9 shows, as an example of the luminosity delivered by the LHC, recorded one by CMS and  
<sup>1986</sup> the certified (validated), from the 22nd of April, 2016 to the 27th of October, 2016. Only certified  
<sup>1987</sup> data is available for physics analysis.

<sup>1988</sup> Shifts are a continuous weekly activity (specially during the data taking period), performed in a  
<sup>1989</sup> weekly basis, in order to ensure the availability of certified data, as soon as possible.

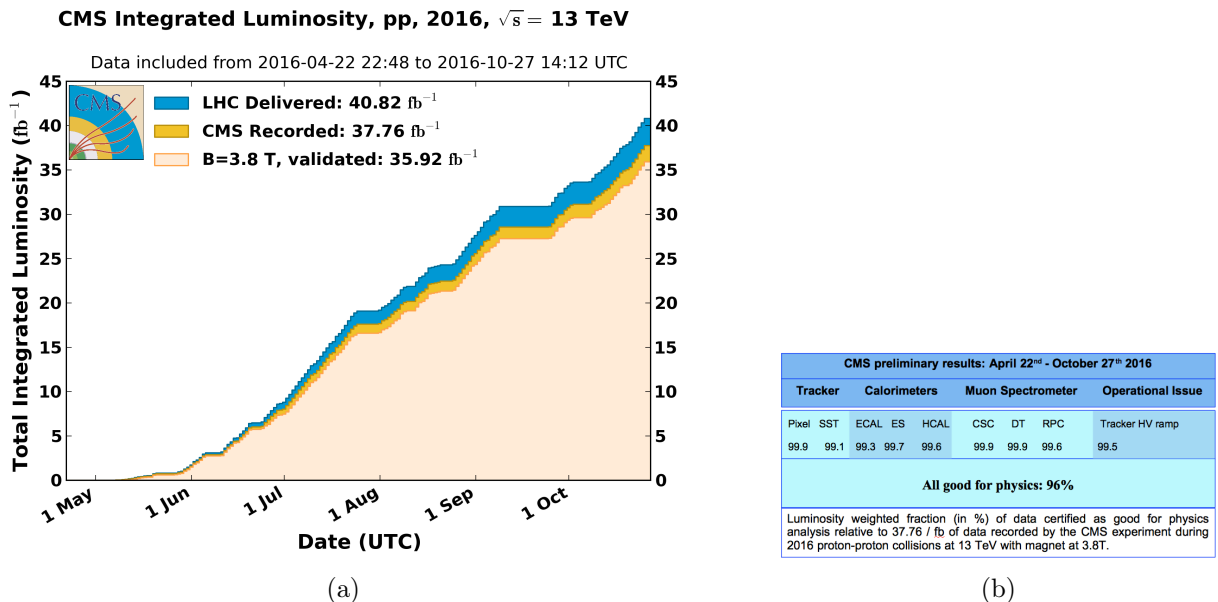


Figure 6.9: (a) Luminosity delivered by the LHC, recorded one by CMS and the certified (validated), from the 22nd of April, 2016 to the 27th of October, 2016. (b) Efficiency of the certification process for each subsystem, from the 22nd of April, 2016 to the 27th of October, 2016. Total CMS efficiency is above 90%. Source: [146]

<sup>3</sup>Groups of reconstruction and performance experts for different high-level reconstructed objects from CMS, i.e. muons, taus, jets/MET, electrons/photons

1990 **6.4 RPC Online Software**

1991 On what concerns the Online Software (OS) of the CMS RPC system, the main contribution given  
 1992 was the upgrade of the Trigger Supervisor libraries.

1993 The Trigger Supervisor is a web-based software, which run over the xDAQ backend and provides,  
 1994 through a modules organized in a tree system, called cells, a standard interface for the operation and  
 1995 monitoring of different system at CMS. In principle only systems which contribute directly to the  
 1996 L1 trigger should have a Trigger Supervisor implementation. This was the case for the RPC during  
 1997 the Run1. Since Run2, RPC contributes to the trigger indirectly, by providing data to the muon  
 1998 processors (CPPF, OMTF and TwinMux). The Trigger Supervisor implementation is a legacy from  
 1999 that period.

2000 Each subsystem is responsible for its own implementation of the Trigger Supervisor, based on the  
 2001 functionalities that it wants to have (requirements). The xDAQ [147] is a middleware, developed by  
 2002 CERN and widely used at CMS, as a tool for control and monitoring of data acquisition system in  
 2003 a distributed environment. It is capable of providing a software layer for direct access of hardware  
 2004 functionalities and monitoring.

2005 The upgrade made (figure 6.10), consists in upgrade the higher level of the RPC online software.  
 2006 In summary, up to 2017, the online software, was using Scientific Linux 6 as operational system,  
 2007 which executed xDAQ 12, in turn, servers as backend for Trigger Supervisor 2. A upgrade of  
 2008 the operational system to Centos 7, demanded the upgrade to xDAQ 14. On top of that, Trigger  
 2009 Supervisor 2 would not work and had to be updated to Trigger Supervisor 5 in order to be functional  
 2010 in 2018.

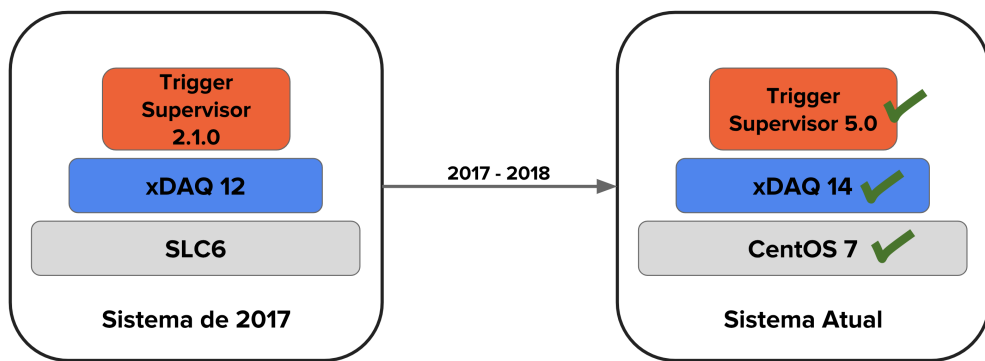


Figure 6.10: Upgrade of the RPC online software.

2011 Between versions 2 and 5 of Trigger Supervisor, part of the source-code had to be reworked, keep  
 2012 the majority of the code structures. Most of the changes were made in the front-end of the system.  
 2013 The standard JavaScript library Dojo [148], used in version2, was deprecated in favor of Google's  
 2014 Polymer[149]. The main reason for this change was to isolate C++ code from HTML, which  
 2015 was impossible with Dojo. This implied to rewrite all the screen of the RPC Trigger Supervisor  
 2016 implementation, as in figure 6.11.

2017 The upgrade was done in time to ensure the control and operation of the RPC for 2018 data taking.

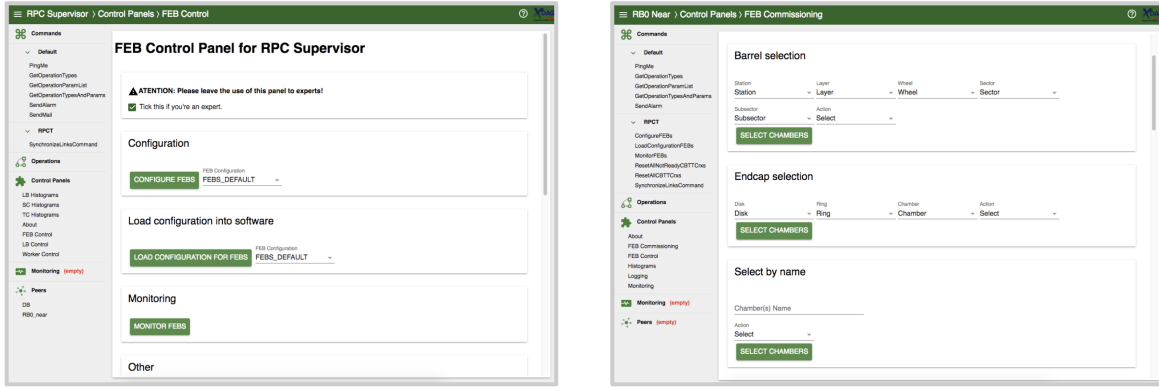
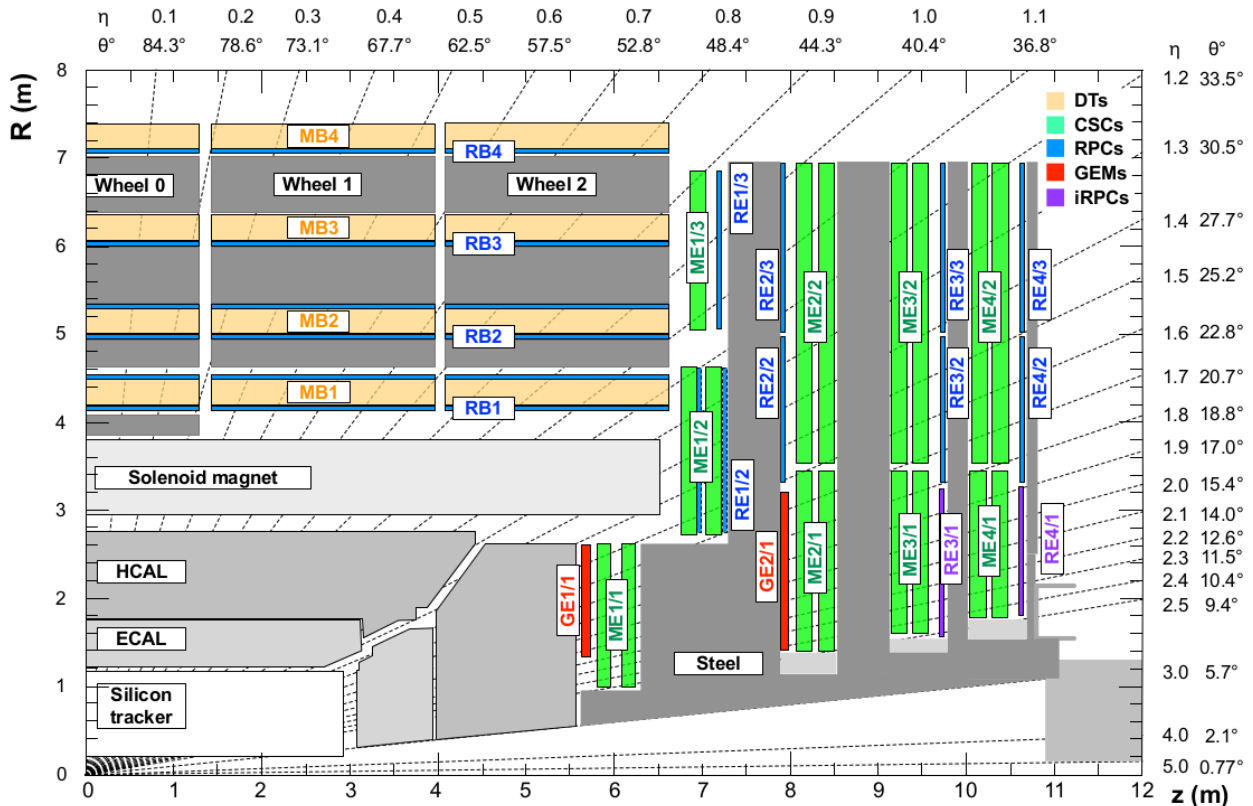


Figure 6.11: Example of the updated screens, using Trigger Supervisor 5.

### 2018 6.4.1 iRPC R&D

2019 For the next 4 year of CMS activities it is foreseen the upgrade of the the Muon Systems [73].  
 2020 These upgrades are planed in order to extend the pseudorapidity coverage ( $\eta$ ) and to guarantee the  
 2021 operation conditions of the present system in the HL-LHC (High Luminosity LHC) era. The RPC  
 2022 (Resistive Plate Chambers) [73] subsystem, it will have maintenance of the present chambers and  
 2023 installation of new chambers in the region of  $|\eta| < 1,8$  para  $|\eta| < 2,4$  [150]. These new chambers  
 2024 (iRPC) will be added in the most internal part of the muon spectrometer, RE3/1 e RE4/1, as in  
 2025 Figure 6.12.

Figure 6.12:  $\eta$  projection of the Muon System subdetectors. In purple, is labeled the iRPCs to be installed during the CMS upgrade.

Even thought this region is covered by the CSC detectors CSC (Cathode Strip Chambers), there are some loss of efficiency due the the system geometry. The installation of additional chambers will mitigate this problem and potentially increase the global efficiency of the muon system. The new chamber, called iRPC (*improved RPC*), will be different them the present one. For a luminosity of  $5 \times 10^{34} cm^{-2}s^{-1}$  the neutrons, photons, electrons and positrons background in the high  $|\eta|$  region is expected to be around  $700 Hz/cm^2$  (for the chambers in RE3-4/1). Applying a safety factor of 3, the new chambers should support up to  $2 Hz/cm^2$  of gamma radiation and still keep more than 95% of efficiency. Studies indicate, so far, that the use of High Pressure Laminates (HPL) for the double gap chambers is the most suitable choice. In order to reduce the aging and increase the rate capability, the electrodes and the gap size should be reduced in comparison with the present system.

One of the challenges for the R&D of the iRPC chambers is measuring the their performance in a high radiation environment, as the one for HL-LHC. For this, the CMS RPC project uses the Gamma Irradiation Facility (GIF++) [151], at CERN. The GIF++ is located at the H4 beam line in EHN1 providing high energy charged particle beams (mainly muon beam with momentum up to 100 GeV/c), combined with a 14 TBq 137-Cesium source. In the GIFF++ it is possible to achieve the HL-LHC total dose in a much reasonable amount of time. With the shutdown of LHC, the muon beam source is also off and will stay like this for 3 years. This means that the only muon sources for studies in GIF++ are cosmic muons.

In order to create a trigger system for iRPC R&D, the usual procedure is to use scintillators, on the top and on the bottom of the chamber. This is effective, but in a high gamma radiation environment, scintillators can be very sensitive which could lead to an undesirable amount of fake triggers which can degrade the measurements. Also, if one wants to covers a large area with scintillators, this can be expensive and they will not provide any means of tracking to measuring not only the global, but also the local chamber performance.

To provide a solution, the CMS RPC got in agreement with the LHCb [152] Muon Project to use their Multiwire Proportional Chambers (MWPC) [153], which were removed from LHCb, to be replaced by new chambers, and use them as trigger and/or tracking system at GIF++. This chambers, by design, have relatively low gamma sensitivity, already have some 1-dimensional resolution ( $O(cm)$ ) and, the biggest advantage, with respect to any other gaseous particle detector option: LHCb has hundreds of vacant chambers. Any other detector would have to be build.

Not going in details of the MWPC technology nor the LHCb chamber construction [154], these chambers have a total active area of  $968 \times 200 mm^2$  divided 2 layers (top and bottom) of 24 wire pads ( $40 \times 200 mm^2$ ) composed of around 25 wires/channel, grouped by construction. Each chamber is equipped with 3 FEBs (Front-End Boards) with 16 pads each.

A channel is a logical combination of a top layer (pads) and a bottom layer readout. These readouts can be combined in AND or OR logics. One can have 8 channels per FEB, each channel being a logical combination of top and bottom pads. In this mode they are called AND2 and OR2. It is also possible to have the FEB configured in a 2 channels mode, each one corresponding to one sixth of the total readout pads. In this mode, all the pads can be combined in OR (called OR8) or they

2066 can be AND'ed in top and bottom pads and then group in OR (called OR4AND2). Figures 6.13  
 2067 and 6.14 presents a logical diagram for each readout mode.

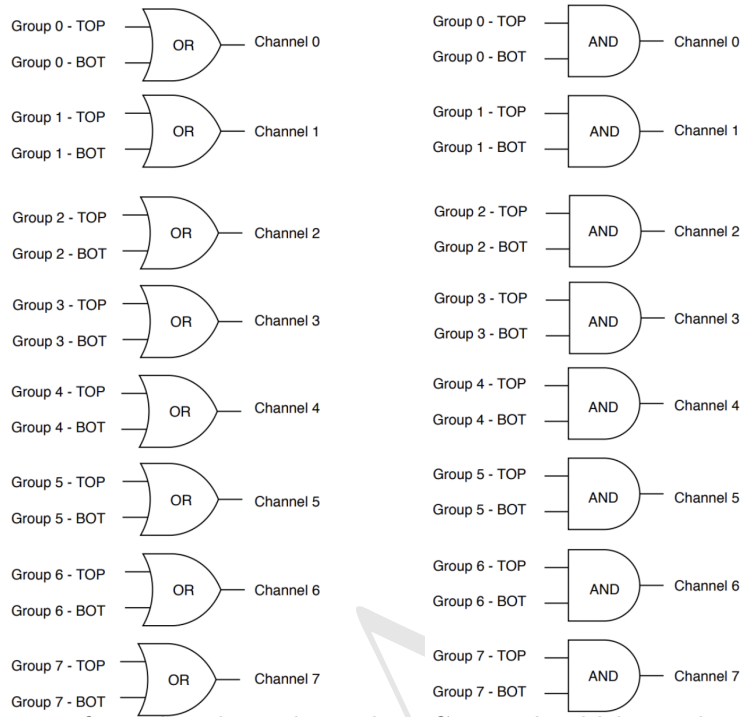


Figure 6.13: FEB configured 8 channels modes. Group should be understood as wire pad. Left: Logical diagram for OR2. Right: Logical diagram for AND2.

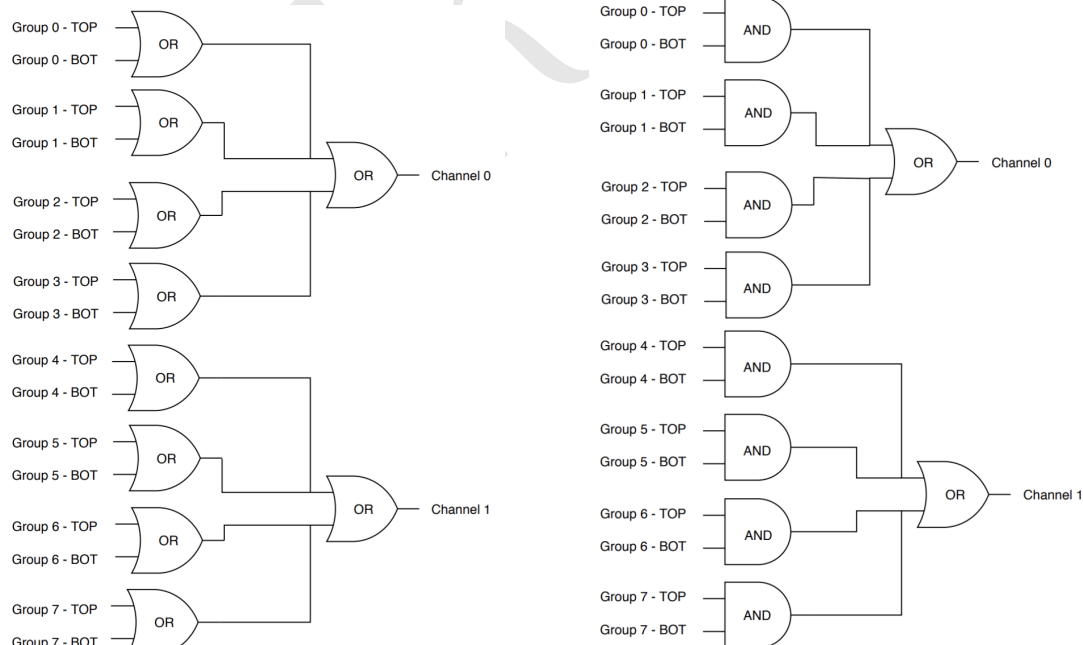


Figure 6.14: FEB configured 2 channels modes. Group should be understood as wire pad. Left: Logical diagram for OR8. Right: Logical diagram for OR4AND2.

2068 The nominal gas mixture for these chambers is Ar/CO<sub>2</sub>/CF<sub>4</sub> (40:55:5). For a matter of simplicity,  
 2069 it was used an already available similar gas line in the same building, used by CMS CSC (Cathode

2070 Strip Chamber) [73], which has a similar composition (40:50:10). Optimal conditions are obtained  
 2071 with 2 to 4 liters/hour of gas flux and 2.65 kV of applied voltage.

2072 Figure 6.15 shows the setup that was prepared for commissioning of this chambers. It was mounted  
 2073 two chambers on top of another (chambers A and B) above an RPC R&D chamber and two other  
 2074 chambers on the bottom (chambers C and D). These four MWPC will be used as telescope for  
 2075 the RPC chamber. All the services were mounted in rack, as in Figure 6.15. This includes power  
 2076 supply (low voltage and high voltage), distribution panel, VME crate and boards for FEB control,  
 2077 computer for control (high voltage, and FEB control) and NIM crate and boards for LVDS to NIM  
 2078 signal conversion, logics and counting.

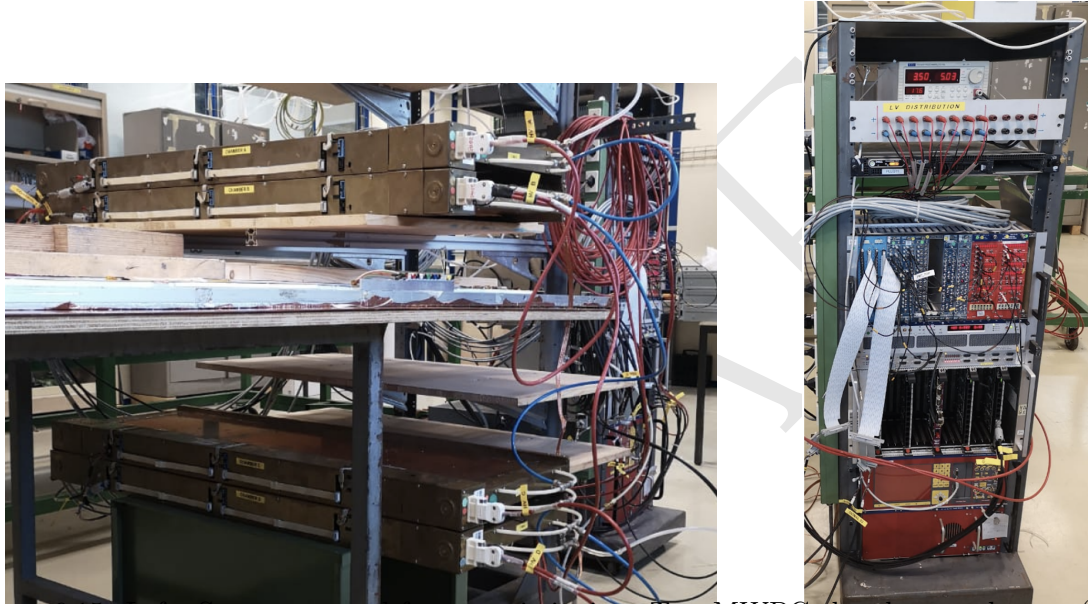


Figure 6.15: Left: Setup mounted for commissioning. Two MWPC chamber on the top (chambers A and B) and two (chambers C and D) on the bottom with a RPC R&D in the middle. Right: Rack with all the services for the operation of these chambers.

2079 Due to the short amount of time available for the commissioning, only two measurements measurements were made with these chambers. They were meant to be a proof of concept for future  
 2080 activities.

2082 The first measurement was to measure the coincidence rate of two chambers as a function of the  
 2083 distance between the two top planes (Figure 6.16). This measurements were done with nominal  
 2084 working point, with one FEB configured in 2 channels mode with 7 pC threshold, in (160 mm x  
 2085 160 mm) area per chamber. One can observe that, if we go for a telescope trigger in the order of  
 2086 1 meter of separation between the chamber, the logical combination chosen has negligible effect in  
 2087 the coincidence rate. Also, the fits can be used to estimate the rate in a configuration with chamber  
 2088 on the roof and under the floor. This could be the case of a universal trigger, to be mounted in  
 2089 GIF++ with these chamber.

2090 The second measurement consist on evaluate the impact of  $\gamma$  background by placing a small Cs-137  
 2091 source on top of the chamber A (Figure 6.17). For this measurement, the distance between top  
 2092 planes of each pair of chamber (A to B and C to D) is 65 mm, while the distance between the top

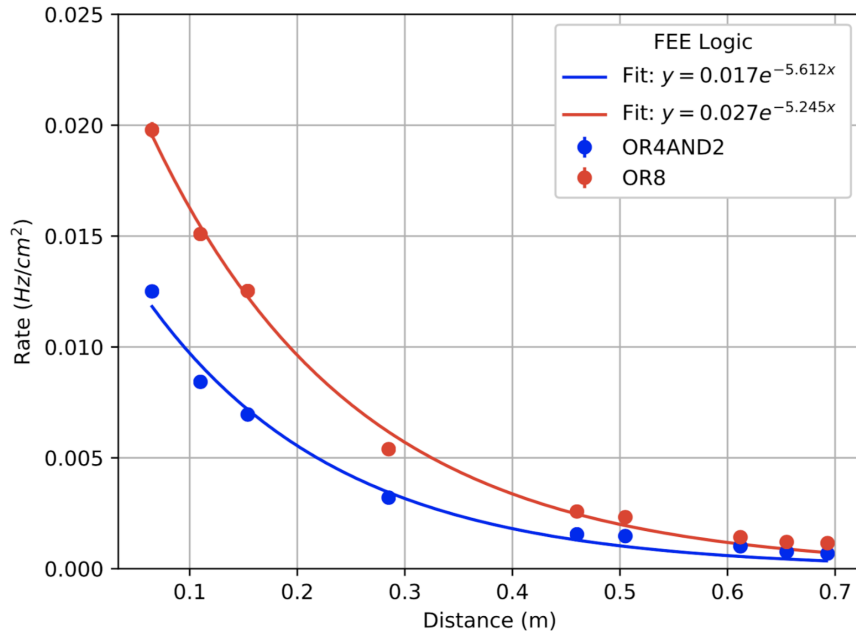


Figure 6.16: Coincidence rate of two chambers with respect to an arbitrary distance between the two top planes. Measured in 10 minutes, for 2 logical combinations (OR8 and OR4AND2). Applied high voltage: 2.65 kV. Threshold: 7 pC. Active area: readout of 160 mm x 160 mm per chamber.

2093 planes of A and C is 570 mm. It is clear the the  $\gamma$  source has an impact on chamber A rate, but  
 2094 this is negligible when we take into account the coincidence between two chambers.

2095 This two measurements were enough to validate this chambers as possible trigger pro RPC R&D  
 2096 with cosmic muons in the laboratory and at GIF++. The next steps would be use this MWPC  
 2097 chamber to implement a tracking system from triggering. This would demand some developments,  
 2098 since, due to bandwidth restrictions, the signal from each FEB would have to go to a programmable  
 2099 fast electronics, i.e. a FPGA, which would reconstruct muon tracks and provide the trigger to the  
 2100 DAQ system. This can be done by placing the two pair of chambers (AB and CD) in orthogonal  
 2101 configuration and read the signal in a CAEN V2495 board [155].

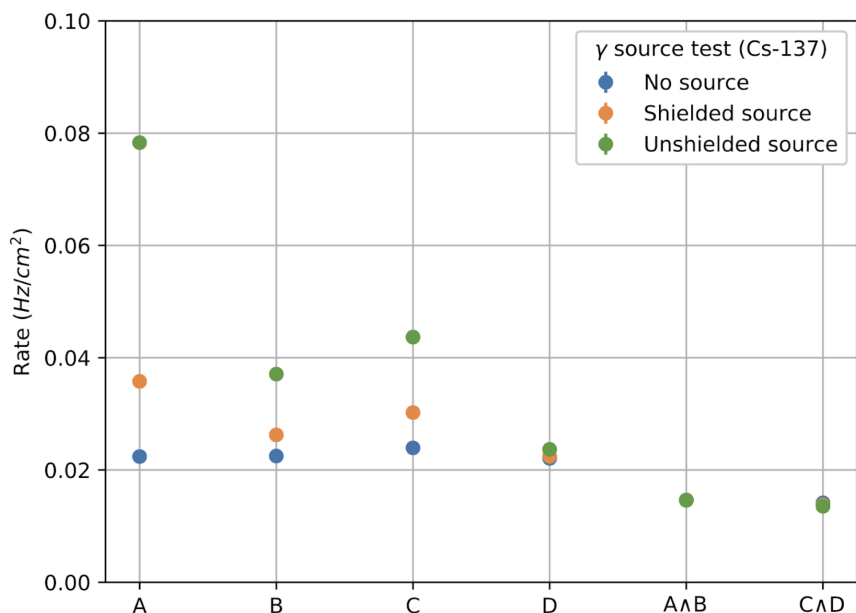


Figure 6.17: Individual rates (chambers A, B, C and D) and coincidence rates for two chambers (A AND B, C AND D), for without  $\gamma$  source (blue), a shielded  $\gamma$  source (orange) and an unshielded  $\gamma$  source (green). Source sitting on top of chamber A. Applied high voltage: 2.65 kV. Threshold: 7 pC. Active area: readout of 160 mm x 320 mm per chamber. Logical combination: AND2

## 2102 6.4.2 LS2 and the RPC Standard Maintenance

2103 In December 2018, the LS2 (Long Shutdown 2) was started. This a period in which the LHC and  
2104 its detectors (CMS included) stop their operation for maintenance and upgrade. The LS2 will go  
2105 up to 2021, when LHC and CMS restart the data taking with the Run3.

2106 During the LS2 it is being installed services for the new chambers (gas pipes, low voltage (LV), cables,  
2107 signal and control optical fibers, high voltage (HV) cable and support equipment, and HV/LV power  
2108 supplies), as well as continuity to the to the RPC R&D studies, besides the reparation of broken  
2109 elements of the present system, i.e. chamber in the barrel region which present gas leak problems,  
2110 maintenance of the LV and HV connectivity and power system, maintenance of the control system  
2111 of problematic chambers (Front-Ends boards, cabling and Distribution Boards) and the dismount  
2112 and reinstallation of four stations in the endcap (RE4) on both sides of CMS [156].

2113 What concerns the standard maintenance of the present RPC system, the main LS2 activities in  
2114 which the student was involved, can be divided in three main tasks: (a) HV maintenance, (b) LV  
2115 and control maintenance and (c) detector commissioning.

### 2116 HV maintenance

2117 A key factor of and RPC performance is the applied high voltage (HV). The CMS RPC achieve  
2118 their optimal performance with, around, 9.5 kV applied in each gap. This voltage is in the range  
2119 of the dielectric breakdown of many gases, which could lead to potential current leakages, if some  
2120 part of the system is damaged, poorly operated or badly installed. If the currents are high enough  
2121 this can make impossible the operation of the chamber. In cases like this, during the operation  
2122 period (data taking), the problematic HV channel is identified and turned off (each chamber has  
2123 two channels, one for each lawyer of gaps). Chambers in this situation are said to be operating in  
2124 single gap mode (SG).

2125 The goal for the HV maintenance is to, now that the CMS is off and the chambers are accessible,  
2126 identify which part of the HV supply system is causing the current leak and fix it the best way  
2127 possible. Usually the problem is beyond the power supply, very often connectors or the gap itself  
2128 are damaged.

2129 The CMS RPCs uses two kind of HV connectors, monopolar and tripolar connector. The monopolar  
2130 are used to connect the chamber to the power supply. If mounted properly, rarely they present  
2131 problems. The connection to the chamber is made by tripolar connectors, in which the ground and  
2132 the HV for both gaps arrives to the chamber in a single connector, for simplicity and to save space in  
2133 the patch panel. Unfortunately these connectors are relatively fragile, and they could be a potential  
2134 source of leak, specially if they were poorly mounted, badly operated or with aging itself. Also,  
2135 since this was a connector made exclusively for the CMS RPC system, some design choices had to  
2136 be improved after the installation of other chamber. Those installed with old batches of tripolar  
2137 connectors are sensitive ones. The reparation of this connectors consists in isolate the connector  
2138 from the chamber and power it up to 15 kV (maximum voltage allowed by the system). If the tested

2139 connector is broken one will observe a very fast increase in the current of the HV channel. The only  
 2140 solution to this kind of problem is to replace the connector.

2141 On the other hand, if the connector is powered isolated and pass the test, the problem beyond  
 2142 the connector (assuming that the power system have already been tested), i.e. inside the chamber.  
 2143 When a chamber is in SG mode it means that a full layer is off, but not necessarily all the gaps  
 2144 in that layer are bad (a RPC can have up to three per layer). In this situation, the procedure  
 2145 consists in cutting the cables that comes from the gaps to the chamber side connector one by one  
 2146 and identify which gap of the problematic layer is the broken by powering it. Once identified, this  
 2147 gap should isolated and the other ones reconnected. The broken gap is unrecoverable, since it is  
 2148 inside the chamber, but 5% to 10 % of efficiency can be retaken, without changing the applied HV  
 2149 and increasing the longevity of the chamber.

2150 Another contribution to the HV maintenance was the proposal of a procedure to replace the prob-  
 2151 lematic tripolar connector by a monopolar (also called jupiter) connector, which are known for being  
 2152 much more stable and reliable. The figure 6.18 (left) show the designed adapter for the chamber  
 2153 patch panel which would made this change possible. Figure 6.18 (right) shows a tryout of a cham-  
 2154 ber in which this procedure was tested. The proposal was presented to the RPC community and  
 2155 approved to be used from now on. Technical drawings and instructions were provided.

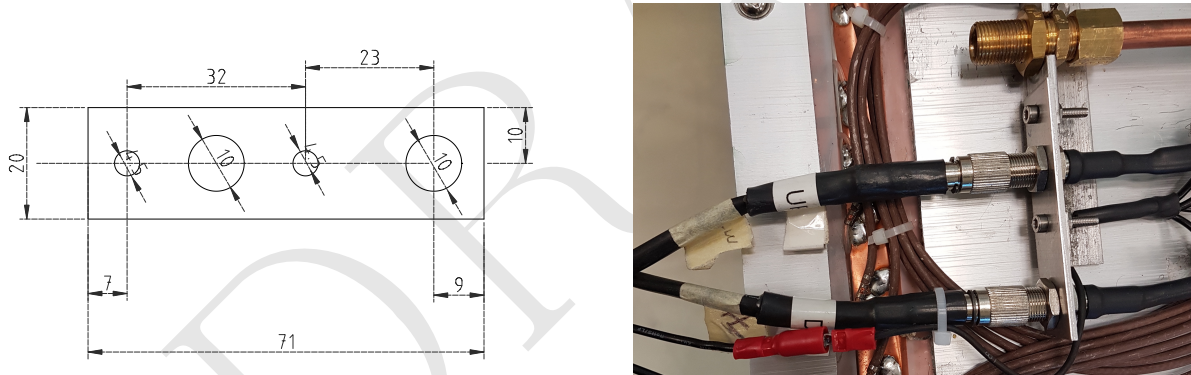


Figure 6.18: Left: Proposed adapter the chamber patch panel which make it possible to replace a tripolar by a jupiter HV connector. Right: Try out of the proposed HV connector replacement.

## 2156 LV and control maintenance

2157 The low voltage (LV) and control maintenance consists in make sure that the Front-End Boards  
 2158 (FEBs) are powered and configurable, which means that the LV power system is working from  
 2159 supply board to the cable, that the signal cables are in good state and properly connected to the  
 2160 chamber and to the link boards and that the on-detector electronics (FEBs and Distribution Boards  
 2161 - DBs) are working fine.

2162 Usually, this system is very reliable. The weak point, in most of the cases, is the detector electronics.  
 2163 When a FEB [157] (as in Figure 6.19) is problematic it can present regions of very high noise or no  
 2164 signal at all (silent), which can not be recovered by the threshold control. In cases like this, when  
 2165 the FEB is accessible, it can be replaced in order to recover efficiency in the problematic chamber.

2166 This procedure is done by extracting the chamber from inside the detector (only for barrel chamber)  
 2167 and opening its cover to have access to the problematic component. Removed boards are send back  
 2168 to production labs for refurbishment.



Figure 6.19: RPC Front-end board (FEB) used in the barrel chambers.

2169 The most usual problem is a chamber in which the threshold control was lost. For those chamber,  
 2170 most probably, the problem is in the distribution board of the chamber, which is a piece of hardware  
 2171 responsible for distribute the LV power to the FEBs (3 to 6 per chamber) and send the threshold  
 2172 control signal to the FEBs via I2C line. If a chamber has no threshold control, it means that the  
 2173 RPC operation has no control over the signal selection, which can potentially induce performance  
 2174 issues.

2175 For the barrel this maintenance happens concomitantly with the gas leak reparations on the barrel  
 2176 chamber, since both demands the chamber extraction, which is a complex procedure in terms of  
 2177 operation and demands specialized equipment and manpower. For technical reasons, the gas leak  
 2178 extractions have precedence over LV ones.

### 2179 **Detector commissioning**

2180 All the LS2 activities demands uncabling of the chamber to be repaired and possibly some neighbor  
 2181 chambers. Also, it can involve the replacement of components of the chamber. To avoid damage to  
 2182 the system a compromising procedure is needed after all this activities. Given the responsibilities  
 2183 of the commissioning it was necessary to: (a) make sure that the the RPC system keep tracks of all  
 2184 the interventions, (b) maintain all the algorithms used in the commissioning procedure, (c) together  
 2185 with the RPC Coordination, define a pool of people and a schedule to the commissioning of the  
 2186 system and (d) follow-up, with other CMS RPC experts, the availability of materials and resources  
 2187 for the commissioning operations.

2188 Besides the organizational tasks, the commissioning demanded to establish procedures to ensure the  
 2189 connectivity and functionality of HV and LV connections. For the HV, it is needed to make sure  
 2190 that the chambers are properly connected, without miscabling <sup>4</sup> and that the currents at stand-by

---

<sup>4</sup>Mixed cable connections.

2191 HV and working point HV are compatible with the ones in the end of last data-taking (end of  
 2192 2018). This activity will start in November/2019, when the CMS RPC Standard Gas Mixture will  
 2193 be available again.

2194 For the LV point of view, the LV power cable and signal cables should also be properly connected,  
 2195 and presenting a noise profile compatible with last data-taking. One key point for this task is to  
 2196 make sure that there are no miscabling of signal cable. One RPC chamber can have from 6  
 2197 to 18 signal cable, which are connected very close one to another. There is a good chance that a  
 2198 chamber, after reparation, have its signal cables mixed. In order to diagnose situations like this, it  
 2199 was validated a algorithm present in the RPC Online Software, but never used since LS1, which,  
 2200 by changing the threshold of each component of the RPC system, from very high to very low values  
 2201 (component by component), can spot miscabled chambers. Since the control line is independent of  
 2202 the signal line, a misclabeled will present a different noise from what is expected.

2203 Besides the validation of this algorithm, it was also implemented a web system (Figure 6.20),  
 2204 developed in Flask [158] which automatize the execution of the algorithm, making transparent to the  
 2205 shifter (or the one performing the commissioning) the procedure to get miscabling report.

#### FEB Connectivity Test - Analysis

Worker	Date (YY-MM-DD)	Time (HH:MM:SS)	Hash	
RBP2_Far	2019-06-20	23:43:19	387534dst	<a href="#">Run Analyzer</a>
RBP1_Far	2019-06-20	20:12:20	458306dst	<a href="#">Run Analyzer</a>
RBP1_Far	2019-06-20	20:04:46	336162dst	<a href="#">Run Analyzer</a>
RBP1_Near	2019-06-20	19:02:00	377883dst	<a href="#">Run Analyzer</a>
RBP1_Near	2019-06-19	18:59:00	858950dst	<a href="#">Run Analyzer</a>
RBP1_Far	2019-06-19	18:58:26	994787dst	<a href="#">Run Analyzer</a>
YEN3_Far	2019-05-07	10:28:23	176278dst	<a href="#">Run Analyzer</a>
YEN3_Near	2019-05-07	10:28:08	347504dst	<a href="#">Run Analyzer</a>
YEN1_Far	2018-12-07	15:03:24	575561	<a href="#">Run Analyzer</a>
RBO_Far	2018-12-07	14:45:42	101463	<a href="#">Run Analyzer</a>
RBP1_Far	2018-12-07	09:12:00	477689	<a href="#">Run Analyzer</a>

Figure 6.20: RPC FEB Commissioning Analyzer.

2206 The LV commissioning is ongoing, since it happens, as much as possible, right after the chamber  
 2207 reparation.

# Bibliography

- [1] Stephen Myers. “The LEP collider, from design to approval and commissioning”. In: (Oct. 1991). DOI: 10.5170/CERN-1991-008.
- [2] S. Chatrchyan et al. “The CMS experiment at the CERN LHC”. In: *JINST* 3 (2008), S08004. DOI: 10.1088/1748-0221/3/08/S08004.
- [3] The ATLAS Collaboration et al. “The ATLAS Experiment at the CERN Large Hadron Collider”. In: *Journal of Instrumentation* 3.08 (Aug. 2008), S08003–S08003. DOI: 10.1088/1748-0221/3/08/s08003. URL: <https://doi.org/10.1088%2F1748-0221%2F3%2F08%2Fs08003>.
- [4] Serguei Chatrchyan et al. “Observation of a new boson at a mass of 125 GeV with the CMS experiment at the LHC”. In: *Phys. Lett. B* 716 (2012), pp. 30–61. DOI: 10.1016/j.physletb.2012.08.021. arXiv: 1207.7235 [hep-ex].
- [5] G. Aad et al. “Observation of a new particle in the search for the Standard Model Higgs boson with the ATLAS detector at the LHC”. In: *Physics Letters B* 716.1 (2012), pp. 1–29. ISSN: 0370-2693. DOI: <https://doi.org/10.1016/j.physletb.2012.08.020>. URL: <http://www.sciencedirect.com/science/article/pii/S037026931200857X>.
- [6] NobelPrize.org. *The Nobel Prize in Physics 2013*. 2013. URL: <https://www.nobelprize.org/prizes/physics/2013/summary/>.
- [7] CMS Collaboration. *Dimuon spectrum 2015*. Tech. rep. CMS-DP-2015-055. Dec. 2015. URL: <http://cds.cern.ch/record/2115428>.
- [8] Cliff Burgess and Guy Moore. *The Standard Model: A Primer*. Cambridge University Press, 2006. DOI: 10.1017/CBO9780511819698.
- [9] M. Anselmino et al. *Introdução à QCD Perturbativa*. LTC, 2013. ISBN: 9788521622994.
- [10] F. Halzen and Alan D. Martin. *QUARKS AND LEPTONS: AN INTRODUCTORY COURSE IN MODERN PARTICLE PHYSICS*. Jan. 1984. ISBN: 978-0-471-88741-6.
- [11] I.J.R. Aitchison and A.J.G. Hey. *Gauge theories in particle physics: A practical introduction. Vol. 2: Non-Abelian gauge theories: QCD and the electroweak theory*. CRC Press, 2012. ISBN: 978-1-4665-1307-5.
- [12] Wikimedia Commons. *Standard Model*. 2020. URL: [https://en.wikipedia.org/wiki/File:Standard\\_Model\\_of\\_Elementary\\_Particles.svg](https://en.wikipedia.org/wiki/File:Standard_Model_of_Elementary_Particles.svg).
- [13] Particle Data Group et al. “Review of Particle Physics”. In: *Progress of Theoretical and Experimental Physics* 2020.8 (Aug. 2020). 083C01. ISSN: 2050-3911. DOI: 10.1093/ptep/ptaa104. eprint: <https://academic.oup.com/ptep/article-pdf/2020/8/083C01/33653179/ptaa104.pdf>. URL: <https://doi.org/10.1093/ptep/ptaa104>.

- [14] A. Salam and J. C. Ward. “On a gauge theory of elementary interactions”. In: *Il Nuovo Cimento (1955-1965)* 19.1 (1961), pp. 165–170. DOI: 10.1007/BF02812723. URL: <https://doi.org/10.1007/BF02812723>.
- [15] RH Dalitz. *Proceedings of the XIIIth International Conference on High Energy Physics*. 1967.
- [16] Wolfgang Ochs. “The Status of Glueballs”. In: *J. Phys. G* 40 (2013), p. 043001. DOI: 10.1088/0954-3899/40/4/043001. arXiv: 1301.5183 [hep-ph].
- [17] F. Abe et al. “Observation of top quark production in  $\bar{p}p$  collisions”. In: *Phys. Rev. Lett.* 74 (1995), pp. 2626–2631. DOI: 10.1103/PhysRevLett.74.2626. arXiv: hep-ex/9503002.
- [18] S. Abachi et al. “Observation of the top quark”. In: *Phys. Rev. Lett.* 74 (1995), pp. 2632–2637. DOI: 10.1103/PhysRevLett.74.2632. arXiv: hep-ex/9503003.
- [19] John Ellis. “Outstanding questions: physics beyond the Standard Model”. In: *Philosophical Transactions of the Royal Society A: Mathematical, Physical and Engineering Sciences* 370.1961 (2012), pp. 818–830. DOI: 10.1098/rsta.2011.0452. eprint: <https://royalsocietypublishing.org/doi/pdf/10.1098/rsta.2011.0452>. URL: <https://royalsocietypublishing.org/doi/abs/10.1098/rsta.2011.0452>.
- [20] CMS Collaboration. *Summary of the cross section measurements of Standard Model processes*. 2020. URL: <https://twiki.cern.ch/twiki/bin/view/CMSPublic/PhysicsResultsCombined> (visited on 08/21/2020).
- [21] M. Baak et al. “The global electroweak fit at NNLO and prospects for the LHC and ILC”. In: *Eur. Phys. J. C* 74 (2014), p. 3046. DOI: 10.1140/epjc/s10052-014-3046-5. arXiv: 1407.3792 [hep-ph].
- [22] LHC Higgs Cross Section Working Group. “Handbook of LHC Higgs Cross Sections: 4. Deciphering the Nature of the Higgs Sector”. In: (2016). DOI: 10.23731/CYRM-2017-002. arXiv: 1610.07922 [hep-ph].
- [23] Albert M Sirunyan et al. “Combined measurements of Higgs boson couplings in proton–proton collisions at  $\sqrt{s} = 13\text{ TeV}$ ”. In: *Eur. Phys. J. C* 79.5 (2019), p. 421. DOI: 10.1140/epjc/s10052-019-6909-y. arXiv: 1809.10733 [hep-ex].
- [24] A. M. Sirunyan et al. “Observation of Higgs boson decay to bottom quarks”. In: *Phys. Rev. Lett.* 121.12 (2018), p. 121801. DOI: 10.1103/PhysRevLett.121.121801. arXiv: 1808.08242 [hep-ex].
- [25] CMS Collaboration. *Measurement of Higgs boson decay to a pair of muons in proton-proton collisions at  $\sqrt{s} = 13\text{ TeV}$* . CMS Physics Analysis Summary CMS-PAS-HIG-19-006. 2019. URL: <http://cdsweb.cern.ch/record/1279362>.
- [26] Albert M Sirunyan et al. “Observation of the Higgs boson decay to a pair of  $\tau$  leptons with the CMS detector”. In: *Phys. Lett. B* 779 (2018), pp. 283–316. DOI: 10.1016/j.physletb.2018.02.004. arXiv: 1708.00373 [hep-ex].
- [27] Albert M Sirunyan et al. “A search for the standard model Higgs boson decaying to charm quarks”. In: *JHEP* 03 (2020), p. 131. DOI: 10.1007/JHEP03(2020)131. arXiv: 1912.01662 [hep-ex].
- [28] Albert M Sirunyan et al. “Measurement and interpretation of differential cross sections for Higgs boson production at  $\sqrt{s} = 13\text{ TeV}$ ”. In: *Phys. Lett. B* 792 (2019), pp. 369–396. DOI: 10.1016/j.physletb.2019.03.059. arXiv: 1812.06504 [hep-ex].

- [2284] [29] Albert M Sirunyan et al. “Measurement of the inclusive and differential Higgs boson production cross sections in the leptonic WW decay mode at  $\sqrt{s} = 13$  TeV”. In: (July 2020). DOI: 10.3204/PUBDB-2020-02624. arXiv: 2007.01984 [hep-ex].
- [2285]
- [2286]
- [2287] [30] Albert M Sirunyan et al. “A measurement of the Higgs boson mass in the diphoton decay channel”. In: *Phys. Lett. B* 805 (2020), p. 135425. DOI: 10.1016/j.physletb.2020.135425. arXiv: 2002.06398 [hep-ex].
- [2288]
- [2289]
- [2290] [31] M. Spira et al. “Higgs boson production at the LHC”. In: *Nucl. Phys. B* 453 (1995), pp. 17–82. DOI: 10.1016/0550-3213(95)00379-7. arXiv: hep-ph/9504378.
- [2291]
- [2292] [32] CMS Collaboration. *List of CMS Higgs publications*. 2020. URL: <http://cms-results.web.cern.ch/cms-results/public-results/publications/HIG/index.html> (visited on 08/21/2020).
- [2293]
- [2294]
- [2295] [33] CMS Collaboration. *List of CMS Higgs public results*. 2020. URL: <http://cms-results.web.cern.ch/cms-results/public-results/preliminary-results/HIG/index.html> (visited on 08/21/2020).
- [2296]
- [2297]
- [2298] [34] CMS Collaboration. *Combined Higgs boson production and decay measurements with up to 137 fb-1 of proton-proton collision data at  $\sqrt{s} = 13$  TeV*. CMS Physics Analysis Summary CMS-PAS-HIG-19-005. 2019. URL: <http://cdsweb.cern.ch/record/1279362>.
- [2299]
- [2300]
- [2301] [35] L.D. Landau. “On the angular momentum of a system of two photons”. In: *Dokl. Akad. Nauk SSSR* 60.2 (1948), pp. 207–209. DOI: 10.1016/B978-0-08-010586-4.50070-5.
- [2302]
- [2303] [36] Chen-Ning Yang. “Selection Rules for the Dematerialization of a Particle Into Two Photons”. In: *Phys. Rev.* 77 (1950), pp. 242–245. DOI: 10.1103/PhysRev.77.242.
- [2304]
- [2305] [37] CMS Collaboration. *List of CMS Higgs publications involving spin-parity tests*. 2020. URL: <http://cms-results.web.cern.ch/cms-results/public-results/publications/HIG/SPIN.html> (visited on 08/21/2020).
- [2306]
- [2307]
- [2308] [38] Geoffrey Bodwin et al. “Higgs boson decays to quarkonia and the  $H\bar{c}c$  coupling”. In: *Phys. Rev. D* 88 (5 Sept. 2013), p. 053003. DOI: 10.1103/PhysRevD.88.053003. URL: <https://link.aps.org/doi/10.1103/PhysRevD.88.053003>.
- [2309]
- [2310]
- [2311] [39] Geoffrey T. Bodwin et al. “Relativistic corrections to Higgs boson decays to quarkonia”. In: *Phys. Rev. D* 90 (11 Dec. 2014), p. 113010. DOI: 10.1103/PhysRevD.90.113010. URL: <https://link.aps.org/doi/10.1103/PhysRevD.90.113010>.
- [2312]
- [2313]
- [2314] [40] G. Aad, B. Abbott, et al. “Combined Measurement of the Higgs Boson Mass in  $pp$  Collisions at  $\sqrt{s} = 7$  and 8 TeV with the ATLAS and CMS Experiments”. In: *Phys. Rev. Lett.* 114 (19 May 2015), p. 191803. DOI: 10.1103/PhysRevLett.114.191803. URL: <https://link.aps.org/doi/10.1103/PhysRevLett.114.191803>.
- [2315]
- [2316]
- [2317]
- [2318] [41] Cédric Delaunay et al. “Enhanced Higgs boson coupling to charm pairs”. In: *Phys. Rev. D* 89 (3 Feb. 2014), p. 033014. DOI: 10.1103/PhysRevD.89.033014. URL: <https://link.aps.org/doi/10.1103/PhysRevD.89.033014>.
- [2319]
- [2320]
- [2321] [42] M. A. PÉREZ, G. TAVARES-VELASCO, and J. J. TOSCANO. “NEW PHYSICS EFFECTS IN RARE Z DECAYS”. In: *International Journal of Modern Physics A* 19.02 (2004), pp. 159–178. DOI: 10.1142/S0217751X04017100.
- [2322]
- [2323]
- [2324] [43] Grossman, Yuval and König, Matthias and Neubert, Matthias. “Exclusive radiative decays of W and Z bosons in QCD factorization”. In: *Journal of High Energy Physics* 2015.4 (Apr. 2325)

- 2326 2015), p. 101. ISSN: 1029-8479. DOI: 10.1007/JHEP04(2015)101. URL: [https://doi.org/10.1007/JHEP04\(2015\)101](https://doi.org/10.1007/JHEP04(2015)101).
- 2327 [44] Geoffrey T. Bodwin et al. “ $Z$ -boson decays to a vector quarkonium plus a photon”. In: *Phys.*  
2328 *Rev. D* 97 (1 Jan. 2018), p. 016009. DOI: 10.1103/PhysRevD.97.016009. URL: <https://link.aps.org/doi/10.1103/PhysRevD.97.016009>.
- 2329 [45] Geoffrey T. Bodwin et al. “Addendum: New approach to the resummation of logarithms in  
2330 Higgs-boson decays to a vector quarkonium plus a photon [Phys. Rev. D 95, 054018 (2017)]”.  
2331 In: *Phys. Rev. D* 96 (11 Dec. 2017), p. 116014. DOI: 10.1103/PhysRevD.96.116014. URL:  
2332 <https://link.aps.org/doi/10.1103/PhysRevD.96.116014>.
- 2333 [46] Gino Isidori, Aneesh V. Manohar, and Michael Trott. “Probing the nature of the Higgs-like  
2334 boson via  $h \rightarrow Vf$  decays”. In: *Physics Letters B* 728 (2014), pp. 131–135. ISSN: 0370-  
2335 2693. DOI: <https://doi.org/10.1016/j.physletb.2013.11.054>. URL: <http://www.sciencedirect.com/science/article/pii/S037026931300960X>.
- 2336 [47] Alexander L. Kagan et al. “Exclusive Window onto Higgs Yukawa Couplings”. In: *Phys.*  
2337 *Rev. Lett.* 114 (10 Mar. 2015), p. 101802. DOI: 10.1103/PhysRevLett.114.101802. URL:  
2338 <https://link.aps.org/doi/10.1103/PhysRevLett.114.101802>.
- 2339 [48] Dao-Neng Gao. “A note on Higgs decays into  $Z$  boson and  $J/\psi(\Upsilon)$ ”. In: *Physics Letters B* 737  
2340 (2014), pp. 366–368. ISSN: 0370-2693. DOI: <https://doi.org/10.1016/j.physletb.2014.09.019>. URL: <http://www.sciencedirect.com/science/article/pii/S0370269314006698>.
- 2341 [49] A. M. Sirunyan et al. “Observation of Higgs Boson Decay to Bottom Quarks”. In: *Phys.*  
2342 *Rev. Lett.* 121 (12 Sept. 2018), p. 121801. DOI: 10.1103/PhysRevLett.121.121801. URL:  
2343 <https://link.aps.org/doi/10.1103/PhysRevLett.121.121801>.
- 2344 [50] G Apollinari et al. *High-Luminosity Large Hadron Collider (HL-LHC): Preliminary Design*  
2345 *Report*. CERN Yellow Reports: Monographs. Geneva: CERN, 2015. DOI: 10.5170/CERN-  
2346 2015-005. URL: <https://cds.cern.ch/record/2116337>.
- 2347 [51] G. Aad et al. “Search for Higgs and  $Z$  Boson Decays to  $J/\psi\gamma$  and  $\Upsilon(nS)\gamma$  with the ATLAS  
2348 Detector”. In: *Phys. Rev. Lett.* 114 (12 Mar. 2015), p. 121801. DOI: 10.1103/PhysRevLett.  
2349 114.121801. URL: <https://link.aps.org/doi/10.1103/PhysRevLett.114.121801>.
- 2350 [52] Morad Aaboud et al. “Searches for exclusive Higgs and  $Z$  boson decays into  $J/\psi\gamma$ ,  $\psi(2S)\gamma$ ,  
2351 and  $\Upsilon(nS)\gamma$  at  $\sqrt{s} = 13$  TeV with the ATLAS detector”. In: *Phys. Lett. B* 786 (2018),  
2352 pp. 134–155. DOI: 10.1016/j.physletb.2018.09.024. arXiv: 1807.00802 [hep-ex].
- 2353 [53] S. Chatrchyan et al. “The CMS experiment at the CERN LHC”. In: *JINST* 3 (2008), S08004.  
2354 DOI: 10.1088/1748-0221/3/08/S08004.
- 2355 [54] Albert M Sirunyan et al. “Search for rare decays of  $Z$  and Higgs bosons to  $J/\psi$  and a photon  
2356 in proton-proton collisions at  $\sqrt{s} = 13$  TeV”. In: *Eur. Phys. J. C* 79.2 (2019), p. 94. DOI:  
2357 10.1140/epjc/s10052-019-6562-5. arXiv: 1810.10056 [hep-ex].
- 2358 [55] Albert M Sirunyan et al. “Search for Higgs and  $Z$  boson decays to  $J/\psi$  or  $\Upsilon$  pairs in proton-  
2359 proton collisions at  $\sqrt{s} = 13$  TeV”. In: *Phys. Lett. B* 797. arXiv: 1905.10408. CMS-HIG-18-025-  
2360 003 (May 2019). All figures and tables can be found at [http://cms-results.web.cern.ch/cms-results/public-results/publications/HIG-18-025](http://cms-results.web.cern.ch/cms-<br/>2361 results/public-results/publications/HIG-18-025) (CMS Public Pages), 134811. 31 p. DOI: 10.  
2362 1016/j.physletb.2019.134811. URL: <https://cds.cern.ch/record/2676242>.

- [56] Albert M. Sirunyan et al. “Observation of the  $Z \rightarrow \psi\ell^+\ell^-$  decay in pp collisions at  $\sqrt{s} = 13$  TeV”. In: *Phys. Rev. Lett.* 121.arXiv:1806.04213. CMS-BPH-16-001-003 (June 2018). Submitted to Phys.Rev.Lett., 141801. 17 p. DOI: 10.1103/PhysRevLett.121.141801. URL: <https://cds.cern.ch/record/2623687>.
- [57] Albert M Sirunyan et al. “Search for decays of the 125 GeV Higgs boson into a Z boson and a  $\rho$  or  $\phi$  meson”. In: (July 2020). DOI: 10.3204/PUBDB-2020-02812. arXiv: 2007.05122 [hep-ex].
- [58] “LHC Machine”. In: *JINST* 3 (2008). Ed. by Lyndon Evans and Philip Bryant, S08001. DOI: 10.1088/1748-0221/3/08/S08001.
- [59] Oliver Sim Brüning et al. *LHC Design Report*. CERN Yellow Reports: Monographs. Geneva: CERN, 2004. DOI: 10.5170/CERN-2004-003-V-1. URL: <http://cds.cern.ch/record/782076>.
- [60] Oliver Sim Brüning et al. *LHC Design Report*. CERN Yellow Reports: Monographs. Geneva: CERN, 2004. DOI: 10.5170/CERN-2004-003-V-2. URL: <http://cds.cern.ch/record/815187>.
- [61] Michael Benedikt et al. *LHC Design Report*. CERN Yellow Reports: Monographs. Geneva: CERN, 2004. DOI: 10.5170/CERN-2004-003-V-3. URL: <http://cds.cern.ch/record/823808>.
- [62] Christiane Lefèvre. “The CERN accelerator complex. Complexe des accélérateurs du CERN”. Dec. 2008. URL: <http://cds.cern.ch/record/1260465>.
- [63] S Baird. *Accelerators for pedestrians; rev. version*. Tech. rep. AB-Note-2007-014. CERN-AB-Note-2007-014. PS-OP-Note-95-17-Rev-2. CERN-PS-OP-Note-95-17-Rev-2. Geneva: CERN, Feb. 2007. URL: <http://cds.cern.ch/record/1017689>.
- [64] Jr. Alves A.Augusto et al. “The LHCb Detector at the LHC”. In: *JINST* 3 (2008), S08005. DOI: 10.1088/1748-0221/3/08/S08005.
- [65] K. Aamodt et al. “The ALICE experiment at the CERN LHC”. In: *JINST* 3 (2008), S08002. DOI: 10.1088/1748-0221/3/08/S08002.
- [66] “High-Luminosity Large Hadron Collider (HL-LHC): Technical Design Report V. 0.1”. In: 4/2017 (Nov. 2017). Ed. by G. Apollinari et al. DOI: 10.23731/CYRM-2017-004.
- [67] Tai Sakuma. “Cutaway diagrams of CMS detector”. In: (May 2019). URL: <http://cds.cern.ch/record/2665537>.
- [68] Serguei Chatrchyan et al. “Description and performance of track and primary-vertex reconstruction with the CMS tracker”. In: *JINST* 9 (2014), P10009. DOI: 10.1088/1748-0221/9/10/P10009. arXiv: 1405.6569 [physics.ins-det].
- [69] Vardan Khachatryan et al. “Performance of electron reconstruction and selection with the CMS detector in proton-proton collisions at  $\sqrt{s} = 8$  TeV”. In: *JINST* 10 (2015), P06005. DOI: 10.1088/1748-0221/10/06/P06005. arXiv: 1502.02701 [physics.ins-det].
- [70] Vardan Khachatryan et al. “Performance of photon reconstruction and identification with the CMS detector in proton-proton collisions at  $\sqrt{s} = 8$  TeV”. In: *JINST* 10 (2015), P08010. DOI: 10.1088/1748-0221/10/08/P08010. arXiv: 1502.02702 [physics.ins-det].

- [71] Matteo Cacciari, Gavin P. Salam, and Gregory Soyez. “The anti- $k_t$  jet clustering algorithm”. In: *JHEP* 04 (2008), p. 063. DOI: 10.1088/1126-6708/2008/04/063. arXiv: 0802.1189 [hep-ex].
- [72] Matteo Cacciari, Gavin P. Salam, and Gregory Soyez. “FastJet User Manual”. In: *Eur. Phys. J.* C72 (2012), p. 1896. DOI: 10.1140/epjc/s10052-012-1896-2. arXiv: 1111.6097 [hep-ph].
- [73] *The CMS muon project: Technical Design Report*. Technical Design Report CMS. Geneva: CERN, 1997. URL: <https://cds.cern.ch/record/343814>.
- [74] A M Sirunyan et al. “Performance of the CMS muon detector and muon reconstruction with proton-proton collisions at  $\sqrt{s} = 13$  TeV”. In: *JINST* 13 (2018), P06015. DOI: 10.1088/1748-0221/13/06/P06015. arXiv: 1804.04528 [physics.ins-det].
- [75] Serguei Chatrchyan et al. “The Performance of the CMS Muon Detector in Proton-Proton Collisions at  $\sqrt{s} = 7$  TeV at the LHC”. In: *JINST* 8 (2013), P11002. DOI: 10.1088/1748-0221/8/11/P11002. arXiv: 1306.6905 [physics.ins-det].
- [76] Fabio Sauli. “The gas electron multiplier (GEM): Operating principles and applications. The gas electron multiplier (GEM): Operating principles and applications”. In: *Nucl. Instrum. Methods Phys. Res., A* 805 (2016), 2–24. 23 p. DOI: 10.1016/j.nima.2015.07.060. URL: <http://cds.cern.ch/record/2262884>.
- [77] Daniel Francois Teyssier. *CMS Drift Tubes performance*. Tech. rep. 2016, pp. 709–713.
- [78] Vardan Khachatryan et al. “The CMS trigger system”. In: *JINST* 12 (2017), P01020. DOI: 10.1088/1748-0221/12/01/P01020. arXiv: 1609.02366 [physics.ins-det].
- [79] A. M. Sirunyan et al. “Particle-flow reconstruction and global event description with the CMS detector”. In: *JINST* 12 (2017), P10003. DOI: 10.1088/1748-0221/12/10/P10003. arXiv: 1706.04965 [physics.ins-det].
- [80] Vardan Khachatryan et al. “Jet energy scale and resolution in the CMS experiment in pp collisions at 8 TeV”. In: *JINST* 12 (2017), P02014. DOI: 10.1088/1748-0221/12/02/P02014. arXiv: 1607.03663 [hep-ex].
- [81] Albert M Sirunyan et al. “Performance of missing transverse momentum reconstruction in proton-proton collisions at  $\sqrt{s} = 13$  TeV using the CMS detector”. In: *JINST* 14 (2019), P07004. DOI: 10.1088/1748-0221/14/07/P07004. arXiv: 1903.06078 [hep-ex].
- [82] Jesse Thaler and Ken Van Tilburg. “Identifying Boosted Objects with  $N$ -subjettiness”. In: *JHEP* 03 (2011), p. 015. DOI: 10.1007/JHEP03(2011)015. arXiv: 1011.2268 [hep-ph].
- [83] Mrinal Dasgupta et al. “Towards an understanding of jet substructure”. In: *JHEP* 09 (2013), p. 029. DOI: 10.1007/JHEP09(2013)029. arXiv: 1307.0007 [hep-ph].
- [84] Jonathan M. Butterworth et al. “Jet substructure as a new Higgs search channel at the LHC”. In: *Phys. Rev. Lett.* 100 (2008), p. 242001. DOI: 10.1103/PhysRevLett.100.242001. arXiv: 0802.2470 [hep-ph].
- [85] Andrew J. Larkoski et al. “Soft drop”. In: *JHEP* 05 (2014), p. 146. DOI: 10.1007/JHEP05(2014)146. arXiv: 1402.2657 [hep-ph].
- [86] Albert M Sirunyan et al. “Pileup mitigation at CMS in 13 TeV data”. In: *JINST* 15 (2020), P09018. DOI: 10.1088/1748-0221/15/09/p09018. arXiv: 2003.00503 [hep-ex].

- [87] CMS Collaboration. *CMS Luminosity Measurements for the 2016 Data Taking Period*. CMS Physics Analysis Summary CMS-PAS-LUM-17-001. 2010. URL: <http://cdsweb.cern.ch/record/1279362>.
- [88] S. Agostinelli et al. “GEANT4—a simulation toolkit”. In: A506 (2003), pp. 250–303. DOI: 10.1016/S0168-9002(03)01368-8.
- [89] Paolo Nason. “A New method for combining NLO QCD with shower Monte Carlo algorithms”. In: *JHEP* 11 (2004), p. 040. DOI: 10.1088/1126-6708/2004/11/040. arXiv: hep-ph/0409146 [hep-ph].
- [90] Stefano Frixione, Paolo Nason, and Carlo Oleari. “Matching NLO QCD computations with Parton Shower simulations: the POWHEG method”. In: *JHEP* 11 (2007), p. 070. DOI: 10.1088/1126-6708/2007/11/070. arXiv: 0709.2092 [hep-ph].
- [91] Simone Alioli et al. “A general framework for implementing NLO calculations in shower Monte Carlo programs: the POWHEG BOX”. In: *JHEP* 06 (2010), p. 043. DOI: 10.1007/JHEP06(2010)043. arXiv: 1002.2581 [hep-ph].
- [92] Abdelhak Djouadi. “The anatomy of electroweak symmetry breaking: Tome I: The Higgs boson in the Standard Model”. In: *Physics Reports* 457.1 (2008), pp. 1–216. ISSN: 0370-1573. DOI: <https://doi.org/10.1016/j.physrep.2007.10.004>. URL: <http://www.sciencedirect.com/science/article/pii/S0370157307004334>.
- [93] Torbjörn Sjöstrand, Stephen Mrenna, and Peter Skands. “A brief introduction to PYTHIA 8.1”. In: *Computer Physics Communications* 178.11 (2008), pp. 852–867. ISSN: 0010-4655. DOI: <https://doi.org/10.1016/j.cpc.2008.01.036>. URL: <http://www.sciencedirect.com/science/article/pii/S0010465508000441>.
- [94] Torbjörn Sjöstrand et al. “An Introduction to PYTHIA 8.2”. In: *Comput. Phys. Commun.* 191 (2015), pp. 159–177. DOI: 10.1016/j.cpc.2015.01.024. arXiv: 1410.3012 [hep-ph].
- [95] Vardan Khachatryan et al. “Event generator tunes obtained from underlying event and multiparton scattering measurements”. In: *Eur. Phys. J. C* 76.3 (2016), p. 155. DOI: 10.1140/epjc/s10052-016-3988-x. arXiv: 1512.00815 [hep-ex].
- [96] The NNPDF collaboration et al. “Parton distributions for the LHC run II”. In: *Journal of High Energy Physics* 2015.4 (Apr. 2015), p. 40. ISSN: 1029-8479. DOI: 10.1007/JHEP04(2015)040. URL: [https://doi.org/10.1007/JHEP04\(2015\)040](https://doi.org/10.1007/JHEP04(2015)040).
- [97] J. Alwall et al. “The automated computation of tree-level and next-to-leading order differential cross sections, and their matching to parton shower simulations”. In: *Journal of High Energy Physics* 2014.7 (July 2014), p. 79. ISSN: 1029-8479. DOI: 10.1007/JHEP07(2014)079. URL: [https://doi.org/10.1007/JHEP07\(2014\)079](https://doi.org/10.1007/JHEP07(2014)079).
- [98] Ali Abbasabadi et al. “Radiative Higgs boson decays  $H \rightarrow f\bar{f}\gamma$ ”. In: *Phys. Rev. D* 55 (9 May 1997), pp. 5647–5656. DOI: 10.1103/PhysRevD.55.5647. URL: <https://link.aps.org/doi/10.1103/PhysRevD.55.5647>.
- [99] D. de Florian et al. *Handbook of LHC Higgs Cross Sections: 4. Deciphering the Nature of the Higgs Sector*. CERN Yellow Reports: Monographs. 869 pages, 295 figures, 248 tables and 1645 citations. Working Group web page: <https://twiki.cern.ch/twiki/bin/view/LHCPhysics/LHCHXSWG>. Oct. 2016. DOI: 10.23731/CYRM-2017-002. URL: <https://cds.cern.ch/record/2227475>.

- [100] Ye Li and Frank Petriello. “Combining QCD and electroweak corrections to dilepton production in the framework of the FEWZ simulation code”. In: *Phys. Rev. D* 86 (9 Nov. 2012), p. 094034. DOI: 10.1103/PhysRevD.86.094034. URL: <https://link.aps.org/doi/10.1103/PhysRevD.86.094034>.
- [101] John M. Campbell and R.K. Ellis. “MCFM for the Tevatron and the LHC”. In: *Nuclear Physics B - Proceedings Supplements* 205-206 (2010). Loops and Legs in Quantum Field Theory, pp. 10–15. ISSN: 0920-5632. DOI: <https://doi.org/10.1016/j.nuclphysbps.2010.08.011>. URL: <http://www.sciencedirect.com/science/article/pii/S0920563210001945>.
- [102] Vardan Khachatryan et al. “Search for a Higgs boson decaying into  $\gamma^*\gamma \rightarrow \ell\ell\gamma$  with low dilepton mass in pp collisions at  $\sqrt{s} = 8$  TeV”. In: *Phys. Lett. B* 753 (2016), pp. 341–362. DOI: 10.1016/j.physletb.2015.12.039. arXiv: 1507.03031 [hep-ex].
- [103] N. Brambilla, S. Eidelman, B.K. Heltsley, et al. “Heavy quarkonium: progress, puzzles, and opportunities”. In: *The European Physical Journal C* 71.2 (Feb. 2011), p. 1534. ISSN: 1434-6052. DOI: 10.1140/epjc/s10052-010-1534-9. URL: <https://doi.org/10.1140/epjc/s10052-010-1534-9>.
- [104] Sandro Palestini. “Angular distribution and rotations of frame in vector meson decays into lepton pairs”. In: *Phys. Rev. D* 83 (3 Feb. 2011), p. 031503. DOI: 10.1103/PhysRevD.83.031503. URL: <https://link.aps.org/doi/10.1103/PhysRevD.83.031503>.
- [105] A.M. Sirunyan et al. “Particle-flow reconstruction and global event description with the CMS detector”. In: *Journal of Instrumentation* 12.10 (2017), P10003. URL: <http://stacks.iop.org/1748-0221/12/i=10/a=P10003>.
- [106] Albert M Sirunyan et al. “Measurements of properties of the Higgs boson decaying into the four-lepton final state in pp collisions at  $\sqrt{s} = 13$  TeV”. In: *JHEP* 11 (2017), p. 047. DOI: 10.1007/JHEP11(2017)047. arXiv: 1706.09936 [hep-ex].
- [107] V. Khachatryan et al. “Observation of the diphoton decay of the Higgs boson and measurement of its properties”. In: *The European Physical Journal C* 74.10 (Oct. 2014), p. 3076. ISSN: 1434-6052. DOI: 10.1140/epjc/s10052-014-3076-z. URL: <https://doi.org/10.1140/epjc/s10052-014-3076-z>.
- [108] S. Bernstein. “Démonstration du théorème de Weierstrass fondée sur le calcul des probabilités”. In: *Commun. Soc. Math. Kharkov* 13.1–2 (1912).
- [109] John Erthal Gaiser. “Charmonium Spectroscopy From Radiative Decays of the  $J/\psi$  and  $\psi'$ ”. PhD thesis. SLAC, 1982. URL: <http://www-public.slac.stanford.edu/sciDoc/docMeta.aspx?slacPubNumber=slac-r-255.html>.
- [110] P. D. Dauncey et al. “Handling uncertainties in background shapes: the discrete profiling method”. In: *JINST* 10.04 (2015), P04015. DOI: 10.1088/1748-0221/10/04/P04015. arXiv: 1408.6865 [physics.data-an].
- [111] S. S. Wilks. “The Large-Sample Distribution of the Likelihood Ratio for Testing Composite Hypotheses”. In: *Ann. Math. Statist.* 9.1 (Mar. 1938), pp. 60–62. DOI: 10.1214/aoms/1177732360. URL: <https://doi.org/10.1214/aoms/1177732360>.
- [112] Higgs to Gamma Gamma Working Group. *Further measurement of  $H \rightarrow \gamma\gamma$  at  $\sqrt{13}$  TeV*. CMS Note 2016/209. CERN, 2016. URL: [http://cms.cern.ch/icMS/jsp/db\\_notes/noteInfo.jsp?cmsnoteid=CMS%20AN-2016/209](http://cms.cern.ch/icMS/jsp/db_notes/noteInfo.jsp?cmsnoteid=CMS%20AN-2016/209).

- 2531 [113] *Updated measurements of Higgs boson production in the diphoton decay channel at  $\sqrt{s} =$*
- 2532  $13\text{ TeV}$  in  $pp$  collisions at CMS. CMS Physics Analysis Summary CMS-PAS-HIG-16-020.
- 2533 Geneva: CERN, 2016. URL: <http://cds.cern.ch/record/2205275>.
- 2534 [114] Jon Butterworth et al. “PDF4LHC recommendations for LHC Run II”. In: *J. Phys.* G43 (2016), p. 023001. DOI: 10.1088/0954-3899/43/2/023001. arXiv: 1510.03865 [hep-ph].
- 2535 [115] A. D. Martin et al. “Parton distributions for the LHC”. In: *Eur. Phys. J.* C63 (2009), pp. 189–285. DOI: 10.1140/epjc/s10052-009-1072-5. arXiv: 0901.0002 [hep-ph].
- 2536 [116] Hung-Liang Lai et al. “New parton distributions for collider physics”. In: *Phys. Rev.* D82 (2010), p. 074024. DOI: 10.1103/PhysRevD.82.074024. arXiv: 1007.2241 [hep-ph].
- 2537 [117] Sergey Alekhin et al. “The PDF4LHC Working Group Interim Report”. In: (2011). arXiv: 1101.0536 [hep-ph].
- 2538 [118] Michiel Botje et al. “The PDF4LHC Working Group Interim Recommendations”. In: (2011). arXiv: 1101.0538 [hep-ph].
- 2539 [119] Richard D. Ball et al. “Impact of Heavy Quark Masses on Parton Distributions and LHC Phenomenology”. In: *Nucl. Phys.* B849 (2011), pp. 296–363. DOI: 10.1016/j.nuclphysb.2011.03.021. arXiv: 1101.1300 [hep-ph].
- 2540 [120] Giampiero Passarino. “Higgs Boson Production and Decay: Dalitz Sector”. In: *Phys. Lett.* B727 (2013), pp. 424–431. DOI: 10.1016/j.physletb.2013.10.052. arXiv: 1308.0422 [hep-ph].
- 2541 [121] A.M. Sirunyan et al. “Performance of the CMS muon detector and muon reconstruction with proton-proton collisions at  $\sqrt{s}=13\text{ TeV}$ ”. In: *Journal of Instrumentation* 13.06 (June 2018), P06015–P06015. DOI: 10.1088/1748-0221/13/06/p06015. URL: <https://doi.org/10.1088%2F1748-0221%2F13%2FP06%2Fp06015>.
- 2542 [122] Vardan Khachatryan et al. “Performance of photon reconstruction and identification with the CMS detector in proton-proton collisions at  $\sqrt{s}=8\text{ TeV}$ ”. In: *JINST* 10.CMS-EGM-14-001. CMS-EGM-14-001. CERN-PH-EP-2015-006 (Feb. 2015). Comments: Submitted to JINST, P08010, 59 p. DOI: 10.1088/1748-0221/10/08/P08010. URL: <http://cds.cern.ch/record/1988093>.
- 2543 [123] A L Read. “Presentation of search results: the CL<sub>s</sub> technique”. In: *Journal of Physics G: Nuclear and Particle Physics* 28.10 (Sept. 2002), pp. 2693–2704. DOI: 10.1088/0954-3899/28/10/313. URL: <https://doi.org/10.1088%2F0954-3899%2F28%2F10%2F313>.
- 2544 [124] J. Neyman and E. S. Pearson. “On the Problem of the Most Efficient Tests of Statistical Hypotheses”. In: *Philosophical Transactions of the Royal Society of London. Series A, Containing Papers of a Mathematical or Physical Character* 231 (1933), pp. 289–337. ISSN: 02643952. URL: <http://www.jstor.org/stable/91247>.
- 2545 [125] Glen Cowan et al. “Asymptotic formulae for likelihood-based tests of new physics”. In: *The European Physical Journal C* 71.2 (Feb. 2011), p. 1554. ISSN: 1434-6052. DOI: 10.1140/epjc/s10052-011-1554-0. URL: <https://doi.org/10.1140/epjc/s10052-011-1554-0>.
- 2546 [126] *Procedure for the LHC Higgs boson search combination in Summer 2011*. Tech. rep. CMS-NOTE-2011-005. ATL-PHYS-PUB-2011-11. Geneva: CERN, Aug. 2011. URL: <https://cds.cern.ch/record/1379837>.

- [127] David H. Annis. "Kendall's Advanced Theory of Statistics, Vol. 1: Distribution Theory (6th ed.). Alan Stuart and J. Keith Ord; Kendall's Advanced Theory of Statistics, Vol. 2A: Classical Inference and the Linear Model (6th ed.). Alan Stuart and J. Keith Ord, and Steven F. Arnold". In: *Journal of the American Statistical Association* 101 (2006), pp. 1721–1721. URL: <https://EconPapers.repec.org/RePEc:bes:jnlasa:v:101:y:2006:p:1721-1721>.
- [128] *Procedure for the LHC Higgs boson search combination in Summer 2011*. Tech. rep. CMS-NOTE-2011-005. ATL-PHYS-PUB-2011-11. Geneva: CERN, Aug. 2011. URL: <https://cds.cern.ch/record/1379837>.
- [129] M. Aaboud et al. "Searches for exclusive Higgs and  $Z$  boson decays into  $J/\psi\gamma$ ,  $\psi(2S)\gamma$ , and  $\Upsilon(nS)\gamma$  at  $\sqrt{s} = 13\text{TeV}$  with the ATLAS detector". In: *Physics Letters B* 786 (Nov. 2018), pp. 134–155. ISSN: 0370-2693. DOI: 10.1016/j.physletb.2018.09.024. URL: <http://dx.doi.org/10.1016/j.physletb.2018.09.024>.
- [130] R. Santonico and R. Cardarelli. "Development of resistive plate counters". In: *Nuclear Instruments and Methods in Physics Research* 187.2 (1981), pp. 377–380. ISSN: 0167-5087. DOI: [https://doi.org/10.1016/0029-554X\(81\)90363-3](https://doi.org/10.1016/0029-554X(81)90363-3). URL: <http://www.sciencedirect.com/science/article/pii/0029554X81903633>.
- [131] Marcello Abbrescia, Paulo Fonte, and Vladimir Peskov. *Resistive gaseous detectors: designs, performance, and perspectives*. Weinheim: Wiley-VCH, 2018. DOI: 10.1002/9783527698691.
- [132] A Beroual and I Fofana. "The background of air gap discharge theory". In: *Discharge in Long Air Gaps*. 2053-2563. IOP Publishing, 2016, 2-1 to 2-22. ISBN: 978-0-7503-1236-3. DOI: 10.1088/978-0-7503-1236-3ch2. URL: <http://dx.doi.org/10.1088/978-0-7503-1236-3ch2>.
- [133] Leonard B. Loeb and John M. Meek. "The Mechanism of Spark Discharge in Air at Atmospheric Pressure. I". In: *Journal of Applied Physics* 11.6 (1940), pp. 438–447. DOI: 10.1063/1.1712792. eprint: <https://doi.org/10.1063/1.1712792>. URL: <https://doi.org/10.1063/1.1712792>.
- [134] Dong Hyun, Kim. "Work on CMS Muon Detector (RPC) during Long Shutdown 1 (LS1) - Point 5, Cessy, CMS cavern". CMS Collection. May 2015. URL: <https://cds.cern.ch/record/2016815>.
- [135] P. Bernardini et al. "Precise measurements of drift velocities in helium gas mixtures". In: *Nuclear Instruments and Methods in Physics Research Section A: Accelerators, Spectrometers, Detectors and Associated Equipment* 355.2 (1995), pp. 428–433. ISSN: 0168-9002. DOI: [https://doi.org/10.1016/0168-9002\(94\)01144-3](https://doi.org/10.1016/0168-9002(94)01144-3). URL: <http://www.sciencedirect.com/science/article/pii/0168900294011443>.
- [136] E. Gorini et al. "Drift velocity measurements in C<sub>2</sub>H<sub>2</sub>F<sub>4</sub> based mixtures". In: *Proceedings of the 4th International Workshop on Resistive Plate Chamber and Related Detectors, in Napoli, Italy, 15-16 October* (1997).
- [137] G. Bressi et al. "AN APPARATUS TO SEARCH FOR FREE NEUTRON ANTI-NEUTRON OSCILLATIONS". In: *Nucl. Instrum. Meth. A* 261 (1987), pp. 449–461. DOI: 10.1016/0168-9002(87)90353-6.
- [138] H.L. Ge et al. "The production of residual nuclides in Pb irradiated by 400 MeV/u carbon ions". In: *Nucl. Instrum. Meth. B* 337 (2014), pp. 34–38. DOI: 10.1016/j.nimb.2014.07.024.

- 2614 [139] M. Abbrescia et al. “A Horizontal muon telescope implemented with resistive plate chambers”.  
2615 In: *Nucl. Instrum. Meth. A* 336 (1993), pp. 322–329. DOI: 10.1016/0168-9002(93)91116-5.
- 2616 [140] L. Antoniazzi et al. “The E771 RPC muon detector”. In: *Nucl. Instrum. Meth. A* 315 (1992),  
2617 pp. 92–94. DOI: 10.1016/0168-9002(92)90686-X.
- 2618 [141] A. Di Ciacio et al. “Muon tracking and hadron punchthrough measurements using resistive  
2619 plate chambers”. In: *Nucl. Instrum. Meth. A* 315 (1992), pp. 102–108. DOI: 10.1016/0168-  
2620 9002(92)90688-Z.
- 2621 [142] R. de Asmundis. “Performances of the RPC trigger system in the L3 experiment”. In: *3rd*  
2622 *International Workshop on Resistive Plate Chambers and Related Detectors (RPC 95)*. 1995,  
2623 pp. 139–155.
- 2624 [143] D. Boutigny et al. “BaBar technical design report”. In: (Mar. 1995).
- 2625 [144] Andrea Gelmi. *Longevity studies for the CMS-RPC system*. Tech. rep. CMS-CR-2018-136.  
2626 Geneva: CERN, July 2018. URL: <https://cds.cern.ch/record/2634505>.
- 2627 [145] M.A. Shah et al. “Experiences from the RPC data taking during the CMS RUN-2”. In: *15th*  
2628 *Workshop on Resistive Plate Chambers and Related Detectors*. May 2020. arXiv: 2005.12532  
2629 [*physics.ins-det*].
- 2630 [146] *Public CMS Data Quality Information*. twiki.cern.ch/twiki/bin/view/CMSPublic/DataQuality.  
2631 Acessado em: 20/02/2018.
- 2632 [147] Johannes Guteleber, Steven Murray, and Luciano Orsini. “Towards a homogeneous archi-  
2633 tecture for high-energy physics data acquisition systems”. In: *Computer Physics Commu-*  
2634 *nications* 153.2 (2003), pp. 155–163. ISSN: 0010-4655. DOI: [https://doi.org/10.1016/S0010-4655\(03\)00161-9](https://doi.org/10.1016/S0010-4655(03)00161-9). URL: <http://www.sciencedirect.com/science/article/pii/S0010465503001619>.
- 2637 [148] *Dojo*. <https://dojotoolkit.org/>. Acessado em: 20/02/2018.
- 2638 [149] *Polymer Project*. Acessado em: 20/02/2018.
- 2639 [150] M. I. Pedraza-Morales. *RPC upgrade project for CMS Phase II*. 2018. arXiv: 1806.11503  
2640 [*physics.ins-det*].
- 2641 [151] Dorothea Pfeiffer et al. “The radiation field in the Gamma Irradiation Facility GIF++ at  
2642 CERN”. In: *Nuclear Instruments and Methods in Physics Research Section A: Accelerators,*  
2643 *Spectrometers, Detectors and Associated Equipment* 866 (2017), pp. 91–103. ISSN: 0168-9002.  
2644 DOI: <https://doi.org/10.1016/j.nima.2017.05.045>. URL: <http://www.sciencedirect.com/science/article/pii/S0168900217306113>.
- 2646 [152] A. Augusto Alves Jr. et al. “The LHCb Detector at the LHC”. In: *JINST* 3 (2008), S08005.  
2647 DOI: 10.1088/1748-0221/3/08/S08005.
- 2648 [153] Georges Charpak et al. “The Use of Multiwire Proportional Counters to Select and Localize  
2649 Charged Particles”. In: *Nucl. Instrum. Meth.* 62 (1968), pp. 262–268. DOI: 10.1016/0029-  
2650 554X(68)90371-6.
- 2651 [154] *LHCb Muon Group Home Page*. [Online; accessed 1-October-2019]. 2019. URL: <http://lhcb-muon.web.cern.ch/lhcb-muon/>.
- 2653 [155] *CAEN Programmable Logic Unit - V2495*. [Online; accessed 1-October-2019]. 2019. URL:  
2654 <https://www.caen.it/products/v2495/>.

- 2655 [156] *Resistive Plate Chambers are getting dolled up.* <https://cms.cern/news/resistive-plate-chambers-are-getting-dolled>. Acessado em: 20/09/2019.
- 2656
- 2657 [157] C. Binetti et al. “A new Front-End board for RPC detector of CMS”. In: (Sept. 1999).
- 2658 [158] *Flask (web framework)*. [Online; accessed 1-October-2019]. 2019. URL: <https://palletsprojects.com/p/flask/>.
- 2659

DRAFT